

AD_____

Award Number: DAMD17-98-1-8156

TITLE: Energy- and Intensity- Modulated Electron Beam for Breast
Cancer Treatment

PRINCIPAL INVESTIGATOR: Chang Ming Ma, Ph.D.

CONTRACTING ORGANIZATION: Stanford University
Stanford, California 94305-5401

REPORT DATE: October 1999

TYPE OF REPORT: Annual

PREPARED FOR: U.S. Army Medical Research and Materiel Command
Fort Detrick, Maryland 21702-5012

DISTRIBUTION STATEMENT: Approved for public release
distribution unlimited

The views, opinions and/or findings contained in this report are those of the author(s) and should not be construed as an official Department of the Army position, policy or decision unless so designated by other documentation.

20010419 049

REPORT DOCUMENTATION PAGEForm Approved
OMB No. 074-0188

Public reporting burden for this collection of information is estimated to average 1 hour per response, including the time for reviewing instructions, searching existing data sources, gathering and maintaining the data needed, and completing and reviewing this collection of information. Send comments regarding this burden estimate or any other aspect of this collection of information, including suggestions for reducing this burden to Washington Headquarters Services, Directorate for Information Operations and Reports, 1215 Jefferson Davis Highway, Suite 1204, Arlington, VA 22202-4302, and to the Office of Management and Budget, Paperwork Reduction Project (0704-0188), Washington, DC 20503

1. AGENCY USE ONLY (Leave blank)**2. REPORT DATE**
October 1999**3. REPORT TYPE AND DATES COVERED**
Annual (01 Oct 98 - 30 Sep 99)**4. TITLE AND SUBTITLE**Energy- and Intensity- Modulated Electron
Beam for Breast Cancer Treatment**5. FUNDING NUMBERS**

DAMD17-98-1-8156

6. AUTHOR(S)

Chang Ming Ma, Ph.D.

7. PERFORMING ORGANIZATION NAME(S) AND ADDRESS(ES)Stanford University
Stanford, California 94305-5401**e-mail:**

cma@Reyes.stanford.edu

**8. PERFORMING ORGANIZATION
REPORT NUMBER****9. SPONSORING / MONITORING AGENCY NAME(S) AND ADDRESS(ES)**U.S. Army Medical Research and Materiel Command
Fort Detrick, Maryland 21702-5012**10. SPONSORING / MONITORING
AGENCY REPORT NUMBER****11. SUPPLEMENTARY NOTES**

This report contains colored photos

12a. DISTRIBUTION / AVAILABILITY STATEMENTApproved for public release
distribution unlimited**12b. DISTRIBUTION CODE****13. ABSTRACT (Maximum 200 Words)**

This project is aimed at exploring energy- and intensity-modulated radiotherapy (EIMRT) to deliver dose distributions that closely match the target volume and minimize the dose to critical normal structures. The scope includes (1) to characterize electron beams from Helium-filled accelerators for EIMRT, (2) to develop optimization algorithms for EIMRT using these electron beams, (3) to verify these optimized dose distributions using the Monte Carlo simulation technique, and (4) to compare the optimized dose plans obtained by EIMRT with conventional treatment plans and those obtained by photon intensity-modulated radiotherapy (IMRT). During the first year research, we have performed accurate Monte Carlo simulations of the electron beams in He-filled accelerators. Our results demonstrated that electron beams could be modulated to deliver superior dose distributions for EIMRT. We have implemented practical source models for clinical application and beam commissioning. Different dose algorithms have been compared for "Inverse treatment planning" beamlet calculations. The results confirmed that the Monte Carlo method is needed to generate the dose distributions for EIMRT. Further studies will be performed to verify the dose plans for realistic patients. The outcome will determine whether EIMRT offers a significant advantage over conventional photon/electron treatment and over photon IMRT.

14. SUBJECT TERMS

Breast Cancer

15. NUMBER OF PAGES

197

16. PRICE CODE**17. SECURITY CLASSIFICATION
OF REPORT**

Unclassified

**18. SECURITY CLASSIFICATION
OF THIS PAGE**

Unclassified

**19. SECURITY CLASSIFICATION
OF ABSTRACT**

Unclassified

20. LIMITATION OF ABSTRACT

Unlimited

FOREWORD

Opinions, interpretations, conclusions and recommendations are those of the author and are not necessarily endorsed by the U.S. Army.

MM Where copyrighted material is quoted, permission has been obtained to use such material.

_____ Where material from documents designated for limited distribution is quoted, permission has been obtained to use the material.

CM Citations of commercial organizations and trade names in this report do not constitute an official Department of Army endorsement or approval of the products or services of these organizations.

_____ In conducting research using animals, the investigator(s) adhered to the "Guide for the Care and Use of Laboratory Animals," prepared by the Committee on Care and use of Laboratory Animals of the Institute of Laboratory Resources, national Research Council (NIH Publication No. 86-23, Revised 1985).

_____ For the protection of human subjects, the investigator(s) adhered to policies of applicable Federal Law 45 CFR 46.

_____ In conducting research utilizing recombinant DNA technology, the investigator(s) adhered to current guidelines promulgated by the National Institutes of Health.

_____ In the conduct of research utilizing recombinant DNA, the investigator(s) adhered to the NIH Guidelines for Research Involving Recombinant DNA Molecules.

_____ In the conduct of research involving hazardous organisms, the investigator(s) adhered to the CDC-NIH Guide for Biosafety in Microbiological and Biomedical Laboratories.

 10/14/98

PI - Signature Date

Table of Contents

FRONT COVER	1
STANDARD FORM (SF) 298	2
FOREWORD.....	3
TABLE OF CONTENTS	4
INTRODUCTION.....	5
BODY.....	5
KEY RESEARCH ACCOMPLISHMENTS	14
REPORTABLE OUTCOMES.....	15
CONCLUSIONS	18
REFERENCES	19
APPENDICES	21
<i>List of Figures quoted in the body of text:</i>	21
<i>List of manuscripts submitted with this report:</i>	30

Introduction

Radiation therapy has been used for the treatment of all stages of localized breast cancer. Breast conservation with lumpectomy followed by radiation (BCT) has proven to be effective for early stage (T1 – T2) patients. This project is aimed at exploring energy- and intensity-modulated electron beams to deliver optimized conformal radiotherapy dose distributions that closely match the target volume and minimize the dose to critical normal structures. The specific aims are (1) to characterize electron beams from Helium-filled accelerators, (2) to develop optimization algorithms for energy- and intensity-modulated radiotherapy (EIMRT) using these electron beams, (3) to verify these optimized dose distributions using the Monte Carlo simulation technique, and (4) to compare the optimized dose plans obtained by EIMRT with conventional treatment plans and those obtained by photon intensity-modulated radiotherapy (IMRT).

Body

Photon beams have been an effective modality for breast cancer treatment in radiation therapy while electron beam are occasionally used for a boost dose when the photon beams are intentionally placed to miss part of the target in order to reduce the dose to the lung and heart. Although such conventional treatment with tangential photon fields has been successful. The following problems (or potential areas of improvement) remain: (1) the inclusion of the lung and sometimes of a small volume of the heart in the high-dose volume due to tumor location, patient size or in the case of chest-wall treatments; (2) lower dose near the skin surface due to lack of electron build-up in a photon beam; and (3) high exit or scatter dose to the normal structures such as the lung and heart, and more importantly the contralateral breast, which may be a major cause for the occurrence of secondary cancer in the contralateral breast for women under the age of 45.

Advances in the state of the art of computer-controlled medical linear accelerators have recently available that, along with newly-developed treatment planning techniques, may provide significant improvements in the delivery and control of external beam radiation through beam-intensity modulation¹⁻⁹. It is expected that using photon IMRT, the problem (1) above may be significantly improved but (2) will remain and (3) may become more serious as treatment time increases with the number of fields used (increased leakage or scattering dose). With modulated electron beams¹⁰⁻¹⁵, on the other hand, problem (1) may also be significantly improved and problems (2) and (3) can be

completely eliminated due to the nature of electron beams.

We hypothesized that by using He-filled accelerators equipped with computer-controlled multi-leaf collimators and the Monte Carlo treatment planning technique, energy- and intensity-modulated electron beams may be optimized to significantly improve the dose uniformity in the target volume, to exclude the lung and heart from the high or moderate dose volume and to eliminate the scatter dose to the lung, the heart and the contralateral breast to reduce complications and late effects associated with breast cancer radiotherapy. The purpose of this study is to determine the degree of feasibility of using electron EIMRT to improve breast cancer treatment.

This project has 4 specific aims: (1) To perform Monte Carlo beam simulation; (2) To develop an optimization algorithm for EIMCRT; (3) To perform Monte Carlo dose verifications; and (4) To evaluate the optimized treatment plans.

We report on the research accomplishments associated with the tasks outlined in the approved "Statement of Work" below:

1. Simulation of realistic electron beams from He-filled clinical accelerators

The EGS4¹⁶ BEAM¹⁷ system has been used in this work to investigate the electron beams from clinical linear accelerators. The BEAM code produces a phase-space output of the beam (i.e., the energy, charge, position, direction, and a tag called LATCH to record the particle history) at any specified plane in a simulation geometry. The simulation geometry may consist of a series of individual component modules (CMs) positioned perpendicularly to the beam axis. The CMs used in this work to simulate the clinical linear accelerators included SLABS and CONESTAK for electron scattering foils, CONESTAK for photon target and primary collimators, and shielding rings, FLATFILT for photon flattening filters, CHAMBER for the monitor chamber, and dose simulation phantoms, APPLICAT for electron applicators, JAWS for the secondary photon collimators, MLC for the multileaf collimator, MIRROR for the light mirror and BLOCK for electron cutouts. The actual dimensions and materials used for each of the components were handled by an input data file, which also contained the parameters required for the Monte Carlo transport simulations such as the energy cutoffs for electron (ECUT) and photon (PCUT) transport, minimum energy for creation of knock on electrons (AE) or bremsstrahlung photons (AP), maximum electron step length (SMAX), maximum energy loss per

electron step (ESTEPE), and the incident beam parameters. The simulated phase-space data can be used as source input for further BEAM simulations or dose calculations using the code DOSXYZ (see below) or analyzed using various software such as BEAMDP (BEAM Data Processor) to derive particle energy spectra, fluence and angular distributions.

The EGS4/DOSXYZ code system was designed for dose calculations in a 3D rectilinear voxel geometry^{17,20}. Voxel dimensions are completely variable in all three directions. Every voxel (volume element) can be assigned to a different material. The cross-section data for the materials used are available in a pre-processed PEGS4 cross-section data file. The density of the material defaults to that in the PEGS4 data file but can be varied in a DOSXYZ calculation for use with the patient's CT data although the density effect corrections for the stopping powers of the material remain unchanged^{18,24}. The phase-space data obtained from a BEAM simulation can also be used as a source input to imitate all possible beam positions and directions from the linear accelerator. Dose contributions from different beam components were selectively calculated based on the particle charge or the LATCH settings specified in the BEAM simulation. DOSXYZ produced a data file that contained geometry specifications such as the number of voxels in all the three directions and their boundaries as well as the dose values and the associated (1σ) statistical uncertainties in the individual voxels.

We have simulated 6 – 20 MeV electron beams from Varian Clinac 2100C and 2300CD clinical accelerators. We have replaced the air in the treatment head and in the gap between the treatment head and the patient with Helium to study the effect of air scattering in air and the potential improvement with He-filled accelerators. Figure 1 (see Appendix) shows the calculated planar fluence distributions at a source-detector distance of 90 cm for 10.08 MeV electrons from the Clinac 2300. The thick solid histogram represents standard geometry (case 1) and the thin solid histogram represents helium atmosphere (case 2). The fluence distributions can be significantly improved by replacing the air in the linac head with Helium. This is especially important for lower incident electron energies (below 10 MeV) and large gaps between the treatment head and the patient^{19,21-24}.

We have also investigated the effect of the MLC leaf shape on the beam profiles. The Varian MLC has rounded leaf ends while the MLCs from other manufacturers have double focused leaf shape. Figure 2 shows the calculated dose distributions at phantom surface for a 20 MeV electrons from the Clinac 2100CD accelerator (see Appendix). The blue histogram represents a focused photon MLC and the red histogram represents unfocused photon MLC (straight edge). For comparison, a specially designed electron MLC with straight edge was also simulated with 7 cm air gap (i.e., at the electron applicator

level). The photon MLC simulations were performed for a 20 cm He gap. It is clear that focused MLC will result in significant improvement in the dose profile for modulated electron beams. Unfocused MLC will degrade the dose profiles near the beam penumbra and the effects can be seen at different depths. This means the Varian MLC rounded leaf shape has to be modified if it is used to deliver modulated electron beams.

Although this work is designed to investigate the feasibility of He-filled accelerators for energy and intensity modulated electron beam therapy. The results have been presented to the accelerator manufacturers for evaluation. Possibilities have been discussed regarding fill the accelerator with He by sealing the treatment head or installing a He-filled balloon. Further studies will be made when the sealing (or balloon) materials and thicknesses are known.

2. Commission simulated beam data by comparisons with measurements

In order to commission the simulated the clinical beams, we have compared the dose distributions simulated by the Monte Carlo method and those measured using ion chambers and diodes. The calculations were performed using the DOSXYZ user code. The simulation parameters were modified to improve the simulated beam data to match the measured data until the two sets of data agreed with each other to within 2% of the maximum dose. We have also compared the dose distributions in heterogeneous phantoms. Figure 3 shows the heterogeneity correction factors for layered lung or layered bone phantoms irradiated by 12 MeV electron beams (see Appendix). They are calculated as ratios of the doses in a heterogeneous phantom to the doses in a water phantom calculated by Monte Carlo, by FOCUS (3D pencil beam) and by measurements. Figure 3a is for a layered-bone phantom for a $3\text{ cm} \times 3\text{ cm}$ field and Figure 3b is for a layered-lung phantom for a $3\text{ cm} \times 3\text{ cm}$ field. The field size was defined at 100 cm SSD. The results clearly demonstrate that the Monte Carlo method can faithfully reproduce the dose distributions in these phantoms while the conventional dose calculations may significantly underestimate or overestimate the dose in or near heterogeneous regions. These findings are consistent with the previous results²²⁻²⁶.

3. Study the characteristics of intensity-modulated electron beams

We have studied the characteristics of small field electron beams collimated by blocks and an electron

MLC. We have studied the beam profiles from different MLC leaf shapes. It is found that the MLC shape will affect the dose profile near the phantom surface but have little effect on the dose profiles at depth beyond the depth of maximum dose. This supports the idea of using a photon MLC or an electron MLC to deliver small field electron beams to form intensity modulated electron fields. We show in Fig. 4 the dose distributions for a 2 cm x 2 cm field and a 4 cm x 4 cm field collimated by a photon MLC and an electron MLC (see Appendix). The difference between these dose distributions is insignificant clinically. Fig. 5 shows the dose distributions formed by four 1 cm x 1 cm fields and those formed by one 1 cm x 4 cm field. The dose distributions are identical at depths beyond the depth of maximum dose but are slightly different on the surface – the four small fields give more fluctuations. However, the leakage dose outside the treatment is more significant for the multiple small fields because of the longer delivery time. This leakage can be reduced by increasing the MLC leaf thickness.

4. Characterize the simulated beams using simplified source models

A multiple source model was developed by Ma et al for electron beam Monte Carlo treatment planning¹⁹. The algorithm has been further improved by Jiang et al²⁶ for beam commissioning in clinical routine dose calculations. A hybrid approach for commissioning electron beam Monte Carlo treatment planning systems is studied. The approach is based on the assumption that accelerators with similar designs have similar electron beam characteristics. For one type of accelerators, a reference machine is selected and simulated with the Monte Carlo method. A beam model is built for this type of accelerators using the Monte Carlo simulated phase space information for the reference machine. When commissioning another accelerator of the same type, the appropriate parameters in the beam model are tuned according to the standard measured data such as output factors, depth-dose and dose profiles. A Varian Clinac 2100C accelerator is chosen as the reference machine and simulated using the EGS4/BEAM code. A four-source beam model is established based on the simulated beam information to reconstruct electron phase space down to the last applicator scraper. The model includes a point electron source for direct electrons and electrons scattered from the primary collimator and jaws, a point photon source for all contaminant bremsstrahlung photons, and two square ring electron sources representing electrons scattered from the two scrapers above the last scraper. A Varian Clinac 2300C/D machine, which is similar in design to the reference machine, is commissioned using this beam model. By tuning the appropriate parameters in the model, accurate dose calculation is achieved using the model, compared to the corresponding measurement.

In this work, we have characterized the Monte Carlo simulated beams using this improved source model. We have compared the dose distributions calculated using the source model and the original simulated phase space data and achieved good agreement (within 2% of maximum dose). Figure 6 shows the dose distributions calculated by the Monte Carlo method using our source model and the dose distributions calculated using the original simulated phase space beam data at 3.2 cm in a water phantom for a 12 MeV electron beam from the Clinac 2100C (see Appendix). The dose distributions calculated by the source model and measured by an ion chamber for a 12 MeV electron beam from a Varian Clinac 2300CD accelerator are also shown. The agreement was within 1% for both cases. Similar results have been obtained for other beam energies and field sizes (not shown). This demonstrated the validity of the source model for beam commissioning for this study.

5. Install and test MCDOSE for photon calculations

We have further developed a Monte Carlo EGS4 user code MCDOSE for photon/electron beamlet and treatment plan dose calculations. Good agreement was achieved between the MCDOSE results and measurements. The MCDOSE code has been implemented on a 32-PC network for Monte Carlo dose calculations. Features of MCDOSE include a multiple-source model to reconstruct the beam phase space, inclusion of beam modifiers such as jaws, wedges, blocks, compensators and electron cutouts in the patient simulation, the implementation of several variance reduction techniques, and suitable for both conventional and intensity modulated radiation therapy (IMRT) treatment planing. Before MCDOSE is used reliably for dose calculation in clinic, it must be properly validated. The clinical validations for beam modifiers and dose calculation are presented. A comparison of the dose distribution with 45-degree wedge in a water phantom made between MCDOSE and EGS4/BEAM/DOSXYZ^{17,20} demonstrates that MCDOSE can give accurate result with wedge. The dose distributions for a blocked 10x10 15MV photon beam in a water phantom are also compared between them. They agree very well. The comparison of Electron cutout factors between MCDOSE and measurements show a good agreement too. After applying variance reduction techniques in MCDOSE, the agreement of dose distributions in specifically designed inhomogeneous phantoms between MCDOSE and DOSXYZ is within the statistical uncertainty of 0.5%. All these results demonstrate that MCDOSE is accurate for routine dose calculation in radiotherapy treatment planing. The heterogeneity correction factors calculated by MCDOSE for layered-lung or layered-bone phantoms were consistent with results from measurement to within 1%. Due to the elegant variance reduction techniques, MCDOSE is also faster than EGS4/DOSXYZ²⁰ dose calculation by a factor of

up to 30. A nine field IMRT planing can be done in 1-4 hours on a personal computer, including pre- and post-optimization dose calculation.

To test the accuracy of dose calculation by the MCDOSE code, comparison calculations were performed with DOSXYZ, which is an EGS4 usercode developed by the NRCC group and well benchmarked by the radiotherapy investigators. Each example has been calculation with source surface distance (SSD) of 100cm and field size of 6cm x 6cm or 10 cm x 10cm. The global electron cut off energy (ECUT) was set to 0.7MeV and photon cut off energy (PCUT) was set to 0.01MeV in MCDOSE and DOSXYZ respectively. The fractional energy loss per step (ESTEPE) was limited to 40% for DOSXYZ and 20% for MCDOSE. The maximum step size (SMAX) is set to default 5cm for DOSXYZ and 2mm for MCDOSE. Voxel size in the phantom is set to 4mm x 4mm x 5mm. The material compositions and densities are taken from ICRU Report No. 46. Mono-energetic point sources and phase space files, multiple source models for Clinac 2300C/D linear accelerator are used as input to do simulation. Since dose per incident fluence is calculated, absolute dose distributions produced by MCDOSE and DOSXYZ are compared. Fig. 7 Depth dose curves in tissue-bone-tissue phantoms calculated by DOSXYZ and MCDOSE for 15MeV and 6MeV electron beams with field size 6 cm x 6 cm. For 15MeV electron beam, the material from depth 2.7cm to 4.5cm is bone in the phantom. For 6MeV electron beam, the material is bone between depth 0.6cm and 1.6cm. Fig. 8 shows the dose profiles at depths 3.4cm and 5.0cm in a tissue-bone-tissue phantom calculated by DOSXYZ and MCDOSE for the same calculations (see Appendix).

Initial schedule included the implementation of the PEREGRINE code system for this study. This was not done because of the delay of the commercial availability of the PEREGRINE system and the complication of the commercialization of the PEREGRINE system. The system has been exclusively licensed to the NOMOS, Corp. and it is no longer available as a free software. Instead, we have developed the MCDOSE system, which is based on the EGS4 system, which is free for research and education use. The MCDOSE code has been validated against the DOSXYZ code and proved to be equally accurate but about 20 times faster in computation speed. This is therefore our suggestion to replace the PEREGRINE software with MCDOSE for this study.

6. Evaluate dose calculation algorithms for optimization calculation

We have compared the dose distributions calculated by the conventional dose calculation algorithms

(the pencil beam algorithm in a commercial treatment planning system, the FOCUS system by Computerized Medical System, St. Luis, MO) and the Monte Carlo method (with MCDOSE). It was found the dose distributions predicted by the pencil beam were very uncertain under the conditions of extended source surface distance (SSD), oblique incidence and for heterogeneous phantoms^{15,18,21,22}. We have calculated dose distributions for different field sizes, incident beam energies, SSDs and phantom geometries. Figure 9 shows the pencil beam dose distributions calculated by the FOCUS system and the Monte Carlo system for a 20 MeV electron beam (see Appendix). Monte Carlo correctly predicted the dose variations near the interface between tissue and air and between tissue and bone while the FOCUS calculation shows almost symmetrical distributions in these cases. It is concluded that Monte Carlo is needed for the electron beamlet calculation to ensure the accuracy of the optimization process. In our future studies, we have scheduled to compare dose distributions using these algorithms and the optimization algorithms for realistic patient treatment plans.

7. Develop fast iterative optimization algorithms

A fast iterative optimization algorithm has been developed for electron beam optimization. The algorithm has been tested for both electron treatment planning optimization and photon beam optimization. The dose calculation can be cast as the matrix equation,

$$\mathbf{D} = \mathbf{M} \cdot \mathbf{I}$$

where \mathbf{D} is the vector whose elements are the dose deposited in the voxels in the calculation volume, \mathbf{I} is the vector whose elements are the beamlet weights, and \mathbf{M} is the matrix relating the weights of each beamlet to the dose deposited in each voxel. Using the Monte Carlo method, the individual beamlet distributions that make up the matrix elements of \mathbf{M} will be calculated separately taking into considerations of the location of the beamlet in the field, patient contour, inhomogeneous patient anatomy, organ motion and patient setup uncertainty. The beamlet dimensions will be specified through the RTP module, based on the MLC leaf width. For the Varian MLC, the beamlet size will be variable between 10mm x 1mm and 10mm x 10mm. The beamlet profile will be different depending on the location of the beamlet (its slight spatial dependence on the accelerator head scatter, beam flatness and SSD variation). This will be automatically included when using the simulated phase-space data as source input. The MCDOSE code has been modified for the dose calculations in the patient. The beam incident angles and patient CT data will be obtained from the RTP system. Each beamlet will require 1 – 10 million phase space photons depending on the dimensions of the beamlet. For a typical IMRT case with 9 gantry angles, the beamlet calculation (for 1 – 10 thousand beamlets) will be

completed in a few minutes on the PC network after the variance reduction techniques are implemented.

Our optimization procedure developed to calculate the optimal intensity profiles consists of the following two stages. First, the planner inputs the patient geometry and defines the treatment setup, such as the beam energy, number and orientations of beams, etc. The target volume and the critical structures are defined by the clinician. The planner also determines the size of the beamlets and number of dose or constraint points placed inside the target or critical structures, according to the patient anatomy, the required computation accuracy and the available computation time. Each broad beam is divided into beamlets and the dose and constraint points are uniformly and randomly placed inside the corresponding area. Then a reference monitor unit is assigned to each open rectangular beam and the dose deposition coefficients, which is defined as the dose contribution from a beamlet to a point, are calculated using MCDOSE and a conventional dose calculation model for comparison.

Second, using the calculated dose deposition coefficients as input, the optimal intensity profile for each beam is achieved by using the Zangwill's penalty function method and the center-of-mass method to minimize the augmented objective function. An improved conjugate vector method will also be investigated. For the target area, a quadratic form of objective function is specified. In addition, two target dose-uniformity constraints are used to ensure a uniform target dose distribution and to distinguish the clinical importance of cold and hot spots. For the critical structures, maximum-dose constraint and several levels of dose-volume constraints are assigned to each structure. For each objective function and constraint, an importance weight relative to the target objective function is assigned. All the constraints are mathematically transformed to the penalty functions of quadratic forms. The augmented objective function, which should be minimized, is a combination of the original objective functions and all penalty functions. The results of the optimization process are the intensity profiles for the individual gantry angles (photon fields).

After the optimization calculation, beam intensity maps at each gantry angle (the elements of \mathbf{I}) will be generated and leaf-setting sequences will be computed using a leaf sequencing algorithm. The final dose calculation will be performed again using MCDOSE. The effect associated with leaf and jaw movement will be accounted for in these calculations. Figure 10 (see Appendix) shows the intensity map of a photon field calculated by the optimizer and the real intensity map measured using a BEAM Imaging System. The intensity patterns were blurred because of the extended source^{27,28}, photon

scattering and leakage through the leaves, which may cause a change in the dose profile delivered by a few percent. Figure 11 shows the Monte Carlo simulated intensity map which agrees well with the measured map.

The monitor units MU_k required for the k^{th} field can be calculated using the following equation:

$$MU_k = D_p w_k F_k / (N S_p)$$

The weight assigned to the k^{th} field, w_k , will be the maximum weight for the beamlets included in field k . The plan normalization factor, N , will be the ratio of the Monte Carlo calculated maximum dose in the patient to that in water under the reference conditions. The modulation scaling factor, F_k , will be the ratio of the total MUs required to deliver all the beamlets in field k using the leaf-setting sequence to the MUs required to deliver the beamlet that has the maximum weight. In preliminary tests, the Monte Carlo calculated output factors for fields 1 cm x 1 cm to 40 cm x 40 cm agreed to within 2% with measurements. No fudge factors will be needed in the Monte Carlo based monitor unit calculations. The dose values for different beam energies under the reference conditions will be calculated only once and stored in the system database for calculating the normalization factor N .

We have been evaluating different leaf sequencing algorithms suitable for both “stop and shoot” and dynamic delivery. A new algorithm also synchronizes the leaf sequences to remove the “tongue and groove” effect. The results showed that the difference in the beam delivery time using a dynamic MLC between “stop and shoot” (including beam-off time for leaf movement) and dynamic delivery was clinically insignificant. We will install a leaf sequence algorithm for our project which uses the stop and shoot algorithm and also synchronizes the leaf’s movement to remove the “tongue and groove” effect. We will further work on other MLCs when the leaf sequence file format becomes available for operation with electron beams.

Key Research Accomplishments

We have accomplished the following tasks:

- *Simulation of realistic electron beams from He-filled clinical accelerators:* We have simulated 6 – 20 MeV electron beams from a Varian Clinac 2100C clinical accelerator. We have replaced the air in the treatment head and in the gap between the treatment head and the patient with Helium to study the effect of air scattering in air and the potential improvement with He-filled accelerators.

- *Commission simulated beam data by comparisons with measurements:* We have compared the dose distributions simulated by the Monte Carlo method and those measured using ion chambers and diodes. The simulation parameters were modified to improve the simulated beam data to match the measured data until the two sets of data agreed with each other to within 2% of the maximum dose.
- *Study the characteristics of intensity-modulated electron beams:* We have studied the characteristics of small field electron beams collimated by blocks and an electron MLC. We have studied the beam profiles from different MLC leaf shapes.
- *Characterize the simulated beams using simplified source models:* We have developed simplified source models for all clinical electron beams simulated with the Monte Carlo method. We have compared the dose distributions calculated using the source model and the original simulated phase space data and achieved good agreement (within 2% of maximum dose).
- *Install and test MCDOSE for photon calculations:* We have further developed a Monte Carlo EGS4 user code MCDOSE for photon/electron beamlet and treatment plan dose calculations. Good agreement was achieved between the MCDOSE results and measurements.
- *Evaluate dose calculation algorithms for optimization calculation:* We have compared the dose distributions calculated by the conventional dose calculation algorithms (the pencil beam algorithm) and the Monte Carlo method (with MCDOSE). It is concluded that Monte Carlo is needed for the electron beamlet distribution calculation to ensure the accuracy of the optimization process.
- *Develop fast iterative optimization algorithms:* A fast iterative optimization algorithm has been developed for electron beam optimization. The algorithm has been tested for both electron treatment planning optimization and photon beam optimization.

Reportable Outcomes

Peer-reviewed papers resulting from or supported in part by this grant:

- C.-M. Ma, E. Mok, A. Kapur, T. Pawlicki, D. Findley, S. Brain, K. Forster and A.L. Boyer, Clinical implementation of a Monte Carlo treatment planning system, Med. Phys. 26: 2133-43 (1999)
- C.-M. Ma and S.B. Jiang, Topical review: Monte Carlo modeling of electron beams from medical accelerators, Phys. Med. Biol., 45: (Dec) (1999) in press
- A. Kapur and C.-M. Ma, Stopping-powers for clinical electron beams for a scatter-foil linear accelerator, Phys. Med. Biol., 45:2321-41 (1999)
- C.-M. Ma, T. Pawlicki, S.B. Jiang, E.Mok, A. Kapur, L. Xing, L. Ma and A.L. Boyer, Verification of IMRT dose distributions using Monte Carlo simulations, Phys. Med. Biol., (1999) submitted
- S.B.Jiang, A. Kapur and C.-M. Ma, Electron beam modelling and commissioning for Monte Carlo treatment planning, Med. Phys. (1999) accepted
- S.B.Jiang, J. Deng, A. L. Boyer and C.-M. Ma, An extrafocal source model for photon beam dose calculation, Med. Phys. (1999) submitted

Meeting abstracts resulting from or supported in part by this grant:

- C.-M. Ma, T. Pawlicki, S.B. Jiang, E.Mok, A. Kapur, L. Xing, L. Ma and A.L. Boyer, Verification of IMRT dose distributions using Monte Carlo simulations, ASTRO Annual Meeting (Phoenix, AZ, 1998)
- S.B.Jiang, A. Kapur and C.-M. Ma, Electron beam modelling and commissioning for Monte Carlo treatment planning, AAPM Annual Meeting (Nashville, TN, 1999)
- S.B.Jiang, J. Deng, A. L. Boyer and C.-M. Ma, An extrafocal source model for photon beam dose calculation, AAPM Annual Meeting (Nashville, TN, 1999)

- J. Deng, S.B.Jiang, J.S. Li, T. Pawlicki and C.-M. Ma, Photon beam characterization and modeling for Monte Carlo treatment planning, AAPM Annual Meeting (Nashville, TN, 1999)
- C.-M. Ma, S.B. Jiang, T. Pawlicki, S.B. Jiang, J.S. Li, J. Deng, E.Mok, A. Kapur, G. Luxton and A.L. Boyer, MCDOSE- a Monte Carlo dose calculation tool for radiotherapy treatment planning, AAPM Annual Meeting (Nashville, TN, 1999)
- C.-M. Ma, S.B. Jiang, T. Pawlicki, S.B. Jiang, J.S. Li, J. Deng, E.Mok, A. Kapur, M. Lee, G. Luxton and A.L. Boyer, Energy- and intensity-modulated electron beams for treatment breast cancer, ASTRO Annual Meeting (San Antonio, TX, 1999)
- C.-M. Ma, Monte Carlo as a QA tool for radiotherapy treatment planning, ESTRO Biannual Physics Meeting Symposium on treatment planning QA, (Göttingen, Germany, 1999)
- C.-M. Ma, Monte Carlo treatment planning for electron beam radiotherapy, AAPM Annual Meeting Symposium on Monte Carlo treatment planning, (Nashville, TX, 1999)

Funding applied for based on work resulting from or supported in part by this grant:

1. US Army Breast Cancer Research Program: Postdoctoral Training Grant (PI: S.B. Jiang; Mentor: C.-M. Ma): Investigation of an electron MLC for energy and intensity modulated electron beam radiotherapy of breast cancer
2. US Army Breast Cancer Research Program: Postdoctoral Training Grant (PI: T. Pawlicky; Mentor: C.-M. Ma): Effect of organ motion and patient setup uncertainty on the treatment of breast cancer with energy and intensity modulated electron beam radiotherapy

Conclusions

We have made significant progress during our first-year investigation. We have successfully performed the tasks scheduled in the “Statement of Work”. We have simulated the electron beam characteristics for energy and intensity modulated radiotherapy (EIMRT) by simulating medical accelerators with different MLC leaf designs and filling gases (air or He). We have characterized our electron beams using a well tested source model. We have implemented new dose calculation software for dose calculations to optimize treatment plans for EIMRT of breast cancer. The new software replaces the scheduled PEREGRINE software and provides not only the capability of performing photon dose calculation but electron dose calculations (the PEREGRINE system is designed only for photon dose calculations). The new software is also significantly (a factor of 20-30) faster than the PEREGRINE system. We have developed optimization algorithms for comparisons of the optimized treatment plans with photon IMRT or electron EIMRT.

“So what?”

Our first year results have provided evidence to support the hypothesis of this proposal that by using He-filled accelerators equipped with computer-controlled multi-leaf collimators and the Monte Carlo treatment planning technique, energy- and intensity-modulated electron beams may be optimized to significantly improve the dose uniformity in the target volume, to reduce the dose to the critical structures nearby and therefore reduce the late effects associated with breast cancer radiotherapy. Further studies as scheduled in the “Statement of Work” are needed to investigate suitable objective functions for electron beam optimization and to verify photon IMRT and electron EIMCART dose plans using EGS4/DOSXYZ and MCDOSE. By comparing the treatment plans for realistic breast cases generated using different beam modalities, we shall be able to finally determine the degree of feasibility of using electron EIMRT to improve breast cancer treatment.

References

1. R Boesecke, G Becker, K Alandt, *et al.* Modification of a three-dimensional treatment planning system for the use of multileaf collimators in conformation radiotherapy. *Radioth. and Oncol.* 21:261-268, 1991.
2. AL Boyer, TG Ochrn, CE Nyerick and TJ Waldron. Clinical dosimetry for implementation of a multileaf collimator. *Med. Phys.* 19:1255-1261, 1992.
3. A Brahme. Optimal setting of multileaf collimators in stationary beam radiation therapy. *Strahlenther. Onkol.* 164:343-350, 1988.
4. DJ Convery and M E Rosenbloom. The generation of intensity-modulated fields for conformal radiotherapy by dynamic collimation. *Phys. Med. Biol.*, 37:1359-1374, 1992.
5. WD Powlis, A Smith, E Cheng, *et al.* Initiation of multileaf collimator conformal radiation therapy. *Int. J. Radiat. Oncol. Biol. Phys.* 25:171-179, 1993.
6. JM Galvin, X Chen, and RM Smith. Combining multileaf fields to modulate fluence distributions. *Int. J. Radiat. Oncol. Biol. Phys.* 27:697-705, 1993.
7. T Bortfeld, A L Boyer, W Schlegel, D L Kahler, and T J Waldron. Realization and verification of three-dimensional conformation radiotherapy with modulated fields. *Int. J. Radiat. Oncol. Biol. Phys.* 30:899-908, 1994.
8. CX Yu, M J Symons, MN Du, AA Martinez, and J Wong. A method for implementing dynamic photon beam intensity modulation using independent jaws and multileaf collimator. *Phys. Med. Biol.*, 40:769-787, 1995.
9. R Mohan, X Wang, A Jackson, T Bortfeld, A L Boyer, G J Kutcher, S A Leibel, Z Fuks, and CC Ling. The potential and limitations of the inverse radiotherapy technique. *Radiotherapy and Oncology*, 32: 0232-248, 1994.
10. S Hyodynmaa, A Gastafsson and A Brame. Optimization of conformal electron beam therapy using energy- and fluence-modulated beams, *Med. Phys.*, 23: 659-666, 1996.
11. EP Lief, A Larsson and JL Humm. Electron dose profile shaping by modulation of a scanning elementary beam, *Med. Phys.*, 23: 33-44, 1996.
12. B Zackrisson and M Karlsson, Matching of electron beams for conformal therapy of target volumes at moderate depths, *Radiotherapy and Oncology*, 39: 261-270, 1996.
13. MG Karlsson, M Karlsson, CM Ma and A Satherberg, MLC-collimated electron beams – a Monte Carlo based optimization, *World Congress on Med. Phys.* (Nice, France) 1997 submitted

14. AAPM TG-21, A protocol for the determination of absorbed dose from high-energy photons and electrons, *Med. Phys.*, 10: 741, 1983.
15. C-M Ma, E Mok, A Kapur and D Findley, Improvement of small-field electron beam dosimetry by Monte Carlo simulations *Proc. XIIth ICCR* (Salt Lake City, Utah) 159-162, 1997.
16. R. Nelson, H Hirayama and DWO Rogers. *The EGS4 code system*, Stanford Linear Accelerator Center Report SLAC-265 (SLAC, Stanford, CA) 1985.
17. DWO Rogers, BA Faddegon, GX Ding, CM Ma, J Wei and TR Mackie, BEAM: a Monte Carlo code to simulate radiotherapy treatment units, *Med. Phys.* 22:503-525, 1995.
18. A Kapur, C-M Ma, E Mok and D Findley, Characterization of small field electron beams for radiotherapy using Monte Carlo simulations, *Proc. XIIth ICCR* (Salt Lake City, Utah) 157-158, 1997.
19. C-M Ma , BA Faddegon, DWO Rogers and TR Mackie, Accurate characterization of the Monte Carlo calculated electron beams for radiotherapy, *Med. Phys.*, 24:401-417, 1997.
20. C-M Ma, PJ Reckwerdt, M Holmes, DWO Rogers and B Geiser, *DOSXYZ Users Manual*, national Research Council of Canada report PIRS-509B (NRCC, Ottawa, Canada) 1995.
21. C-M Ma, E Mok, A Kapur, D Findley and AL Boyer, Monte Carlo treatment planning: output factors for small-irregular field electron beams, *Med. Phys.*, 24: 6 (abstract) 1997.
22. C.-M. Ma, E. Mok, A. Kapur, T. Pawlicki, D. Findley, S. Brain, K. Forster and A.L. Boyer, Clinical implementation of a Monte Carlo treatment planning system, *Med. Phys.* 26: 2133-43 (1999)
23. C.-M. Ma and S.B. Jiang, Topical review: Monte Carlo modeling of electron beams from medical accelerators, *Phys. Med. Biol.*, 45: (Dec) (1999) in press
24. A. Kapur and C.-M. Ma, Stopping-powers for clinical electron beams for a scatter-foil linear accelerator, *Phys. Med. Biol.*, 45:2321-41 (1999)
25. C.-M. Ma, T. Pawlicki, S.B. Jiang, E.Mok, A. Kapur, L. Xing, L. Ma and A.L. Boyer, Verification of IMRT dose distributions using Monte Carlo simulations, *Phys. Med. Biol.*, (1999) submitted
26. S.B.Jiang, A. Kapur and C.-M. Ma, Electron beam modelling and commissioning for Monte Carlo treatment planning, *Med. Phys.* (1999) accepted
27. S.B.Jiang, J. Deng, A. L. Boyer and C.-M. Ma, An extrafocal source model for photon beam dose calculation, *Med. Phys.* (1999) submitted
28. J. Deng, S.B.Jiang, J.S. Li, T. Pawlicki and C.-M. Ma, Photon beam characterization and modeling for Monte Carlo treatment planning, *Phys. Med. Biol.* (1999) submitted

Appendices

List of Figures quoted in the body of text:

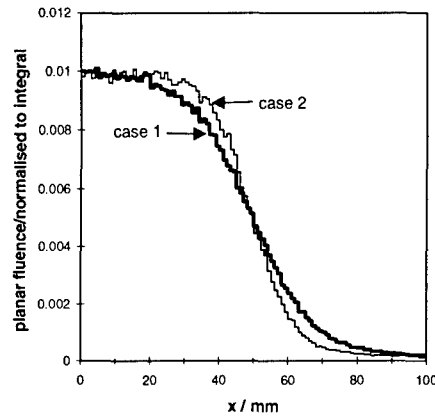


Fig. 1 Calculated planar fluence distributions at a source-detector distance of 90 cm for 10.08 MeV electrons from the Clinac 2300. The thick solid histogram represents standard geometry (case 1) and the thin solid histogram represents helium atmosphere (case 2).

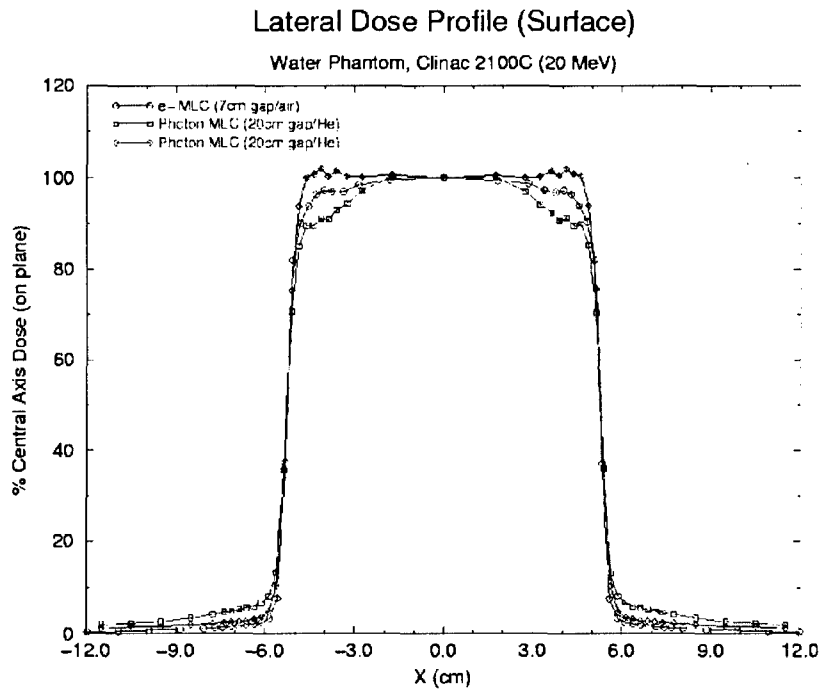
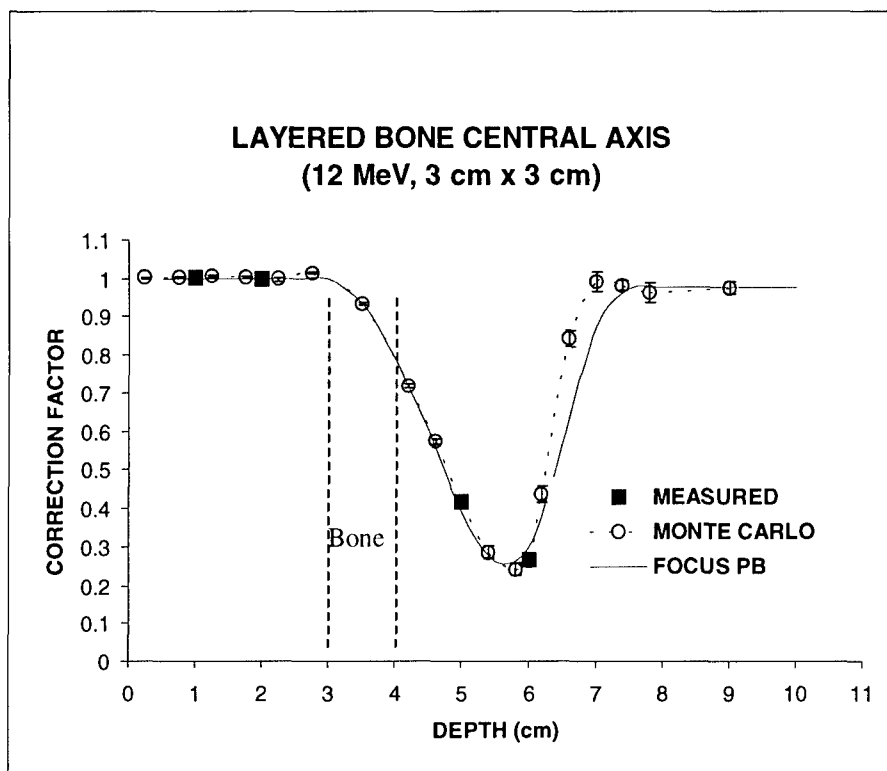
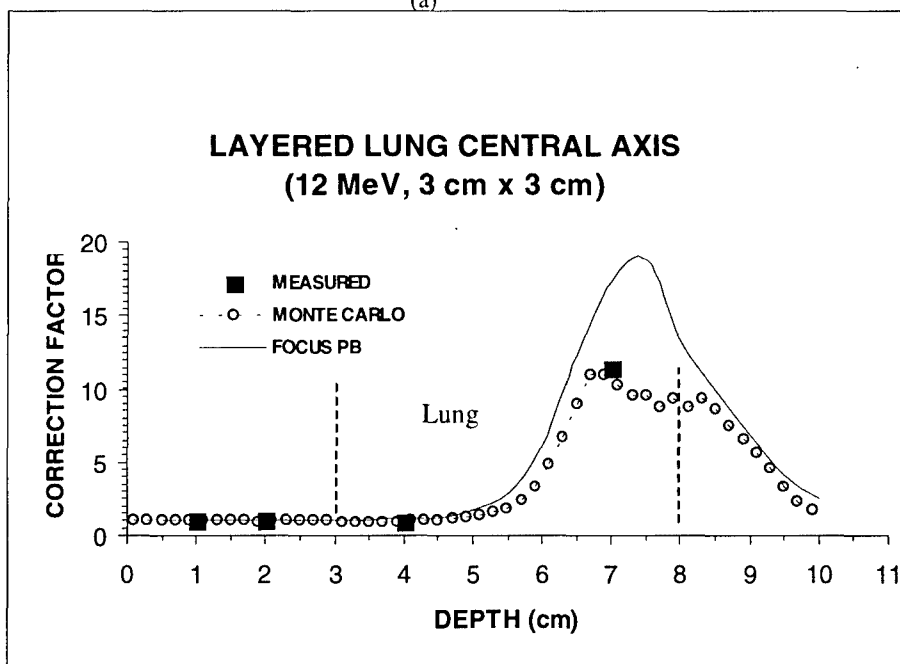


Fig. 2 Calculated dose distributions at phantom surface for a 20 MeV electrons from the Clinac 2100CD. The blue histogram represents a focused photon MLC and the red histogram represents unfocused photon MLC. For comparison, a specially designed electron MLC was also simulated with 7 cm air gap. The photon MLC simulations were performed for a 20 cm He gap.



(a)



(b)

Fig. 3 Comparisons of heterogeneity correction factors calculated by Monte Carlo, by FOCUS (3D pencil beam) and by measurements for a 12 MeV electron beam: (a) in a layered-bone phantom for a 3 cm x 3 cm field and (b) in a layered-lung phantom for a 3 cm x 3 cm field. The field size was defined at 100 cm SSD.

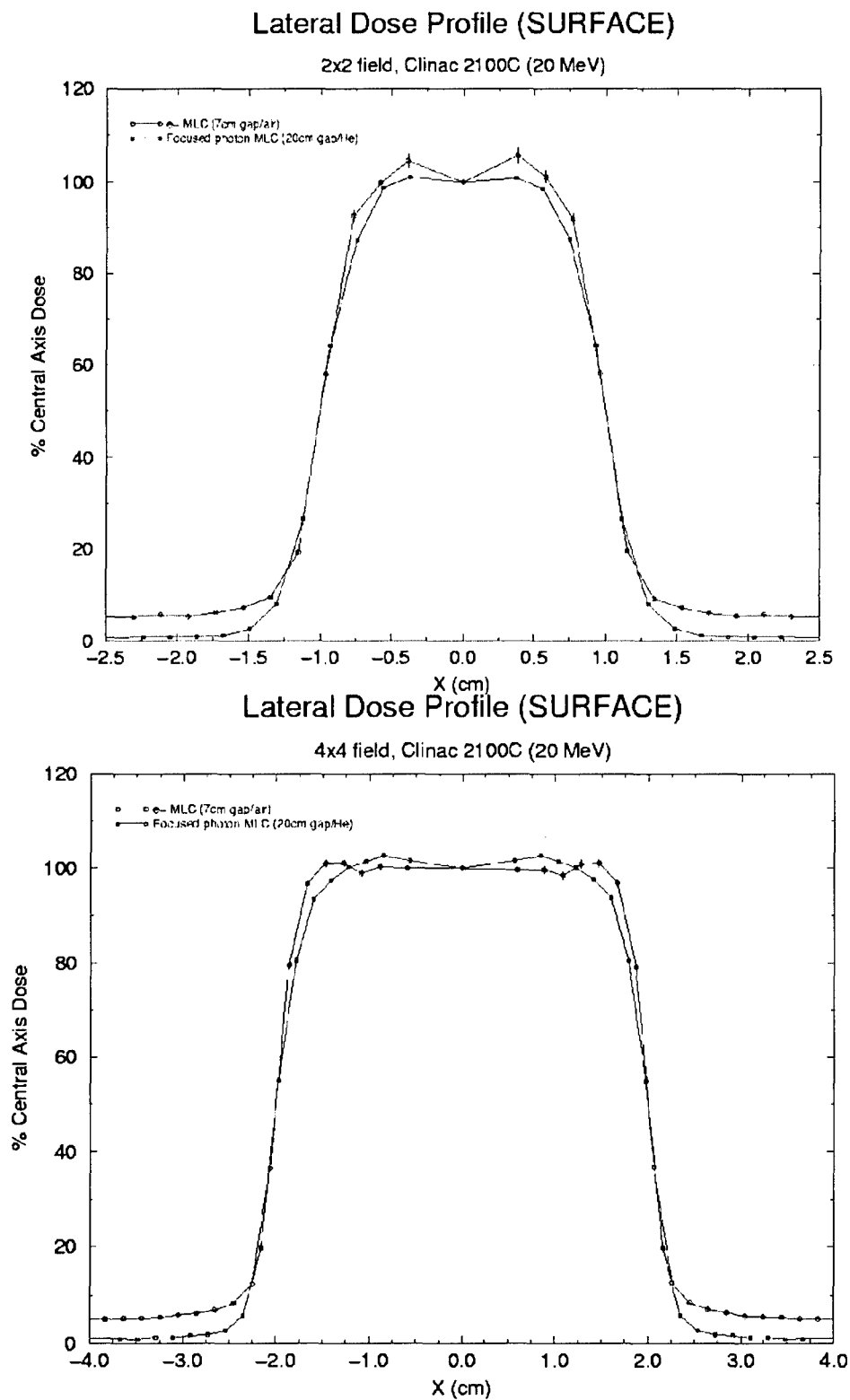
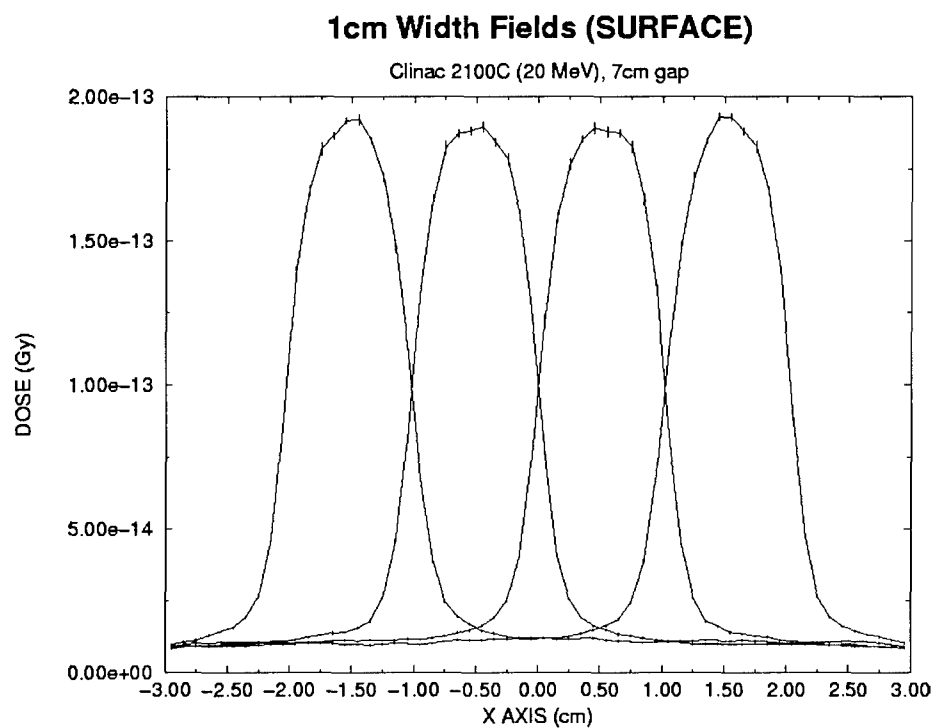
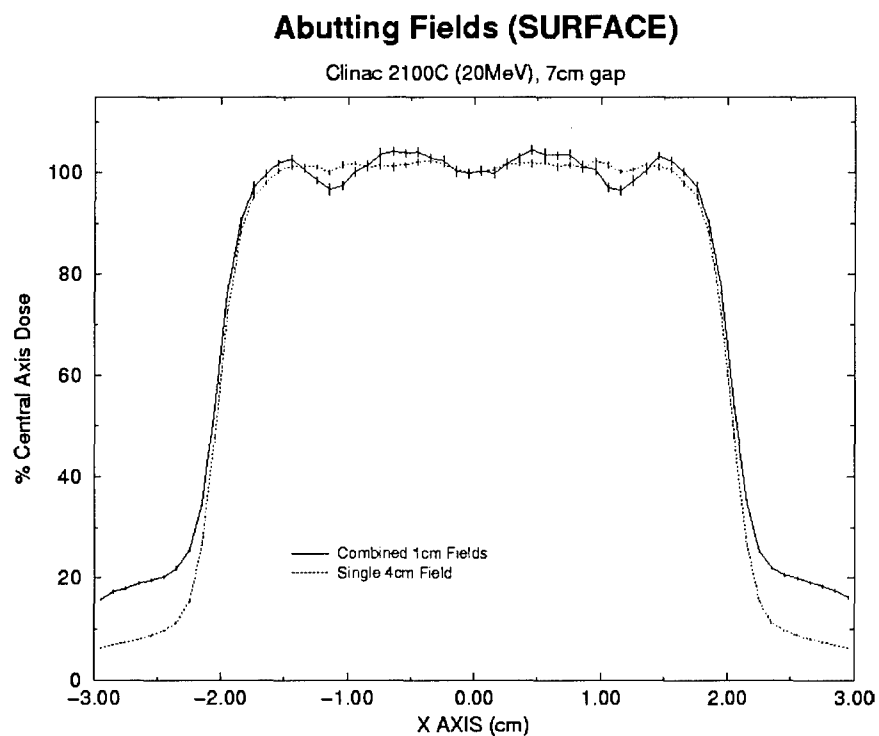


Fig. 4 Calculated dose distributions at phantom surface for a 20 MeV electrons from the Clinac 2100C for different field sizes. The black line represents a specially designed electron MLC while the red line represents the existing photon MLC with air replaced by Helium.



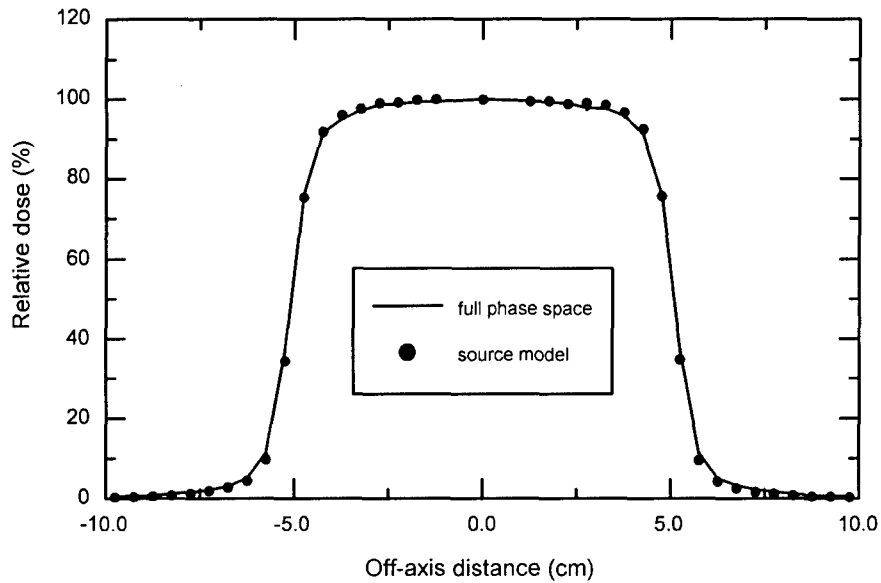
separate_20MeV_surface



total_abutting_20MeV_surface

Fig. 5 Dose distributions at phantom surface for a 20 MeV electrons from the Clinac 2100C for four 1cm x 1cm fields and a single 1 cm x 4 cm field. The four 1 cm x 1 cm beam profile shows more leakage and slight fluctuation on the surface.

12 MeV electron beam from 2100C with 10x10 cone (SSD=100 cm, depth=2 cm)



12 MeV electron beam from 2300C/D with 10x10 cone (SSD=120 cm, depth=3.2 cm)

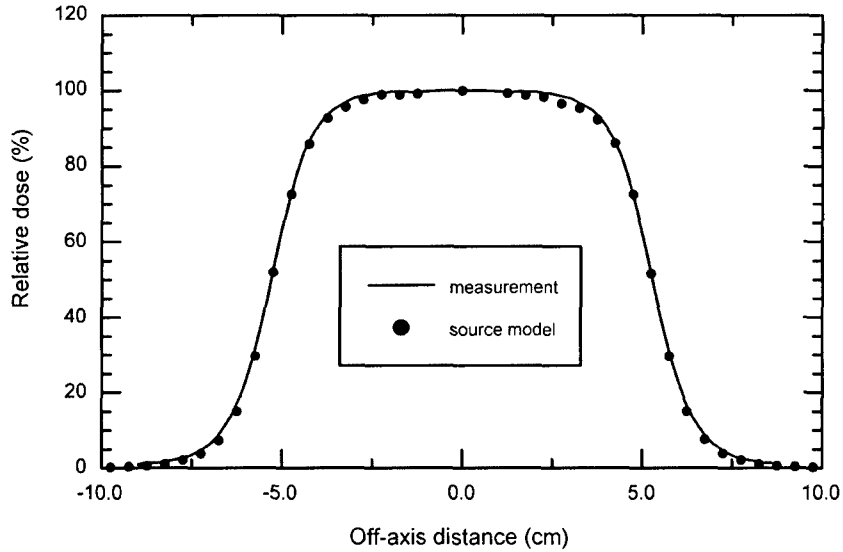


Fig. 6 Dose profiles at 3.2 cm in a water phantom for a 12 MeV electron beam from the Clinac 2100C calculated using the source model and the original phase space data, and the dose distributions calculated by the source model and measured by ion chamber for a 12 MeV electron beam from a Varian Clinac 2300CD accelerator. The agreement was within 1% for both cases.

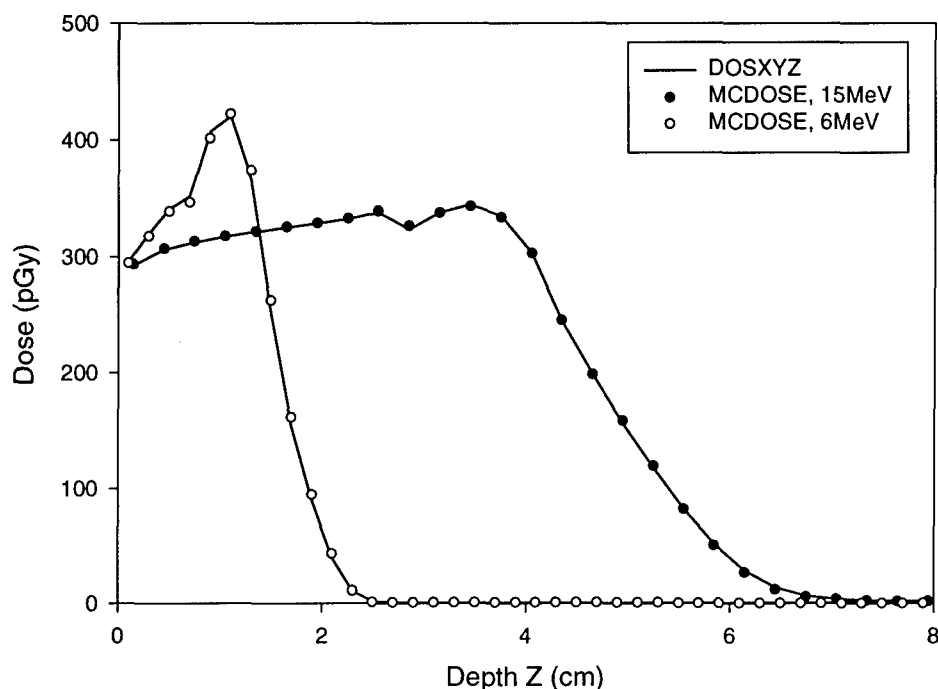


Fig. 7 Depth dose curves in Tissue-Bone-Tissue phantoms calculated by DOSXYZ and MCDOSE for 15MeV and 6MeV electron beams with field size 6 cm x 6 cm. For 15MeV electron beam, it is material of bone from depth 2.7cm to 4.5cm in the phantom. For 6MeV electron beam, the material of bone is between depth 0.6cm and 1.6cm.

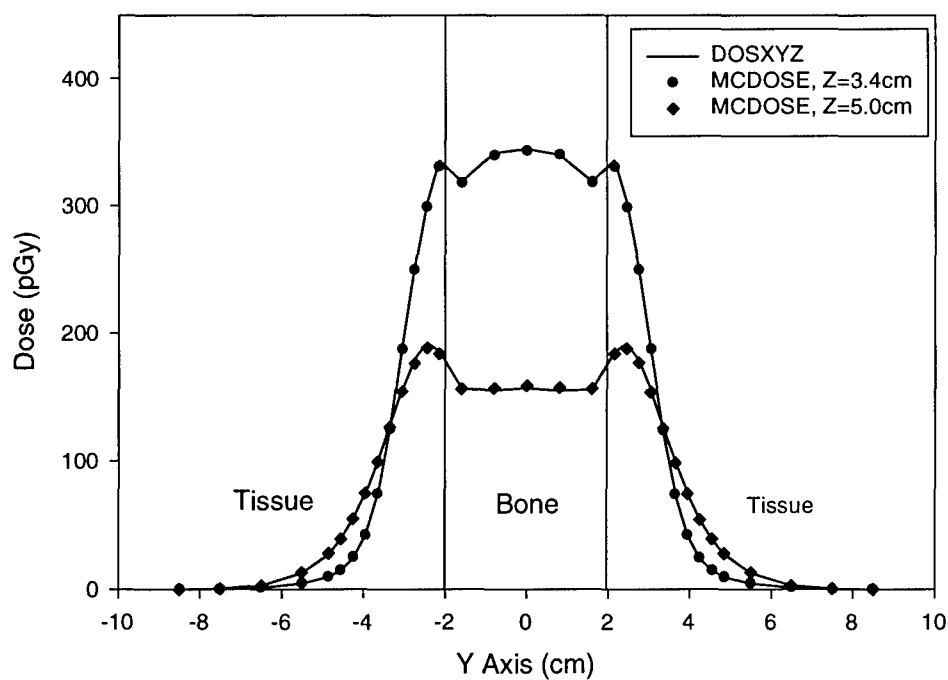


Fig. 8 Lateral dose profiles at depths 3.4cm and 5.0cm in a Tissue-Bone-Tissue phantom calculated by DOSXYZ and MCDOSE for a 15MeV electron beam with field size 6 cm x 6 cm. It is the same calculation as Fig. 7 for 15MeV electronic beam. At depth 3.4cm, it is material of Bone from -2.0cm to 2.0cm in Y dimension.

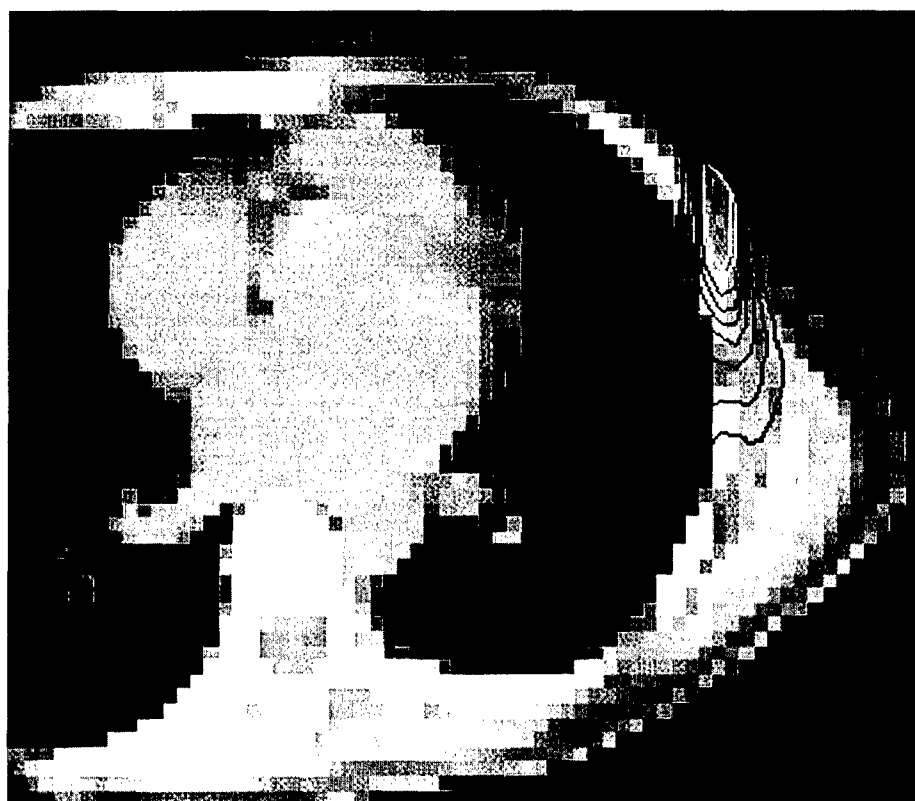
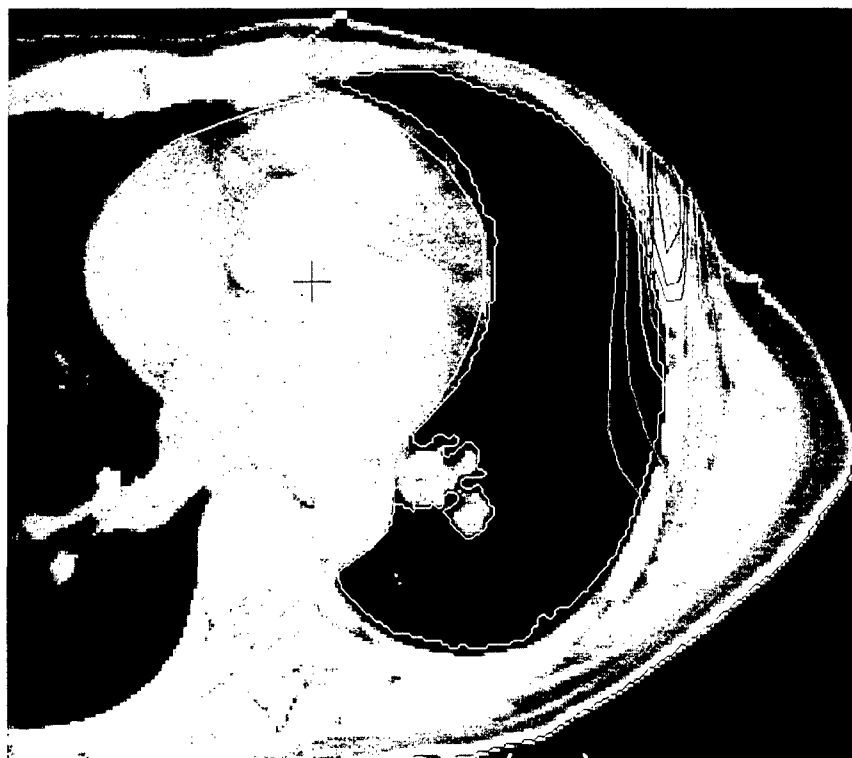


Fig. 9 Dose distributions calculated by the FOCUS system (using a pencil beam algorithm) and by the Monte Carlo method. The Monte Carlo correctly predicted the dose variations near the interface between tissue and air and the interface between tissue and bone while the FOCUS calculation shows almost symmetrical distributions in such cases.

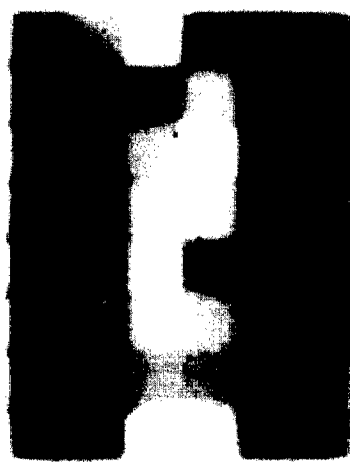
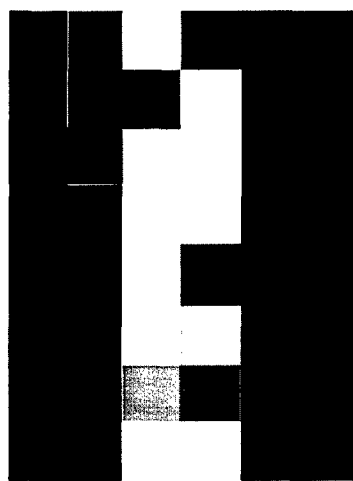


Fig. 10 Photon intensity map for a field used in an optimized treatment plan calculated by the optimization system (above) and measured by the Beam Imaging System (BIS). The blurring effect is caused by photon scattering in the treatment head (extended source) and the MLC and leaf leakage. This effect may introduce a change in the dose profile by a few percent if uncorrected.

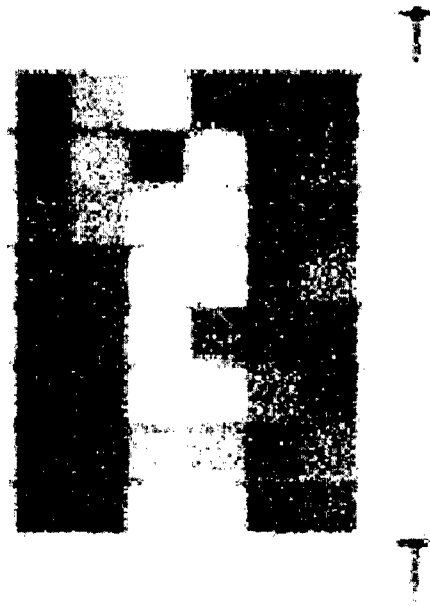


Fig. 11 Intensity map simulated by the Monte Carlo method for the same field as shown in Fig. 10. The blurring effect has been simulated accurately by tracking the particles in the treatment head and going through the MLC.

List of manuscripts submitted with this report:

1. C.-M. Ma, E. Mok, A. Kapur, T. Pawlicki, D. Findley, S. Brain, K. Forster and A.L. Boyer, Clinical implementation of a Monte Carlo treatment planning system, Med. Phys. 26: 2133-43 (1999)
2. C.-M. Ma and S.B. Jiang, Topical review: Monte Carlo modeling of electron beams from medical accelerators, Phys. Med. Biol., 45: (Dec) (1999) in press
3. A. Kapur and C.-M. Ma, Stopping-powers for clinical electron beams for a scatter-foil linear accelerator, Phys. Med. Biol., 45:2321-41 (1999)
4. C.-M. Ma, T. Pawlicki, S.B. Jiang, E.Mok, A. Kapur, L. Xing, L. Ma and A.L. Boyer, Verification of IMRT dose distributions using Monte Carlo simulations, Phys. Med. Biol., (1999) submitted
5. S.B.Jiang, A. Kapur and C.-M. Ma, Electron beam modelling and commissioning for Monte Carlo treatment planning, Med. Phys. (1999) accepted
6. S.B.Jiang, J. Deng, A. L. Boyer and C.-M. Ma, An extrafocal source model for photon beam dose calculation, Med. Phys. (1999) submitted

Verification of IMRT dose distributions using Monte Carlo simulations

C.-M. Ma, T. Pawlicki, S. B. Jiang, J.S. Li, J. Deng, E. Mok, A. Kapur, L. Xing,

L. Ma and A. L. Boyer

Radiation Oncology Department

Stanford University School of Medicine

Stanford, CA 94305

Submitted to Phys. Med. Biol. 8/20/99

Please send correspondence to:

C.-M. Charlie Ma, Ph.D.

Radiation Oncology Department

Stanford University School of Medicine

Stanford, CA 94305

Tel.: (650) 723-5591

Fax: (650) 498-4015

Email: cma@reyes.stanford.edu

Abstract

The purpose of this work was to verify the accuracy of the dose distributions calculated by a commercial treatment planning optimization system for intensity-modulated radiotherapy (IMRT) using Monte Carlo simulations. A Monte Carlo treatment planning system has been implemented clinically to improve the accuracy of radiotherapy dose calculations. The EGS4/DOSXYZ code system was modified to compute the dose in a patient for multiple fixed-gantry IMRT fields. Phantom measurements were performed to commission the Monte Carlo dose calculation system. The dose distributions in the experimental phantoms and in the patients were calculated and used to verify the optimized treatment plans generated by the inverse-planning system. The Monte Carlo calculated dose distributions agreed with the measurements to within 2% for all the beam energies and field sizes for both the homogeneous and heterogeneous phantoms. The dose distributions predicted by the inverse-planning system agreed with the Monte Carlo and measurements within 4% in a cylindrical water phantom with various hypothetical target shapes. Discrepancies in local dose up to 10% in the target region and 50% in the critical structures were found in some IMRT patient calculations. The photon dose calculation algorithm used in the commercial inverse-planning system is adequate for homogeneous phantoms (such as prostate) but may result in significant uncertainty in the doses near heterogeneities such as the air-tissue, lung-tissue and tissue-bone interfaces. Caution should be exercised for treatments involving small target volumes or heterogeneities in the case of nasal cavities, head and neck and the lung.

Keywords: Intensity modulated radiotherapy (IMRT), dosimetry, dose verification, Monte Carlo dose calculation

Running title: Monte Carlo verification of IMRT dose distributions

1. Introduction

For the last few years, extensive research has been carried out to develop conformal radiotherapy using computer-controlled linear accelerators equipped with multi-leaf collimators (MLC) (Boesecke et al 1988, Boyer et al 1992, Leibel et al 1992, LoSasso et al 1993, Powlis et al 1993, Mageras et al 1994, Brewster et al 1995, Fraass et al 1995, McShan et al 1995, Yu et al 1995, Haedinger et al 1997). More recently, intensity modulated radiotherapy (IMRT) has been developed (Brahme et al 1988, Convery and Rosenbloom 1992, Webb 1992, Boyer et al 1997) and implemented (Ling et al 1996, Boyer et al 1998a) that uses computer-controlled modulation of x-ray fields by the MLC. It is anticipated that conformal radiotherapy will provide radiation oncologists with a significantly improved means to deliver high doses of ionizing radiation to some tumor sites while reducing doses to adjacent normal tissue below levels to which they are unavoidably exposed by currently available techniques. Thus, acute and chronic toxicity associated with treatment of a tumor volume by radiation may be significantly reduced or delayed for certain sites of malignant presentations.

The use of conformal radiotherapy, especially with the IMRT technique, is a major departure from the way radiotherapy is currently delivered. Although the use of MLCs provides the possibility of achieving better dose distributions conformed to tumor targets, it also increases the treatment complexity. The sequences of leaf movement and their associated effects on the dose delivered to the patient may vary significantly depending on the accelerator and the MLC design. Important factors include the variation of the accelerator head scatter component in the MLC-collimated beam (Convery and Webb 1997), the amount of photon leakage through the leaves (Wang et al 1996, Webb 1997, Holmes et al 1997), and the scatter from the leaf ends, the "tongue and groove" effect (Chui et al 1994, Wang et al 1996), and the effect of back-scattered photons from the moving jaws and MLC leaves on the monitor chamber signal (Hounsell et al 1998). Traditionally, patient dose calculations in radiotherapy were based on correcting measured dose distributions. New dose calculation algorithms have been developed to predict the patient dose from "first principles" using a model of radiation transport (Mackie et al 1995). Comparisons of the traditional photon algorithms and the newer ones have been reviewed by Wong and Purdy (1990), Cunningham and Battista (1995) and Mackie et al (1996). Due to the lack of electron transport, the conventional dose calculation algorithms often failed to predict the dose distribution accurately near inhomogeneities (Mackie et al 1986, Mohan 1997, DeMarco et al 1998, Wang et al 1998, Ma et al 1999). Furthermore, the inverse-planning algorithms for beam optimization have all used approximations to speed up the dose computation that may introduce significant uncertainty in the calculated dose distributions, especially in the presence of heterogeneities. When simple source models are used in the dose computation, the correlation between the calibrated reference dose and the dose related to a beam segment may be lost. All the above imply a potential problem with the prediction of the dose distributions in a patient for an IMRT treatment.

Oldham and Webb (1997) reported differences in excess of 10% in the absolute dose between the optimization dose calculations and measurements (using film) of fields delivered by a dynamic MLC. The differences were attributed partially to the nonlinearity of dose per monitor unit (MU) for small MU deliveries (the actual dose delivered per MU

increased by more than 10% from MU = 20 to MU = 1). Wang et al (1996) reported that for the Memorial Hospital's dynamic MLC delivery process, the discrepancies between the calculated dose and the measured dose were in excess of 5% if various effects related to the MLC construction, such as accelerator head scatter, were not properly accounted for. The uncertainty in the doses calculated by a conventional dose calculation algorithm was 5 – 10% in the presence of heterogeneities (Mohan 1997). Our recent Monte Carlo results were consistent with these findings (Ma et al 1999).

The purpose of this work was to verify the accuracy of the dose distributions calculated by a commercial treatment planning optimization system for IMRT using Monte Carlo simulations. We have used the EGS4/BEAM Monte Carlo code system (Nelson et al 1985, Rogers et al 1995a, 1995b) to simulate the clinical electron and photon beams from three linear accelerators, Varian Clinac 1800, 2100C and 2300C/D (Varian Oncology, Palo Alto, CA). The EGS4/ DOSXYZ code (Rogers et al 1995a, Ma et al 1995) was modified to compute the dose in a patient (a 3-dimensional phantom built from the CT data) for multiple fixed-gantry fields. Phantom measurements were performed to commission the Monte Carlo system. The dose distributions in the experimental phantoms and in the patients were calculated and used to verify the optimized treatment plans generated by the CORVUS inverse-planning system (CORVUS, NOMOS Corp., Sewickley, PA). In the following sections, we will describe the details of the dose calculations used in the inverse-planning system and the Monte Carlo simulations. We will show the dose distributions for homogeneous and heterogeneous phantoms and discuss the effect of material density and atomic number, electron transport and energy cutoff values on the accuracy of the final dose calculations.

2. Materials and Method

2.1 Treatment planning and dose measurement

The treatment planning optimization system used in this work is the CORVUS inverse-planning system. The dose calculation algorithm used for the optimization process is a finite-size pencil beam algorithm, which uses predetermined beamlet dose distributions. The beamlet profiles were derived from measured beam profiles and normalized to produce consistent output factors for various field sizes. The patient inhomogeneity correction is made by "stretching" the beamlet profiles proportionally based on the equivalent pathlength. The details of the dose calculations have been described by Holmes et al (1998). The monitor unit calculations for a "step-and-shoot" leaf sequence algorithm have been discussed by Boyer et al (1999). The CORVUS system has been commissioned for clinical IMRT treatment planning (Xing et al 1998, 1999) and used for treating head and neck patients with IMRT (Boyer et al 1998).

In order to test the inverse-planning algorithm and the Monte Carlo dose calculations, inverse plans were computed for various target shapes placed in the center of a cylindrical water phantom having a diameter of 30 cm. The results have been reported in detail by Boyer et al (1999). Inverse plans were computed for these hypothetical targets with different numbers of beams directed toward the axis of the cylinder at the center of the target and spaced at equal angles. A beamlet size of 1 cm x 1 cm was used in the calculation. The leaf sequencing algorithm used 20 intensity levels.

The treatments were delivered using a Dynamic Multileaf Collimator (Varian Oncology Systems, Palo Alto, California). The leaf sequences computed within the NOMOS software were written into files with formats conformed to the requirements of the Varian digital control software. The leaf sequences were delivered using the monitor units calculated by the CORVUS system. The absolute dose delivered by the leaf sequences was measured in the 30-cm diameter cylindrical water phantom using a 0.147 cm³ ionization chamber (Wellhöfer Dosimetrie, Schwartzenbruck, Germany) following the AAPM TG-21 protocol (AAPM 1983). No corrections were made for the variation in the chamber displacement effect, which depends on the dose gradient at the measurement point and the chamber diameter. This may introduce an up to 2% uncertainty in the measured dose for the 6-mm diameter chamber used (the dose gradient was 5-8% per centimeter at some measurement points). The chamber positioning uncertainty was about 0.1 cm. The overall uncertainty in the measured dose was estimated to be about 3% (1 σ).

2.2 The Monte Carlo simulation

We have used BEAM and DOSXYZ (Rogers et al 1995a, Rogers et al 1995b, Ma et al 1995) Monte Carlo codes for the accelerator head simulation and dose calculation in the patient respectively. Both codes were EGS4 (Electron Gamma Shower version 4, Nelson et al 1985) user codes, running under the UNIX operating system, developed through the OMEGA project for Monte Carlo treatment planning dose calculations (Mackie et al 1994). Detailed descriptions of the software can be found from Rogers et al (1995a). A detailed description of the clinical implementation of the Monte Carlo code system was given in a previous publication (Ma et al 1999).

Three types of clinical linear accelerators were simulated for the clinical implementation of Monte Carlo treatment planning in our center: Varian Clinac 1800, 2100C and 2300C/D (Varian Oncology Systems, Palo Alto, California). The dimensions and materials for the accelerator components were incorporated according to the manufacturer's specifications. Electron beams emerging from the vacuum exit window were assumed to be monoenergetic and monodirectional with a beam radius of 0.1-0.2 cm. These were found to be reasonable assumptions to achieve an acceptable dose calculation accuracy of about 2% of the dose maximum (D_{\max}) anywhere in the phantom for clinical radiotherapy applications (Kapur et al 1998). We obtained accurate phase-space data for photon beams with nominal energies of 4, 6, and 15 MV. The energy cutoffs for electron transport in the accelerator simulation (ECUT and AE) 700 keV (kinetic + rest mass) and for photon transport (PCUT and AP) 10 keV. The ESTEPE value was 0.04. The bremsstrahlung splitting and Russian roulette options were implemented for photon beam simulations (Rogers et al 1995b). The ICRU recommended compositions and stopping power values were used for the materials used in the accelerator simulations (ICRU 1984). The phase-space data were scored at a plane immediately above the photon jaws. The number of particles in a photon beam file was about 50 million. Field shaping by photon jaws, blocks and the MLC was further simulated using BEAM and the phase-space data could be stored temporarily or used directly for dose calculations. The phase-space data for each beam was divided and stored separately on a 32-PC network. For further BEAM simulations or dose calculations, the phase-space data stored locally were used. The final statistical uncertainty was determined after combining the results from all the 32 PCs.

The DOSXYZ code was designed for dose calculations in a 3D rectilinear voxel geometry (Ma et al 1995). Voxel dimensions were completely variable in all three directions. Every voxel (volume element) could be assigned to a different material. The cross-section data for the materials used were available in a pre-processed PEGS4 cross-section data file. The mass density of the material in a DOSXYZ calculation was varied based on the patient's CT data although the density effect corrections for the stopping powers of the material remain unchanged. The voxel dimensions and materials were defined in a DOSXYZ input file together with the transport parameters such as the energy cutoffs (ECUT and PCUT), the maximum fractional energy loss per electron step (ESTEPE), and the parameters required by PRESTA (Bielajew and Rogers 1987). For use with the CT data, a separate program CTCREATE was used to convert the patient's CT data to desired dimensions, material types and densities. The phase-space data obtained from a BEAM simulation was used as a source input with variable source positions and beam incident angles. Dose contributions from different beam components were selectively calculated based on the particle charge or the LATCH settings specified in the BEAM simulation. DOSXYZ produced a data file that contained geometry specifications such as the number of voxels in all the three directions and their boundaries as well as the dose values and the associated (1σ) statistical uncertainties in the individual voxels.

The DOSXYZ code has been modified to read the MLC leaf sequence files for IMRT treatment. For this study, the Varian dynamic MLC leaf sequence files (G-version) generated using a step-and-shoot leaf sequencing algorithm, were used. The monitor units for each leaf sequence were integrated into a two-dimensional map (grids). The dimensions of the map at the isocenter (100 cm from the virtual point source position) are 40 cm in both the x and y directions and the grid sizes were 0.1 cm. The monitor units for the open areas were accumulated for each of the pixels while for the closed areas, a fraction of the monitor units were accumulated based on the measured MLC transmission factor for each beam energy. Thus, the integrated intensity map has included the averaged leaf leakage effect but ignored the influence of the leaf shape (tongue and groove) and the variation of the spatial and spectral distributions due to photon attenuation and scattering in the MLC leaves. The transmission factor for the areas under the photon jaws was assumed to be zero. The photon jaw positions were fixed for each gantry angle. The dimensions of the photon jaw opening were set to 0.8 cm greater than the MLC opening in the x-direction and to 0.2 cm greater than the MLC opening in the y-direction (to reduce the leakage between the leaf ends). Further modifications were made to simulate several gantry angles in the same run. The leaf sequence files were read sequentially and the gantry angle was changed automatically after the simulation of a photon field was completed.

During the Monte Carlo simulations, the weight of a phase-space particle was altered based on the value of the pixel in the intensity map through which the particle was traveling. To improve the simulation efficiency, two variance reduction techniques were implemented in the DOSXYZ code, particle splitting and Russian roulette. The former was applied to the particles with weight greater than unity and the latter was applied to the particles with weight smaller than unity. The parameters used for the splitting and Russian roulette processes were set to such values that the resulting particles would have

similar weighting factors. Using uniform weighting factors will generally improve the statistical uncertainty of a simulation.

For patient dose calculations, the simulation phantom was built from the patient's CT data with up to $128 \times 128 \times 128$ voxels (uniform in any dimensions). The side of a voxel varied from 0.2 to 0.4 cm. The energy cutoffs were $ECUT = AE = 700$ keV and $PCUT$ and $AP = 10$ keV. The ESTEPE value was 0.04. The number of particle histories simulated ranged from 300 million to one billion for up to 9 gantry angles for an IMRT treatment. The $1-\sigma$ statistical uncertainty in the dose was generally 1-2% of the D_{max} value. The CPU time required for an IMRT simulation was about 0.2 – 1 hours on the 32-PC (Pentium Pro 200 MHz and Pentium III 450 MHz) network or about 3-15 hour on a single Pentium III 450 MHz PC.

3. Results

3.1 Comparisons in homogeneous water phantoms

Both the inverse-planning system and the Monte Carlo dose calculation system have been commissioned for routine clinical applications (Xing et al 1998; Ma et al 1999). Both systems regenerated the PDD curves and the dose profiles at various depths to within 2% of the dose maximum values of the measured beam data for various field sizes and source to surface distances (SSD). The dose distributions given by the CORVUS system agreed with the Monte Carlo and measurements to about 3% in a cylindrical water phantom with various hypothetical target shapes (Boyer et al 1999). Figure 1 shows the dose distributions in a 30-cm diameter water cylinder irradiated by 7 6-MV intensity-modulated photon beams calculated by COVUS and by the Monte Carlo simulations. The critical structure is in the center of the water cylinder immediately next to the C-shaped target. The isodose lines calculated by both systems agreed well for percentage dose values above 50% (the difference is generally within 4% or a shift in isodose lines within 0.3 cm). The discrepancies in the low-dose ($< 30\%$) regions were thought mainly due to the difference in accounting for the effect of MLC leaf leakage and photon scattering in the phantom, which are considered to be not clinically significant.

Comparisons in CT phantoms

In this work, we have compared the dose distributions calculated by Monte Carlo and conventional dose calculation algorithms for various treatment sites to identify potential treatment situations that may benefit from dose accuracy improvements. Currently, all potential IMRT cases are planned using the CORVUS system and compared with the conventional plans generated using the FOCUS system (Computerized Medical Systems, Inc., St. Louis, MO). All the IMRT plans used clinically have been analyzed by both the oncologists and physicists and considered to be clearly superior to the conventional plans. Monte Carlo simulations were performed for selected IMRT plans prior to the treatment. A clinical judgement was made based on the Monte Carlo calculated dose distributions and a decision was made whether an IMRT plan would be used clinically. In the following examples, we show two typical IMRT treatment plans computed by the COVUS inverse planning system and verified by the Monte Carlo system.

Prostate

To explore the effect of full photon and electron transport on IMRT dose calculations, we show in Figure 2 an IMRT prostate treatment plan calculated by the Monte Carlo simulation and the CORVUS system. The plan was generated using the CORVUS system for 15-MV photon beams with 8 gantry angles. The beam intensity was modulated using a Varian dynamic MLC with 80 leaves. In both calculations, the isodose lines represent the percentage dose values normalized to the maximum dose values in the dose distributions. In general, the dose values in the target (the prostate) and in the nearby critical structure (the rectum) agreed between the CORVUS calculations and the Monte Carlo simulations. This confirms that both calculation algorithms can predict dose distributions in homogeneous phantoms with clinically acceptable accuracy (within 4%). However, the dose values in the regions near the bony structures were somewhat different between the CORVUS and the Monte Carlo systems.

The observed discrepancies may be partially explained by the effect of electron backscatter from the bone (high atomic number and high density) to the soft tissue, which was accounted for by the Monte Carlo simulation but not in any conventional photon dose calculation algorithms. There have been several Monte Carlo studies in the literature showing similar discrepancies between the Monte Carlo algorithm and the conventional dose calculation algorithm in dose build up or build down regions near air cavities, lung and large bony structures (DeMarco et al 1997, Mohan 1997, Wang et al 1997, Ma et al 1999). It should be mentioned that the difference in the dose to the bone was partially due to the fact that the conventional dose calculation algorithms usually used water as the phantom material and the inhomogeneity corrections were computed using varying electron density (based on the CT numbers) while the Monte Carlo algorithm used different materials such as air, tissue, lung and bone with varying mass density calculated from the CT data. If we convert the dose to the bone material to the dose to tissue using the stopping power ratio for bone to tissue (assuming the same electron energy fluence) the dose in the bone regions will be about 3.5% higher for soft bone and about 10% higher for compact bone. However, the dose in the surrounding tissue will remain the same, which was mainly caused by the perturbation of the electron fluence by the nearby inhomogeneous anatomy.

Vertebra

Figure 3 shows the dose distributions for the treatment of the vertebra calculated by both Monte Carlo simulation and the CORVUS system. The plan was generated using the CORVUS system for 15 MV photon beams with 9 gantry angles. The intensity was modulated using a Varian dynamic MLC with 80 leaves. In the regions near large bony structures (such as the cord) differences of more than 50% of the local dose could be seen between the CORVUS dose distribution and the Monte Carlo simulations. This increase in the dose to the cord was thought due to electron scattering from the surrounding bone, which could not be modeled properly by CORVUS using a "finite size pencil beam" algorithm. Another possible reason might be due to the implementation of the heterogeneity corrections in the finite size pencil beam. Although the photon beams were optimized to avoid the cord, electrons could reach the cord and the dose to the cord was

enhanced due to the high-density material surrounding it.

4. Discussion

We have investigated the effect of the conversion of the CT numbers to different material types and densities. Figure 4 shows the dose distributions for the IMRT case as shown in Figure 3. In Figure 4a, the dose distribution was calculated using tissue with unity density and air. In Figure 4b, the dose distribution was calculated using air and tissue with variable density converted from the CT data. In Fig. 4c, the dose distribution was calculated with air, unity density tissue and 10 g/cm³ density bone. For comparison, the dose distribution calculated using air, tissue and bone with proper densities converted from the CT data was shown in each figure. The isodose curves were computed by normalizing the dose values to the prescribed target dose. The differences in the isodose lines in Fig. 4 a and b are very small. The difference between dose to tissue and dose to bone at these beam energies is about 3.5% for soft bone and about 10% for hard bone assuming the same electron energy fluence. It is known that electron backscattering from the high atomic number materials may perturb the dose in tissue near the tissue-bone interface. This effect became less significant when dose values were averaged over course scoring volumes (0.3 – 0.4 cm voxels). In Fig. 4c, the density of bone was artificially increased to 10 g/cm³ which caused significant attenuation of the beams and therefore altered the doses behind the bones. The effects on the surface doses are smaller compared with the high dose regions. The maximum dose for the artificial high density bone geometry is about 15% lower than that for the phantom with normal material density.

We have also investigated the effect of energy cutoff values used for electron transport. Figure 5 shows the dose distributions calculated with electron transport energy cutoff ECUT = 700 keV, 1 MeV, 1.5 MeV and 2.5 MeV (total energy), respectively. Other energy cutoff values remained unchanged. The same material types and densities were used in the calculations as those used in Figure 3. The difference between the dose distributions calculated using 700 keV and 1 MeV was negligible. However, the simulation time for the 1 MeV run was about 30% less compared to the 700 keV run. The isodose curves calculated using 1.5 MeV ECUT were within 0.1 – 0.2 cm consistent with those calculated using lower ECUT values although the CPU time for this run was further reduced by another 40% compared to the 1 MeV run. The shift in the isodose lines for the 2.5 MeV case (0.2-0.4 cm), however, may be considered to be unacceptable clinically. As the electron CSDA range for 1 MeV kinetic energy is about 0.4 cm in soft tissue, which is about the same as the voxel size used in the dose calculations. The shift in the isodose curves was expected to be within a voxel for the 1.5 MeV ECUT case. For ECUT smaller than 1 MeV, the electron CSDA range in soft tissue is smaller than half of the voxel size used. The changes in the isodose lines should be generally negligible.

It seems clear that the conventional dose calculation algorithm may not be accurate enough in some IMRT cases where the dose perturbation effect due to inhomogeneities requires accurate simulations of the electron transport. Monte Carlo simulation for IMRT dose calculation may be a practical solution to this problem. Our experiences show that a factor of 2 – 3 more Monte Carlo particle histories are needed for

an IMRT treatment simulation compared with a conventional photon treatment simulation. This is because more monitor units are needed to deliver intensity modulated photon fields; more particles will be simulated in a Monte Carlo calculation but many of them will be stopped by the MLC leaves. Therefore, the CPU time per photon history for an IMRT simulation is less than that for a conventional field. Using the existing computing power (8 CPUs) of the CORVUS system, the calculation time for a typical "inverse plan" would be increased from the currently 0.5 – 1 hour to 2 - 4 hours with two Monte Carlo calculations. The pre-optimization dose calculation will provide the beamlet profiles for the optimization process, which take into account the effect of the accelerator head scatter and patient inhomogeneous anatomy. The post-optimization dose calculation will include the effects due to leave leakage, leaf scatter and photon backscatter into the monitor chamber after the sequence of MLC leaf movement and jaw positions has been generated. Further studies are under way on a Monte Carlo dose calculation based inverse planning system (Pawlicki et al 1999).

5. Summary

We have implemented a Monte Carlo system for routine radiotherapy treatment planning dose calculations. The implementation included the simulation and characterization of the clinical radiotherapy beams, software development for efficient dose calculations for both conventional photon and electron beams and intensity-modulated radiotherapy using a dynamic MLC, and display of the Monte Carlo 3D dose data on an existing treatment planning system.

Comparisons of the dose distributions in water calculated by Monte Carlo simulations and the measurements showed general agreement within 2% for various clinical beam setups for electron beams as well as for photon beams. The Monte Carlo calculated dose distributions in heterogeneous phantoms were confirmed (within 1%) using specially designed phantom measurements while the conventional dose calculation algorithms may underestimate or overestimate by 5 – 10% in the regions within or adjacent to large air cavities, lung or bony structures.

Our results indicated that more accurate dose calculation algorithms than those currently used in the "inverse-planning" systems are needed for intensity-modulated radiotherapy treatment planning. The conventional dose calculation algorithms may not accurately predict the dose distributions in and near inhomogeneities due to the lack of electron transport and charged particle equilibrium. The uncertainty in the dose may be "magnified" in an IMRT plan due to the "optimization effort" made for the escalation of the dose in the target volume combined with a steep dose gradient when a critical structure is nearby. The dose in the target volume may be in error by about 5 – 7% as calculated by the optimization system while the uncertainty in the dose to the critical organ may be more than 50% of the local dose for cases involving nasal cavities, head and neck, the lung and large bony structures.

Acknowledgments

We would like to acknowledge Varian Oncology Systems, Palo Alto, CA, for providing detailed information on the Varian Clinac linear accelerators and NOMOS

Corp., Sewickley, PA, for the inverse-planning system. We would like to thank our colleagues, Dr. Sam Brain, Todd Koumrian,, Behrooz Tofighrad and Michael Luxton for help with the computers and software support. We are grateful to Dr. Iwan Kawrakow for the DOSXYZ_SHOW program to plot isodose distributions, and to Jinsheng Li and Michael Luxton for modifications to the program to compare two isodose distributions on the same plot. This investigation was supported in part by grants CA78331 from the NIH, BC971292 from the DOD, Seed Cycle 1 from the RSNA Research and Education Fund, and a consortium agreement with the NumeriX, LLC.

References

AAPM (1983) AAPM TG-21, A protocol for the determination of absorbed dose from high-energy photons and electrons, Med. Phys., 10: 741, 1983.

Boesecke R, Doll J, Bauer B, Schlegel W, Pastyr O, Lorenz M (1988). Treatment planning for conformation therapy using a multileaf collimator. Strahlenther Onkol 164:151-154.

Brewster L, Mohan R, Mageras G, Burman C, Leibel S, Fuks Z (1995). Three dimensional conformal treatment planning with multileaf collimators. Int. J. Radiat. Oncol. Biol. Phys. 33:1081-1089.

Boyer AL, Geis PB, Grant W, Kendall R, Carol M (1997). Modulated-beam conformal therapy for head and neck tumors. Int. J. Radiat. Oncol. Biol. Phys. 39: 227-236.

Boyer AL, Xing L, Ma L and Forster K (1998) Verification and Delivery of Head and Neck Intensity Modulated Radiotherapy, Med. Phys. 25 (abstract)

Boyer AL, Xing L, Ma C-M, Curran B, Hill R, Holmes T and Bleier A (1999), Theoretical consideration of monitor unit calculations for intensity modulated beam treatment planning. Med. Phys. 26: 187-195

Brahme A (1988). Optimal setting of multileaf collimators in stationary beam radiation therapy. Strahlenther. Onkol. 164:343-350.

Cunningham JR and Battista JJ, "Calculation of dose distributions for x-ray therapy," Phys. Canada 51, 190-218 (1995)

Chui CS, LoSasso T and Spirou S (1994) Dose calculations for photon beams with intensity modulation generated by dynamic jaw or multileaf collimators, Med. Phys. 21: 1237-43

Convery DJ, Rosenbloom ME (1992). The generation of intensity-modulated fields for conformal radiotherapy by dynamic collimation. Phys. Med. Biol. 37:1359-1374.

Convery DJ and Webb S (1997) Calculation of the distribution of head-scattered radiation in dynamically-collimated MLC fields. Proc. XII Int. Conference on the Use of Computers in Radiation Therapy (Salt Lake City, USA) 350-353

DeMarco JJ, Solberg TD and Smathers JB (1998), "A CT-based Monte Carlo simulation tool for dosimetry planning and analysis," Med. Phys. 25 1-11

Holmes T M, Bleier A, Carol M, Curran B, Kania A, Lalonde R, Larson L and Sternick E (1997) The effect of MLC leakage on the calculation and delivery of intensity modulated radiotherapy, Med. Phys. 24: 997 (abstract)

Holmes T M, Bleier A, Carol M, Curran B, DeNisi J, Hill R, Kania A, Lalonde R, Larson L and Sternick E (1998) The CORVUS dose model revealed, Med. Phys. 25: 144 (abstract)

Hounsell AR (1998) Monitor chamber backscatter for intensity modulated radiation therapy using multileaf collimators, Phys. Med. Biol. 43: 445-54

ICRU (1984) Report 37, Radiation dosimetry: Stopping powers for electrons and positrons (ICRU, Bethesda, MD20814, 1984)

Kapur A, Ma C-M, Mok E and Findley D (1997) Characterization of small field electron beams for radiotherapy using Monte Carlo simulations, *Proc. XIIIth ICCR* (Salt Lake City, Utah) 157-158

Kapur A, Ma C-M, Mok E, Findley D and Boyer AL (1998), "Monte Carlo calculations of clinical electron beam output factors," Phys. Med. Biol. In press

Kutcher GJ, Mageras GS and Leibel SA (1995), Control, correction and modeling of setup errors and organ motion, *Semin. Radiat. Oncol.* 5, 134-45

Leibel SA, Kutcher GJ, Mohan R, et al. (1992). Three-dimensional conformal radiation therapy at the Memorial Sloan-Kettering Cancer Center *Semin. Radiat. Oncol.* 2:274-289.

Ling CC, Burman C, Chui CS, G.J. Kutcher, S.A. Leibel, T.LoSasso, R. Mohan, T. Bortfeld, L. Reinstein, S. Spirou, X.H.Wang, Q. Wu, M. Zelefsky, Z. Fuks (1996). Conformal Radiation Treatment of prostate cancer using inversely-planned intensity-modulated photon beams produced with dynamic multileaf collimation. Int. J. Radiation Oncology Biol. Phys. 35:731-730.

LoSasso T, Chui CS, Kutcher GJ, Leibel SA, Fuks Z, Ling CC (1993). The use of multileaf collimators for conformal radiotherapy of carcinomas of the prostate and nasopharynx. Int. J. Radiat. Oncol. Biol. Phys. 25:161-170.

Ma C-M, Reckwerd P, Holmes M, Rogers DWO and Geiser B (1995) *DOSXYZ Users Manual*, National Research Council Report PIRS-0509(B), Ottawa, Canada

Ma C-M, Mok E, Kapur A, Findley D (1997) Improvement of small-field electron beam dosimetry by Monte Carlo simulations, *Proc. XIIIth ICCR* (Salt Lake City, Utah) 159-162

Ma C-M, Mok E, Kapur A, Pawlicki T A, Findley D, Brain S, Forster K and Boyer AL (1999) Clinical implementation of a Monte Carlo treatment planning system for radiotherapy, Med. Phys. 25: (Oct) in press

Mackie TR, Reckwerdt P and Papanikolaou N (1995), "3-D photon beam algorithms," in 3-D Radiation Treatment Planning and Conformal Therapy, Ed. By J.A. Purdy and B. Emami (Medical Physics Publishing Corp., Madison WI)

Mackie TR, Reckwerdt P, McNutt T, Gehring M and Sanders C (1996), "Photon beam dose calculations," in Teletherapy: Present and Future, Ed. By T.R. Mackie and J.R. Palta (Advanced Medical Publishing, Madison WI)

Mackie TR, Reckwerdt PJ, Wells CM, Yang JN, Deasy JO, Podgorsak M, Holmes MA, Rogers DWO, Ding GX, Faddegon BA, Ma C-M, Bielajew AF and Cygler J (1994) The OMEGA project: comparison among EGS4 electron beam simulation, 3D Fermi-eyges calculations and dose measurements, Proc. Xith ICCR (Manchester, UK) 152-153

Mackie TR, Holmes TW, Reckwerdt PJ, Yang J (1995). Tomotherapy: optimized planning and delivery of radiation therapy. Int. J. Imaging Systems and Technology 6: 43-55.

Mageras GS, Fuks Z, O'Brien J, Brewster LJ, Burman C, Chui CS, Leibel SA, Ling CC, Masterson ME, Mohan R, Kutcher GJ (1994). Initial clinical experience with computer-controlled conformal radiotherapy using the MM50 microtron. Int. J. Radiat. Oncol. Biol. Phys. 30: 971-978.

McShan DL, Fraass BA, Kessler ML, Matrone GM, Lewis JD, Weaver TA.(1995). A computer-controlled conformal radiotherapy system. II: sequence processor. Int. J. Radiat. Oncol. Biol. Phys. 33:1159-1172. Mohan R (1997) Why Monte Carlo? Proc. XII Int. Conference on the Use of Computers in Radiation Therapy (Salt Lake City, USA) 16-18

Nelson R, Hirayama H and Rogers DWO (1985). *The EGS4 code system*, Stanford Linear Accelerator Center Report SLAC-265 (SLAC, Stanford, CA)

Oldhan M and Webb S (1997) Intensity-modulated radiotherapy by means of static tomotherapy: a planning and verification study, Med. Phys. 24:827-836

Pawlicki TA, Jiang SB, Deng J, Li JS and Ma C-M (1999) "Monte Carlo calculated beamlets for photon beam inverse planning", Med. Phys. 26: 1064-65 (abstract)

Powlis WD, Smith A, Cheng E, et al.(1993). Initiation of multileaf collimator conformal radiation therapy. Int. J. Radiat. Oncol. Biol. Phys. 25:171-179.

Rogers DWO, Faddegon BA, Ding GX, Ma CM, Wei JS, Mackie TR (1995a). BEAM: A Monte Carlo code to simulate radiotherapy treatment units. Med. Phys. 22: 503-25.

Rogers DWO, Ma CM, Ding GX and Walters B (1995b) *BEAM Users Manual*, National Research Council Report PIRS-0509(A), Ottawa, Canada

Wang L, Chui C and Lovelock M (1998) A patient-specific Monte Carlo dose-calculation method for photon beams, *Med. Phys.* 25: 867-78

Wang X, Spirou S, LoSasso T, Stein J, Chui C and Mohan R (1996) Dosimetric verification of intensity modulated fields. *Med. Phys.* 23:317-328.

Wong JW and Purdy JA (1990) "On the methods of inhomogeneity corrections for photon transport", *Med. Phys.* 17, 807-814, 1990

Webb S (1992). Optimization by simulated annealing of three-dimensional conformal treatment planning for radiation fields defined by multi-leaf collimator: II. Inclusion of two-dimensional modulation of x-ray intensity. *Phys. Med. Biol.* 37: 1689-1704.

- (1997) *The Physics of Conformal Radiotherapy: Advances in Technology* (IOP Publishing: Pristol, UK)

Yu CX, Symons JM, Du MN, Martinez AA and Wong JW (1995). A method for implementing dynamic photon beam intensity modulation using independent jaws and multileaf collimators. *Phys. Med. Biol.* 40: 769-787.

Xing L, Curran B, Hill R, Holmes T, Ma L, Forster K and Boyer AL (1999) Dosimetric verification of a commercial inverse treatment planning system, *Phys. Med. Biol.* 44: 463-78

Xing L, Hai J, Findley D, Ma L, Ma C-M, Kapur A and Boyer AL (1999) Dosimetric study of a commercial inverse planning system, *Int. J. Radiat. Oncol. Biol. Phys.* submitted

List of Figures

Figure 1 Comparison of 6-MV photon beam dose distributions in a water cylinder measured using an ion chamber and calculated by CORVUS and by Monte Carlo.

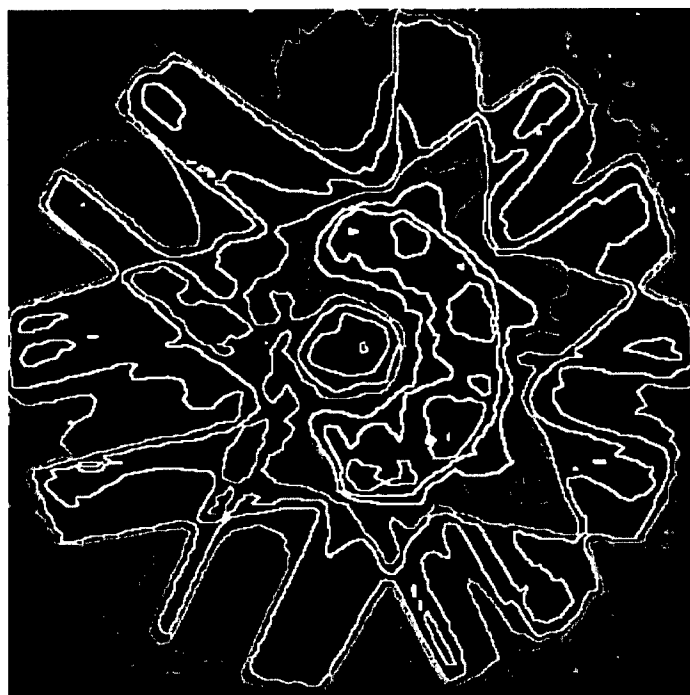
Figure 2 Comparison of 15-MV photon beam (7 fields) dose distributions for a prostate treatment calculated by CORVUS and by Monte Carlo.

Figure 3 Dose distributions for the treatment of the vertebra calculated by Monte Carlo (a and c) and by CORVUS (b and d) for 15-MV photons (9 fields). The isodose lines are given as 10, 20, 30, 40, 50, 60, 70, 80 and 90% of the prescribed target dose.

Figure 4 Dose distributions for different tissue types and material densities: (a) tissue and bone with variable density (thick line) and tissue with unity density (thin line); (b) tissue and bone with variable density (thick line) and tissue with variable density (thin line); and (c) tissue and bone with variable density (thick line) and tissue with unity density and bone with 10 g/cm³ density (thin line). The phantom geometry and beam arrangements are the same as in Figure 3. The isodose lines are given as 10, 30, 50, 70 and 80% of the prescribed target dose.

Figure 5 Dose distributions for different EGS4 energy cutoffs: (a) ECUT = 0.7 MeV (thick line) and ECUT = 1.0 MeV (thin line); (b) ECUT = 0.7 MeV (thick line) and ECUT = 1.5 MeV (thin line); and (c) ECUT = 0.7 MeV (thick line) and ECUT = 2.5 MeV (thin line). The isodose lines are given as 10, 30, 50, 70 and 80% of the prescribed target dose.

(a)



(b)

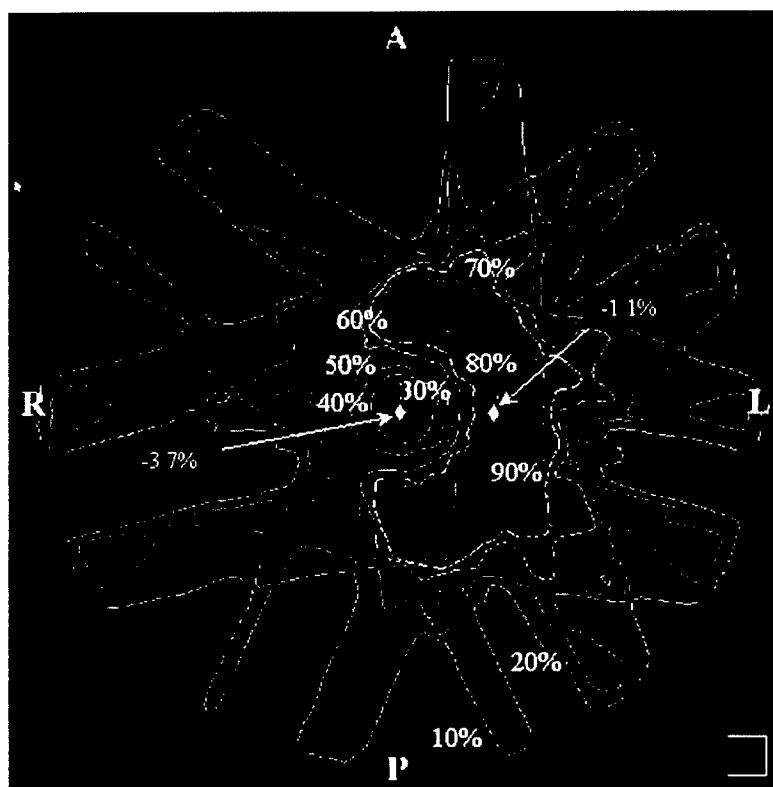
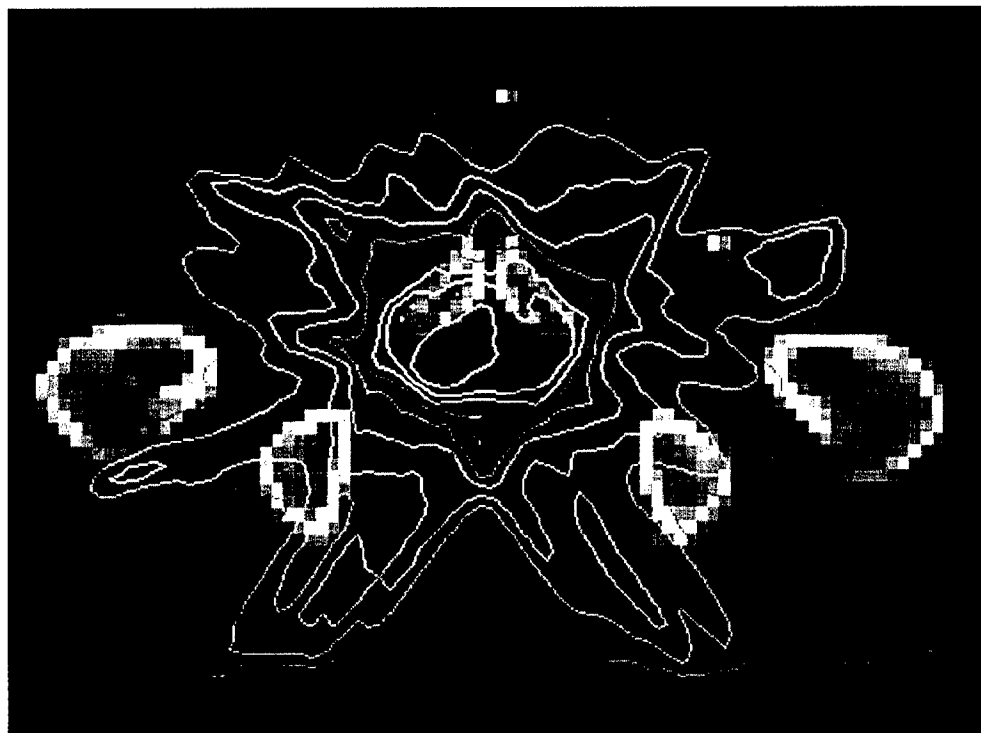


Fig. 1

(a)



(b)

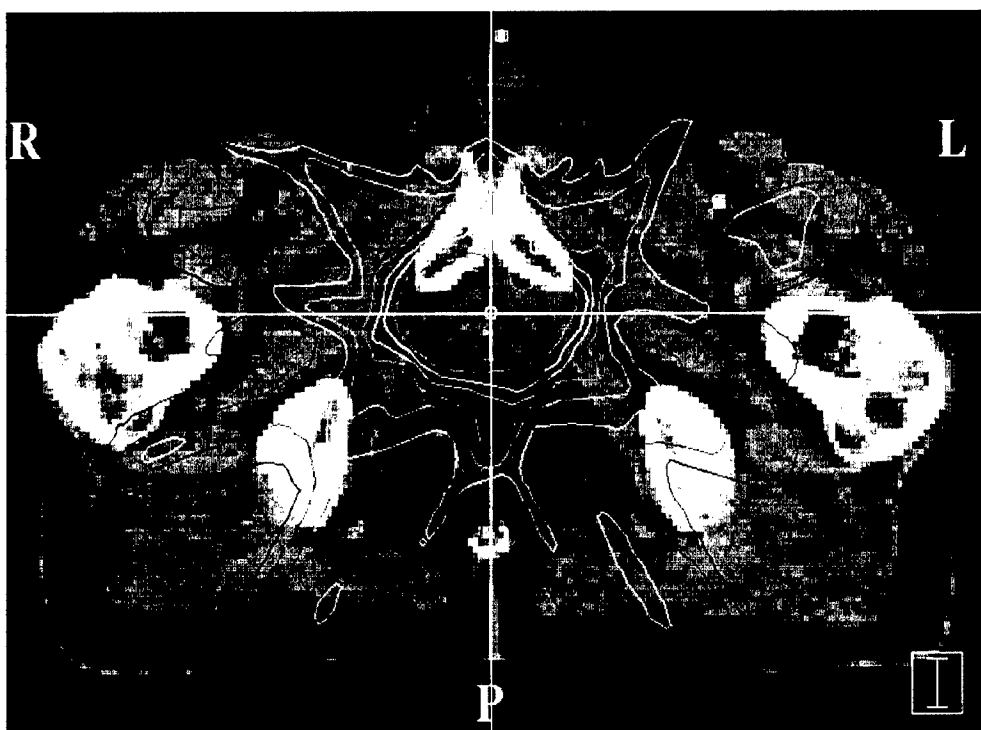
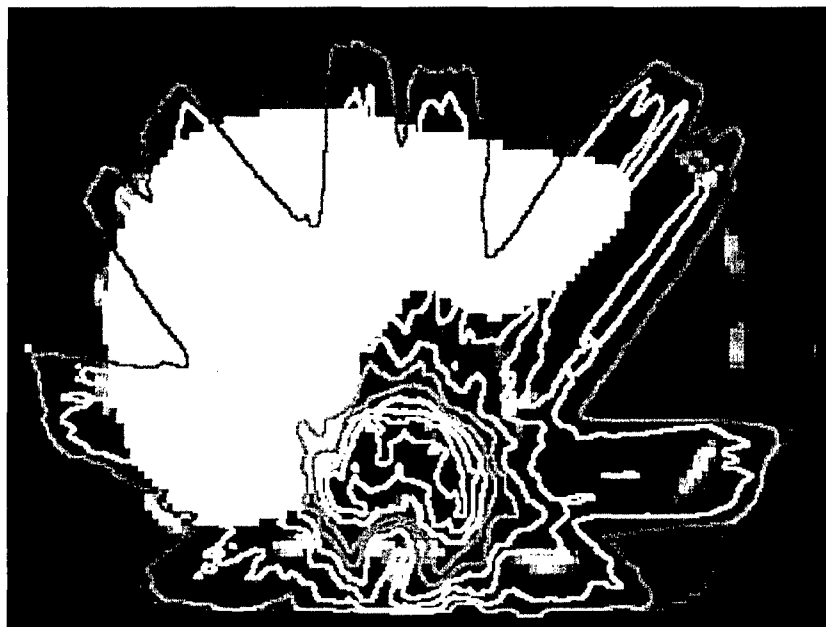
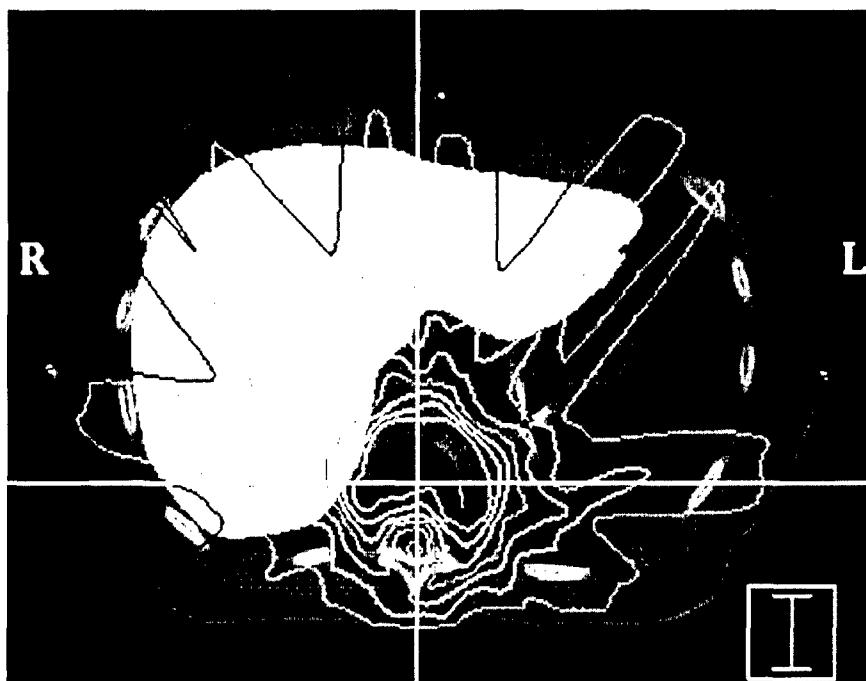


Fig. 2

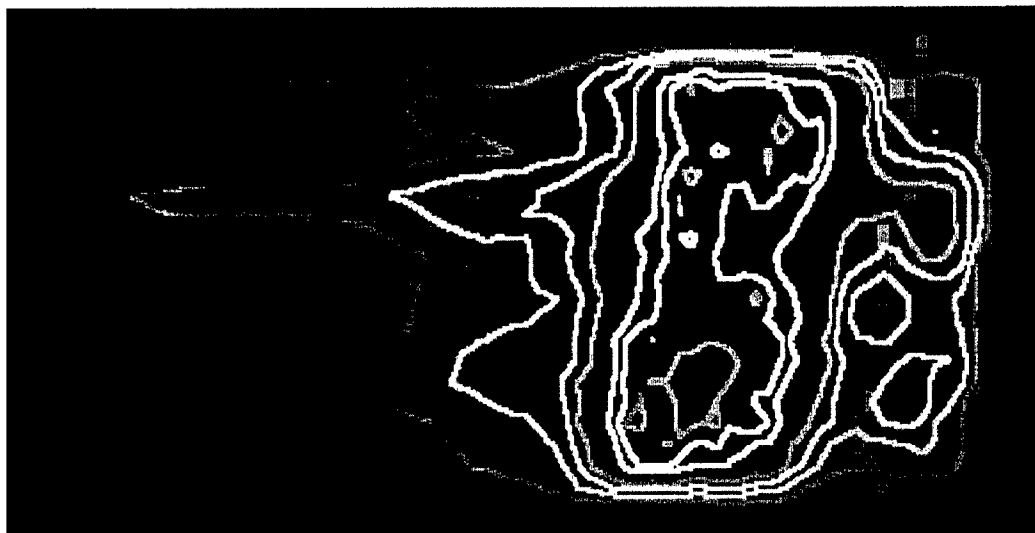
(a)



(b)



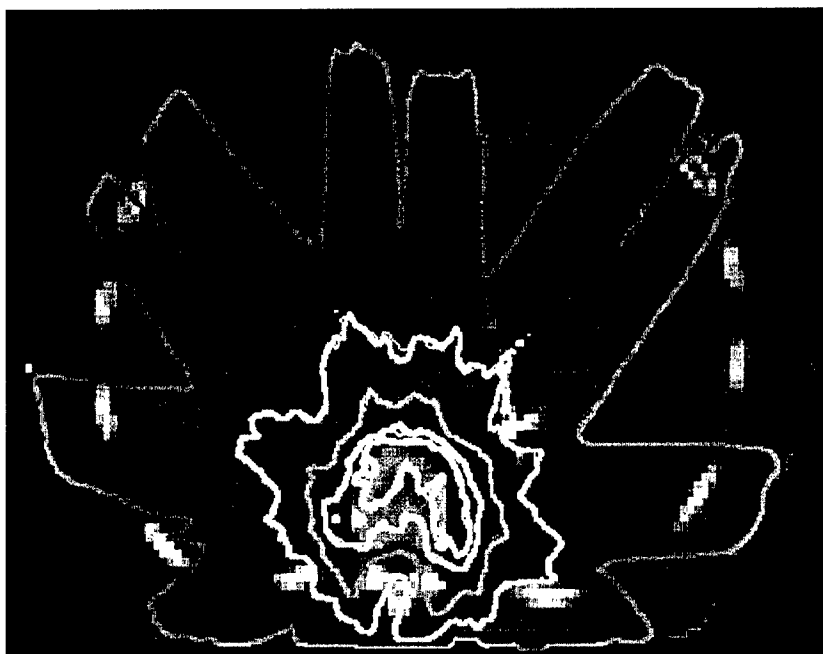
(c)



(d)



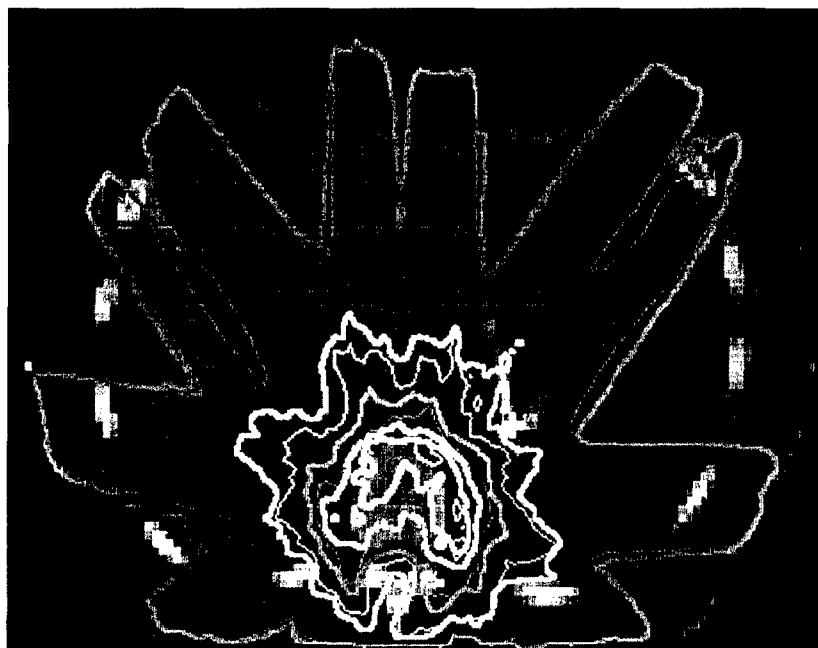
Fig. 3



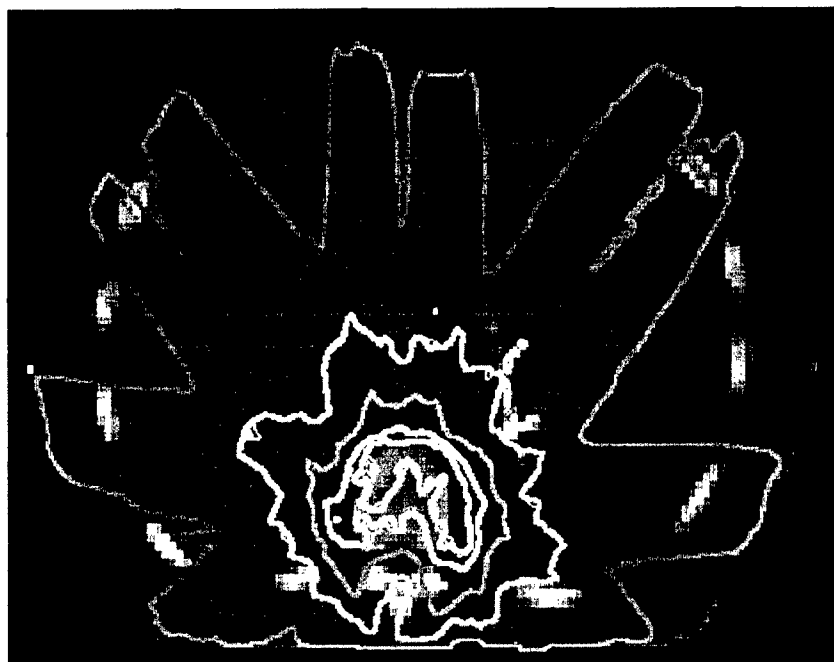
(a)



(b)



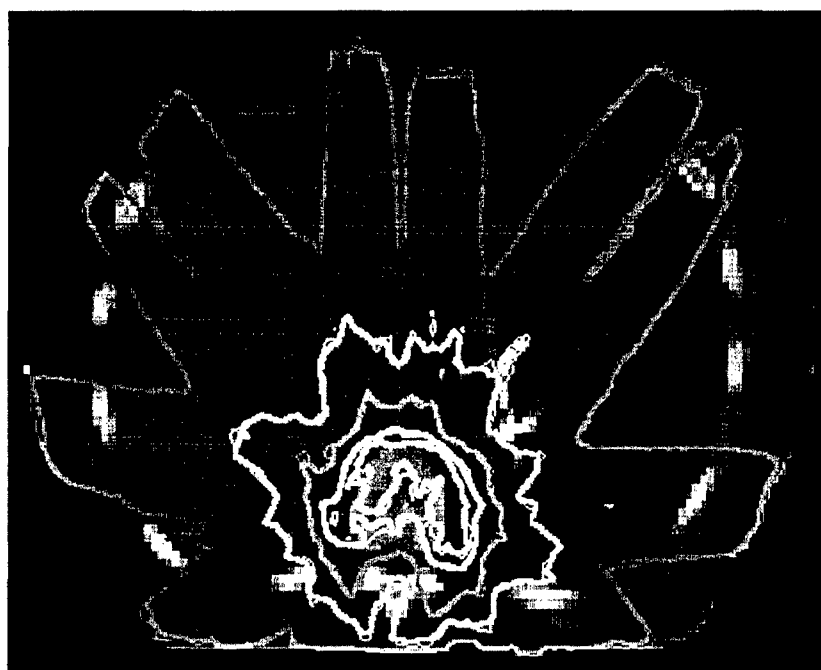
(c)
Fig. 4



(a)



(b)



(c)

Fig. 5

Clinical implementation of a Monte Carlo treatment planning system

C.-M. Ma,^{a)} E. Mok, A. Kapur, T. Pawlicki, D. Findley, S. Brain, K. Forster, and A. L. Boyer

Radiation Oncology Department, Stanford University School of Medicine, Stanford, California 94305

(Received 16 July 1998; accepted for publication 9 July 1999)

The purpose of this study was to implement the Monte Carlo method for clinical radiotherapy dose calculations. We used the EGS4/BEAM code to obtain the phase-space data for 6–20 MeV electron beams and 4, 6, and 15 MV photon beams for Varian Clinac 1800, 2100C, and 2300CD accelerators. A multiple-source model was used to reconstruct the phase-space data for both electron and photon beams, which retained the accuracy of the Monte Carlo beam data. The multiple-source model reduced the phase-space data storage requirement by a factor of 1000 and the accelerator simulation time by a factor of 10 or more. Agreement within 2% was achieved between the Monte Carlo calculations and measurements of the dose distributions in homogeneous and heterogeneous phantoms for various field sizes, source–surface distances, and beam modulations. The Monte Carlo calculated electron output factors were within 2% of the measured values for various treatment fields while the heterogeneity correction factors for various lung and bone phantoms were within 1% for photon beams and within 2% for electron beams. The EGS4/DOSXYZ Monte Carlo code was used for phantom and patient dose calculations. The results were compared to the dose distributions produced by a conventional treatment planning system and an intensity-modulated radiotherapy inverse-planning system. Significant differences (>5% in dose and >5 mm shift in isodose lines) were found between Monte Carlo calculations and the analytical calculations implemented in the commercial systems. Treatment sites showing the largest dose differences were for head and neck, lung, and breast cases. © 1999 American Association of Physicists in Medicine. [S0094-2405(99)00710-5]

Key words: radiotherapy treatment planning, dose calculation, Monte Carlo simulation, Monte Carlo treatment planning, EGS4 Monte Carlo

I. INTRODUCTION

Accurate dose calculations are essential to radiotherapy treatment planning (RTP). Radiotherapy treatments utilize the information provided by the treatment planning systems (TPS) and the clinical outcome can be improved if accuracy in the dose calculation is further improved.¹ Considerable efforts have been made to improve the dose calculation algorithms used in TPS to accurately reproduce all beam geometries and beam modification devices and to account for the effects of heterogeneities in the full three-dimensional (3D) patient geometry. Traditionally, patient dose calculations in radiotherapy have been based on correcting measured dose distributions. Newer dose calculation algorithms have been developed to predict the patient dose distribution from “first principles” using radiation transport models.² Comparisons of the traditional algorithms and the newer ones have been reviewed by Wong and Purdy,³ Cunningham and Battista,⁴ Mackie *et al.*,^{2,5} Jette,⁶ and Hogstrom and Steadham.⁷

Monte Carlo methods which use detailed phase-space information for the particles in the beam (including the energy, charge, angular, and spatial distributions)^{8–11} have been shown to be the most accurate method for radiotherapy dose calculations.^{1,8,12–22} The Monte Carlo technique is the only one that considers all aspects of photon and electron transport within a heterogeneous phantom. This accuracy is accompanied by an increase in the amount of time required to produce a statistically meaningful dose distribution. How-

ever, the rapid decrease in the price-to-performance ratio of general purpose computers has made RTP using Monte Carlo simulations a possibility. This trend is expected to continue for the foreseeable future when parallel and/or networked computer systems become readily available as dose computing engines for commercial TPS.²³

In this work, we investigate the clinical implementation of the Ottawa Madison electron gamma algorithm (OMEGA)²⁴ BEAM²⁵ and DOSXYZ²⁶ Monte Carlo codes for routine RTP dose calculations. We have commissioned the Monte Carlo simulated beam phase-space data by comparisons with the measured beam data. The beam phase-space data were analyzed and modeled using a multiple-source model. Software has been developed to build the 3D patient phantom from the computed tomography (CT) data and to convert the Monte Carlo calculated 3D dose data for display on a commercial RTP system. In this article, we report the implementation procedures, details of the Monte Carlo simulations, and comparisons of the dose distributions calculated using conventional algorithms that were implemented in a commercial TPS with those produced by our Monte Carlo simulations.

II. MATERIALS AND METHOD

A. Monte Carlo codes

The Monte Carlo codes used for the accelerator head simulation and dose calculation in the patient were

BEAM^{8,25} and DOSXYZ,^{8,26} respectively. Both codes were electron gamma shower version 4 (EGS4²⁷) user codes, running under the UNIX operating system, developed through the OMEGA project for Monte Carlo treatment planning dose calculations. Detailed descriptions of the software can be found in Ref. 8. For completeness, we briefly describe the two Monte Carlo codes used in this work.

The EGS4/BEAM code system was designed to simulate the radiation beams from any radiotherapy source, including low-energy x rays, Co-60 units, and photon and electron beams from clinical accelerators. The BEAM code produces a phase-space output of the beam (i.e., the energy, charge, position, direction, and a tag called LATCH to record the particle history) at any specified plane in a simulation geometry. The simulation geometry may consist of a series of individual component modules (CMs) positioned perpendicularly to the beam axis. The CMs used in this work to simulate the clinical linear accelerators included SLABS and CONESTAK for electron scattering foils, CONESTAK for photon target and primary collimators, and shielding rings, FLATFILT for photon flattening filters, CHAMBER for the monitor chamber, and dose simulation phantoms, APPLICAT for electron applicators, JAWS for the secondary photon collimators, MLC for the multileaf collimator, MIRROR for the light mirror, and BLOCK for electron cutouts. The actual dimensions and materials used for each of the components were handled by an input data file, which also contained the parameters required for the Monte Carlo transport simulations such as the energy cutoffs for electron (ECUT) and photon (PCUT) transport, minimum energy for the creation of knock on electrons (AE) or bremsstrahlung photons (AP), maximum electron step length (SMAX), maximum energy loss per electron step (ESTEPE), and the incident beam parameters. Several variance reduction techniques were implemented in the BEAM code including electron range rejection, photon interaction forcing, bremsstrahlung splitting, and Russian roulette.¹⁷ The BEAM code uses the default PRESTA electron transport algorithm²⁸ that has demonstrated results comparable (within 2%) to measured results in homogeneous phantoms. The simulated phase-space data can be used as source input for further BEAM simulations or dose calculations using the code DOSXYZ (see below) or analyzed using various software such as BEAM data processor (BEAMDP)²⁹ to derive particle energy spectra, fluence, and angular distributions as well as the parameters used by a beam model (see Sec. II C).

The EGS4/DOSXYZ code system was designed for dose calculations in a 3D rectilinear voxel geometry.²⁵ Voxel dimensions are completely variable in all three directions. Every voxel (volume element) can be assigned to a different material. The cross-section data for the materials used are available in a pre-processed PEGS4 cross-section data file. The density of the material defaults to that in the PEGS4 data file but can be varied in a DOSXYZ calculation for use with the patient's CT data although the density effect corrections for the stopping powers of the material remain unchanged. The voxel dimensions and materials were defined in a DOSXYZ input file together with the transport parameters

such as the energy cutoffs, SMAX, ESTEPE, and the parameters required by PRESTA. For use with CT data, a separate program CTCREATE²⁶ was used to convert the patient's CT data to the desired dimensions, material types, and mass densities (see Sec. IID). An earlier version of DOSXYZ had CTCREATE inside DOSXYZ as a subroutine, requiring more memory to run DOSXYZ because of the large data arrays used for the CT data conversion. Different source configurations can be used with DOSXYZ, such as a simple point source, a parallel beam, etc. The phase-space data obtained from a BEAM simulation can also be used as a source input to imitate all possible beam positions and directions from the linear accelerator. Dose contributions from different beam components were selectively calculated based on the particle charge or the LATCH settings specified in the BEAM simulation. DOSXYZ produced a data file that contained geometry specifications such as the number of voxels in all three directions and their boundaries as well as the dose values and the associated (1σ) statistical uncertainties in the individual voxels. The dose distributions can be analyzed using a program called STATDOSE³⁰ for rebinning, error analysis, or plotting dose distributions along any major axis.

The programs were installed on a variety of computers including SUN SPARC workstations, SGI workstations, and a network of 22 Pentium Pro 200 MHz PCs [each unit having 128 Mbyte of random access memory (RAM) and 10 Gbyte of disk space]. The PC network was used as a dose-computing engine for the Monte Carlo treatment planning process.

B. Accelerator simulation

Three models of Varian linear accelerators were simulated for the clinical implementation of Monte Carlo treatment planning at our institution. The modeled accelerators were the Clinac 1800, 2100 C, and 2300 CD (Varian Oncology Systems, Palo Alto, CA). The dimensions and materials for the accelerator components were incorporated according to the manufacturer's specifications or measurements. The electron beams emerging from the vacuum exit window were assumed to be monoenergetic and monodirectional with a beam radius of 0.1–0.2 cm. These were found to be reasonable assumptions to achieve a dose calculation accuracy of about 2% of the dose maximum (D_{\max}) in the phantom. The energy of the electrons emerging from the vacuum exit window was determined using an interactive process based on two criteria. First, the incident electron energy was interactively modified until the R_{50} value agreed with the measured value to within 1 mm for the clinical electron beams while, at the same time, the calculated and measured relative central-axis dose curves agreed to within 2% of D_{\max} . The mean electron energy values derived from measured R_{50} or $TPR_{20/10}$ were used as a starting point in the energy determination process but fine tuning by iteration was found necessary to achieve our criteria for good agreement.

We obtained accurate phase-space data for electron beams with nominal energies of 6, 9, 12, 16, and 20 MeV. The phase-space data were generally scored at a plane immedi-

ately before the lowest scraper of an electron applicator. The photon jaw settings for a particular applicator were fixed and the field shape could be modified using a Cerrobend cutout. The latter was simulated using the component BLOCK and the phase-space data were either scored immediately below the cutout or at an extended source-surface distance (SSD). The electron cone sizes included 6 cm×6 cm, 10 cm×10 cm, 15 cm×15 cm, and 20 cm×20 cm. The number of particles (including electrons, photons, and positrons) in a phase-space data file ranged from a few million to 50 million depending on the applicator size and beam energy. Three nominal energies were simulated for photon beams: 4, 6, and 15 MV. The phase-space data were scored at a plane immediately above the photon jaws. The number of particles in a photon beam file was about 50 million. Field shaping by photon jaws, blocks, and the MLC was further simulated using BEAM and the phase-space data could be stored temporarily or used directly for dose calculations. Each of the 22 PCs stored an individual (statistically independent) phase-space file (or phase-space model) for each clinical beam. Dose calculations for a given patient were performed on all of the PCs to reduce the simulation time. The statistical uncertainty of the final dose distribution was determined after combining the results from all 22 PCs.

The energy cutoffs for the accelerator simulation were $ECUT=AE=700$ keV (kinetic+restmass) for charged particles and $PCUT=AP=10$ keV for photons. The ESTEPE value was 0.04. The electron range rejection option was used for electron beams, and bremsstrahlung splitting and Russian roulette were used for photon beams. The ICRU recommended compositions and stopping power values were used for the materials used in the accelerator simulation.³¹ The CPU time required for the BEAM simulation ranged from a few hours to a few hundred hours on a single PC and the corresponding disk requirement ranged from a few hundred Mbyte to a few Gbyte depending on the field size and beam energy. The disk requirement amounted to hundreds of Gbyte for all the beams simulated.

C. Beam characterization

It has been demonstrated that well-designed beam models can be used to represent and reconstruct the beam phase-space data with the advantage of saving disk space and computing time in the accelerator simulation.^{32,33} In this work, we have characterized our beams using a well-tested multiple-source model.^{32,33}

In the multiple-source model, particles coming from different parts of an accelerator were treated as if they originated from different (sub)sources. We used several sub-sources to model the particles from different accelerator components. A point source was used to model the particles coming directly from the vacuum window and traversing the monitor chamber and mirror without hitting any of the beam defining components such as photon jaws or applicator scrapers. For an electron beam, the spatial and energy distribution of these "direct" particles depends on the dimensions and material of the scattering foils, monitor chamber, and

mirror. The effective SSD for an electron point source was determined using the "pinhole" method.^{32,34} For photon beams, the planar fluence distribution on a plane source was specified in annular bins. Each annular bin had its own energy and angular distributions. Separate "extended" photon sources were necessary to simulate the effect of electron and photon scattering in the target, primary collimator, and the flattening filter.³³ The effect of the thickness of the subsource on the angular distribution was negligible and therefore ignored. Particles from secondary collimators (jaws) were simulated by parallel bars of zero thickness. The electron applicators were modeled using square rings of zero thickness. Particles differing in charge were considered to originate from different subsources. The origin of a particle was classified using the information recorded in LATCH. The parameter LATCH contains the region (i.e., beam defining component) number(s) where a particle had been, had interacted, or was created if it was a secondary particle. The origin of a photon was considered to be the region where it was created or scattered. For a charged particle, the origin is considered to be the last nonair region in which it had been before it reached the scoring plane. The relative subsource intensity was determined according to the relative number of particles from the individual components (using LATCH) with their weight properly considered. Usually, no more than 10 subsources were needed to model a clinical electron or photon beam.

The reconstruction of the phase-space data was composed of the following steps. First, a subsource was randomly selected according to the relative source intensity. The particle energy was then sampled from the energy distribution for the subsource. For an electron beam, a position on the phantom surface was sampled for the particle based on the spatial distributions of the subsource with some parameterization such as the "inverse-square" relation. Because there was a very weak correlation between the particle energy and the position of particles from the same subsource, we sampled the particle position and energy independently. A position on the subsource would then be sampled. The position on the subsource and the position on the phantom surface gave the incident direction of the particle. For photon beams, the particle incident direction was sampled from the angular distributions of the extended photon source (plane source). The planar fluence on the scoring plane was a function of the planar fluence on the plane source and the angular distribution. The final step of the reconstruction was to correct for the effect of charged particles scattering in the air. This was accomplished by creating a small perturbation about each particle's incident direction. However, this angular perturbation has no significant (within statistical uncertainty of 0.5%) effect on the electron depth dose or lateral dose profiles.

The multiple-source model was implemented in BEAM and DOSXYZ. The particle planar fluence, energy spectrum, angular distribution, and other source parameters were derived from the simulated phase-space data using BEAMDP. This code produced a source data file that was read by BEAM or DOSXYZ for the phase-space reconstruction. A source data file usually contained a few hundred kilobytes of

TABLE I. Density range for the four materials used to build the Monte Carlo simulation phantoms (a). Only air, tissue and bone were used if a lung were not present in the regions of interest (b).

(a) Phantom with a lung				
Material	Air	Lung	Tissue	Bone
CT number range	0–70	70–800	800–1250	1250–4000
Density range	0.001–0.07	0.07–0.80	0.80–1.28	1.28–2.88
(b) Phantom without a lung				
Material	Air	Tissue	Bone	
CT number range	0–70	70–1250	1250–4000	
Density range	0.001–0.07	0.07–1.28	1.28–2.88	

data and its size was independent of the original phase-space file size. This resulted in a disk space saving of more than a factor of 1000. For a 10 cm \times 10 cm electron field, 5×10^5 phase-space particles were sufficient to derive the source parameters for the beam model to achieve the same dose calculation accuracy (a factor of 10 less compared to using the raw phase-space data). The number of particles contained in the file determines the uncertainty of a phase-space data set. This implies that, for a given set of phase-space data, the uncertainty in the calculated dose increases with decreasing voxel size because the number of particles traversing a voxel decreases. This problem cannot be resolved by simply recycling the phase-space particles since the statistical uncertainty in the phase-space may become a systematic uncertainty in any further simulations. When the beam model is used, however, all the reconstructed phase-space particles are independent. Therefore, dose calculation accuracy can be retained by simulating more histories if smaller voxels are used.

D. Conversion of CT data and beam setup

Conversion of the CT numbers to materials and mass densities was done using the code CTCREATE.²⁶ The current version of CTCREATE, on the OMEGA BEAM 97 distribution, reads the CT data set in both Pinnacle (ADAC, Sunnyvale, CA) and CADPLAN (Varian Oncology Systems, Palo Alto, CA) formats. Additionally, we developed software to convert CT data from the FOCUS (CMS, Inc., St. Louis, MO) format. Information required to run CTCREATE included the CT format, the CT data file name, and voxel dimensions for the simulation phantom. The user could also sample the CT data set and use various functions to convert CT data to the densities and materials for the simulation phantom. For any material, the mass density and CT number limits were set by the user. The density for a given voxel was assigned by linear interpolation of a mass density versus CT number curve. Table I gives the CT number range and density range for the four materials used in our implementation (Table Ia). These were consistent with the recommendations in an ICRU report.³⁵ The density-effect corrections of the stopping powers for air and tissue were from another ICRU report.³¹ The lung material was only used when a lung was

present. Otherwise, the same CT number range (70–1280) was replaced by tissue with the same density limits (Table Ib). The CT slices were usually scanned at 3 mm intervals. A CT image contained 512 \times 512 pixels with the side of a pixel equal to about 0.94 mm. CTCREATE allowed a subsection of the original CT data to be included in the CT phantom. This enabled the simulation to be performed at a resolution higher than if the calculation used the entire CT volume and enabled the user to trim some of the air surrounding the patient on a typical CT image.

Caution was exercised in converting the beam setups from the FOCUS treatment planning system to DOSXYZ. Although both used a right-hand coordinate system a 270° rotation with respect to the x axis was needed to convert the FOCUS coordinates to the DOSXYZ coordinates for the CT data. Furthermore, the field shape on FOCUS was defined in beam's eye view (BEV) while both BEAM and DOSXYZ used the patient's eye view. This required another conversion (180° rotation with respect to the x axis for the phase space) when BLOCK and MLC components were used. We added additional coding in DOSXYZ to handle field shaping by electron cutouts and the MLC. The cutout shape or the MLC leaf positions were coded in BEV so that the latter conversion could be omitted. This was further facilitated by the symmetry of the phase-space data with respect to the x and y axes because they were either scored at a plane immediately above the lowest scraper for electrons or immediately above the secondary collimators for photons. Other considerations included gantry rotation, collimator rotation, couch rotation, and translation.

E. Details of the dose calculation and measurement

For dose profile calculations in water, the simulation phantom was built using the DOSXYZ input file with voxel dimensions and materials individually defined. The voxel dimensions were variable according to dose gradient in the regions of interest. The x and y dimensions were 1–2 mm on the beam penumbra and 5–20 mm near the field's center and outside the field. The dimension in the z direction was 1–2 mm for electron beams near d_{\max} and in the build-up region for photons and 2–4 mm in the rest of the phantom. For heterogeneity studies, the regions size was also set to 1–2 mm near the interfaces. For central-axis depth dose calculations or output factor calculations, the component module CHAMBER was used with variable ECUT values in different regions and electron range rejection switched on. This resulted in significant CPU time savings compared with the use of DOSXYZ, which does not include any of the variance reduction techniques described previously. The diameter of the scoring region was set as close as possible to that of the sensitive volume of the detector. The z dimensions were 1–2 mm near d_{\max} and in the build-up region. In all the calculations, we set the transport parameters to ECUT=AE=700 keV, PCUT=AP=10 keV, and ESTEPE=0.04. The 1 σ statistical uncertainty for the phantom dose calculation was 1% or better by running a sufficient number

of particle histories (e.g., 5×10^6 phase-space particles for a $10 \text{ cm} \times 10 \text{ cm}$ electron field with 1 cm^3 voxels).

For patient dose calculations, the simulation phantom was built from the patient's CT data with up to $128 \times 128 \times 128$ voxels (uniform in size). The side of a voxel varied from 2 to 5 mm. For single electron beams, a subsection of the CT data was sometimes used to retain the spatial resolution while for photon beams with multiple gantry angles, the entire CT volume was often used. The number of particle histories simulated ranged from a few million for electron beams to up to one billion for photon beams with nine gantry angles for an intensity-modulated radiotherapy (IMRT) treatment. The 1σ statistical uncertainty in the dose was generally 1%–2% of the D_{max} value. The CPU time required for an electron beam calculation was generally at the order of a few minutes and for a photon beam about half an hour on the 22 PC network. A factor of 2–3 more particle histories were needed for an IMRT simulation compared to a conventional treatment plan simulation while the CPU time required was still within an hour since many photons were stopped by the MLC leaves and the average CPU time per history became lower compared to that for a conventional treatment.

All measurements in this work were performed in accordance with the recommendations of the TG-25,³⁴ TG-21,³⁶ and TG-39 (Ref. 37) protocols. Central-axis depth-dose curves were measured in a water phantom using a Scanditronix *p*-type diode detector and a Wellhofer 0.1 cc scanning chamber with WP700 data acquisition software. Dose values in the build-up region were acquired with an Attix parallel-plate chamber in solid water phantoms. The depth-dose curves were normalized to the maximum dose value D_{max} at the depth d_{max} . The transverse profiles at depths of interest were acquired either with the diode detector or with Kodak films that were optically scanned and calibrated. The transverse profiles were normalized to the central-axis values at each depth. The output factor measurement was performed with a PTW/Markus parallel-plate chamber. The water-to-air stopping-power ratios used for the conversion from the measured ionization to the dose to water were calculated in this work using the Monte Carlo simulated beam phase-space data. They differed only slightly (within 1.5%) for small field sizes from the TG-21 values, which were derived from broad beams of monoenergetic electrons. The variation of the perturbation corrections with depth for the PTW/Markus chamber was ignored in the output measurements. The measurement uncertainty was estimated to be 1% or less for large fields where electron lateral equilibrium was established and about 2% for smaller fields. The same experimental procedures as those reported in Ref. 38 were used for the measurement of the inhomogeneity corrections in layered phantoms. The inhomogeneity correction factor was defined as the ratio of the dose in a heterogeneous phantom to that in homogeneous water. A 0.6 cc Farmer chamber was used for the water phantom measurement and a 0.1 cc PTW chamber was used for the heterogeneous phantom measurement. The ionization ratios were converted to the dose ratios using the calculated stopping-power ratios in the phantom. The replacement correction factors were calculated using Monte

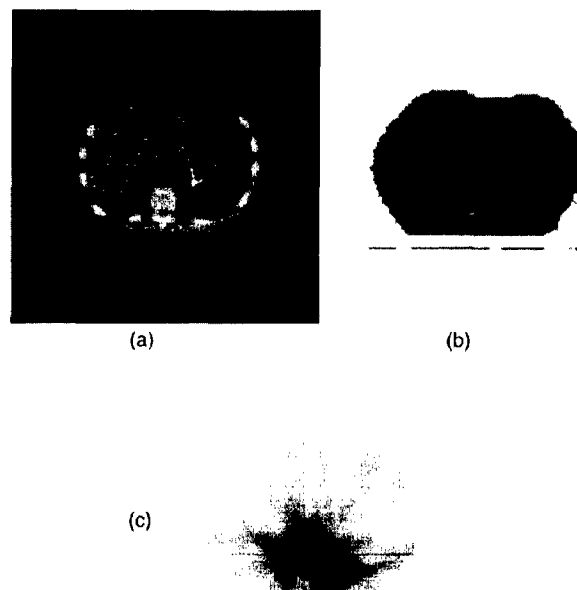


FIG. 1. (a) Mass density map and (b) the material types of a Monte Carlo simulation phantom built from patient CT data. Only three materials were used in this phantom since a lung was not present. A CT artifact caused by a metallic object (or the contrast agent used for magnetic resonance imaging) can be seen. (c) The dose distribution in the same phantom irradiated by nine intensity-modulated 15 MV photon fields calculated by the Monte Carlo method is shown (darker points correspond to higher dose).

Carlo by simulating the dose in water and in a low density cavity of the same volume as the chamber air cavity. The effect of the chamber wall and the central electrode was ignored in the heterogeneity correction factor measurement.

F. Display of the 3D dose data

Software was developed to convert the 3D dose data generated by DOSXYZ for display on a commercial treatment planning system (FOCUS). Rebinning of the 3D dose data was possible. However, the same dose grids were used in this work when comparing with the dose calculations done by the commercial RTP system. Details in the isodose plotting routine and the differences in the dose grids may introduce additional differences in the isodose curves. To be consistent with the commercial system, we also zeroed the dose in the air surrounding the patient's body for the Monte Carlo calculated dose data. The normalization point for the Monte Carlo plan was either at D_{max} or at a specified voxel, consistent with the plan calculated by the commercial system. Figure 1 shows the density and material map used for a patient simulation and the dose distribution for an IMRT plan of nine 15 MV photon fields calculated using the Monte Carlo method.

III. RESULTS AND DISCUSSIONS

A. Comparisons in homogeneous phantoms

We commissioned the radiotherapy beams from our three clinical accelerators, Varian Clinac 1800, 2100C, and 2300CD. The nominal energy of the electron beams ranged from 6 to 20 MeV and the field size ranged from 1 cm \times 1 cm to 20 cm \times 20 cm, shaped using either an electron applicator or a cutout. The nominal energies of the photon beams were 4, 6, and 15 MV. The commissioning procedure included the following steps: (1) verification of the accelerator specifications, (2) measurement of the dose distributions and various correction factors for wedges, blocks, electron applicators, and cutouts, (3) simulation of the phase space for each field/beam, (4) calculation of the dose distributions, and (5) comparison of the calculated and measured dose distributions. Steps (3)–(5) were repeated by changing the simulation parameters in the input file (such as the electron incident energy or the diameter of the pencil beam) until the difference between the Monte Carlo calculated dose distributions agreed with the measurements to 2% of D_{\max} . Detailed descriptions of these results are reported elsewhere.²²

We compared the Monte Carlo calculated output factors with the measured values and obtained good agreement (generally within 2%) for various photon and electron field shapes and sizes. This gave us confidence in computing the monitor units for Monte Carlo calculated treatment plans. Since electron output factors are routinely measured with film at the depth of D_{\max} , the measured output factor for small irregular electron fields might be quite uncertain. For example, a shift of a few mm in the depth of D_{\max} for a 6 MeV beam could result in a change in the measured output factor by 5%–10%. By calculating the output factors using Monte Carlo simulations, we reduced this uncertainty down to about 3%.¹⁹ The D_{\max} for the small irregular field was found by searching the whole simulation phantom. The calculation was completed in 0.5–1 h on the FOCUS treatment-planning computer (an SGI R4400 250 MHz workstation).

The depth-dose curves and lateral profiles calculated using the Monte Carlo method agreed well with the measured data. Both the original phase space and the phase space reconstructed using our multiple-source model were used for the Monte Carlo simulations in this work. The dose distributions were consistent at a 1%–2% level for all the photon and electron beams investigated.^{22,23} The characteristics of the electron beams for the Varian Clinac 2100C accelerator were similar to those reported in Ref. 32 except for the electron incident energy at the vacuum exit window. A separate study³³ also showed that the change in the depth-dose curves or dose profiles due to small variations in electron incident energy (2%–3%) or field size (a few mm) could be predicted using the multiple-source model by varying the corresponding source parameters. This means that the source parameters derived from the phase-space data for a clinical accelerator can be adjusted to reconstruct the phase space of a beam of the same nominal energy and field size for another accelerator of the same type. This can be achieved by comparisons with the measured beam data for the second accelerator.³³

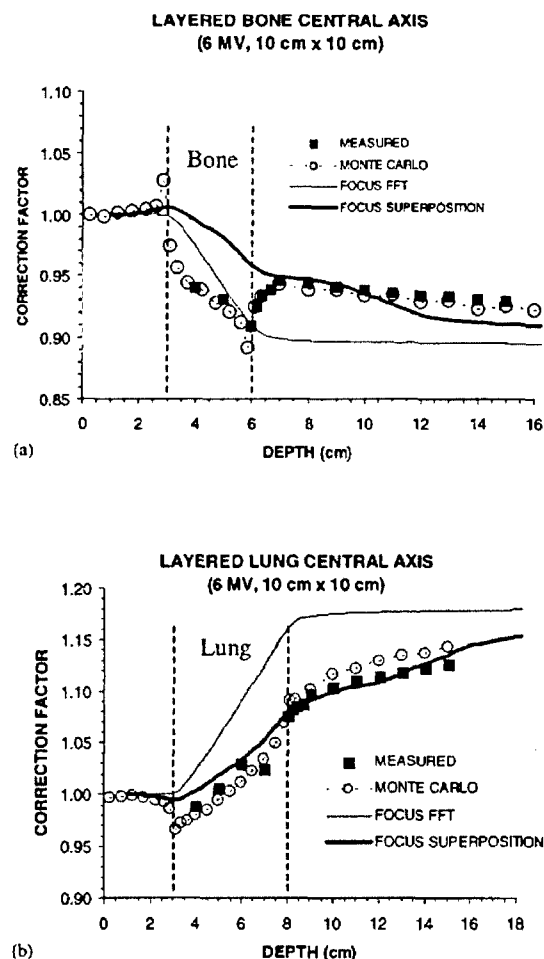


Fig. 2. Comparisons of heterogeneity correction factors calculated by Monte Carlo, by FOCUS (FFT convolution, and by superposition convolution), and by measurements for a 6 MV beam: (a) in a layered-bone phantom for a 10 cm \times 10 cm field and (b) in a layered-lung phantom for a 10 cm \times 10 cm field. The field size is defined at 100 cm SSD.

B. Heterogeneity corrections

Comparisons of dose distributions in heterogeneous phantoms measured using ionization chambers and calculated by Monte Carlo simulations were made for the photon and electron beams available on our accelerators. The heterogeneity corrections, calculated as the ratio of the dose at a point in a heterogeneous phantom to that at the same point in a water phantom, are shown in Fig. 2 for a 6 MV photon beam and in Fig. 3 for a 12 MeV electron beam. The densities of the lung and bone materials were 0.272 and 1.83 g cm⁻³, respectively. The same composition and mass density values were used in the Monte Carlo simulations.

Figure 2(a) shows the correction factor for a water–bone–water phantom. The bone material was 3 cm thick and placed 3 cm below the solid water surface. The solid water behind the bone slab was 12 cm thick. The Monte Carlo calculated correction factors agreed to within 0.5% of the measured values. Similar agreement was achieved for other beam energies (not shown). It is interesting to note that the dose values near the interfaces were significantly perturbed (re-

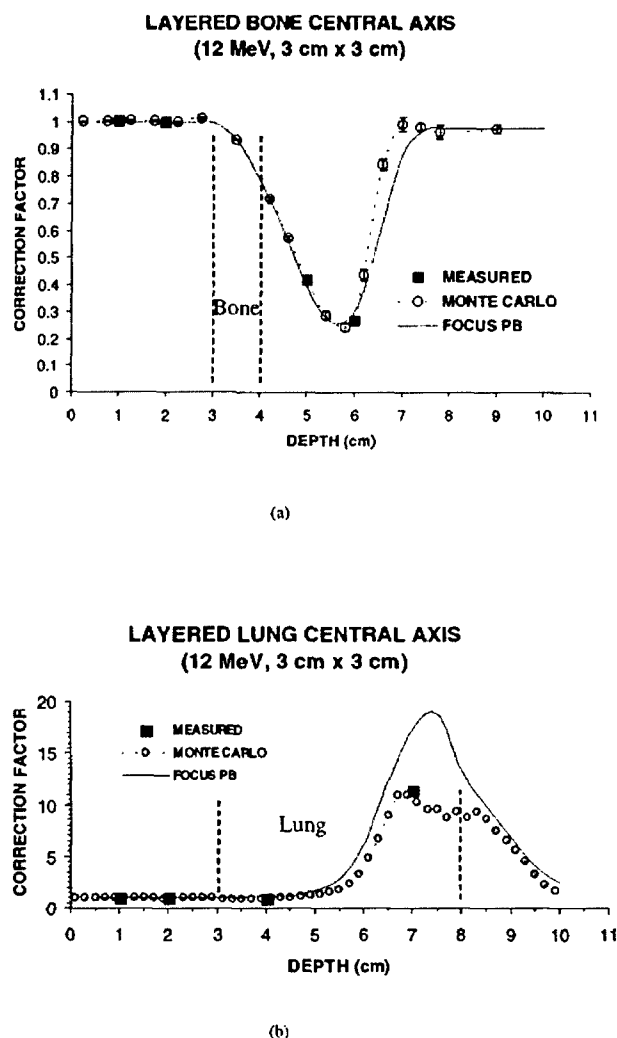


FIG. 3. Comparisons of heterogeneity correction factors calculated by Monte Carlo, by FOCUS (3D pencil beam), and by measurements for a 12 MeV electron beam: (a) in a layered-bone phantom for a 3 cm \times 3 cm field and (b) in a layered-lung phantom for a 3 cm \times 3 cm field. The field size is defined at 100 cm SSD.

quiring up to 10% correction) due to the differences in the photon fluence and electron fluence between the heterogeneous and the water phantoms. The effect of electron disequilibrium diminished at a distance of 1.5 cm from the bone–water interface. Beyond this point, the heterogeneity correction mainly accounted for the perturbation effect caused by the photons. Figure 2(b) shows the heterogeneity correction factors for a layered water–lung–water phantom irradiated by a 6 MV photon beam. The field size was 10 cm \times 10 cm defined at 100 cm SSD. The lung slab was 5 cm thick, and placed 3 cm below the solid water surface. The solid water was 12 cm thick behind the lung slab. The beam axis was centered between the lung blocks. The agreement between the Monte Carlo calculations and the measurements was well within 1%. Our results were consistent with the findings reported in the literature for similar geometry.^{21,38–42}

Recently, a fast fourier transform (FFT) convolution algorithm was implemented and tested in the FOCUS system,

and it showed some improvement in the dose calculations with heterogeneous phantoms over that of the conventional algorithm. However, differences of up to 5%–10% were still found in heterogeneous phantoms between the FFT convolution algorithm and measurements (see Fig. 2). A superposition convolution algorithm is currently being implemented in FOCUS, that can handle the photon scatter component more accurately but still cannot predict the dose in the regions adjacent to the interfaces. It should be noted that the correction factors given in Fig. 2 were calculated as the ratio of the dose to the medium in the heterogeneous phantom to the dose to water in a homogeneous water phantom. While real lung and bone materials were used in the measurement and the Monte Carlo calculations, the FFT and superposition convolution methods used water (with different electron densities) in both phantoms. Thus, comparisons of the correction factors in lung and bone regions could not be made directly without properly converting the dose values to the same medium.

Figure 3(a) shows the heterogeneity correction factors for a layered water–bone–water phantom irradiated by a 12 MeV electron beam. The field was 3 cm \times 3 cm at the phantom surface. The bone slab was 3 cm below the water surface and 1 cm thick. The solid water behind the bone slab was 12 cm thick. Both the Monte Carlo and the FOCUS pencil beam results agreed with the measured data except for deeper depths (6–8 cm) near the practical ranges of the primary electrons. However, the dose values at these depths were small and therefore the actual effect was small. Figure 3(b) shows the corresponding results for a layered water–lung–water phantom irradiated by a 12 MeV electron beam with a 3 cm \times 3 cm field. The lung slab was 5 cm thick and placed 3 cm below the solid water surface. The solid water was 10 cm thick behind the lung slabs. Again, the results were consistent between the calculations and the measurements except for larger depths (5–9 cm) where the FOCUS pencil beam predicted greater corrections compared to Monte Carlo and measurements. In general, the FOCUS pencil beam algorithm worked well for layered heterogeneous phantoms, as has been demonstrated by previous investigators.⁴³

C. Electron beam plans

We now compare the dose distributions for electron beams in different CT phantoms built from patient's CT data computed by a commercial 3D treatment-planning system (the FOCUS system) and by Monte Carlo simulations. The plans were first made on the FOCUS system and then the same beam setup was used in the Monte Carlo simulations. The Monte Carlo calculated 3D dose data were put back into the FOCUS system as separate plans for display.

Figure 4 shows the dose plans for a nasal cavity treatment using a 6 MeV electron beam. The field was 4 cm \times 4 cm defined at 100 cm SSD. Both the FOCUS and the Monte Carlo plans showed hot spots beside the bony structures. However, the locations of the hot spots were shifted a few millimeters. The Monte Carlo calculations also predicted a few more local hot spots which were caused by electron

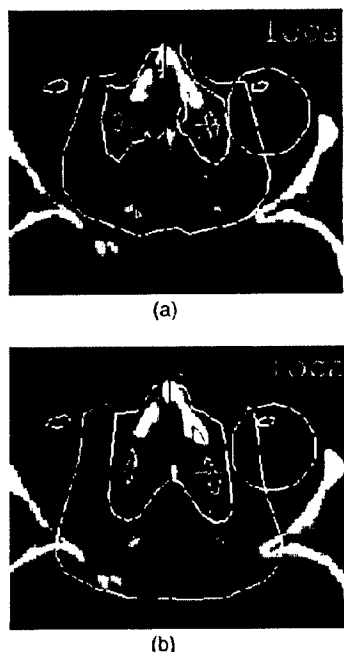


FIG. 4. Treatment plans for a nasal cavity case using a 6 MeV electron beam calculated (a) by Monte Carlo and (b) by the FOCUS 3D RTP system. The electron field is 4 cm \times 4 cm defined at 100 cm SSD (4 cm \times 4 cm cutout on a 10 cm \times 10 cm applicator).

scatter from the bony structures in the upper or lower CT slices. This was not observed in the FOCUS plan. In general, the dose distributions in water calculated by the FOCUS system were consistent with the measurements (at 2%–5% level). However, significant discrepancies (more than 15%) were found for oblique incidence or in the presence of heterogeneities such as lung or bone. The CT phantom in Fig. 4 was much more complex than the layered experimental phantoms used in Figs. 2 and 3. The electron fluence was perturbed by the effect of missing tissue and by the presence of bony structures and air cavities. The overall result was a reduced treatment range, as predicted by the Monte Carlo simulations.

Figure 5 shows another nasal cavity treatment using a 12 MeV electron beam. The field was 4 cm \times 4 cm defined at 100 cm SSD. Again, the dose distributions differed significantly between the FOCUS predictions and the Monte Carlo simulations in terms of the locations of the hot spots and the isodose lines. For example, the 50% isodose lines differed by more than 1 cm. The Monte Carlo calculated dose distributions also showed more variations due to the presence of the air cavities and bony structures whereas the FOCUS dose distributions looked smooth and uniform.

In general, significant discrepancies were found between the Monte Carlo plans and the plans calculated using the 3D pencil beam algorithm implemented in the FOCUS system in the regions near air cavities or/and bones, as well as with oblique incidence, small irregular fields, or/and extended SSDs. Since electron boost fields were not always planned on a RTP system, it was necessary to compute the dose dis-

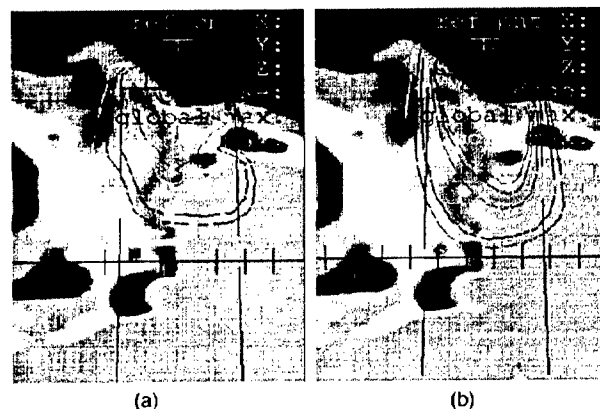


FIG. 5. Treatment plans for a nasal cavity case using a 12 MeV electron beam calculated (a) by Monte Carlo and (b) by the FOCUS 3D RTP system. The electron field is 4 cm \times 4 cm defined at 100 cm SSD (4 cm \times 4 cm cutout on a 10 cm \times 10 cm applicator).

tributions using the Monte Carlo method for some frequently used boost fields. It took from half of an hour to a couple of hours of CPU time on our RTP computer to complete an electron beam Monte Carlo plan. The improvement in the dosimetry accuracy with the use of the Monte Carlo dose calculation was often significant (>5% of the D_{\max} value and a >5 mm shift in the isodose lines). This makes the Monte Carlo dose calculation a valuable component in a RTP system for electron beams despite its CPU time requirement.

D. Photon beam plans

Significant discrepancies between the Monte Carlo calculated patient dose plans and the FOCUS plans were also found for photon beams. The conventional photon dose calculation algorithm used in the current FOCUS system did not properly account for the change in the photon scatter component in the presence of heterogeneities such as lung and bone. The patient dose calculations showed that the doses were often underestimated in the regions behind large bony structures and overestimated in and behind the lung. This is primarily due to the inappropriate treatment of the photon scatter and the lack of electron transport considerations. Figure 6 shows a photon beam plan calculated by Monte Carlo and by the FOCUS system. Part of the target received about 10% less dose compared to the prescribed value. These results were confirmed by our layered water–lung–water phantom measurements (Fig. 2). Our findings were consistent with the results and analysis by previous investigators.^{1,3–5,20,21,38–42,44–47}

To explore the effect of full photon and electron transport in photon beam dose calculations, we show in Fig. 7 an IMRT treatment plan calculated by both Monte Carlo simulation and the CORVUS treatment-planning optimization system (NOMOS Corp., Sewickley, PA). The plan was generated using the CORVUS system for 6 MV photon beams with nine gantry angles. CORVUS also produced the MLC leaf sequence files for operating the Varian dynamic MLC (Varian Oncology Systems, Palo Alto, CA). The same leaf

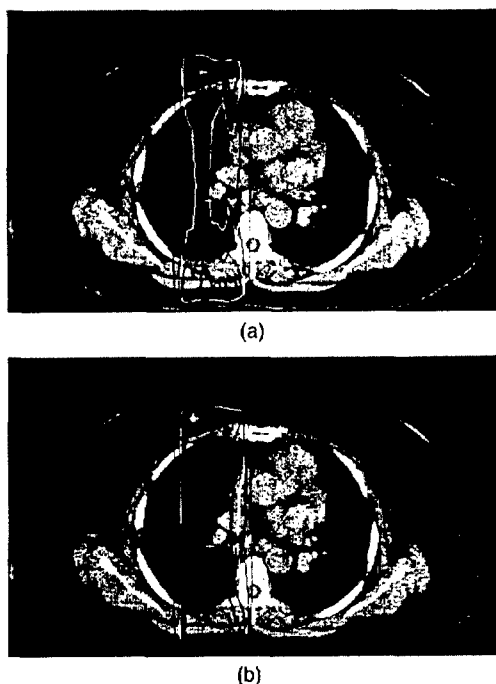


FIG. 6. Treatment plans of an AP/PA lung treatment with a 6 MV photon beam calculated (a) by Monte Carlo and (b) by the FOCUS 3D RTP system using the Clarkson algorithm with pixel-by-pixel heterogeneity corrections applied. The field size is 8 cm \times 9 cm (at 100 cm SSD) and is further defined by Cerrobend blocks. In (a) and (b) the isodose lines given are 10%, 50%, 75%, 80%, 85%, 90%, and 93% of the dose maximum.

sequence files were used in the Monte Carlo simulation to achieve modulation of the photon fluence using the simulated phase-space data. Reasonable agreement was found in the more homogeneous regions between the CORVUS dose distributions and the Monte Carlo predictions while in the regions near large bony structures (such as the spinal cord) differences of more than 10% could be seen. This increase in the dose to the spinal cord was thought to be due to electron scattering from the surrounding bone, which might not be modeled properly by CORVUS using a "finite size pencil beam" algorithm. Although the photon beams were optimized to avoid the cord, electrons could reach the cord and the dose to the cord was enhanced due to the high-density material surrounding it. Each beam going through the vertebra may contribute only a few percent more dose to the cord due to the uncertainty in the beam penumbra. The overall effect from all nine beams was a more than 10% increase in the dose to the cord. Another possible reason was the approximation in the photon leakage correction; the effect of leaf leakage may be underestimated in the regions in a photon field where the beam intensity was supposed to be close to zero.

It should be mentioned that the photon dose calculation algorithm used in the commercial treatment-planning optimization system was demonstrated to be accurate (about 2% for relative dose profiles and 3%–4% for absolute dose) for homogeneous (water) phantoms.⁴⁸ The dose distributions given by the CORVUS system agreed with the Monte Carlo and

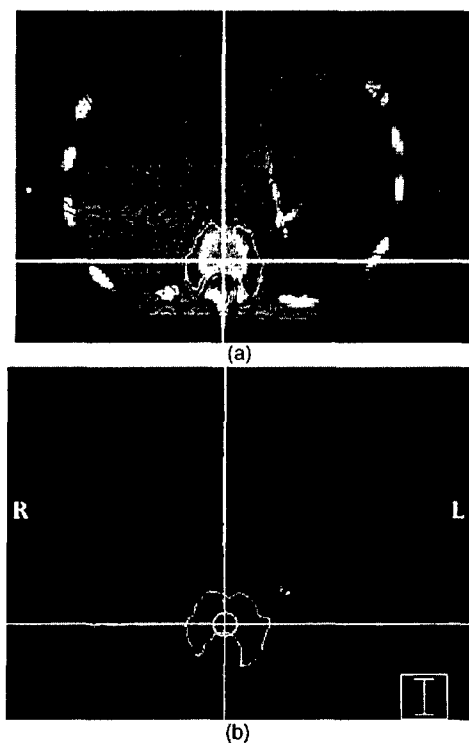


FIG. 7. Dose distributions for an IMRT case with nine intensity-modulated 6 MV photon fields calculated (a) by Monte Carlo and (b) by the CORVUS inverse-planning system. The isodose lines given are 10%, 20%, 30%, 40%, 50%, 60%, 70%, 80%, and 90% of the dose maximum. The patient geometry is the same as that in Fig. 1.

measurements to about 3% in a cylindrical water phantom with various hypothetical target shapes. This indicates that treatment plans for homogeneous phantoms (such as the prostate) may be adequate but they may not be so for treatment sites near heterogeneities such as the air–tissue, lung–tissue, and tissue–bone interfaces. We have verified the "optimized" dose distributions generated by the CORVUS system for treatment sites involving small target volumes and heterogeneities in the case of nasal cavities, head and neck, and the lung using the Monte Carlo simulations. Differences of over 10% were observed in the regions within or near low-density materials such as the lung and air cavities and near large bony structures.

IV. SUMMARY

We have implemented the BEAM and DOSXYZ Monte Carlo codes for radiotherapy RTP dose calculations. The implementation included the simulation and characterization of the clinical radiotherapy beams, the conversion of the patient CT data and beam arrangement for patient dose calculations, and software development for efficient dose calculations and display of the Monte Carlo 3D dose data on the existing treatment-planning system.

Comparisons of the dose distributions in water calculated by Monte Carlo simulations and the measurements showed general agreement within 2% for various clinical beam setups for electron beams as well as for photon beams. Monte

Carlo simulations have been used for computing the monitor units required for small irregular electron fields, which were shown to be more accurate and efficient than routine film or ion chamber measurements (the uncertainty in the output factor was reduced from 5% to 10% using film at a fixed depth to within 3%). The Monte Carlo calculated dose distributions in heterogeneous phantoms were confirmed (within 1%) using specially designed measurements whereas the conventional dose calculation algorithms may underestimate or overestimate by 5%–10% in the regions within or adjacent to the lung or bone materials.

Monte Carlo dose calculations may be more applicable to electron beam treatment planning than to photon beams in terms of computing time and improvement in dose accuracy. The computation time for a typical electron plan was 20 min–2 h on a Pentium Pro 200 MHz PC for 0.5–10 million particle histories. This can be reduced to a few minutes by running the Monte Carlo simulations on today's faster workstations or the multiple-CPU computer systems currently available or being used for treatment-planning and optimization calculations. With Monte Carlo calculations, the uncertainty in the dose for some of these cases may be reduced from 10% to 20% (or a 5–20 mm shift in the isodose lines) to from 3% to 5% (or a 2–3 mm shift in the isodose lines) for the regions of interest. Typical photon plans took 1–20 h of CPU time on a Pentium Pro 200 MHz PC. The computing time was only weakly dependent on the number of beams used since the statistical uncertainty in the dose values was determined only by the number of electron tracks in the volumes of interest, and thus, by the total number of particle histories simulated.

Our results indicate that more accurate dose calculation algorithms than those currently used in the "inverse-planning" systems are needed for intensity-modulated radiotherapy treatment planning. The conventional dose calculation algorithms may not accurately predict the dose distributions in and near inhomogeneities due to the lack of electron transport and charged particle equilibrium. The dose in the target volume may be in error by up to 7% as calculated by the optimization system while the uncertainty in the dose to the critical organ may be over 10% of the maximum target dose for cases involving the head and neck (especially near the nasal cavities), the lung/chestwall, and large bony structures.

ACKNOWLEDGMENTS

The authors are grateful to Dr. A. E. Nahum, Dr. P. Andero, Dr. D. W. O. Rogers, Dr. A. F. Bielajew, Dr. B. A. Faddegon, Dr. T. Holmes, and Dr. M. Miften for useful discussions and valuable comments on the manuscript. They would like to thank Dr. T. R. Mackie, Dr. D. W. O. Rogers, and the OMEGA BEAM team at the National Research Council of Canada, Ottawa, Canada, for the fine-tuned Monte Carlo simulation system. They would like to acknowledge Varian Oncology Systems, Palo Alto, CA, for providing detailed information on the Varian Clinac linear accelerators and CMS, Inc., St. Louis, MO, for information

on the FOCUS 3D treatment planning system. They would like to thank their Stanford colleagues, Gary Luxton, Lei Xing, Lijun Ma, Steve B. Jiang, Jinsheng Li, and Jun Deng, for encouragement and help, and Todd Koumrian, Behrooz Tofighrad, and Michael Luxton for help with the computers and software support. They would like to thank Dr. Moyed Miften of CMS, Inc. for the FOCUS FFT and superposition convolution data in Fig. 2. This investigation was supported in part by Grant Nos. CA78331 and CA43840 from the NIH, by Grant Nos. BC971292 from the DOD, and by the Seed Cycle 1 RSNA Research and Education Fund.

^{a)}Author to whom correspondence should be addressed; electronic mail: cma@reyes.stanford.edu

¹R. Mohan, *Proceedings of the XIIth International Conference on the Use of Computers in Radiation Therapy*, Salt Lake City, 1997 (Medical Physics Publishing, Madison, WI, 1995), pp. 16–18.

²T. R. Mackie, P. Reckwerdt, and N. Papanikolaou, in *3-D Radiation Treatment Planning and Conformal Therapy*, edited by J. A. Purdy and B. Emami (Medical Physics Publishing, Madison, WI, 1995).

³J. W. Wong and J. A. Purdy, *Med. Phys.* **17**, 807–814 (1990).

⁴J. R. Cunningham and J. J. Battista, *Phys. Canada* **51**, 190–218 (1995).

⁵T. R. Mackie, P. Reckwerdt, T. McNutt, M. Gehring, and C. Sanders, in *Teletherapy: Present and Future*, edited by T. R. Mackie and J. R. Palta (Advanced Medical Publishing, Madison, WI, 1996).

⁶D. Jette, in *Radiotherapy Physics*, edited by A. R. Smith (Springer-Berlin, 1995), pp. 95–121.

⁷K. R. Hogstrom and R. E. Steadham, in Ref. 5.

⁸D. W. O. Rogers, B. A. Faddegon, G. X. Ding, C. M. Ma, J. Wei, and T. R. Mackie, *Med. Phys.* **22**, 503–525 (1995).

⁹M. Udale-Smith, Ph.D. thesis, University of Leeds, UK, 1990.

¹⁰R. Mohan, C. S. Chui, and L. Lidofsky, *Med. Phys.* **12**, 592–597 (1985).

¹¹D. M. Lovelock, C. S. Chui, and R. Mohan, *Med. Phys.* **22**, 1387–1394 (1995).

¹²J. Cygler, J. J. Battista, J. W. Scrimger, E. Mah, and J. Antolak, *Phys. Med. Biol.* **32**, 1073–1083 (1987).

¹³K. R. Shortt, C. K. Ross, A. F. Bielajew, and D. W. O. Rogers, *Phys. Med. Biol.* **31**, 235–249 (1986).

¹⁴A. F. Bielajew, D. W. O. Rogers, J. Cygler, and J. J. Battista, *The Use of Computer in Radiation Therapy*, edited by I. A. D. Bruinvis, P. H. van der Giessen, H. J. van Klefens, and F. W. Wittkämper (Elsevier Science, Amsterdam, 1987), pp. 65–68.

¹⁵A. E. Nahum, in *Monte Carlo Transport of Photons and Electrons*, edited by T. M. Jenkins, W. R. Nelson, and A. Rindi (Plenum, New York, 1988), pp. 523–547.

¹⁶T. R. Mackie, in *Dosimetry of Ionizing Radiation*, edited by K. Kase, B. Bjarnagard, and F. H. Attix (Academic, New York, 1990), Vol. III, pp. 541–620.

¹⁷D. W. O. Rogers and A. F. Bielajew, in Ref. 16, pp. 427–539.

¹⁸P. Andreo, *Phys. Med. Biol.* **36**, 861–920 (1991).

¹⁹C.-M. Ma, E. Mok, A. Kapur, and D. Findley, in Ref. 1, pp. 159–1620.

²⁰C. L. Hatmann-Siantar et al., in Ref. 1, pp. 19–22.

²¹J. J. DeMarco, T. D. Solberg, and J. B. Smathers, *Med. Phys.* **25**, 1–11 (1998).

²²A. Kapur, C.-M. Ma, E. Mok, D. Findley, and A. L. Boyer, *Phys. Med. Biol.* **44**, 3479–3994 (1998).

²³A. F. Bielajew, *Proceedings of the XIth International Conference on the Use of Computers in Radiation Therapy*, Manchester, UK, 1994, pp. 2–5.

²⁴T. R. Mackie et al., in Ref. 23, pp. 152–153.

²⁵D. W. O. Rogers, C.-M. Ma, G. X. Ding, and B. Walters, *BEAM Users Manual*, National Research Council of Canada Report No. PIRS-0509A (NRCC, Ottawa, Canada, 1995).

²⁶C.-M. Ma, P. J. Reckwerdt, M. Holmes, D. W. O. Rogers, and B. Geiser, *DOSXYZ Users Manual*, National Research Council of Canada Report No. PIRS-509B (NRCC, Ottawa, Canada, 1995).

²⁷R. Nelson, H. Hirayama, and D. W. O. Rogers, *The EGS4 Code System*, Stanford Linear Accelerator Center Report, No. SLAC-265 (SLAC, Stanford, CA, 1985).

- ²⁸ A. F. Bielajew and D. W. O. Rogers, Nucl. Instrum. Methods Phys. Res. B **18**, 165–181 (1987).
- ²⁹ C.-M. Ma and D. W. O. Rogers, *BEAMDP Users Manual*, National Research Council of Canada Report No. PIRS-0509D (NRCC, Ottawa, Canada, 1995).
- ³⁰ H. C. E. McGowan, B. A. Faddegon, and C.-M. Ma, *STATDOSE for 3D Dose Distributions*, National Research Council Report No. PIRS-0509F (NRCC, Ottawa, Canada, 1995).
- ³¹ *Radiation Dosimetry: Stopping Powers for Electrons and Positrons*, ICRU Report No. 37 (ICRU, Bethesda, MD, 1984).
- ³² C.-M. Ma, B. A. Faddegon, D. W. O. Rogers, and T. R. Mackie, Med. Phys. **24**, 401–417 (1997).
- ³³ C.-M. Ma, Radiat. Phys. Chem. **35**, 329–344 (1998).
- ³⁴ AAPM TG-25, Med. Phys. **18**, 73–109 (1991).
- ³⁵ *Tissue Substitutes in Radiation Dosimetry and Measurement*, ICRU Report No. 44 (ICRU, Bethesda, MD, 1989).
- ³⁶ AAPM TG-21, Med. Phys. **10**, 741–771 (1983).
- ³⁷ AAPM TG-39, Med. Phys. **21**, 1251–1261 (1994).
- ³⁸ Y. P. Zhu and A. L. Boyer, Phys. Med. Biol. **35**, 351–368 (1990).
- ³⁹ E. R. Epp, A. L. Boyer, and K. P. Dopke, Int. J. Radiat. Oncol., Biol., Phys. **2**, 613–619 (1977).
- ⁴⁰ T. R. Mackie, J. W. Scriger, and J. J. Battista, Med. Phys. **12**, 188–196 (1985).
- ⁴¹ C. X. Yu, J. W. Wong, and J. A. Purdy, Med. Phys. **14**, 78–83 (1987).
- ⁴² T. D. Solberg, F. E. Holly, A. A. F. DeSalles, R. E. Wallace, and J. B. Smathers, Int. J. Radiat. Oncol., Biol., Phys. **32**, 235–239 (1995).
- ⁴³ R. Muller-Runkel and S.-H. Cho, Med. Phys. **24**, 91–102 (1997).
- ⁴⁴ R. Mohan, C. Chui, and L. Lidofsky, Med. Phys. **13**, 64–73 (1986).
- ⁴⁵ A. L. Boyer and E. Mok, Med. Phys. **12**, 169–177 (1986).
- ⁴⁶ A. L. Boyer, L. Xing, C.-M. Ma, B. Curran, R. Hill, A. Kania, and A. Blier, Med. Phys. **26**, 187–195 (1999).
- ⁴⁷ B. Faddegon, J. Balogh, R. Mackenzie, and D. Scora, Radiat. Phys. Chem. **217–228** (1998).
- ⁴⁸ L. Wang, C. Chui, and M. A. Lovelock, Med. Phys. **25**, 867–878 (1998).

Stopping-power ratios for clinical electron beams from a scatter-foil linear accelerator*

Ajay Kapur† and Chang-Ming Ma

Department of Radiation Oncology, Stanford University School of Medicine, Stanford, CA 94305, USA

E-mail: kapur@reyes.stanford.edu

Received 9 February 1999

Abstract. Restricted mass collision stopping-power ratios for electron beams from a scatter-foil medical linear accelerator (Varian Clinac 2100C) were calculated for various combinations of beams, phantoms and detector materials using the Monte Carlo method. The beams were of nominal energy 6, 12 or 20 MeV, with square dimensions $1 \times 1 \text{ cm}^2$ to $10 \times 10 \text{ cm}^2$. They were incident at nominal SSDs of 100 or 120 cm and inclined at 90° or 30° to the surface of homogeneous water phantoms or water phantoms interspersed with layered lung or bone-like materials. The broad beam water-to-air stopping-power ratios were within 1.3% of the AAPM TG21 protocol values and consistent with the results of Ding *et al* to within 0.2%. On the central axis the stopping-power ratio variations for narrow beams compared with normally incident broad beams were 0.1% or less for water-to-LiF-100, graphite, ferrous sulfate dosimeter solution, polystyrene and PMMA, 0.5% for water-to-silicon and 1% for water-to-air and water-to-photographic-film materials. The transverse variations of the stopping-power ratios were up to 4% for water-to-silicon, 7% for water-to-photographic-film materials and 10% for water-to-air in the penumbral regions (where the dose was 10% of the global dose maximum) at shallow depths compared with the values at the same depths on the central axis. In the inhomogeneous phantoms studied, the stopping-power ratio correction factors varied more significantly for air, followed by photographic materials and silicon, at various depths on the central axis in the heterogeneous regions. For the simple layered phantoms studied, the estimation of the stopping-power ratio correction factors based on the relative electron-density derived effective depth approach yielded results that were within 0.5% of the Monte Carlo derived values for all the detector materials studied.

1. Introduction

In radiotherapy dosimetry protocols (AAPM 1983, IAEA 1987), the use of restricted mass collision stopping-power ratios is recommended for electron beams to convert the absorbed dose to the detector materials to the absorbed dose to the irradiated media. However, the recommended ratios for electron beams commonly used in radiation therapy were calculated by Berger using Monte Carlo techniques for monoenergetic, monodirectional, infinitely wide electron beams that were perpendicular to semi-infinite water phantoms (AAPM 1983). The TG21 protocol (AAPM 1983) suggests periodic revision of these data to accommodate improved calculation procedures. Recent Monte Carlo calculations of these ratios for broad scattered or scanned realistic-electron beams from various linear accelerators indicated

* Presented at the 40th Annual AAPM Meeting (9–13 August 1998, San Antonio, Texas).

† Address for correspondence: Room A-042, Division of Radiation Physics, Department of Radiation Oncology, 300 Pasteur Drive, Stanford University School of Medicine, Stanford, CA 94305, USA.

agreement with the protocol-recommended values to within 1.5% and 0.5% respectively for water-to-air stopping-power ratios at the depth of maximum dose d_{\max} (Ding *et al* 1995). Larger discrepancies were noted at some other depths. The dependence of water-to-air stopping-power ratios on beam characteristics, energy spectra and photon contamination has thus been demonstrated by this and other studies in the literature (Nahum 1978, ICRU 1984a, Andreo 1988, Andreo *et al* 1989, Andreo and Fransson 1989, Klevenhagen 1994, Ding *et al* 1995).

In this paper we extend these studies using Monte Carlo techniques to a variety of electron beam, phantom and detector combinations—in particular for conditions where lateral-scatter equilibrium is degraded compared with broad-beam conditions (ICRU 1984a, AAPM 1991). With the reduction of field size, the associated loss of lateral-scatter equilibrium is known to cause significant spectral changes (Brahme 1977, Nilsson 1985, Andreo *et al* 1989) and cause the absorbed dose profiles to be markedly different than those in broad-beam conditions (Brahme 1977, McGinley *et al* 1979, Hogstrom *et al* 1981, Sharma *et al* 1984, AAPM 1991). Therefore it is not unreasonable to expect changes in the stopping-power ratios due to the associated spectral variations (Ma *et al* 1997, Zhang *et al* 1998). In this paper we quantitatively re-evaluate the AAPM-recommended stopping-power ratios (AAPM 1983, 1991) by incorporating Monte Carlo derived phase-space data (Kapur *et al* 1998) for narrow electron beams. Variations of stopping-power ratios for medium-to-detector in both homogeneous and heterogeneous media, and therefore the relevance of using stopping-power ratio correction factors for dose measurements in heterogeneous phantoms using various detectors, will be discussed.

The AAPM notation of spectrum-averaged restricted mass collision stopping-power ratios for medium 'med' to detector 'det' ($\bar{L}/\rho_{\text{det}}^{\text{med}}$) will be used throughout the text. Except where otherwise indicated they will be referred to as 'stopping-power ratios' for brevity. Calculations are performed for a Varian Clinac 2100C medical linear accelerator that consists of a dual-scattering foil system to flatten the beams at depth in water phantoms. Scatter-foil linacs produce electron beams with a broader spectrum than those from scanning beam linacs so that larger discrepancies from the idealized beams used for the AAPM TG21 stopping-power ratio calculations can be expected with scatter-foil linacs (Ding *et al* 1995). The stopping-power ratios are calculated in accordance with a modified version of the Spencer-Attix formulation (Spencer and Attix 1955) of the Bragg-Gray cavity theory (Bragg 1912, Gray 1936) as recommended by TG21 (AAPM 1983), IAEA (1987) and ICRU (1984a).

2. Theory

2.1. Homogeneous phantoms

When a detector is placed in a medium that is exposed to electron-beam radiation, the primary electrons and secondary electrons generated in the medium deposit energy in the radiation-sensitive region of the detector. From direct or indirect measurement of this deposited energy, the dose to the detector material can be calculated. The dose to the detector material can be related to the dose to the medium in the absence of the detector. Cavity theories in the literature that deal with the dose-conversion range from the simple Bragg-Gray theory (Bragg 1912, Gray 1936) to the Burlin general-cavity theory (Burlin 1966, 1968, Burlin *et al* 1969) and its various modifications (Holt *et al* 1975, O'Brien 1977, Ogunleye and Paliwal 1985). The stopping-power ratios play an integral role in the dose conversion.

According to the Bragg-Gray theory the dose to the medium ' D_{med} ' is related to the dose to the detector material ' D_{det} ' using the unrestricted mass collision stopping-power ratio of

the medium to the detector $(\bar{S}/\rho)_{\text{det}}^{\text{med}}$ as follows:

$$D_{\text{med}} = D_{\text{det}}(\bar{S}/\rho)_{\text{det}}^{\text{med}}. \quad (1)$$

Spencer and Attix (1955) replaced $(\bar{S}/\rho)_{\text{det}}^{\text{med}}$ in equation (1) by $(\bar{L}/\rho)_{\text{det}}^{\text{med}}$ (restricted mass collision stopping-power ratio of the medium to the detector) to yield the following expression

$$D_{\text{med}} = D_{\text{det}}(\bar{L}/\rho)_{\text{det}}^{\text{med}}. \quad (2)$$

The difference between the theories stems from the different treatment of energy loss processes occurring during radiation transport. While the Bragg-Gray theory assumes continuous energy loss for primary electrons, the Spencer-Attix theory considers energy loss to be continuous for electrons with energy below a certain threshold. In both these theories, however, the underlying assumption is that the detectors are small so that they do not significantly perturb the electron fluence by virtue of their presence.

In the ICRU 35 (ICRU 1984a) and TG21 (AAPM 1983) reports, the dose conversion process applicable to detectors used in radiotherapy dosimetry is decoupled as follows. The perturbation in the fluence of electrons incident on the detector due to the presence of the detector is addressed by calculating a perturbation factor (Harder 1968) and identifying the effective point of measurement (Skaggs 1949) of the detector. The spectrum-averaged mass collision stopping-power ratio of the medium to the detector material is then applied to the perturbation-corrected dose absorbed by the detector. The two-step process yields the dose that would be absorbed by the medium in the absence of the detector. The final expression that can be used for the dose conversion is thus

$$D_{\text{med}} = D_{\text{det}}(\bar{L}/\rho)_{\text{det}}^{\text{med}} P. \quad (3)$$

Here $P = \prod_i P_i$ is the product of various terms P_i and equivalent to the perturbation factor (Ma and Nahum 1994) that takes into account the changes in the fluence and mean energy due to the presence of the detector. The final expression thus contains the stopping-power ratio which will constitute the subject of this paper.

In the Spencer-Attix formulation of the Bragg-Gray theory, secondary electrons are further classified based on the choice of an energy threshold ' Δ '. This threshold is selected by comparing the mean chord length (Spencer and Attix 1955) of the detector with the finite range of those electrons that can just cross it. Secondary electrons that have energy below this threshold are treated as 'track-ends' and assumed to deposit all their energy locally through continuous processes within the detector. If equilibrium exists for these secondary electrons, the assumption of local energy deposition is justified. Electrons with energies higher than the cut-off are assumed to originate outside the detector and to deposit part of their energy locally in the detector. The amount of energy deposited locally can be calculated using the restricted mass collision stopping-power for the detector material at these energies. While the use of the same threshold Δ for the medium and the detector is not rigorous since electrons would have different ranges in the two, Burch's attempt (Burch 1955, 1957) to treat it differently and as 'tail-ends' as opposed to 'track-ends' did not yield an analytical solution. Fortunately the water-to-air stopping-power ratios are not critically sensitive to the cut-off energy (AAPM 1983, ICRU 1984a). Thus for practical reasons the Spencer-Attix approach is recommended by standard protocols for the dose conversion process using stopping-power ratios (AAPM 1983, 1991, IAEA 1987). When secondary electronic equilibrium exists, the stopping-power ratios based on Bragg-Gray approach or its approximate formulation by Harder (1965) yield results that are similar to those obtained using the Spencer-Attix approach for water to solid or liquid detector materials (ICRU 1984a).

The spectrum-averaged Spencer-Attix restricted mass collision stopping-power ratio is calculated by adding the track-end contributions from Δ to 2Δ to the integrated fluence-weighted restricted mass collision stopping-power for the energy components greater than 2Δ

for the medium and detector separately and then taking their ratio (Spencer and Attix 1955). Nahum modified the Spencer-Attix approach for the approximate treatment of the track-end terms by obtaining the product of the fluence of electrons with energy less than or equal to Δ and the unrestricted mass collision stopping-power ratio (S/ρ) at the cut-off energy (Nahum 1978). In his approach the lower limit of integration is changed from 2Δ to Δ . The stopping-powers contributed for each energy component greater than the cut-off can be alternatively weighted by the track lengths of the particles. This leads to the same results as the fluence-weighted approach (Berger 1987). The final expression for the stopping-power ratios is thus given as follows

$$(\bar{L}/\rho)_{\text{det}}^{\text{med}} = \frac{\int_{\Delta}^{E_{\text{max}}} \Phi_E^{\text{med}}(E, \Delta) \left(\frac{L}{\rho}(E, \Delta)\right)^{\text{med}} dE + \Phi_{\Delta}^{\text{med}} \Delta \left(\frac{S}{\rho}(\Delta)\right)^{\text{med}}}{\int_{\Delta}^{E_{\text{max}}} \Phi_E^{\text{med}}(E, \Delta) \left(\frac{L}{\rho}(E, \Delta)\right)^{\text{det}} dE + \Phi_{\Delta}^{\text{med}} \Delta \left(\frac{S}{\rho}(\Delta)\right)^{\text{det}}}. \quad (4)$$

Here ' E_{max} ' is the maximum energy in the spectrum and ' Φ_E^{med} ' is the fluence of electrons at energy ' E ' in the medium at the region of interest.

2.2. Heterogeneous phantoms

In heterogeneous phantoms, such as those used for the verification of dose calculation algorithms (Shiu *et al* 1992, Ayyangar *et al* 1993), measurements of dose with suitable detectors are required. These detector measurements can be converted to the dose of interest according to equation (3). The dose of interest may be the dose to the actual material of the medium or to a small mass of water contained within that medium. The dose to the medium may be converted to the dose to a small mass of water contained within the medium using the stopping-power ratio of water to the medium. The dose measured in heterogeneous phantoms can be compared with the dose in water phantoms measured using the same detectors to study the effects of the heterogeneities (Prasad *et al* 1984, Prasad and Bassano 1989, El-Khatib *et al* 1992, El-Khatib and Connors 1992) using a heterogeneity correction factor 'HCF'. The HCF is defined as the ratio of dose in a heterogeneous phantom ' D_{het} ' to dose at the same point in a water phantom ' D_{water} '. Using equation (3), this may be expressed as follows:

$$\begin{aligned} \text{HCF}_{\text{water}}^{\text{het}} &= \frac{D_{\text{het}}}{D_{\text{water}}} = \frac{[D_{\text{det}}]^{\text{het}} [(\bar{L}/\rho)_{\text{det}}^{\text{het}}]^{\text{het}} [P_{\text{det}}^{\text{het}}]^{\text{het}}}{[D_{\text{det}}]^{\text{water}} [(\bar{L}/\rho)_{\text{det}}^{\text{water}}]^{\text{water}} [P_{\text{det}}^{\text{water}}]^{\text{water}}} \\ &= (D_{\text{det}})_{\text{water}}^{\text{het}} (\text{SPRCF})_{\text{water}}^{\text{het}} (\text{PCF})_{\text{water}}^{\text{het}} \end{aligned} \quad (5)$$

where

$$(\text{SPRCF})_{\text{water}}^{\text{het}} = \frac{[(\bar{L}/\rho)_{\text{det}}^{\text{het}}]^{\text{het}}}{[(\bar{L}/\rho)_{\text{det}}^{\text{water}}]^{\text{water}}} \quad (6)$$

and

$$(\text{PCF})_{\text{water}}^{\text{het}} = \frac{[P_{\text{det}}^{\text{het}}]^{\text{het}}}{[P_{\text{det}}^{\text{water}}]^{\text{water}}}. \quad (7)$$

Here the SPRCFs and PCFs are the stopping-power ratio correction factors and perturbation correction factors respectively. The SPRCF at a given voxel for a given detector measurement is defined as the ratio of the stopping-power ratios for the medium-to-detector to water-to-detector evaluated at the corresponding energies in the voxels in the two phantoms. In this notation the phantom is identified in the superscript outside the square brackets. The PCFs will not be addressed in this paper.

3. Materials and methods

3.1. Electron beams

Varian Clinac 2100C (Varian Oncology Systems, Palo Alto, CA) electron beams of 6, 12 and 20 MeV nominal energy, collimated by Type III accessories (that consist of open-walled applicators with matched scattering foils) were used for this study. Beam sizes as projected at a nominal SSD of 100 cm varied from $1 \times 1 \text{ cm}^2$ to $10 \times 10 \text{ cm}^2$. Air gaps of 5 or 25 cm from the lowermost scraper of the applicator were studied. Angles of incidence of these beams as defined by the angle between the central axis of the beams and the surface of the irradiated phantoms were chosen to be either 90 or 30 degrees corresponding to normal or oblique incidence.

In addition broad, mono-directional and mono-energetic beams of energy 6, 12 and 20 MeV incident at 90° to water phantoms were also studied. The stopping-power ratios calculated for these beams were compared with the values tabulated in the TG21 report (AAPM 1983) for similar beams.

3.2. Phantoms

The homogeneous phantoms simulated were composed of water. The heterogeneous phantoms simulated consisted of slabs of lung 'LN4' or bone-like materials 'SB3' (White *et al* 1977, White 1978) thicknesses of 5 and 3 cm respectively, sandwiched between layers of water (see inserts in figure 7). They were placed beneath a 3 cm slab of water. The physical densities of the heterogeneous materials were 0.3 g cm^{-3} and 1.8 g cm^{-3} respectively. The relative electron densities were calculated to be 0.29 and 1.70 respectively. The phantom dimensions were $20 \times 20 \times 10 \text{ cm}^3$.

3.3. Detector materials

The detector materials were air, graphite, ferrous sulfate dosimeter solution, photographic emulsion, silver halides, lithium fluoride (in TLD-100 chips), polymethyl methacrylate (PMMA), polystyrene and silicon. The physical composition of these materials was derived from ICRU Report 37 (ICRU 1984b). For graphite, a bulk density of 1.7 g cm^{-3} as well as a crystallite density of 2.265 g cm^{-3} were studied. For films, to separate the gel and silver halides, both photographic emulsions and silver halides were studied.

3.4. Cross-sectional data

The stopping powers for all these materials were obtained using the code PEGS4 (Nelson *et al* 1985) with the density effect corrections of ICRU Report 37 as implemented by Duane *et al* (1989). The exceptions were the lung and bone-like materials for which density-effect corrections were evaluated with PEGS4 using the in-built Sternheimer-interpolation scheme (Sternheimer *et al* 1982). The ionization potentials for the compounds were evaluated in PEGS4 using Bragg's additivity rule for compounds (Bragg and Kleeman 1905).

3.5. Phase-space files

Phase-space files for the beams studied were obtained from previous calculations (Kapur *et al* 1998) using the Monte Carlo code EGS4/BEAM (Nelson *et al* 1985, Rogers *et al* 1995) for a

nominal SSD of 100 cm at a plane perpendicular to their central axes. The broad-beam phase-space file was calculated for the open $10 \times 10 \text{ cm}^2$ applicator. The narrow-beam phase-space files were calculated for cut-outs on $6 \times 6 \text{ cm}^2$ applicators.

3.6. Calculation procedures: the Monte Carlo code

The code DOSXYZ (Ma *et al* 1995) was modified to score on the fly the mean kinetic energy of charged particles and the stopping-power ratios for the medium to several detectors in voxels of the calculation grid.

In this code, the mean kinetic energy of charged particles with energy greater than the cut-off energy ECUT (Rogers 1984) is calculated for each voxel using a commonly used procedure (Andreo and Brahme 1981, Rogers and Bielajew 1990, Malamut *et al* 1991, Ding *et al* 1996). The procedure is to determine the kinetic energy at the mid-point of the curved tracks of the charged particle and to compute the average of this mid-step kinetic energy over all the track lengths in that voxel.

Stopping-power ratios for the medium-to-detectors are calculated by a similar averaging procedure for each voxel. If the energy of the charged particle exceeds ECUT, the mass restricted stopping-power is obtained at the mid-step energy of the track for the medium in the voxel and is weighted by the track length. The product so obtained is the dose absorbed by the medium from the track being considered in that voxel. It is accumulated in a register for the medium. Simultaneously, the mass restricted stopping-power for each detector of interest for the same mid-step energy is weighted by the same track length and accumulated in registers for each detector. However, if the energy of the charged particle falls below ECUT the register for the medium is incremented by this energy while the registers for the detectors are incremented by the product of this energy and the ratio of the restricted stopping powers for detector-to-medium evaluated at energy Δ . The differences between the use of the cut-off energy or the EGS4 generated energy for the track-end contributions have been ignored. The ratio of the composite values accumulated in the registers for each voxel for the medium to the detectors yields the stopping power ratios.

3.7. Selection of parameters

In this study we chose to use $\text{ECUT} = \text{AE} = 521 \text{ keV}$ and $\text{PCUT} = \text{PE} = 10 \text{ keV}$. These values were used for the calculation of stopping-power ratios for water-to-air in major protocols (AAPM 1983, IAEA 1987) and studies in the literature (ICRU 1984a). The cut-off value of 10 keV kinetic energy corresponds to electrons with a range (continuous slowing down approximation) of approximately 3 mm in air (ICRU 1984b). In order to account for the range of electrons in the continuous slowing down approximation for other detectors considering the typical sizes of the other detectors, separate calculations were also performed for broad clinical beams using $\text{ECUT} = \text{AE} = 611 \text{ keV}$. For the homogeneous phantoms, a value of $\text{ESTEPE} = 0.04$ was employed with the PRESTA algorithm (Bielajew and Rogers 1987). The differences between water-to-air stopping-power ratios calculated using either this value of ESTEPE or a more conservative value of 0.01 were insignificant. For the heterogeneous phantoms $\text{ESTEPE} = 0.01$ was used for more accurate estimations of the stopping-power ratio variations in the interface regions between water and the heterogeneities (Nahum 1987). The voxels in the calculation grids were cubes with 3 mm sides. A sufficient number of histories were accumulated in the calculations to reduce the statistical uncertainties in the water-to-air stopping-power ratios to less than 0.1% at d_{max} .

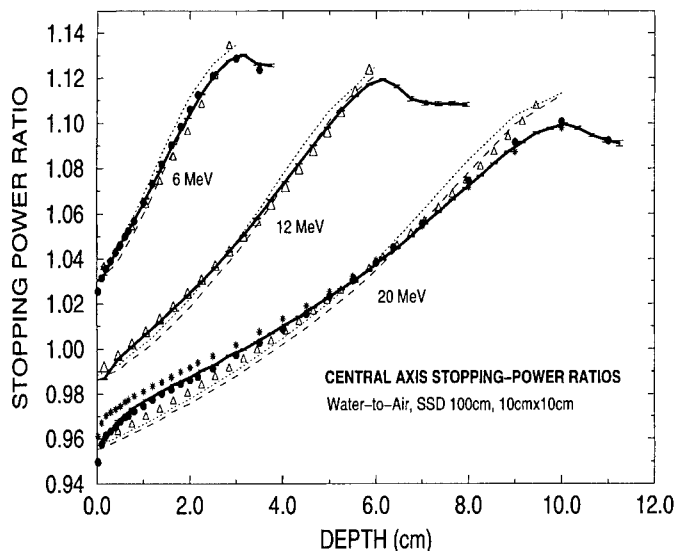


Figure 1. Central axis water-to-air stopping-power ratios for broad beams (ECUT = AE = 521 keV). Bold full curves are values obtained from this study for Varian Clinac 2100C 6, 12 and 20 MeV beams (R_{50} calculated 2.33, 4.97 and 8.29 cm respectively). Dotted curves are AAPM TG21 values obtained using $\bar{E}_0 = 2.33R_{50}$. Broken curves are AAPM TG21 values obtained using the Rogers and Bielajew procedure (1986). Triangles are values obtained using the universal equation by Burns *et al.* Full circles are values from NRC, Canada for Siemens KD2 6 and 21 MeV beams with R_{50} of 2.29 and 8.28 cm respectively. Stars are values for a Philips SL75-20 20-MeV beam with R_{50} of 8.06 cm from NRC, Canada.

4. Results and discussion

4.1. Broad electron beams

The dose distributions evaluated for the various beams studied were identical to those obtained previously with the original version of DOSXYZ. Broad-beam water-to-air stopping-power ratios calculated on central axis for $10 \times 10 \text{ cm}^2$ open-appliator fields for 6, 12 and 20 MeV Varian Clinac-2100C electron beams in homogeneous water phantoms are compared in figure 1 with those obtained from other sources.

4.1.1. Comparison with TG21 stopping-power ratios. Water-to-air stopping-power ratios calculated for broad, monoenergetic (6, 12 or 20 MeV incident energy) and monodirectional beams in this study agreed within 0.1% (1σ) with the values tabulated in the TG21 report (AAPM 1983) except at the surface of the water phantoms. The latter were derived using an older version of the Monte Carlo code ETRAN that has subsequently been improved (Seltzer 1991).

For clinical beams the validity of various procedures to select stopping-power ratios for a given beam based on energy-range relationships has been recently summarized (IAEA 1997). Tabulated TG21 stopping-power ratios were chosen in this study based on either the TG21 ($\bar{E}_0 = 2.33R_{50}$) procedure or the procedure of Rogers and Bielajew (1986) recommended in TG25 (AAPM 1991) to determine the mean surface energy \bar{E}_0 from R_{50} (depth of 50% dose). The largest discrepancy between the calculated and tabulated values is observed for the 20 MeV beams using either procedure and is less than 1.3%. At d_{max} our calculated values are

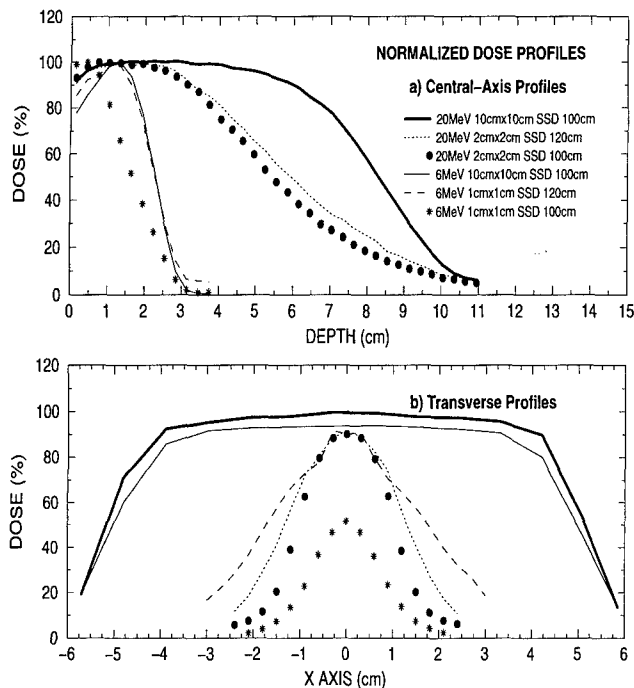


Figure 2. Normalized dose profiles for 6 and 20 MeV beams from Varian Clinac 2100C in a water phantom. Dose is normalized to the maximum value for each beam separately. (a) Central axis profiles and (b) transverse profiles at depth 1.5 cm for 6 MeV and 3 cm for 20 MeV beams. The field size is defined at an SSD of 100 cm.

lower than those of the AAPM TG21 procedure by approximately 0.3% for 6 MeV beams and higher than them by approximately 0.4% and 1.0% for the 12 and 20 MeV beams respectively. They are higher than those calculated using the Rogers and Bielajew (1986) procedure by approximately 0.5%, 0.7% and 1.1% for the 6, 12 and 20 MeV beams respectively.

There is an increase in discrepancies between stopping-power ratios of the monoenergetic beams of TG21 and those of the clinical beams with an increase in energy. Both indirect and direct electrons (which either intersect or do not intersect the collimation devices of the linear accelerator respectively) exist in realistic beams. The higher the nominal energy of the beam, the greater is the absolute difference in mean energy between the indirect and direct electrons (Kapur *et al* 1998). Since water-to-air stopping-power ratios decrease monotonically with an increase in energy, the differences in the stopping-power ratios for the indirect and direct electrons is larger for the 20 MeV beams than it is for the 6 MeV beams. The AAPM TG21 protocol does not consider indirect electrons in the calculation of stopping-power ratios. This explains why our calculated stopping-power ratios exceed the AAPM TG21 values at shallow depths and also why the differences are larger for the higher energy beams. The differences at the surface as explained elsewhere (Malamut *et al* 1991) may be related to the assumption of secondary charged particle equilibrium in the calculations of Berger *et al* (AAPM 1983).

Realistic beams also consist of electrons with energy exceeding \bar{E}_0 and contaminant photons. Thus at deeper depths they are of higher mean energy than the monoenergetic beams. Photon contamination, not considered in the AAPM protocol, plays an increasing role at higher energies (Andreo and Fransson 1989, Klevenhagen 1994, Ding *et al* 1995). This explains why our calculated values are lower than the AAPM values at greater depths.

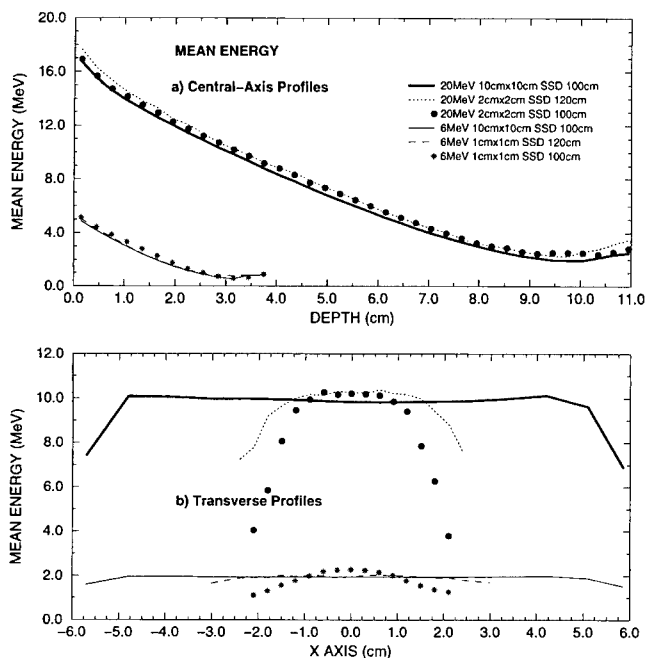


Figure 3. Mean energy profiles (ECUT = AE = 521 keV) for 6 and 20 MeV beams from Varian Clinac 2100C in a water phantom. (a) Central axis profiles and (b) transverse profiles at depth 1.5 cm for 6 MeV and 3 cm for 20 MeV beams. The field size is defined at an SSD of 100 cm.

4.1.2. Comparison with stopping-power ratios from the universal fitting equation of Burns *et al*. The universal fitting equation of Burns *et al* (1996) relates the stopping-power ratios at depth 'z' for water-to-air to R_{50} . It was based on a fit of the data by Ding *et al* (1995) calculated for 24 realistic clinical beams (both scanned and scattered) which in the range of $0.02 < z/R_{50} < 1.1$ showed a maximum deviation of 1% from the actual data. The maximum deviation is 1.7% if depths upto $1.2R_{50}$ are considered. The deviations of our calculated stopping-power ratios can be seen to be less than the maximum deviation reported by Burns *et al* (1996) based on their universal fitting equation. The data for 6 and 12 MeV agreed in the worst case to within 0.6%, and for 20 MeV to within 0.8% in the range $0.02 < z/R_{50} < 1.1$.

4.1.3. Comparison with stopping-power ratios at a reference depth (Burns *et al*). The stopping-power ratio at a reference depth given by $d_{\text{ref}} = 0.6R_{50} - 0.1$ was related to R_{50} with another fitting equation by Burns *et al* (1996). The root-mean-square deviation of their data about this fit for the 24 beams they studied was 0.16% and the maximum deviation was 0.26%.

The stopping-power ratios calculated in this study for the 6, 12 and 20 MeV beams at the reference depth defined by Burns *et al* (1996) agreed to within 0.14%, 0.10% and 0.20% respectively with the values obtained from their fitting equation.

4.1.4. Comparison with stopping-power ratios calculated for other scatter foil accelerators. The agreement between our calculations of stopping-power ratios for Varian Clinac 2100C beams and those for beams from a Siemens KD2 machine with very similar R_{50} values (Ding *et al* 1995) is about 0.2%. The difference in R_{50} for the 6 MeV beams is 0.04 cm. For

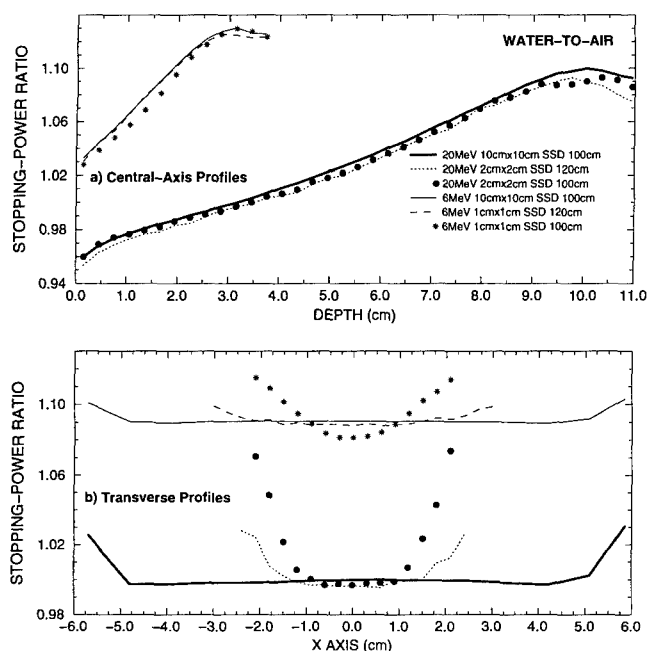


Figure 4. Water-to-air stopping-power ratios (ECUT = AE = 521 keV) for 6 and 20 MeV beams from Varian Clinac 2100C in a water phantom. (a) Central axis profiles and (b) transverse profiles at depth 1.5 cm for 6 MeV and 3 cm for 20 MeV beams. The field size is defined at an SSD of 100 cm.

the Varian 20 MeV beam and the Siemens 21 MeV beam, the difference in R_{50} is 0.01 cm. The 20 MeV beam from a Philips SL75-20 accelerator (Ding *et al* 1995) has an R_{50} of 8.06 cm that is 0.23 cm lower than that from the Varian Clinac 2100C 20 MeV beam. Despite this difference, the stopping-power ratios agree to within 1% for shallow depths and 0.2% for greater depths. The discrepancy at the shallow depths may be attributed partially to the differences in spectra of the indirect particles from these machines (Ding *et al* 1995, Ding and Rogers 1995).

4.2. Homogeneous water phantoms

In figure 2 the dose profiles from various beams of 6 and 20 MeV nominal energy are plotted for the central axis and transverse directions. The dose is normalized to the global-maximum dose value in each phantom respectively. The transverse dose profiles are shown for depths of 1.5 and 3 cm for the 6 and 20 MeV beams respectively. In figure 3 the mean kinetic energy of the charged particles in phantom is shown for the same beams along the central axis and transverse directions at the same depths. The mean energy variations as shown in this figure qualitatively explain the trends in the stopping-power ratios for the same beams that are shown in figures 4 through 6 for water-to-air, water-to-silicon and water-to-film-emulsion respectively. The relative importance of stopping-power ratio variations can be assessed with the help of figure 2. The variations for detector materials other than the ones shown in figures 4–6 were all within 1% or much less, with the exception of the silver halides used in photographic-film materials (ICRU 1984b). Calculated broad-beam water-to-detector stopping-power ratios for the clinical beams are listed in tables 1 and 2 for various detectors for 6 and 20 MeV electron beams for two values of AE, namely 521 and 611 keV. The stopping-power ratios are sensitive

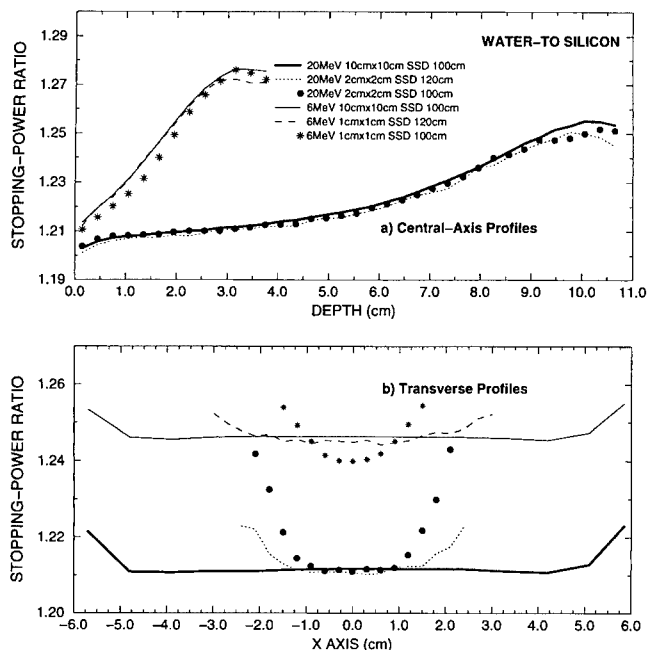


Figure 5. Water-to-silicon stopping-power ratios (ECUT = AE = 521 keV) for 6 and 20 MeV beams from Varian Clinac 2100C in a water phantom. (a) Central axis profiles and (b) transverse profiles at depth 1.5 cm for 6 MeV and 3 cm for 20 MeV beams. The field size is defined at an SSD of 100 cm.

to changes in AE for the photographic materials (up to 5.7% for silver halides and 4.2% for film emulsion) and silicon (up to 2.2%) whereas for the other detector materials studied the differences are within 0.6% for this range of AE values.

4.2.1. Narrow electron beams: variations along the central axis. The observed stopping-power ratio variations are consistent with the mean energy variations seen in figure 3. The narrow beams at a nominal SSD of 100 cm exhibit a consistently higher mean energy on the central axis for both energies compared with the broad beams. At extended SSD, the 20 MeV narrow beam electrons are seen to be more energetic than those at 100 cm; a trend which is reversed for the 6 MeV beam. Consequently the stopping-power ratios vary in a similar manner from the broad-beam data.

The largest variations of the stopping-power ratios studied are seen for water-to-air stopping-power ratios for narrow beams. The stopping-power ratios are within 1% of the broad-beam data within the practical range of the beams. At d_{\max} for the narrow beams, the variation is within 0.5%. For water-to-film-emulsion or the silver halides in photographic films, the variations from corresponding broad-beam data are within 0.8% and 1% respectively. Water-to-silicon ratios are within 0.5% of their corresponding broad-beam data. Minimal variations (at most 0.1%) are seen for the stopping-power ratio variations from broad-beam data for water-to-LiF-100, graphite (the different densities simulated did not indicate any significant differences in the magnitude of these variations), ferrous sulfate dosimeter solution, PMMA and polystyrene. At 6 MeV, water-to-air stopping-power ratios for narrow beams incident at 30° were less than the AAPM TG21 values by up to 0.5%. While this has up to a 0.5% effect

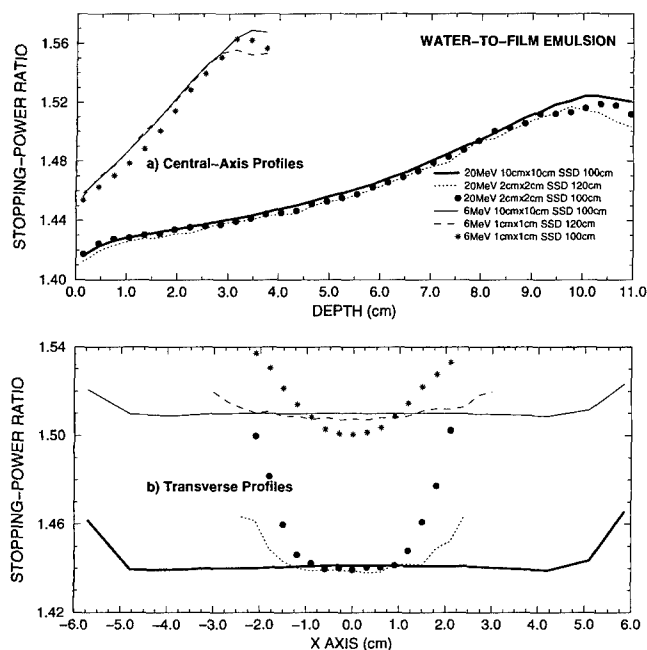


Figure 6. Water-to-film stopping-power ratios ($ECUT = AE = 521$ keV) for 6 and 20 MeV beams from Varian Clinac 2100C in a water phantom. (a) Central axis profiles and (b) transverse profiles at depth 1.5 cm for 6 MeV and 3 cm for 20 MeV beams. The field size is defined at an SSD of 100 cm.

on the output factor calculations, this angle represents an extreme condition and the effects of obliquity for angles larger than this one will be relatively less significant.

The water-to-air stopping-power ratios for the narrow beams incident normally are consistently lower than those for the realistic-broad beams by a maximum of approximately 1%. This implies that for depths shallower than that where the crossover occurs between the AAPM TG21 values and the broad-beam values (figure 1), they are also within 1.3% of the AAPM-recommended ratios and in fact agree to better than 1%. At greater depths, they are lower than the recommended ratios by up to 2% for the 20 MeV beams. However, the relative-dose is lower at these depths. These findings imply that relative dosimetry based on the use of AAPM-recommended stopping-power ratios will introduce minor discrepancies for such narrow fields.

For narrow monoenergetic beams, the IAEA findings (IAEA 1997) on water-to-air stopping-power ratio variations compared to broad beams are similar. However, due to the upward shift of d_{max} in small fields (McGinley *et al* 1979, Hogstrom *et al* 1981, Sharma *et al* 1984, ICRU 1984a, AAPM 1991) the determination of output factors for such fields should take the depth-dependent variations of stopping-power ratios into account (Zhang *et al* 1998, Kapur *et al* 1998).

4.2.2. Narrow electron beams: variations in the transverse direction. The variations of the stopping-power ratios in the transverse direction were also found to be consistent with the variations of the mean energy. The increase in the air gap caused a reduction in the variation of the mean energy along the transverse direction for the narrow beams at both 6 and 20 MeV.

Table 1. Calculated stopping power ratios (ECUT = AE = 521 keV) on central axis for water-to-detector material for 6 MeV ($R_{50} = 2.33$ cm) 10×10 cm² Varian Clinac 2100C electron beams at SSD 100 cm. The quantities in parentheses are the stopping-power ratios evaluated using ECUT = AE = 611 keV. AE values correspond to different mean chord lengths of the detectors.

Depth (cm)	Air	Graphite	FeSO ₄	Silver halides	LiF-100	PMMA	Film emulsion	Silicon
0.15	1.032 (1.030)	1.137 (1.136)	1.005 (1.005)	1.598 (1.522)	1.248 (1.242)	1.032 (1.032)	1.457 (1.404)	1.213 (1.190)
0.45	1.044 (1.042)	1.138 (1.137)	1.005 (1.005)	1.613 (1.535)	1.248 (1.242)	1.032 (1.033)	1.468 (1.414)	1.219 (1.196)
0.75	1.055 (1.053)	1.139 (1.138)	1.005 (1.005)	1.626 (1.546)	1.248 (1.242)	1.033 (1.033)	1.477 (1.422)	1.224 (1.201)
1.05	1.067 (1.064)	1.140 (1.139)	1.005 (1.005)	1.640 (1.558)	1.247 (1.242)	1.033 (1.033)	1.487 (1.431)	1.231 (1.207)
1.35	1.078 (1.075)	1.141 (1.140)	1.005 (1.005)	1.655 (1.571)	1.247 (1.242)	1.033 (1.033)	1.498 (1.440)	1.238 (1.214)
1.65	1.091 (1.087)	1.141 (1.141)	1.005 (1.005)	1.673 (1.586)	1.247 (1.242)	1.033 (1.033)	1.510 (1.452)	1.246 (1.221)
1.95	1.102 (1.099)	1.141 (1.141)	1.005 (1.005)	1.690 (1.602)	1.247 (1.241)	1.033 (1.033)	1.522 (1.462)	1.254 (1.229)
2.25	1.112 (1.110)	1.140 (1.140)	1.005 (1.005)	1.706 (1.619)	1.247 (1.241)	1.032 (1.032)	1.533 (1.474)	1.261 (1.236)
2.55	1.121 (1.118)	1.138 (1.138)	1.005 (1.005)	1.724 (1.632)	1.247 (1.240)	1.031 (1.031)	1.544 (1.483)	1.268 (1.242)
2.85	1.128 (1.125)	1.135 (1.134)	1.005 (1.005)	1.740 (1.646)	1.246 (1.240)	1.030 (1.030)	1.554 (1.491)	1.273 (1.246)
3.15	1.130 (1.128)	1.131 (1.130)	1.005 (1.005)	1.755 (1.655)	1.245 (1.239)	1.028 (1.029)	1.563 (1.497)	1.276 (1.248)

With reference to the broad beams, this resulted in the stopping-power ratio variations for the narrow beams at extended SSD being smaller in comparison with those from the narrow beams at an SSD of 100 cm.

Compared with the water-to-air stopping-power ratio at central axis, at the same depth, the stopping-power ratio at an off-axis region where the dose was 10% of the maximum dose was found to be higher because the mean energy of electrons was lower in that region. This difference was more significant for the higher-energy beam. As discussed in section 4.1, the absolute difference in mean energy between the direct and indirect electrons is greater for the higher-energy beam (Kapur *et al* 1998). The off-axis regions contain a larger fraction of these indirect electrons than regions on the central axis. At greater depths in phantom, these differences in mean energy tend to decrease as shown by our calculations of mean energy at various depths, because the mean energy of electrons within the beam drops rapidly with depth. Thus at greater depths these variations in stopping-power ratios are reduced.

The transverse variations quantified this way were up to 4% for water-to-silicon, 6% for water-to-film-emulsion, 7% for silver halide materials used in photographic films and 10% for water-to-air. They were within 0.2% or less for the other materials studied.

4.3. Narrow electron beams: heterogeneous phantoms

The central-axis depth variation of the absolute dose per incident fluence in the layered-lung and bone phantoms (shown on the inserts in figure 7(a)) is plotted in figure 7(a) for the 3×3 cm² beams of 12 MeV electrons incident at an SSD of 100 cm. Also shown for comparison is the dose profile for a water phantom of the same dimensions, which is the reference phantom

Table 2. Calculated stopping power ratios (ECUT = AE = 521 keV) on central axis for water-to-detector material for 20 MeV ($R_{50} = 8.29$ cm) 10×10 cm² Varian Clinac 2100C electron beams at SSD 100 cm. The quantities in parentheses are the stopping-power ratios evaluated using ECUT = AE = 611 keV. AE values correspond to different mean chord lengths of the detectors.

Depth (cm)	Air	Graphite	FeSO ₄	Silver halides	LiF-100	PMMA	Film emulsion	Silicon
0.15	0.959 (0.956)	1.131 (1.130)	1.004 (1.004)	1.545 (1.472)	1.251 (1.245)	1.032 (1.032)	1.416 (1.365)	1.203 (1.180)
1.05	0.976 (0.972)	1.132 (1.131)	1.005 (1.004)	1.560 (1.484)	1.250 (1.244)	1.032 (1.032)	1.428 (1.374)	1.207 (1.184)
1.95	0.986 (0.985)	1.132 (1.132)	1.005 (1.004)	1.567 (1.494)	1.250 (1.244)	1.032 (1.032)	1.433 (1.382)	1.209 (1.186)
2.85	0.996 (0.993)	1.133 (1.132)	1.005 (1.004)	1.575 (1.499)	1.250 (1.243)	1.032 (1.032)	1.439 (1.386)	1.210 (1.187)
3.75	1.007 (1.004)	1.133 (1.133)	1.005 (1.004)	1.584 (1.508)	1.249 (1.243)	1.032 (1.032)	1.446 (1.392)	1.213 (1.190)
4.95	1.023 (1.019)	1.135 (1.134)	1.005 (1.004)	1.599 (1.519)	1.249 (1.242)	1.032 (1.032)	1.457 (1.401)	1.217 (1.192)
5.85	1.035 (1.031)	1.136 (1.135)	1.005 (1.004)	1.609 (1.528)	1.248 (1.242)	1.032 (1.032)	1.464 (1.408)	1.220 (1.196)
6.75	1.048 (1.046)	1.137 (1.136)	1.005 (1.004)	1.623 (1.543)	1.248 (1.242)	1.032 (1.032)	1.475 (1.420)	1.225 (1.202)
7.95	1.071 (1.068)	1.139 (1.138)	1.005 (1.005)	1.650 (1.567)	1.248 (1.242)	1.033 (1.033)	1.494 (1.437)	1.236 (1.211)
8.85	1.087 (1.083)	1.140 (1.139)	1.005 (1.005)	1.672 (1.584)	1.247 (1.241)	1.033 (1.033)	1.509 (1.449)	1.246 (1.220)
9.45	1.095 (1.092)	1.139 (1.139)	1.005 (1.005)	1.685 (1.596)	1.247 (1.241)	1.032 (1.032)	1.518 (1.458)	1.251 (1.226)
10.05	1.098 (1.097)	1.138 (1.138)	1.005 (1.005)	1.691 (1.606)	1.247 (1.240)	1.032 (1.032)	1.522 (1.464)	1.254 (1.230)

for this study. The dose plotted is that to the various phantom materials with no additional conversions. Figure 7(b) shows the variation of the mean kinetic energy along the central axes of the phantoms.

4.3.1. The stopping power ratio correction factors. The central-axis variations of the SPRCFs (equation (6)) at depth in these phantoms is plotted for various detector materials studied including air, graphite, silver halides, LiF-100, photographic emulsion and silicon in figure 8. The SPRCFs plotted are for the actual materials in the heterogeneous media. In both the phantoms, the SPRCFs in the water layers are close to unity for all the detectors throughout the water regions. Within the non-water regions, however, there are significant variations of the SPRCFs for the detector materials with depth.

In the bone-layered phantom, the SPRCFs within the bone region varied by about 2.5% for air, 2.2% for silver halides, 1.3% for silicon and less than 1% for graphite and LiF-100 as seen in figure 8(a). In the lung-layered phantom, the SPRCFs within the lung region varied by about 5% for air and silver halides, 3.5% for photographic emulsions, 3% for silicon and 1% for graphite and LiF-100 as seen in figure 8(b). For both phantoms, the variations of SPRCFs were within 1% in the transverse direction for all the detector materials studied. The mean energy-difference variations in this direction were not as significant as they were along the central axis.

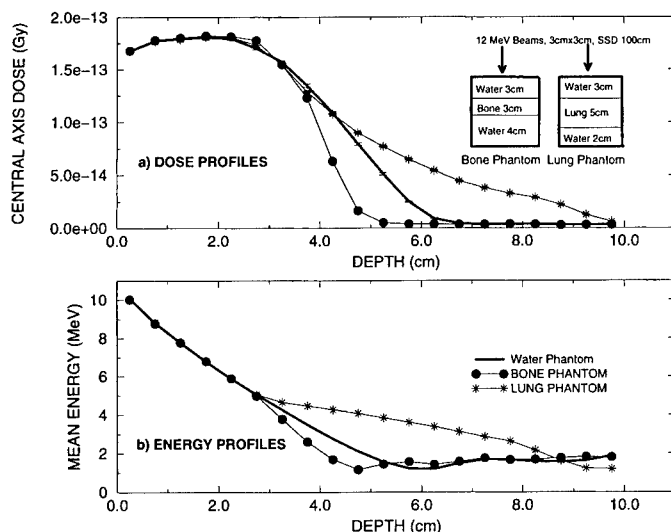


Figure 7. (a) Dose on central axis in water, layered-bone and layered-lung phantoms from 12 MeV beams of $3 \times 3 \text{ cm}^2$ at SSD of 100 cm. (b) Mean energy on central axis for the same phantoms.

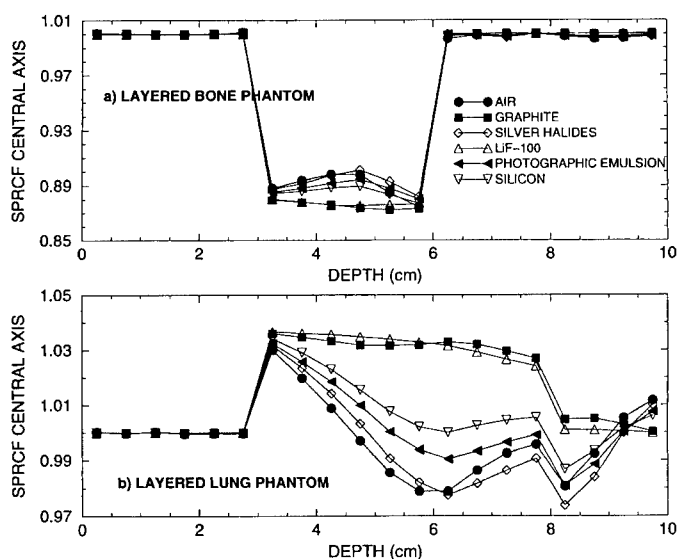


Figure 8. Stopping-power ratio correction factors (SPRCFs) for air, graphite, silver halides, LiF-100, photographic emulsion and silicon, for 12 MeV beams, $3 \times 3 \text{ cm}^2$ in size at SSD of 100 cm for (a) layered-bone and (b) layered-lung phantom using $\text{ECUT} = \text{AE} = 521 \text{ keV}$.

4.3.2. Effect of heterogeneities and detector materials. From these observations, there appears to be some correlation between the trends followed by the SPRCFs and the difference in mean energy between the heterogeneous phantoms and the water phantoms. In addition there appear to be detector-specific dependences. Based on the initial assumption that Spencer–Attix conditions hold (i.e. the detectors do not perturb the spectra of particles they receive), the difference in mean energies arises because of the difference in radiation transport of electrons

through the two phantoms. A detector placed at the same physical depths in the two phantoms will therefore be exposed to electron beams with these different mean energies. Consequently the response of the detector will be different in the two phantoms.

Because water is a standard reference material in dosimetry (AAPM 1983, IAEA 1987), we proceed to interpret the effects of both the heterogeneities and the detector materials on the SPRCFs by expressing the SPRCFs in terms of heterogeneity or detector-to-water stopping-power ratios, rearranging equation (6) as follows:

$$\begin{aligned} (\text{SPRCF})_{\text{water}}^{\text{het}} &= \frac{[(\frac{\bar{L}}{\rho}(E_h))_{\text{det}}^{\text{het}}]}{[(\frac{\bar{L}}{\rho}(E_w))_{\text{det}}^{\text{water}}]} = \left(\frac{\bar{L}}{\rho}(E_h)\right)_{\text{water}}^{\text{het}} \left[\left(\frac{\bar{L}}{\rho}(E_h)\right)_{\text{det}}^{\text{water}} \left(\frac{\bar{L}}{\rho}(E_w)\right)_{\text{water}}^{\text{det}} \right] \\ &= (\text{SPRCF}_{\text{HET}})(\text{SPRCF}_{\text{DET}}) \end{aligned} \quad (8)$$

where

$$\text{SPRCF}_{\text{HET}} = \left(\frac{\bar{L}}{\rho}(E_h)\right)_{\text{water}}^{\text{het}} \quad (9)$$

and

$$\text{SPRCF}_{\text{DET}} = \left[\left(\frac{\bar{L}}{\rho}(E_h)\right)_{\text{det}}^{\text{water}} \left(\frac{\bar{L}}{\rho}(E_w)\right)_{\text{water}}^{\text{det}} \right]. \quad (10)$$

In equations (8)–(10) the phantom specification by the superscript outside the square brackets has been replaced by the terms ' E_h ' and ' E_w ' which are the mean energies in the corresponding voxels in the heterogeneous and water phantoms respectively. The SPRCF has been expressed as a product of two terms—a heterogeneity term ' $\text{SPRCF}_{\text{HET}}$ ' and a detector term ' $\text{SPRCF}_{\text{DET}}$ '. The heterogeneity term relates the stopping-power ratios for the heterogeneities with respect to water for the mean energy E_h in the heterogeneous phantom. It is independent of the detectors. It reflects the differences in radiation transport at the mean energy E_h that would occur if the material were either water or the heterogeneity. It is useful to compute when the dose of interest is that to the actual material in the medium itself rather than dose to a small mass of water contained within the medium. Such would be the case for example when dose enhancement to bone needs to be evaluated (Prasad and Bassano 1989). The detector term reflects the variation in detector-to-water stopping-power ratios at energies E_h and E_w . The magnitude of this term depends on the difference between E_h and E_w through how much the water-to-detector stopping-power ratios change with energy in this range. Note that if the dose of interest (and hence the HCF of interest) were that to a small mass of water contained within the heterogeneous medium, $\text{SPRCF}_{\text{HET}}$ would be unity and SPRCF would be given by $\text{SPRCF}_{\text{DET}}$ exclusively. Thus $\text{SPRCF}_{\text{DET}}$ is the factor that may be associated with accumulated clinical experience (ICRU 1984a).

The implications of expressing the SPRCF this way are that we can get a qualitative feel for how they will vary for any given combination of phantoms and detectors based on our knowledge of how stopping-power ratios for water-to-various materials vary with energy. Consistent with the results in the previous section (figure 3 and table 1) the SPRCFs vary more significantly for air, film and silicon materials than the others studied, even if the variation of the $\text{SPRCF}_{\text{HET}}$ within the heterogeneous regions is small. Should there be significant variations for $\text{SPRCF}_{\text{HET}}$, the overall variations of SPRCF will be enhanced even further. This is because significant variations in $\text{SPRCF}_{\text{HET}}$ suggest significant differences in radiation transport between the heterogeneity and water which in turn suggests greater differences in mean energies between the two phantoms at specific depths. The greater the mean energy difference, the larger the variation of $\text{SPRCF}_{\text{DET}}$ and hence that of SPRCF. In the bone-layered phantom $\text{SPRCF}_{\text{HET}}$ varied by less than 1% within the bony region. The SPRCF variation was

about 2.5%. In the lung-layered phantom $\text{SPRCF}_{\text{HET}}$ varied by about 1.5% and the SPRCF variation increased to about 5%. Similar results were observed for the other detectors.

4.3.3. Evaluation of $\text{SPRCF}_{\text{DET}}$ at the 'effective' depth. While SPRCFs can be calculated using Monte Carlo techniques, the variety of phantom geometries possible and the extensive computations required per phantom geometry make these calculations cumbersome. For the simple layered geometries studied, the correlation of SPRCFs with mean energy variations between the heterogeneous and homogeneous phantoms seen in this study suggests an alternative approach to predict the SPRCFs at various depths along the central axis. This approach is to find for a depth of interest ' z ' in the heterogeneous phantom, a corresponding depth ' z_{eff} ' in the water phantom where the mean energies are the same or are very similar. Since the stopping-power ratios for water-to-detectors are known for various depths in water phantoms, this alternative procedure would involve evaluating $\text{SPRCF}_{\text{DET}}$ as the ratio of the water-to-detector stopping-power ratios evaluated at depths z_{eff} and z in a water phantom instead—an approach equivalent to that of a lookup-table.

The mean energy of charged particles at a given depth in phantom is affected by the loss of energy of these particles in traversing overlying materials and the directions from which they travel. The latter is governed primarily by scatter events. In this regard, several approaches have been suggested in the literature to obtain scaling factors such as detour factors to obtain z_{eff} (AAPM 1983, ICRU 1984a, Grosswendt and Roos 1989, Sorcini and Brahme 1994, Ding *et al* 1996, Fernandez-Varea *et al* 1996, IAEA 1997).

In this study a simple approach of depth scaling using the relative electron densities is attempted. While the relative electron density scaling method to determine the mean energy variations is not as accurate as other methods such as effective density scaling (AAPM 1983, Ding *et al* 1996), the 2–3% loss in accuracy (Fernandez-Varea *et al* 1996) is not expected to cause a significant loss of accuracy in the determination of stopping-power ratios. Tables 3 and 4 demonstrate this to be the case for the lung and bone phantoms studied along the central axis. In column 1, the actual physical depth z is listed. Column 2 lists the effective depth z_{eff} obtained by electron density scaling. Column 3 lists the mean energy in the heterogeneous phantoms at depth z . Column 4 lists the mean energy in the water phantoms at depth z . Column 5 lists the mean energy in the water phantom at depth z_{eff} . Comparing columns 3 and 5 indicates that the estimated mean energy is typically within 0.2 MeV of the calculated mean energy in the heterogeneous phantom. Columns 6, 7 and 8 list $\text{SPRCF}_{\text{DET}}$ as obtained using the stopping power ratios for water-to-air using the calculated data for $3 \times 3 \text{ cm}^2$, $10 \times 10 \text{ cm}^2$ or AAPM TG21 tables respectively and evaluated at z_{eff} and z . Finally column 9 lists the Monte Carlo calculated values of $\text{SPRCF}_{\text{DET}}$. It is clear from these tables that the relative electron density scaling method can accurately reproduce the Monte Carlo stopping-power ratio correction factors for such phantoms to within 0.4%. Furthermore, any of the available data for water-to-detector stopping power ratios—those calculated in this study for narrow realistic beams or broad realistic beams (tables 1 and 2) or AAPM TG21 (for water-to-air) beams can be used for this purpose.

5. Summary

Restricted mass collision stopping-power ratios calculated for water-to-air on the central axis of broad electron beams from the scatter-foil linear accelerator studied were within 1.3% of those reported by the TG21 protocol for broad monoenergetic, monodirectional beams and were consistent with the results of Ding *et al* to within 0.2%. These values for water-to-air on

Table 3. Calculated $\text{SPRCF}_{\text{DET}}$ on the central axis for air-filled detectors in the layered-lung phantom using a relative electron density scaling approach with stopping-power ratios from calculated narrow ($3 \times 3 \text{ cm}^2$), broad ($10 \times 10 \text{ cm}^2$) and TG21 beams.

Depth, <i>z</i> (cm)	Effective depth, <i>z</i> _{eff} (cm)	Mean energy at depth <i>z</i> in lung phantom (MeV)	Mean energy at depth <i>z</i> in water phantom (MeV)	Mean energy at depth <i>z</i> _{eff} in water phantom (MeV)	$\text{SPRCF}_{\text{DET}}$ using $3 \times 3 \text{ cm}^2$ <i>L</i> / ρ values	$\text{SPRCF}_{\text{DET}}$ using $10 \times 10 \text{ cm}^2$ <i>L</i> / ρ values	$\text{SPRCF}_{\text{DET}}$ using TG21 <i>L</i> / ρ values	$\text{SPRCF}_{\text{DET}}$ from Monte Carlo calculations
1.25	1.25	7.77	7.78	7.78	1.000	1.000	1.000	1.000
3.25	3.07	4.65	4.26	4.54	0.996	0.996	0.995	0.995
4.25	3.36	4.25	2.76	4.09	0.978	0.978	0.975	0.974
5.25	3.65	3.84	1.56	3.64	0.958	0.962	0.960	0.956
6.25	3.94	3.38	1.20	3.21	0.954	0.956	0.952	0.950
7.25	4.23	2.86	1.70	2.79	0.969	0.974	0.975	0.968
8.25	4.70	2.17	1.58	2.18	0.980	0.985		0.981

Table 4. Calculated $\text{SPRCF}_{\text{DET}}$ on the central axis for air-filled detectors in the layered-bone phantom using a relative electron density scaling approach with stopping-power ratios from calculated narrow ($3 \times 3 \text{ cm}^2$), broad ($10 \times 10 \text{ cm}^2$) and TG21 beams.

Depth, <i>z</i> (cm)	Effective depth, <i>z</i> _{eff} (cm)	Mean energy at depth <i>z</i> in lung phantom (MeV)	Mean energy at depth <i>z</i> in water phantom (MeV)	Mean energy at depth <i>z</i> _{eff} in water phantom (MeV)	$\text{SPRCF}_{\text{DET}}$ using $3 \times 3 \text{ cm}^2$ <i>L</i> / ρ values	$\text{SPRCF}_{\text{DET}}$ using $10 \times 10 \text{ cm}^2$ <i>L</i> / ρ values	$\text{SPRCF}_{\text{DET}}$ using TG21 <i>L</i> / ρ values	$\text{SPRCF}_{\text{DET}}$ from Monte Carlo calculations
1.25	1.25	7.80	7.79	7.79	1.000	1.000	1.000	1.000
3.25	3.46	3.79	4.54	3.93	1.005	1.005	1.006	1.010
4.25	5.29	1.69	4.09	1.54	1.029	1.025	1.025	1.025
5.25	7.12	1.44	3.64	1.65	1.005	1.006	1.007	1.009
6.25	8.74	1.43	3.20	1.57	0.994	0.990		0.997

the central axis of narrow electron beams from the scatter-foil linear accelerator studied, using commonly applied geometric conditions were up to 1% lower than the corresponding values for broad beams. They agreed to better than 1% with the AAPM TG21 values at depths shallower than the crossover depth between the AAPM TG21 values and the broad beam values (0.8, 3 and 6 cm for 6, 12 and 20 MeV beams respectively), and underestimated them by up to 2% for larger depths at 20 MeV. The use of the AAPM recommended stopping-power ratios for these beams thus introduces minor errors in relative central-axis dosimetry. The depth dependence of the stopping-power ratios should be incorporated for the calculation of output factors.

The central-axis restricted mass collision stopping-power ratios for narrow-to-broad fields agreed to within 0.1% for water-to-LiF-100, graphite, ferrous sulfate dosimeter solution, polystyrene and PMMA, 0.5% for water-to-silicon and 1% for water-to-photographic-film materials in the same geometric conditions. The stopping-power ratios varied by up to 10% for water-to-air, 7% for photographic silver halide materials and 3% for silicon compared to the central-axis values in the penumbral regions where the dose was 10% of the maximum dose in the phantom. The transverse variations were less than 0.2% for LiF-100, graphite, ferrous sulfate dosimeter solution, polystyrene and PMMA. The stopping-power ratios were sensitive to changes in AE from 521 to 611 keV for water-to-silver-halide, water-to-film-emulsion and water-to-silicon by up to 5.7, 4.2 and 2.2% respectively on the central axes of broad beams.

In heterogeneous phantoms, because radiation transport in general differs from that in water, and water-to-detector stopping-power ratios are energy dependent, the stopping-power ratio correction factors vary with energy for different detectors. The variation of the stopping-power ratio correction factors can be significant when radiation transport in the non-water regions differs significantly from that in water. Of all the detector materials studied, air showed the most marked variations, followed by photographic silver halides, photographic emulsions and silicon. A method for predicting the stopping-power ratio correction factors for simple layered phantoms based on the use of relative electron density scaling has been demonstrated to predict the Monte Carlo calculated values accurately to within 0.5%. This is applicable in the situation when the dose of interest is that to a small mass of water in the heterogeneous medium. Thus these values can be calculated for such phantoms using a simple lookup-table approach at the depth of interest.

Acknowledgments

This work was supported in part by the National Cancer Institute Grant CA43840 and the US Army Breast Cancer Research Program DOD BC971292. The authors would like to thank Dr Pedro Andreo of the International Atomic Energy Agency and Dr Dave Rogers of the National Research Council of Canada for valuable comments that significantly improved the quality of the manuscript. The authors also thank Drs Arthur Boyer, Ralph Nelson, Kenneth Kase and Gary Luxton of Stanford University for useful comments.

References

- AAPM (American Association of Physicists in Medicine) 1983 Task Group 21 Radiation Therapy Committee: a protocol for the determination of absorbed dose from high-energy photon and electron beams *Med. Phys.* **10** 741–71
- 1991 Clinical electron-beam dosimetry: report of AAPM Radiation Therapy Committee Task Group 25 *Med. Phys.* **18** 73–109
- Andreo P 1988 Stopping-power ratios for dosimetry *Monte Carlo Transport of Electrons and Photons* ed T M Jenkins, W R Nelson and A Rindi (New York: Plenum) pp 485–501
- Andreo P and Brahme A 1981 Mean energy in electron beams *Med. Phys.* **8** 682–7
- Andreo P, Brahme A, Nahum A E and Mattsson O 1989 Influence of energy and angular spread on stopping-power ratios for electron beams *Phys. Med. Biol.* **34** 751–68
- Andreo P and Fransson A 1989 Stopping-power ratios and their uncertainties for clinical electron beam dosimetry *Phys. Med. Biol.* **34** 1847–61
- Ayyangar K, Palta J R, Sweet J W and Suntharalingam N 1993 Experimental verification of a three-dimensional dose calculation algorithm using a specially designed heterogeneous phantom *Med. Phys.* **20** 325–9
- Berger M J 1987 Electron stopping powers for transport calculations *Monte Carlo Transport of Electrons and Photons* ed T M Jenkins, W R Nelson and A Rindi (New York: Plenum) pp 57–80
- Bielajew A F and Rogers D W O 1987 PRESTA: the parameter reduced electron-step algorithm for electron Monte Carlo Transport *Nucl. Instrum. Methods B* **18** 165–81
- Bragg W H 1912 *Studies in Radioactivity* (New York: Macmillan) p 94
- Bragg W H and Kleeman R 1905 On the alpha particles of radium and their loss of range in passing through various atoms and molecules *Phil. Mag.* **10** 318
- Brahme A 1977 Electron transport phenomena and absorbed dose distribution in therapeutic electron beams *Book of Abstracts XIV* (Rio de Janeiro: International Congress of Radiology) p 198
- Burch P R J 1955 Cavity ion chamber theory *Radiat. Res.* **3** 361–78
- 1957 Comment on recent cavity ionization theories *Radiat. Res.* **6** 79–84
- Burlin T E 1966 A general theory of cavity ionization *Br. J. Radiol.* **39** 727–34
- 1968 Cavity-chamber theory *Radiation Dosimetry* vol I ed F H Attix and W C Roesch (New York: Academic) pp 331–92

- Burlin T E, Snelling R J and Owen B 1969 The application of general cavity ionization theory to the dosimetry of electron fields *Proc. 2nd Symp. on Microdosimetry* pp 455–71
- Burns D T, Ding G X and Rogers D W O 1996 R_{50} as a beam quality specifier for selecting stopping-power ratios and reference depths for electron dosimetry *Med. Phys.* **23** 383–8
- Ding G X and Rogers D W O 1995 Energy, spectra, angular spread and dose distributions of electron beams from various accelerators used in radiotherapy *NRCC Report PIRS-0439* (Ottawa: National Research Council of Canada)
- Ding G X, Rogers D W O and Mackie T R 1995 Calculation of stopping-power ratios using realistic clinical electron beams *Med. Phys.* **22** 489–501
- 1996 Mean energy, energy-range relationships and depth-scaling factors for clinical electron beams *Med. Phys.* **23** 361–75
- Duane S, Bielajew A F and Rogers D W O 1989 Use of ICRU-37/NBS Collision stopping powers in the EGS4 system *NRCC Report PIRS-0177* (Ottawa: National Research Council of Canada)
- El-Khatib E, Antolak J and Scrimger J 1992 Evaluation of film and thermoluminescent dosimetry of high-energy electron beams in heterogeneous media *Med. Phys.* **19** 317–23
- El-Khatib E and Connors S 1992 Conversion of ionization measurements to radiation absorbed dose in non-water density material *Phys. Med. Biol.* **37** 2083–94
- Fernandez-Varea J M, Andreo P and Tabata T 1996 Detour factors in water and plastic phantoms and their use for range and depth-dose scaling in electron beam dosimetry *Phys. Med. Biol.* **41** 1119–39
- Gray L H 1936 An ionization method for the absolute measurement of γ -ray energy *Proc. R. Soc. A* **156** 578–96
- Grosswendt B and Roos M 1989 Electron beam absorption in solid and in water phantoms: depth scaling and energy-range relations *Phys. Med. Biol.* **34** 509–18
- Harder D 1965 Berechnung der energiedosis aus ionisationsmessungen bei sekundarelektronen-gleichgewicht *Symposium on High-Energy Electrons* ed A Zuppinger and G Poretti (Berlin: Springer)
- 1968 Einfluss der Vielfachstreuung von Elektronen auf die Ionisation in gas-gefüllten Hohlräumen *Biophysik* **5** 157–64
- Hogstrom K R, Mills M D and Almond P R 1981 Electron beam dose calculations *Phys. Med. Biol.* **26** 445–59
- Holt J G, Edelstein G R and Clark T E 1975 Energy dependence of the response of LiF TLD rods in high energy electron fields *Phys. Med. Biol.* **20** 559–70
- IAEA (International Atomic Energy Agency) 1987 Absorbed dose determination in photon and electron beams, an international code of practice for dosimetry *IAEA Technical Report Series 277* (Vienna: IAEA)
- 1997 The use of plane parallel ionization chambers in high energy electron and photon beams, an international code of practice for dosimetry *IAEA Technical Report Series 381* (Vienna: IAEA)
- ICRU 1984a Radiation dosimetry: electron beams with energies between 1 and 50 MeV *ICRU Report 35* (Bethesda, MD: ICRU)
- 1984b Stopping powers for electrons and positrons *ICRU Report 37* (Bethesda, MD: ICRU)
- Kapur A, Ma C-M, Mok E C, Findley D O and Boyer A L 1998 Monte Carlo calculations of electron beam output factors for a medical linear accelerator *Phys. Med. Biol.* **43** 3479–94
- Klevenhagen S C 1994 An algorithm to include the bremsstrahlung contamination in the determination of the absorbed dose in electron beams *Phys. Med. Biol.* **39** 1103–12
- Ma C-M, Mok E, Kapur A and Findley D 1997 Improvement of small-field electron beam dosimetry using Monte Carlo simulation *Proc. 12th Int. Conf. on the use of Computers in Radiation Therapy* ed D D Leavitt and G Starkschall (Madison, WI: Medical Physics Publishing) pp 159–62
- Ma C-M and Nahum A E 1994 Plane parallel chambers in electron beams: Monte Carlo findings on the perturbation factor *Proc. Int. Symp. on Measurement Assurance in Dosimetry* (Vienna: International Atomic Energy Agency) pp 481–93
- Ma C-M, Reckwerdt P, Holmes M, Rogers D W O, Geiser B and Walters B 1995 DOSXYZ users manual *NRCC Report PIRS-0509b*, (Ottawa: National Research Council of Canada)
- Mackie T R 1990 Applications of the Monte Carlo method in radiotherapy *The Dosimetry of Ionizing Radiation* vol III ed K R Kase, B E Bjørnsgaard and F H Attix (New York: Academic) pp 541–620
- Malamut C, Rogers D W O and Bielajew A F 1991 Calculation of water/air stopping-power ratios using EGS4 with explicit treatment of electron-positron differences *Med. Phys.* **18** 1222–8
- McGinley P H, McLaren J R and Barnett B R 1979 Small electron beams in radiation therapy *Radiology* **131** 231–4
- Nahum A E 1978 Water/air mass stopping power ratios for megavoltage photon and electron beams *Phys. Med. Biol.* **23** 24–38
- 1987 Simulation of dosimeter response and interface effects *Monte Carlo Transport of Electrons and Photons* ed T M Jenkins, W R Nelson and A Rindi (New York: Plenum) pp 523–47
- Nelson W R, Hirayama H and Rogers D W O 1985 The EGS4 code system *SLAC Report 265* (Stanford, CA:

- Stanford Linear Accelerator Center)
- Nilsson B 1985 Analysis of quality characteristics of radiotherapeutic photon beams *PhD Thesis* University of Stockholm
- O'Brien 1977 Monte Carlo calculations of the energy response of lithium dosimeters to high energy electrons (<30 MeV) *Phys. Med. Biol.* **22** 836–51
- Ogunleye O T and Paliwal B R 1985 A proposed modification of cavity theory for electrons *Health Phys.* **49** 937–44
- Prasad S C, Ames T E, Howard T B, Bassano D A, Chung C T, King G A and Sagerman R H 1984 Dose enhancement in bone in electron beam therapy *Radiology* **151** 513–16
- Prasad S C and Bassano D A 1989 Comparison of absorbed dose in bone substitute material and water using ionization measurements *Med. Phys.* **16** 81–3
- Rogers D W O 1984 Low energy electron transport with EGS *Nucl. Instrum. Methods* **227** 535–48
- Rogers D W O and Bielajew A F 1986 Differences in electron depth dose curves calculated with EGS and ETRAN and improved energy range relationships *Med. Phys.* **13** 687–94
- 1990 Monte Carlo techniques of electron and photon transport for radiation dosimetry *The Dosimetry of Ionizing Radiation* vol III, ed K R Kase, B E Bjarnagard and F H Attix (New York: Academic) pp 427–539
- Rogers D W O, Faddegon B A, Ding G X, Ma C-M, Wei J and Mackie T R 1995 BEAM: A Monte Carlo code to simulate radiotherapy treatment units *Med. Phys.* **22** 503–24
- Seltzer S M 1991 Electron-photon Monte Carlo calculations: the ETRAN code *Appl. Radiat. Isot.* **42** 917–41
- Sharma S C, Wilson D L and Jose B 1984 Dosimetry of small fields for Therac 20 electron beams *Med. Phys.* **11** 697–702
- Shiu A S, Tung S, Hogstrom K R, Wong J W, Gerber R L, Harms W B and Purdy J A 1992 Verification data for electron beam dose algorithms *Med. Phys.* **19** 623–36
- Skaggs L S 1949 Depth dose of electrons from the betatron *Radiology* **53** 868–73
- Sorcini B B and Brahme A 1994 An accurate energy-range relationship for high-energy electron beams in arbitrary materials *Phys. Med. Biol.* **39** 795–11
- Spencer L V and Attix F H 1955 A theory of cavity ionization *Radiat. Res.* **3** 239–54
- Sternheimer R M, Seltzer S M and Berger M J 1982 Density effect for the ionization loss of charged particles in various substances *Phys. Rev. B* **26** 6067
- White D R, Martin R J and Darlison R 1977 Epoxy resin based tissue substitutes *Br. J. Radiol.* **50** 814–21
- White D R 1978 Tissue substitutes in experimental radiation physics *Med. Phys.* **5** 467–79
- Zhang G G, Rogers D W O, Cygler J E and Mackie T R 1998 Effects of changes in stopping-power ratios with field size on electron beam relative output factors *Med. Phys.* **25** 1711–16

TOPICAL REVIEW

Monte Carlo modelling of electron beams from medical accelerators

Chang-Ming Ma and Steve B Jiang

Department of Radiation Oncology, Stanford University School of Medicine, Stanford,
CA 94305-5304, USA

E-mail: cma@reyes.stanford.edu

Received 8 June 1999

Editorial Enterprises
Marked Proof
PMB/78019/TOP
17288ap
Printed on 12/10/99
at 14.32



Abstract. Monte Carlo simulation of radiation transport is considered to be one of the most accurate methods of radiation therapy dose calculation. With the rapid development of computer technology, Monte Carlo based treatment planning for radiation therapy is becoming practical. A basic requirement for Monte Carlo treatment planning is a detailed knowledge of the radiation beams from medical linear accelerators. A practical approach to obtain the above is to perform Monte Carlo simulation of radiation transport in the linear accelerator. Additionally, Monte Carlo modelling of the treatment machine head can also improve our understanding of clinical beam characteristics, help accelerator design and improve the accuracy of clinical dosimetry by providing more realistic beam data. This paper summarizes work over the past two decades on Monte Carlo simulation of clinical electron beams from medical accelerators.

1. Introduction

The Monte Carlo method is a statistical simulation method. For radiation transport problems, it simulates the tracks of individual particles by sampling appropriate quantities from the probability distributions governing the individual physical processes using machine-generated (pseudo-) random numbers. Average values of macroscopic quantities such as particle fluence, energy spectrum and absorbed dose distribution can be calculated by simulating a large number of particle histories. The Monte Carlo method and its application in medical radiation physics, especially in radiation therapy physics, have been discussed in a number of publications (Burlin *et al* 1973, Raeside 1976, Nelson and Jenkins 1980, Rogers and Bielajew 1984, 1990, Turner *et al* 1985, Nahum 1985, Jenkins *et al* 1988, Mackie 1990, Rogers 1991, Andreo 1991).

The Monte Carlo method can precisely model the physical processes involved in radiation therapy and is powerful in dealing with any complex geometry. It is widely accepted that Monte Carlo simulation of radiation transport is one of the most accurate methods for predicting absorbed dose distributions in radiation therapy. In particular, Monte Carlo simulation can handle backscatter from high-density materials such as bone, or scatter perturbations by air cavities more accurately than any other existing dose calculation model (Rogers and Bielajew 1990, Nahum 1985, 1988, Mackie 1990, Rogers 1991, Andreo 1991, Bielajew 1994, Mohan 1997a). The major shortcoming of the Monte Carlo method, namely being computationally intensive, has become much less severe due to the rapid increase in speed and decrease in cost of computers, and the employment of innovative variance reduction techniques (Ma and Nahum 1993, Holmes *et al* 1993). Monte Carlo simulation is fast becoming the next generation

dose calculation engine for radiation treatment planning systems in routine clinical practice (Manfredotti *et al* 1987, 1990, al-Beteri and Raeside 1992, Neuenschwander *et al* 1995, van der Zee 1996, Kawrakow *et al* 1996, Mohan 1997a, 1997b, Hartmann-Siantar *et al* 1997, Ayyangar and Jiang 1998, DeMarco *et al* 1998, Solberg *et al* 1998, Wallace and Allen 1998, Wang *et al* 1998, Ma *et al* 1999).

A Monte Carlo treatment planning system needs detailed information about the beams incident on the patient. In order to initiate the transport of particles in the patient CT model, accurate phase space information about particles on the patient surface is required. A direct measurement of this information for a clinical beam is very difficult, if not impossible, due to the very high radiation intensities encountered in clinical beams (Deasy *et al* 1996). Calculation of beam phase space parameters using analytical methods is not flexible and usually employs approximations, for example ignoring higher-order Compton scatter events (Desobry and Boyer 1994). Currently, the most practical way to obtain detailed information about the incident radiation beam is the Monte Carlo simulation of the treatment head (Petti *et al* 1983a, b, Mohan *et al* 1985, Han *et al* 1987, Rogers *et al* 1988, 1995a, Udale 1988, Udale-Smith 1990, 1992, Chaney *et al* 1994, Kassaei *et al* 1994, Lovelock *et al* 1994, 1995, Sixel and Faddegon 1995, Ma *et al* 1997a, Lee 1997, Hartmann-Siantar *et al* 1997, Liu *et al* 1997, DeMarco *et al* 1998, Jiang and Ayyangar 1998, Balog *et al* 1999, Faddegon *et al* 1999). In addition, detailed information about radiotherapy beams has a wide variety of applications in clinical physics. Monte Carlo simulation of medical accelerators can increase our understanding of clinical beam characteristics, help accelerator design and improve the accuracy of clinical dosimetry by providing more realistic beam data.

Over the past 20 years or so, many investigations have been carried out on the Monte Carlo simulation of photon beams from medical accelerators or ^{60}Co teletherapy units. McCall *et al* (1978) investigated the effects of various targets and flattening filters on the mean energy of photon beams using the EGS3 code (Ford and Nelson 1978). Patau *et al* (1978) pioneered the Monte Carlo simulation of a complete photon accelerator. They simulated the generation of photons in a W-Cu target, the transport of photons through a flattening filter and the collimators, and the attenuation of photons in slabs of various materials. Nilsson and Brahme (1981) investigated the contaminant photons scattered from flattening filters and collimators. To investigate the electron contamination in photon beams, Petti *et al* (1983a, b) simulated a treatment machine head in great detail using a cylindrical geometry package to approximate various components of the linear accelerator. Mohan *et al* (1985) performed similar detailed simulations based on the EGS3 system to calculate photon spectra and fluence distributions from several accelerators. A special geometry package was also developed to model the exact shape of the flattening filter. Han *et al* (1987) also employed the EGS3 code to simulate in detail the treatment head of a ^{60}Co unit. They approximated the complex geometry of a Theratron-780 ^{60}Co unit as a source capsule, the source housing, and the collimator assembly. Similar studies of clinical photon beams were carried out using the EGS4 code system (Nelson *et al* 1985). Rogers *et al* (1988) investigated the sources of electron contamination in a ^{60}Co beam. Chaney *et al* (1994) simulated a 6 MV photon accelerator to study the origins of head scatter. Lovelock *et al* (1994) simulated the photon beams from a Scanditronix MM50 machine to obtain the beam characteristics needed for treatment planning. An EGS4 user code, McRad, which was a generic Monte Carlo model of a photon linear accelerator, was developed by Lovelock *et al* (1995). Sixel and Faddegon (1995) simulated a Therac-6 treatment head in radiosurgery mode using the cylindrically symmetric EGS4 user code FLURZ with the PRESTA algorithm (Bielajew and Rogers 1987). They calculated the 6 MV radiosurgical x-ray spectra both with and without the flattening filter and compared the results with the Schiff's thin target analytical spectra and the flattened Monte Carlo spectrum calculated by Mohan *et al* (1985). To study

the differential beam hardening effect of the flattening filter, Lee (1997) simulated the 6 MV beam from a Varian Clinac 2100C accelerator using the EGS4 code. Liu *et al* (1995) used a Combinatorial Geometry package to characterize treatment head components, which were modelled as 3D objects and combined using Boolean algebra. Simulations were performed with the ACCEPT code of the ITS 3.0 Monte Carlo system (Halbeib and Mehlhorn 1984). The MCNP Monte Carlo code (Hendricks and Briesmeister 1992, Briesmeister 1993) was also used to model the clinical photon beams. To determine the parameters in their photon source model used for dose calculation in the PEREGRINE system, Hartmann-Siantar *et al* (1997) simulated linacs using MCNP and the EGS4/BEAM code (Rogers *et al* 1995a). DeMarco *et al* (1998) simulated photon beams from Philips SL-15/25 linear accelerators to obtain the phase space information for the dose calculation in a patient's CT phantom. Lewis *et al* (1999) also simulated a Philips SL 75/5 linear accelerator using the MCNP code. Another Monte Carlo system, PENELOPE (Salvat *et al* 1996), has also been used to simulate photon beams from a Saturne 43 accelerator (Mazurier *et al* 1999). The EGS4/BEAM code (Rogers *et al* 1995a) has been extensively used to simulate various types of linear accelerators for photon beams. Liu *et al* (1997) simulated the photon beams from a Clinac 2100C machine and, by analysing the simulation results, developed an extra-focal source model for the dose calculation using a convolution/superposition method (Mackie *et al* 1985). Jiang and Ayyangar (1998) simulated a Varian Clinac 1800 accelerator and studied the perturbation effect of the compensator on photon beam characteristics. Their simulation results were also used to investigate the feasibility and necessity of developing a radiosurgical Monte Carlo treatment planning system (Ayyangar and Jiang 1998) and to study the dose perturbation caused by high-density inhomogeneities in small radiosurgical beams (Rustgi *et al* 1998). A more detailed report on the simulation of clinical photon beams using the EGS4/BEAM code was given by Sheikh-Bagheri (1998). Most recently, Balog *et al* (1999) studied the multileaf collimator (MLC) interleaf transmission by simulating the NOMOS MIMiC MLC attached to a GE Orion 4 MV linear accelerator. Their results were incorporated into the design of an MLC used in a prototype tomotherapy machine (Mackie *et al* 1993, 1995). By simulating the treatment head for a Siemens MXE accelerator, Faddegon *et al* (1999) designed a new flattening filter for the 6 MV photon beam for this machine. Verhaegen *et al* (1999) applied the EGS4/BEAM code to the simulation of radiotherapy kV x-ray units. Some of the above work has been reviewed by Mohan (1988) and Andreo (1991). Ebert *et al* (1996) also reviewed some recent work on the modelling of both clinical photon and electron beams using both analytical and Monte Carlo methods.

In this review paper, we focus on the Monte Carlo simulation of clinical electron beams from medical accelerators. Electron beam Monte Carlo dose calculation was considered to require more detailed beam phase space information on the patient surface than photon beams (Mackie 1990). The difficulty was considered to be that, compared with photon beam simulations, the simulation of electron beams was more sensitive to the details of the accelerator model (Rogers 1991). The work on Monte Carlo simulation of the clinical electron beams can be roughly grouped into two categories. The simulations included in the first category were mainly performed over 10 years ago with limited computation power. A medical accelerator had to be simplified to one or two components of most dosimetric significance in order to perform the Monte Carlo simulation within a reasonable timeframe and acceptable accuracy (Berger and Seltzer 1978, Borrell-Carbonell *et al* 1980, Rogers and Bielajew 1986, Manfredotti *et al* 1987, Andreo *et al* 1989). Even more recently, some studies were still carried out in this way to investigate the influence of an accelerator component on the electron beam characteristics, at a relatively low computing expense (Keall and Hoban 1994, Ebert and Hoban 1995b). The second category includes the Monte Carlo simulation of a complete accelerator (Udale 1988, Udale-Smith 1990, 1992, Kassaei *et al* 1994). This category has been greatly

enhanced since the OMEGA BEAM system was developed (Rogers *et al* 1990, 1995a, b, Mackie *et al* 1990). Since then, the Monte Carlo modelling of medical accelerators has become easier and more systematic. This review is organized to cover these two categories separately. Because of its significance and the large number of applications, the OMEGA BEAM system will be described in detail in a separate section. We also discuss the modelling of Monte Carlo simulated electron beams using different source models, which is one approach to form the link between the Monte Carlo simulation of clinical electron beams and Monte Carlo treatment planning (Ma and Rogers 1995a, b, c, Ma *et al* 1997a, Faddegon *et al* 1998, Ma 1998, Jiang *et al* 1999). Finally, we discuss some existing problems and possible future directions for Monte Carlo simulation of the clinical electron beams generated by medical accelerators.

2. Simulation of the accelerator components

The application of the Monte Carlo technique to the simulation of electron beams has a long history. In the early years, mainly due to the low speed of computers and the relatively simple Monte Carlo codes available, a full simulation of the accelerator geometry was an extremely difficult task. Simulations were usually carried out for treatment heads with great simplification; only one or two components of dosimetric importance, for example the scattering foil or intervening air, in an electron treatment machine head were simulated and the influence of these components on the beam characteristics and dose distributions was studied.

2.1. The work of Berger and Seltzer

Berger and Seltzer (1978) studied the effect of scattering foils on the dose distributions in a water phantom for electron beams with energies from 5 to 40 MeV. A two-step approach was proposed; the accelerator treatment head, simplified as the scattering foil and intervening air, was simulated first and then the simulation results were used for the dose calculation in the phantom. A monoenergetic electron pencil beam was assumed to be incident perpendicularly on the lead scattering foils of thickness between 0.1 mm and 0.6 mm. The effect of 100 cm of air between the scattering foil and the phantom was simulated using a layer of condensed air-equivalent material. The simulation results were recorded at the phantom surface, including the distribution in energy and angle of the electrons and bremsstrahlung photons. The correlation between the energy and direction was ignored, and therefore the energy spectrum and angular distribution were recorded separately. A superposition approach was developed to calculate the dose distribution in the phantom. For both electrons and bremsstrahlung photons, dose kernels for monoenergetic pencil beams were pre-calculated. Then the dose distribution in the phantom was the superposition of different pencil beam dose kernels weighted with different energies, directions and incident positions at the phantom surface. By limiting the summation over directions to certain cones around the central axis, the effect of collimation to finite field size was simulated. Figure 1 shows the energy spectra calculated by Berger and Seltzer (1978) for electrons passing through 0.1 mm lead foil alone or 0.1 mm lead foil plus 100 cm air. It is clear that the effect of intervening air on the electron energy spectrum is significant.

2.2. The work of Borrell-Carbonell *et al*

Borrell-Carbonell *et al* (1980) simulated three GGR MeV/AECL accelerators, i.e. Therac 40 Sagittaire, Therac 20 Saturne and Therac 10 Neptune, using a Monte Carlo code based on the condensed history scheme. Both Sagittaire and Saturne machines generated scanned electron beams controlled by electromagnets while in the Neptune machine electron beam flatness was

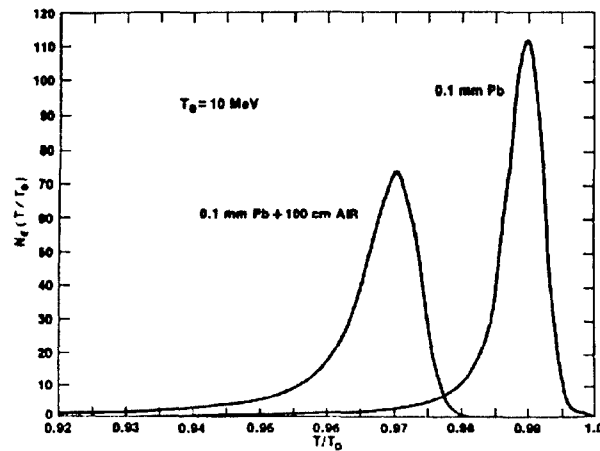


Figure 1. Energy spectra of electrons transmitted through lead foil, or through lead foil plus 100 cm air layer. Electrons with energy T_0 are assumed to be incident perpendicularly onto the foil, and T is the energy with which the transmitted electrons emerge from the foil, or from the layer of air behind the foil. The spectra include all transmitted electrons that emerge with directions within a cone of 20° half-angle around the direction of incidence. The curves are normalized to have unit area under each curve (Berger and Seltzer 1978).

produced by a pencil beam incident on a scattering foil. For all the machines, a simplified treatment head configuration was used in the Monte Carlo simulation. A monoenergetic and isotropic point source was assumed at the exit window of the accelerator. The beam defining system was modelled as a diaphragm with a square opening and zero thickness. Therefore, there was actually no simulation of the interactions of electrons with the components of the treatment machine head, except for the intervening air. Also there was no simulation of the secondary particles generated by electron interactions in the accelerator components.

The transport of the particles through air was simulated for a given collimator opening. In their work, Borrell-Carbonell *et al* (1980) used a two-step approach similar to that proposed by Berger and Seltzer (1978). The simulation results were recorded at the phantom surface, which included the electron energy, direction and position. The electron energy was calculated by subtracting the mean energy loss in air from the initial energy. Using the recorded electron phase space information, the dose distributions in a water phantom were calculated using a superposition approach similar to that of Berger and Seltzer (1978), i.e. by superposition of the pencil beam dose kernels pre-calculated with Monte Carlo simulation.

By comparing the calculated depth dose curves with measured data, Borrell-Carbonell *et al* (1980) checked their simple model for the treatment head. They found that the monoenergetic source was a good approximation for the scanned beams from Therac 40 Sagittaire and Therac 20 Saturne, but not for scattered beams from Therac 10 Neptune. For very high-energy (25 MeV) beams, they found that scattering from the beam defining system contributed significantly to the depth dose distribution, even for the scanned beams; therefore they concluded that the collimating system could not be approximated as a thin diaphragm.

2.3. The work by Rogers and Bielajew

Rogers and Bielajew (1986) calculated electron depth dose curves in a water phantom using the EGS4 Monte Carlo code (Nelson *et al* 1985) by assuming point sources of monoenergetic



electrons passing through 100 cm of vacuum. Compared with the corresponding measured data, they found that the calculation underestimated the dose near the surface and predicted a steeper fall-off beyond d_{\max} , the depth of the maximum dose. Trying to explain the discrepancies, they modelled the clinical electron beam as a monoenergetic beam of electrons passing through the 0.0127 cm Ti exit window of an accelerator, the 0.0127 cm Pb scattering foil, 102 cm of air and 3.9 cm of styrofoam. The electron energy spectrum near the central axis of the beam was scored at the phantom surface. The depth dose curves in the phantom were then calculated for incident broad parallel beams with the scored energy spectra. They found that the calculated depth dose distributions were improved by using the realistic spectrum. They also noticed that the mean energies of the spectra were significantly influenced by the very small low-energy tails. The depth of 50% maximum dose and the practical range were not ideal indices for the electron mean energy and the most probable energy respectively. Comparisons of dose distributions near inhomogeneities between Monte Carlo calculations and measurements were reported in a separate paper (Shortt *et al* 1986), which gave the first clear proof that Monte Carlo could handle electron heterogeneity problems correctly.

2.4. The work of Manfredotti *et al*

Manfredotti *et al* (1987) used the EGS3 code system (Ford and Nelson 1978) to simulate the electron collimator and the intervening air. A source of diameter 2 mm emitting monoenergetic electrons of 17 MeV was used in the simulation. The collimator was simulated with a 10 mm thick slab with a square window to obtain a $10 \times 10 \text{ cm}^2$ field at the phantom surface. The two-step approach was used; the simulated results, including energy, charge, impact points and direction cosines of particles that arrived on the phantom surface, were scored and later used in the three-dimensional phantom dose calculations.

2.5. The work of Andreo *et al*

Andreo *et al* (1989) studied the influence of energy and angular spread on the depth dependence of the stopping power ratio for clinical electron beams using the Monte Carlo method. In a similar way to Berger and Seltzer (1978), the accelerator treatment head was simplified as a lead scattering foil and 100 cm air. The lead thicknesses were chosen to give energy and angular distributions equivalent to those produced by all materials (except for air) within the treatment head. The EGS4 code (Nelson *et al* 1985) was used to simulate a monoenergetic electron pencil beam passing through the lead scattering foil and the air volume. The beam collimation was simulated by restricting the direction of the electrons emitted from the scattering foil to a forward cone, as done by Berger and Seltzer (1978). The electron energy spectrum was scored at the phantom surface and then used for the dose calculation in the phantom by combining with the Gaussian angular distributions of various root mean square angles. The phantom simulation was done using the MCEF Monte Carlo code (Andreo 1980, Andreo and Brahme 1984).

2.6. The work of Keall and Hoban

Keall and Hoban (1994) calculated the energy and angular distributions for primary electrons as well as contaminant bremsstrahlung photons for a Siemens KD2 machine using the EGS4 code (Nelson *et al* 1985). Like Berger and Seltzer (1978) and Andreo *et al* (1989), the accelerator treatment head was simplified as the scattering foils and intervening air while the influence of other components was ignored. For this type of accelerator, the scattering

foil system consists of two foils, i.e. the first scattering foil (stainless steel at 6 MeV and gold at other energies) and the second scattering foil (aluminium of a pyramid shape). The transport of an initially monoenergetic electron pencil beam through the scattering foils and air in the treatment head was simulated and the resulting energy and angular distributions were scored at the phantom surface. The simulated electron angular distribution was found to agree closely to those calculated with the Fermi-Eyges theory (Fermi 1941, Eyges 1948, Keall and Hoban 1996, Jiang *et al* 1998, 1999), indicating that a Gaussian approximation to the incident angular distribution of the primary electron beam might be adequate for use in treatment planning algorithms. The depth dose curve in water for the bremsstrahlung photons alone was calculated using the simulated bremsstrahlung spectrum. They found that the photon component of a 15 MeV electron beam had a similar d_{\max} to the 18 MV photon beam depth dose and similar fall-off to the 10 MV photon beam depth dose. The influence of electron energy and angular spread on the depth dose distribution was also studied. They found that, compared with the measured data with the applicator removed, the calculated depth dose curve using a monoenergetic beam with no angular spread had a lower surface dose and a sharper fall-off. When the simulated energy spectrum was used, excellent agreement in both the build-up and fall-off regions was achieved. The inclusion of the initial angular spread into the phantom dose calculation had a negligible effect on the depth dose curve. However, the initial angular spread was important in determining the penumbral width at the surface.

2.7. The work of Ebert and Hoban

Ebert and Hoban (1995b) performed a detailed study on the effects of electron beam cones and cerrobend cutouts on clinical electron beams using the EGS4 system (Nelson *et al* 1985). The EGS4 user code they used, RTPCART_XYZ, was based on another user code RTPCART (Murray 1990) with elements of XYZDOS (Rogers and Bielajew 1990, Bielajew and Rogers 1992). The energy and angular characteristics of Siemens KD-2 electron beams were taken from the Monte Carlo simulations of Keall and Hoban (1994).

In their study, simulations were performed for a variety of beam energies (6, 12 and 18 MeV) and beam angles incident on elements of the trimming plates or cutouts. The simulated element was a semi-infinite edge of the applicator or cutout in air. The area of the element irradiated by the electron beam was limited by a 5 mm width along the edge, the thickness of the edge and the maximum lateral range of electrons from the edge. They found that there were two processes significant to the dose distribution in the water phantom beneath the edge (see figure 2). One is the scattering of the primary electrons from the vertical face of the edge, the other is contaminant photon transmission through the edge. Other processes, such as transmitted primary electrons, and photons and electrons generated within the edge, etc, are negligible. The effect of the edge on the photon component in the primary beam can be treated as simple attenuation. The electrons scattered from the vertical face of the edge are dominantly forward directed and mostly inside the field. By studying the effect of beam incident angle, they also found that the scattered electron fluence was significantly influenced by the area of the vertical face of the exposed edge; more electrons were scattered from a large exposed area. This finding indicated that cutouts with diverging edges would produce fewer scattered electrons and thus flatter profiles than those with vertical edges. Ebert and Hoban (1995b) also studied the influence of beam energy on the scattered electron fluence, as well as the energy spectrum and mean energy of scattered electrons at various distances from the applicator edge. This information helped them to build a model for applicator scatter (Ebert and Hoban 1995a).

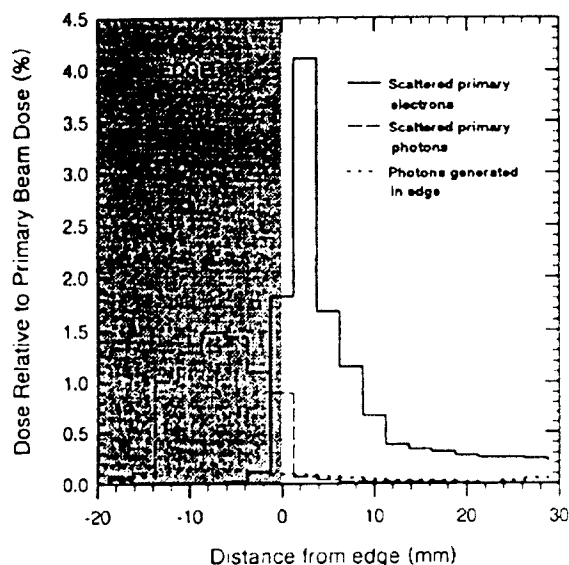


Figure 2. Profiles of dose to water of three components considered (primary beam scattered electrons, primary beam photons, photons generated in the edge by primary beam electrons) for a 12 MeV beam incident on the edge of the applicator or cutout. The edge is 50 mm above the water surface and profiles are taken at the depth of maximum buildup for the component considered, parallel to the line from the beam central axis to the edge. Normalization is to the dose due to primary open beam (Ebert and Hoban 1995b).

3. Simulation of the complete accelerator treatment head

A full Monte Carlo simulation of the medical accelerator geometry is a very difficult task. A large number of physical data (e.g. component dimensions and materials) need to be obtained and validated with high precision. A large amount of careful coding has to be done to accurately and efficiently model the individual accelerator components. Most of all, the simulation results are very sensitive to the details of the model. Therefore, it requires Monte Carlo expertise and deep understanding of electron beam characteristics to obtain good agreement with measurements.

3.1. The work of Udale/Udale-Smith

This difficult problem was first tackled by Udale/Udale-Smith (1988, 1990, 1992), who did very extensive coding (about 18 000 lines of FORTRAN) based on the EGS4 code system (Nelson *et al* 1985). Udale (1988) simulated a 10 MeV electron beam from a Philips SL75-20 accelerator. In this work, all the treatment head components of dosimetric importance were modelled, including the exit window, primary collimator, scattering foil, monitor chamber, mirror, movable jaws, accessory ring and applicator. In order to see the effects of different parts of the treatment head on the beam, she simulated five cases (denoted from case A to case E) at various levels of gradually increasing sophistication (see figure 3). An additional part of the beam defining system was introduced into the simulation in each successive case. In case A, a monoenergetic pencil beam was incident directly on the phantom. In case B a

monoenergetic isotropic point source at 95 cm from the phantom was used and the effect of intervening air was simulated. This was similar to the work of Borrell-Carbonell *et al* (1980). In case C the simulation was performed for a monoenergetic pencil beam incident on the electron window 95 cm above the phantom and interacting with the scattering foil, ionization chamber, mirror and air. In this case everything in the beam's path was simulated, but no collimating components. The geometry used in this case was more complex than that used by Berger and Seltzer (1978), Andreo *et al* (1989) and Keall and Hoban (1994). In case D the movable jaws and accessory ring were added to case C and in case E the electron applicator was added additionally.

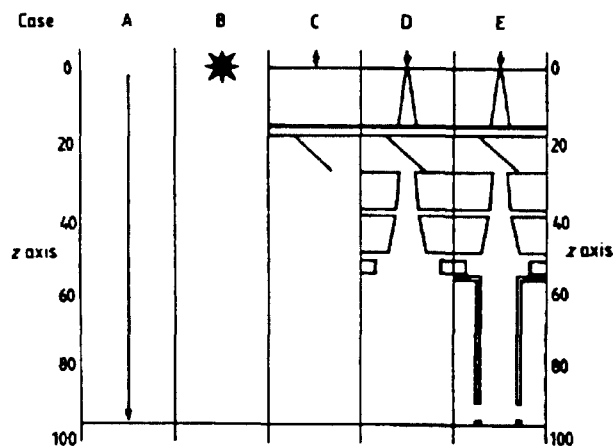


Figure 3. Schematic diagram of five simulation geometries with gradually increased sophistication used by Udale (1988) to study the influence of treatment head components on beam characteristics at the phantom surface. In case A, a monoenergetic pencil beam was incident directly on the phantom. In case B a monoenergetic isotropic point source at 95 cm from the phantom was used and the effect of intervening air was simulated. In case C the simulation was performed for a monoenergetic pencil beam incident on the electron window 95 cm above the phantom and interacting with the scattering foil, ionization chamber, mirror and air. In case D the movable jaws and accessory ring were added to case C and in case E the electron applicator was added.

Some approximations were made in the modelling of accelerator components in the work of Udale (1988). The primary collimator system was described as a series of concentric cylinders. The monitor ionization chamber and primary collimator extended to infinity radially, and movable jaws were semi-infinite. The initial energy of the pencil electron beam at the exit window for a nominally 10 MeV beam was determined by matching the 50% dose depth (R_{50}) and the electron practical range (R_p) between calculated and measured depth dose curves. Some variance reduction techniques were employed, such as the range rejection technique, i.e. particles were discarded if they did not have enough energy to reach the scoring plane at the bottom of the treatment head.

The two-step approach was adopted in the simulation of Udale (1988). In the first step, the treatment head was simulated and the simulation results (the particle phase space data) were recorded at a scoring plane at the phantom surface. The phase space information included particle type, energy, angle to the beam central axis and position at the phantom surface, which were stored in a four-dimensional array. In the second step, the dose distributions in the phantom were calculated using the scored phase space data as input.

To reduce the number of storage data about the beam exiting the treatment head and to simplify the phantom simulation, Udale (1988) used a so-called *planar approximation*. The energy spectrum was integrated over radius and angle, and the angular distribution was integrated over radius and energy. The angular distribution was defined relative to the beam central axis and there was no dependence on the azimuthal angle at any point. Under this simplification, beam divergence and the correlation among particle energy, angle and position were ignored. The beam was considered to comprise identical pencil beams all incident parallel to the beam central axis. Each pencil beam had the same energy and angular distributions. The dose distribution for each pencil beam was radially symmetric with respect to the beam central axis. A circular field was used to approximate the square field. Using the reciprocity principle, the depth dose to a region centred on the central axis with a radius of 0.25 cm was calculated by simulating a beam of radius 0.25 cm and scoring dose deposition in a cylindrical region with a cross-sectional area equal to that of the cylindrical beam. In this way the calculation efficiency was significantly improved, which was crucial at the time when this work was done.

Another technique used by Udale (1988) to reduce the statistical uncertainty and thus to speed up the simulation was to simulate primary electrons, secondary electrons and contaminant photons separately in a water phantom. The resulting dose distributions were scaled according to the relative numbers of each particle type and summed to give the total distribution. An extra benefit of using this approach was that some correlation between particle energy and angle was retained; for primary and secondary electrons energy spectra and angular distributions were used which were significantly different.

By simulating five cases with gradually increasing sophistication, Udale (1988) studied the influence of treatment head components on beam characteristics at the phantom surface. The effect of cone size on the beam characteristics was also investigated. The contributions to the central axis depth dose from the secondary electron component and photon component were calculated. The calculated depth dose curves were compared with the measurement to verify the simulation. The agreement was better for the smaller fields. Range-energy relationship was also checked.

In a follow-up study, Udale-Smith (1992) extended the EGS4 Monte Carlo simulation to two other Philips machines, the SL75-14/N and SL15, in addition to the SL75-20. One of the purposes of this work was to verify the dosimetric improvement of these two new machines over the SL75-20. The major improvement of the SL75-14/N over the SL75-20 included the use of a dual-foil scattering system rather than the single-foil scattering system, a low-mass ionization chamber and the aperture-plate applicator rather than the tubular electron applicator. As in the previous work (Udale 1988), the information on the component dimensions and materials for all machines was supplied by the manufacturer. But there were two pieces of information which could not be obtained from the manufacturer. One was the source spot size. A monoenergetic pencil beam was assumed. The other was the actual energy of the pencil electron beam at the exit window. Udale-Smith (1992) chose the incident energy, which gave depth-dose curves with practical ranges close to the measured values. As pointed out by Udale-Smith (1992), the introduction of empirical procedures was not satisfactory but could not be avoided.

Some important improvements of the simulation techniques were proposed. For the simulation of the SL75-20 machine, the entire treatment head geometry was treated as a single system. It was extremely complicated to modify the geometry. For SL75-14/N and SL15 machines a modular approach was used. Each treatment head component was treated as an independent module. Along the beam direction there was no overlapping between any two neighbouring components. The transport of particles in each module was independent of the geometry of the neighbouring components. This concept of component module (CM) was later adopted and extended by Rogers *et al* (1995a) in the design of the EGS4/BEAM system.

For the simulations of the SL75-20 and SL75-14/N machines, the planar approximation was used as in the previous work (Udale 1988). Four particle types were scored separately: primary electrons, secondary electrons, photons and positrons. These assumptions were reasonable for the SL75-20 accelerator. However, the simulation of the SL75-14/N machine indicated that they were not adequate for cleaner beams produced by the modified collimating system. Therefore a more realistic model was used in the simulation of the SL15 machine. Five particle types were scored: applicator scattered electrons, jaw scattered electrons, direct electrons (not scattered by the secondary collimating devices), contaminant photons and positrons. For direct electrons, beam divergence and the correlation between energy and direction were taken into account. Five energy bands were used for the direct electrons and for each band there was an appropriate angular distribution. Beam divergence was considered by storing the angle between the electron direction at the scoring plane and a ray from the source incident at the same point on the scoring plane.

The phantom simulations for SL75-20 and SL75-14/N were the same as in the previous work (Udale 1988). The planar approximation was found to be inadequate for SL75-14/N and SL15. Hence, two different approximations were used to include beam divergence into the phantom simulation for the SL15 machine. In one approximation, the central axis depth dose was calculated using the reciprocity principle. Then, an inverse-square correction was applied to the resulting central axis depth dose curve for direct electrons. In the other approximation, a voxel geometry was modelled and then the divergence of the direct electron component was considered explicitly.

The simulations of Udale-Smith (1992) verified the improvement of SL75-14/N and SL15 over SL75-20. For these two new types of Philips accelerator, the beams were cleaner because (a) there were fewer secondary electrons and contaminant photons in the beams, (b) the contaminant photons had much lower mean energy thus contributed less to the dose distributions, (c) there were fewer low-energy electrons in the electron energy spectra, and (d) the electron angular distributions were narrower.

Udale-Smith (1992) benchmarked the simulations by comparing the calculated and measured depth dose distributions. It was found that the introduction of some correlation between energy and direction for direct electrons improved the calculation accuracy. Allowing for the beam divergence also had a beneficial effect. The use of a simple inverse-square correction was shown to be a useful first-order estimate of the effect of beam divergence, allowing quick calculations to be performed and then corrected. Using voxel geometry for phantom simulation took into account the beam divergence explicitly and was shown to give excellent results. It was a useful starting point for the development of CT based Monte Carlo treatment planning as the patient body can be approximated as voxel geometry built from CT numbers.

3.2. Work by other investigators

In addition to the work of Udale-Smith (1990) and the development of the BEAM system (Rogers *et al* 1995a), there were also some other efforts to simulate a complete electron medical accelerator. To evaluate changes in the electron energy spectrum, depth dose and dose profile for two cone designs for Varian Clinac 2100C accelerators, Kassaei *et al* (1994) performed Monte Carlo simulation for the treatment head using the cylindrical symmetry CYLTRAN option in ITS Monte Carlo code (Halbeib and Mehlhorn 1984). The treatment head components modelled were scattering foil, photon jaws, electron cones and intervening air. Cones were modelled as a series of circular apertures. Energy spectrum and beam profile were investigated for a 9 MeV monoenergetic electron beam impinging on the 0.025 mm thick Be exit window. Like Udale (1988), to study the influence of different components and

the difference of two cone designs, Kassaei *et al* (1994) simulated four cases of different geometrical arrangements of the beam defining system, which were (a) scattering foil only, (b) scattering foil and photon jaws, (c) scattering foil, photon jaws and new cone design, and (d) scattering foil, jaws and old cone design. It was found that the presence of the movable jaws did not significantly modify the electron energy spectrum. The low-energy secondary electron component of the beam exiting the new cone was significantly reduced because the trimming plates were thick enough to absorb all the incident primary electrons, which was verified by Rogers *et al* (1995a) and consistent with the simulation results of Ebert and Hoban (1995b). The dose in the beam penumbral region was lower for the new cones because the leakage of secondary electrons from the cone aperture and housing was appreciably reduced.

Burns *et al* (1995) briefly mentioned a full Monte Carlo simulation of an accelerator treatment head to determine the electron stopping powers and practical ranges for clinical electron beams. An EGS4 user code was developed to model the scattering foil, the collimating system and the intervening air. Unfortunately, no further details were given in the paper.

More recently, Pawlicki (1998) modelled a Varian Clinac 1800 accelerator using the geometry package PENGEO of the PENELOPE Monte Carlo code system (Salvat *et al* 1996). He combined the accelerator simulation with the patient dose calculation in a 3D rectilinear phantom built from CT data.

4. The OMEGA BEAM system

The work of Udale/Udale-Smith (1988,1990,1992) brought the Monte Carlo simulation of electron accelerators to a new stage. Her simulation was no longer restricted to cylindrical symmetry. However, without a large effort, her code could hardly be applied to other types of accelerators, although it was well structured. As pointed out by herself (Udale 1988), 'In many ways the simulation has been very crude'. In order to supply accurate clinical beam information from a wide variety of medical accelerators for electron beam Monte Carlo simulation, a better code system with greater flexibility and extensibility was needed. This led to the development of the BEAM system (Rogers *et al* 1995a,b). Because of the significance of the BEAM code, it is worthwhile devoting this entire section to a description of this code system and its applications.

4.1. Descriptions of the BEAM code

The OMEGA (Ottawa Madison Electron Gamma Algorithm) project was a collaborative effort between the University of Wisconsin, Madison, and the National Research Council of Canada, Ottawa (Mackie *et al* 1990, 1994, Rogers *et al* 1990). The goal was to develop a full 3D electron beam treatment planning system using the Monte Carlo simulation technique to calculate dose distributions in a patient. A major achievement of this project was the development of the BEAM and DOSXYZ code systems (Rogers *et al* 1995a,b, Ma and Rogers 1995a,c, Ma *et al* 1995). Both BEAM and DOSXYZ were based on the PRESTA extension of the EGS4 Monte Carlo system (Nelson *et al* 1985, Bielajew and Rogers 1987, Rogers and Bielajew 1990, Bielajew *et al* 1994).

Although the original emphasis was on the simulation of clinical electron beams from medical accelerators, the BEAM code was equally applicable to all other radiation therapy units, including high-energy photon beams from accelerators, ^{60}Co beams or kilovoltage x-ray beams. The code was also a versatile, general-purpose Monte Carlo transport package, which could be used in a wide variety of applications besides simulating radiation therapy beams. There were many important and useful new features in the BEAM code (Rogers *et al* 1995a).

These included the use of the component modules (CMs), scoring particles' phase space information, tracking each particle's history, applying various variance reduction techniques, setting up a file/structure for parallel processing and developing a user-friendly interface.

The concept of component module was used in the code design of Udale-Smith (1992). In the BEAM code, this method was extended and played a very important role (Rogers *et al* 1995a). Component modules were actually a variety of elementary geometric entities and could be used to represent the components of an accelerator. Each CM dealt with a specific class of geometric shape and was contained between two planes, which were perpendicular to the beam axis. No overlapping between CMs was allowed. Each CM operated completely independently of the other CMs. A CM was defined with a variety of parameters rather than explicit values related to the geometric shape and material type. The parameter values were specified in an input file given by the user to model a specific accelerator component when performing a simulation. Figure 4 shows the diagrams for nine different CMs.

The beauty of this element of the design philosophy of BEAM was that each CM acted like a 'brick' and the model for the whole treatment head could be easily built up by simply putting a series of CMs together according to the technical drawing of an accelerator treatment head. This feature allowed accelerators of different manufacturers and different designs to be modelled at any level of complexity with little effort, even for users without much Monte Carlo coding experience. Also, this feature reduced the chance of making mistakes during the modelling process and made the quality assurance easier. The independence of each component of the geometry package allowed each CM to be tested and debugged in isolation.

Another important element of the basic design philosophy in the BEAM code was the recording of the complete phase space information of each individual particle crossing the scoring planes (Rogers *et al* 1995a). The information included the charge, energy, position, direction and a history tag (see below) for each particle. The phase space data could be recorded at the back plane, perpendicular to the beam axis, of any specified component module in the accelerator model. There could be an arbitrary number of scoring planes and a phase space data file could be created at each plane.

An important parameter in the phase space data file was the history tag variable, LATCH, which was a feature of EGS4 (Nelson *et al* 1985). In the BEAM code, however, each bit of LATCH was manipulated separately to fully utilize this tag. Using LATCH one could easily keep track of each particle's history and the information to score dose components separately, and then analyse the relative dose contributions from various accelerator components. In order to evaluate the influence of different accelerator components, Udale (1988) and Kassaei *et al* (1994) simulated several cases of different levels of complexity. With LATCH, it can be done in one simulation (Rogers *et al* 1995a). The phase space data file could be analysed using various data analysis programs (Ma and Rogers 1995a, b, c). LATCH provided a powerful tool for studying the characteristics of clinical electron beams with these programs.

A phase space file could be re-used by the BEAM code itself (Rogers *et al* 1995a). This allowed the user to simulate a treatment head in separate steps. For example, the user could simulate the treatment head from the exit window down to the upper surface of the last trimming plate of the electron applicator and then re-use the recorded phase space data to simulate the last scraper with various patient-specific cutouts. For an energy/cone combination, the first step of the simulation could be done once and for all, and thus avoid the repetition of the simulation for the subsequent simulation for different electron cutouts (Zhang *et al* 1998, 1999, Kapur *et al* 1998, Jiang *et al* 1999). The phase space data could also be used by the DOSXYZ code (Ma *et al* 1995, Rogers and Bielajew 1990, Bielajew and Rogers 1992), which was designed to perform dose calculations in a 3D rectilinear geometry to simulate various phantoms and the patient geometry built from CT data.

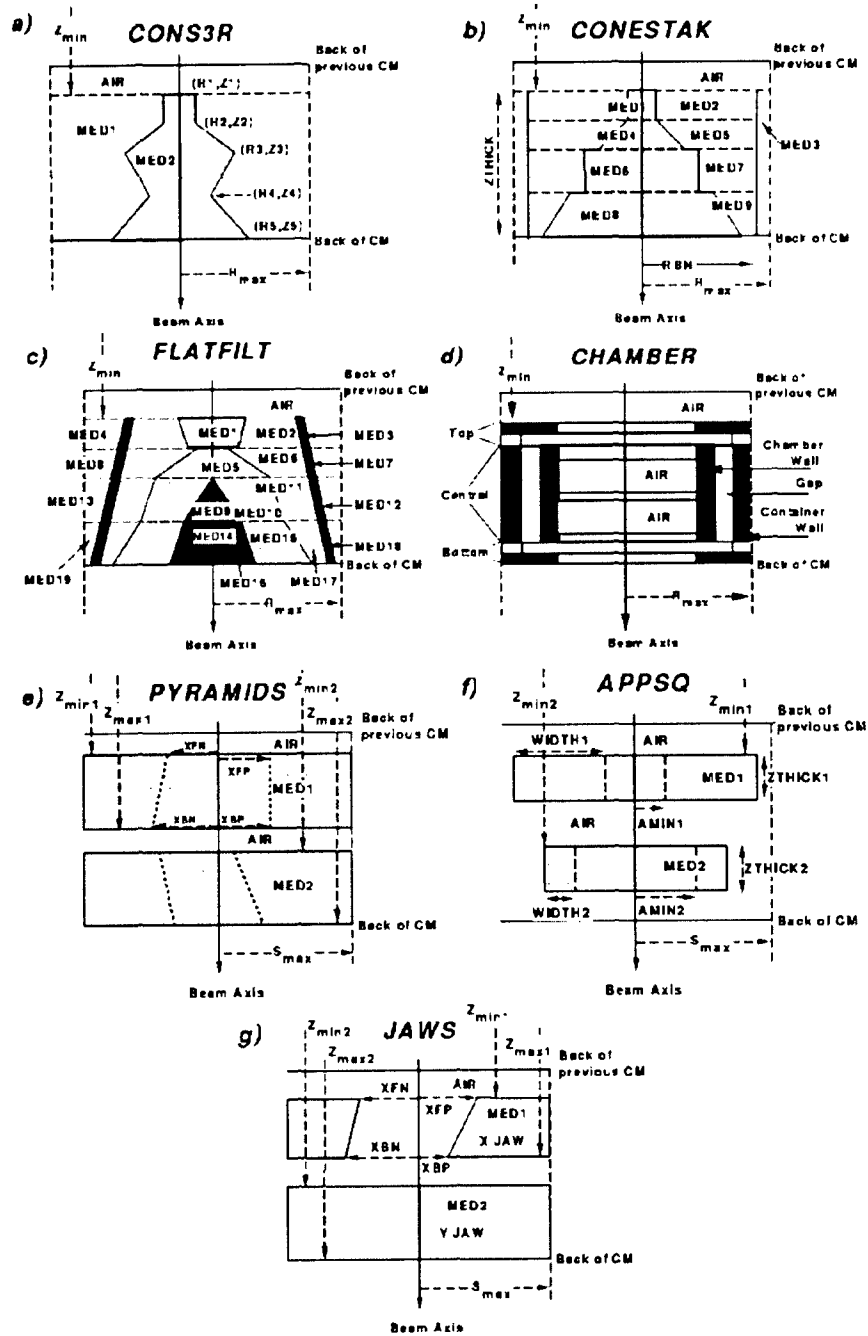


Figure 4. Schematic diagram of some component modules developed for the BEAM code by Rogers *et al* (1995a, b): (a) CONS3R, (b) CONESTAK, (c) FLATFILT, (d) CHAMBER, (e) PYRAMIDS, (f) APPSQ (which was later changed to APPLICAT), (g) JAWS, (h) MIRROR, (i) XTUBE.

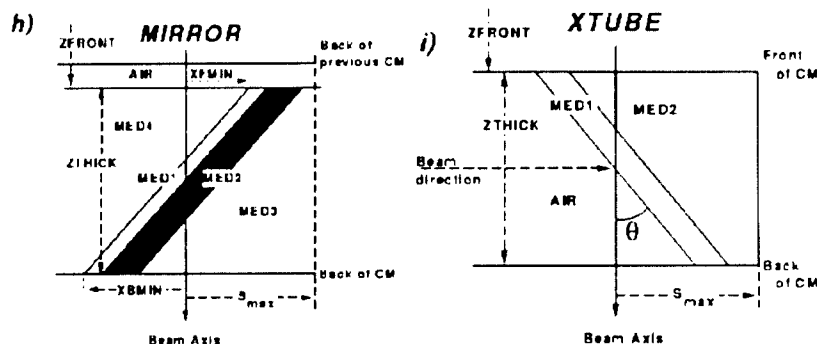


Figure 4. (Continued)

The two-step approach was a common technique for simulating accelerator treatment head and performing phantom dose calculations (Berger and Seltzer 1978, Borrelli-Carbonell *et al* 1980, Manfredotti *et al* 1987, Udale 1988, Udale-Smith 1990, 1992). For disk space and other reasons, the correlation between particle energy, direction and position was usually broken, which led to inaccuracies in the reconstructed incident beam as demonstrated by Andreo and Fransson (1989) and in the dose distributions as shown by Udale-Smith (1992). BEAM also used the two-step approach. However, since the full phase space information for each particle was recorded, the correlation was completely retained. Actually, because BEAM used the phase space data file, this two-step approach was almost equivalent to a complete simulation of the treatment head and the phantom; particles were only 'frozen' temporally at the scoring plane, with all the information to continue for further BEAM simulation or performing phantom dose calculation. The approach of scoring a particle's full phase space information was proved to be not only flexible but also, and even more importantly, a solution to the correlation problem. The major drawback with the approach was that it generated large data files and thus took a large amount of disk space, hundreds of megabytes for an electron beam and several gigabytes for a photon beam (Rogers *et al* 1995a, Kapur *et al* 1998).

Some useful variance reduction techniques were used in the BEAM code (Rogers *et al* 1995a, b). One was the range rejection method. In the BEAM code, however, this technique was further improved. Tables of the residual ranges to the threshold energy (AE) in each medium as a function of electron energy were pre-calculated using the restricted stopping powers. If a charged particle could not escape from the current region or reach a scoring plane, it was terminated. Other variance reduction techniques used in BEAM included photon interaction forcing, bremsstrahlung splitting and Russian roulette. These techniques have been described by Bielajew and Rogers (1988) and can be easily implemented in an EGS4 user code using the Mortran macros included in the EGS4 distribution. When a photon is forced to interact in the phantom the weight of the photon and all its descendents will be reduced to reflect the actual probability for such an interaction in the phantom. This photon forcing method worked for dose calculation in the phantom but failed for fluence scoring, as those photons, which did not interact in the phantom, were not transported. Ma (1992) improved the photon forcing technique by forcing the photons to interact not only in the entire phantom but also in any selected regions of interest. A fictitious photon that carried the remaining weight of the incident photon was transported to ensure the accuracy of both dose and photon fluence calculations (Ma 1992). This new photon forcing technique was implemented in the

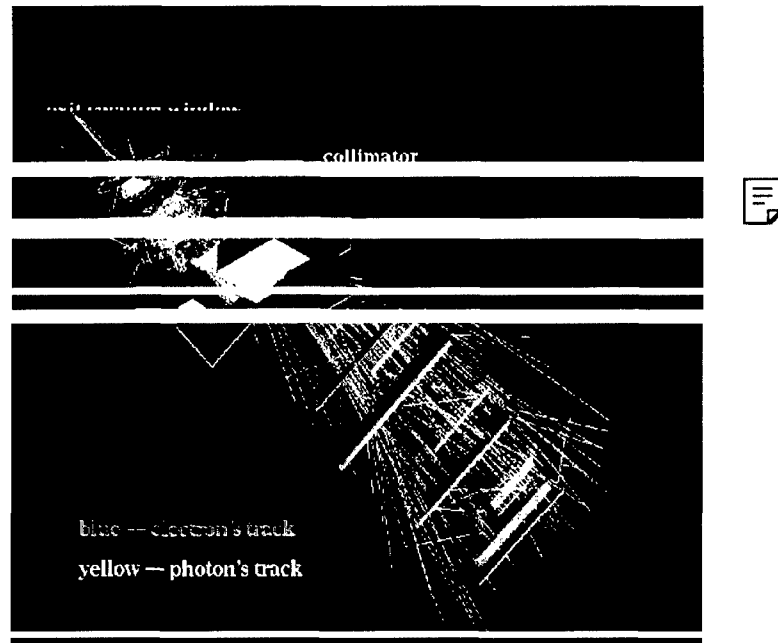


Figure 5. The treatment head of the Varian Clinac 2100C as shown by EGS_windows. About 100 electrons coming from the exit vacuum window are simulated and their tracks are shown in the picture (Rogers *et al* 1995a).

(This figure can be viewed in colour in the electronic version of the article; see www.iop.org)

BEAM code and the photons could be forced to interact in any accelerator component as required (Rogers *et al* 1995b). The Russian roulette technique was recommended for use with the bremsstrahlung splitting technique. In a photon beam simulation, the efficiency of the bremsstrahlung photon production can be significantly improved using the particle splitting technique. However, fewer electrons generated by these photons in the treatment head can reach the scoring plane. The simulation efficiency can be significantly improved by applying the Russian roulette technique to these electrons.

Recently, a user interface program, BEAM_GUI, has been written which has greatly simplified the process for writing BEAM input files. A similar user interface was also developed for the DOSXYZ program (Treurniet and Rogers 1998). This has made the BEAM system more user-friendly. Furthermore, the code can be used to score data to produce a 3D display of the accelerator geometry and particle histories using a graphics package called EGS_windows (Bielajew and Weibe 1991). Figure 5 shows a Varian Clinac 2100C machine using EGS_windows and the simulated tracks of some electrons and photons. A file structure can be set up to run the dose calculation in parallel. Different input files can be generated for the same beam and phantom configuration but with different random number seeds to ensure the independence of the individual results. The final results can be combined using the software provided. Many efforts were also made to document the code well, especially in the source code (Rogers *et al* 1995b, Ma *et al* 1995, Ma and Rogers 1995a, b, c).

4.2. Benchmarks and applications of the BEAM code

4.2.1. The work by the NRCC group. The BEAM code has been first benchmarked extensively for electron beams from medical accelerators and used in a wide variety of applications by its developer, the NRCC (National Research Council of Canada) group.

Rogers *et al* (1995a) compared the calculated dose distributions with measurements in a homogeneous water phantom for a wide variety of accelerators, including the NRC 35 MeV research accelerator, a Varian Clinac 2100C, a Philips SL75-20, an AECL Therac 20 and a Scanditronix MM50. The NRC research accelerator has a narrow, well-known electron energy. They found that the calculated and measured depth dose curves and dose profiles were in excellent agreement using no free parameters. The energy and angular distribution of electrons at the exit window of a commercial medical accelerator is usually unknown to the user. Like Udale-Smith (1990), Rogers *et al* (1995a) assumed that all beams in the accelerator vacuum were monoenergetic and on-axis, and selected the incident electron energy by matching the calculated and measured values of the 50% dose depth, R_{50} . The depth dose curves could be calculated with an accuracy better than 2% of D_{\max} for almost any beams simulated. A more detailed benchmark was given in a compilation by Ding and Rogers (1995). In addition to those five linear accelerators studied by Rogers *et al* (1995a), Ding and Rogers (1995) also simulated a Siemens KD2 machine. For each accelerator, they calculated the dose distributions in a water phantom for up to five electron beams with an energy range of 5–50 MeV. For all cases, the calculated and measured dose distributions agreed well.

A detailed study on electron beams from a Varian Clinac 2100C machine was also presented by Rogers *et al* (1995a). The contributions from electrons and photons from different parts of the accelerator to the depth dose curve and dose profiles were analysed. Consistent with the results of Kassae *et al* (1994), they also found that the new applicator design reduced low-energy electrons from the applicator and gave a significantly cleaner beam. As a substitute to the new cone design, they found that an equivalent dosimetric effect could be achieved by adding an additional piece of lead on top of an aluminium scraper. They found that the dose distributions were sensitive to the details of the accelerator. For example, for a Clinac 2100C machine, either using a different monitor chamber or changing the jaw setting slightly would result in distinct changes in the dose distributions.

Ma *et al* (1993a, 1994) used the BEAM code to study the characteristics of the electron beams from three different linear accelerators, Philips SL75-20, AECL Therac 20 and Varian Clinac 2100C. Electron beams of nominal energies 6–20 MeV were simulated using the BEAM code. The results showed that for a Varian Clinac 2100C accelerator, electrons from individual components had distinct energy and angular distributions. The normalized energy spectra for each component varied by less than 5% for the same energy bin within a collimated $10 \times 10 \text{ cm}^2$ field. About 10% of the electrons from the applicator are incident at relatively large angles, peaked at 6 and 15 degrees. These observations led to the development of simplified beam models to replace the simulated phase space data (Ma and Rogers 1995b, c).

A key parameter in the simplified beam model is the virtual point source (VPS) position. Ma *et al* (1997a) simulated electron beams emerging from the treatment head and calculated the dose distributions in a water phantom with varying air gap thicknesses. Dose distributions were also calculated for an ideal point source with various SSD values in order to verify several commonly used methods for VPS position measurements. The results showed that the 'pin-hole' method and the 'full-width half-maximum' (FWHM) method could accurately predict the source positions while the 'inverse square' method usually gave smaller SSD values, especially for lower electron energies. The virtual SSD values obtained using the first two methods were suitable for direct Monte Carlo or analytical calculations, with a point source model, of dose

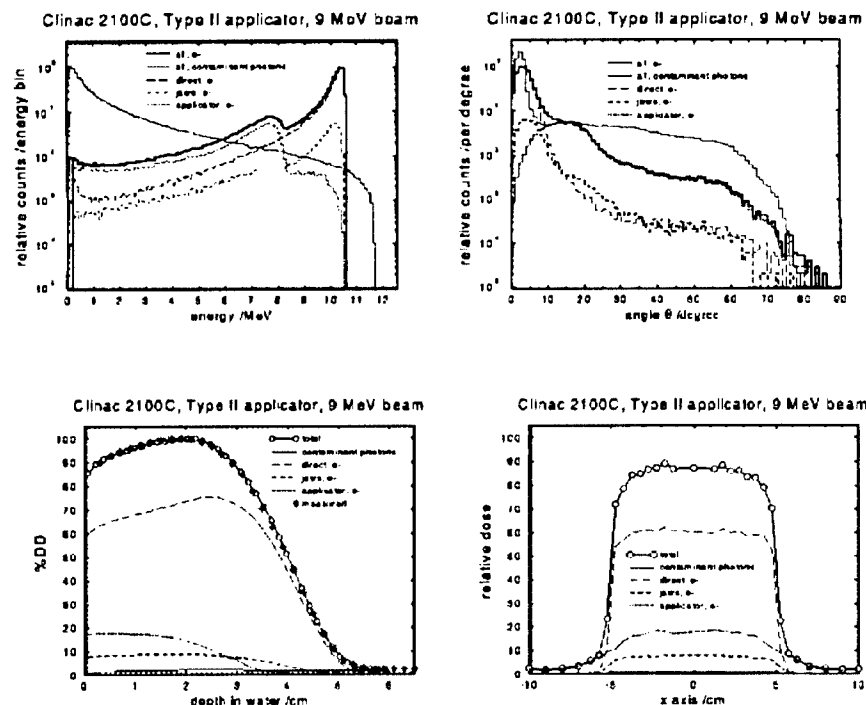


Figure 6. Calculated components of electron energy spectrum, angular distribution (at the phantom surface), depth-dose curve and dose profile (at 0.1 cm depth) for a Clinac 2100C with beam energy 9 MeV, field size = 10×10 cm² and SSD = 100 cm, using BEAM and DOSXYZ codes (Ding and Rogers 1995).

distributions with correct FWHM values. Based on these studies, Ma and Rogers (1995b, c) and Ma *et al* (1997a) proposed a multiple source model consisting of a series of sources based on the energy and angular distributions of individual accelerator components. The user could predetermine the complexity of these models so that the full phase-space data for these beams could be reproduced with the desired accuracy.

Using the BEAM code, the energy and angular spectra of electrons and photons could be easily obtained. Rogers *et al* (1995a) calculated 18 electron spectra for four different clinical accelerators, including a non-standard Varian Clinac 2100C with a Type II applicator, Philips SL75-20 with a tubular applicator and the scanned beams from the Therac 20 and MM50 Racetrack Microtron. The results for the SL75-20 accelerator were compared with those of Udale-Smith (1990). Some differences were seen for a 10 MeV beam and could be partially attributed to the different values of AE and cutoff energy, as well as different regions from where electrons were included in the spectra. Figure 6 shows the detailed analysis of the components of the electron energy spectrum, angular distribution, depth dose distribution and dose profile for a 9 MeV beam from a Varian Clinac 2100C accelerator. These results showed that most large-angle electrons were contributed by scattered electrons from applicators while scattered electrons from jaws had a relatively smaller angular spread for beams from accelerators with scattering foils. They also found that the contaminant photons were forward directed with a small angular spread because they were mainly produced in scattering foils.

Using the BEAM simulation results for a variety of clinical accelerators, Ding *et al* (1996) studied the mean energy in a water phantom for realistic electron beams from a variety of accelerators. They calculated the Spencer–Attix water/air restricted mass stopping power ratio for realistic electron beams in the energy range from 5–50 MeV and compared the results with those determined according to AAPM and IAEA protocols based on monoenergetic parallel beams (Ding *et al* 1995). A universal correction to the stopping power ratios for electron beam reference dosimetry was presented in terms of per cent depth dose in the photon tail. Ding *et al* (1997) also performed detailed studies of fluence correction factors using the realistic beam data simulated with the BEAM code.

The BEAM code has also been used to study the beam monitor chamber backscatter effect for electron beams. Ding *et al* (1994) found that, for a Clinac 2100C machine, the amount of backscatter decreased from 8% to 3% as the beam energy went from 6 to 18 MeV. They also found that 99% of the backscatter came from a fixed shielding ring downstream of the monitor chamber in the Clinac 2100C. The rest came from the collimator and applicator, and almost none from the water phantom. Using the BEAM code, Zhang *et al* (1998) studied the effects of changes in stopping power ratios with field size on electron beam relative output factors. They simulated electron beams for different field size, energies and machines and then calculated the stopping power ratios. It was found that this effect was negligible, due to error cancellation, as long as the AAPM TG-25 protocol (AAPM 1991) was followed with stopping power ratio data for broad monoenergetic beams (AAPM 1983). Zhang *et al* (1999) calculated the output factors versus size of square cutouts for electron beams with energies between 6 and 13 MeV and from a Siemens MD2 machine. The calculated relative output factors at 100 cm and 115 cm SSD agreed within 1% with the measurements.

4.2.2. The work of the Stanford group. The research group at Stanford University has been actively working on the clinical implementation of the Monte Carlo technique for radiotherapy treatment planning (Ma *et al* 1999). They have investigated the various aspects in the implementation procedure: simulation of electron beams from clinical accelerators (Kapur *et al* 1998, Ma *et al* 1999), beam characterization and modelling for dose calculations (Ma 1998), beam commissioning procedures for clinical implementation (Ma *et al* 1997c, Jiang *et al* 1999), and calculations of electron output factors for small fields (Kapur *et al* 1997, 1998, Ma *et al* 1997b) and extended air gaps (Mok *et al* 1997, Ma *et al* 1999). Further studies were carried out to calculate the dosimetric data required for performing accurate dose measurements for beam commissioning (Kapur and Ma 1999). More studies were reported on the effect of heterogeneous patient anatomy on the dose distributions and comparisons with conventional dose algorithms (Ma *et al* 1999).

Ma *et al* (1999) reported on the simulation of the electron beams (4–20 MeV) from three types of Varian accelerators, namely Clinac 1800, 2100C and 2300C/D, using the BEAM code. The dose distributions in a solid water phantom were calculated using the DOSXYZ code (Ma *et al* 1995) and compared with measured beam data according to specially designed commissioning procedures (Ma *et al* 1997c). The accelerator simulation was refined by adjusting the incident energy and simulating the details of the accelerator components until the difference between the Monte Carlo results and measurements was reduced to within 2% of the maximum dose value. The Monte Carlo calculated isodose curves agreed well with the measured data (using film and ionization chamber) while the results from a commercial treatment planning system with a 3D pencil beam algorithm differed significantly in some typical cases (e.g. >5 mm shift in the depth of the maximum dose, d_{max} , and the 90% isodose line). The Monte Carlo method accurately predicted the beam output (agreed to within 2% with the measured value) for small irregular fields while the film

measurements at a fixed d_{\max} resulted in an uncertainty of up to 10% for a 6 MeV electron beam.



Mok *et al* (1997) studied the air gap factor for electron fields at extended source distances, the air gap factor being defined as the ratio of the machine output for a field defined by a cutout at an extended SSD to the output of the same field at the standard SSD. They used the BEAM code to simulate the phase space data for the electron beams (6–20 MeV) from a Varian Clinac 2100C accelerator and the DOSXYZ code to calculate the dose values in a water phantom. Comparisons of the Monte Carlo calculations and the measured results showed that the air gap factors could be accurately predicted (within 2%) for square fields of sizes from $10 \times 10 \text{ cm}^2$ to $2 \times 2 \text{ cm}^2$. Similar results were found for elongated fields and irregular fields of various sizes (Mok *et al* 1997, Ma *et al* 1999). They concluded that when set up properly the Monte Carlo program could be used for output factor calculations for small and irregular electron fields by a dosimetrist or a medical physicist with little Monte Carlo knowledge.

Ma *et al* (1997c) reported on the procedures for commissioning the computer simulated clinical beams for the implementation of the Monte Carlo technique for treatment planning. The EGS4/BEAM system was used for the simulation of the beams from several clinical accelerators: Varian Clinac 1800, 2100C and 2300C/D. The EGS4/DOSXYZ code was used for the dose calculations in water and in patients (phantoms built from CT data). The simulated beam data were compared with measurements performed using ionization chambers, diode detectors, TLDs and film. The dosimeter readings were converted using the stopping power ratios calculated for the realistic beams (Kapur and Ma 1999) and the dosimeter perturbation effects were properly corrected. They were able to keep the difference between the calculated and the measured dose, anywhere in the phantom, to about 2% of D_{\max} . The output factor (OF) calculation was more sensitive to the details of the linear accelerator; the photon jaw positions in an electron beam could significantly change the OF values which had to be simulated accurately to match the measured data to within 2%. They have developed procedures and successfully commissioned the beams used at the Stanford Medical Center. As a result, the uncertainty in the OF for small irregular field electrons was reduced from 5–10% to about 3% with Monte Carlo treatment planning.

Output factors for electron beams from a Varian Clinac 2100C accelerator were investigated systematically by Kapur *et al* (1998). Electron beams of 6–20 MeV nominal energy for rectangular and square inserts varying in field size from $1 \times 1 \text{ cm}^2$ to $20 \times 20 \text{ cm}^2$ were simulated using the Monte Carlo calculated phase space files. The calculations for water phantoms yielded values that were consistent with the measured values to within 2% for the range of applicator and square/rectangular insert combinations used on these machines for all the beam energies. The variations of output factors for different applicator–insert combinations were quantitatively assessed by separating the contributions of the direct and indirect particles to the total output factor. Beam characteristics such as the energy spectrum, planar fluence and angular distribution were studied to correlate the observed trends qualitatively. The use of these phase space files to compute output factors for arbitrarily shaped electron cutouts such as those used clinically for electron boosts in breast or head-and-neck cancers was examined. It was found that Monte Carlo calculations reproduced the measured values in water phantoms more accurately than a commercial treatment planning system which uses a 3D pencil beam dose calculation algorithm (Hogstrom *et al* 1981), especially under the conditions of compromised lateral scatter equilibrium.

Kapur and Ma (1999) also studied the restricted mass collision stopping power ratios for clinical electron beams of 6–20 MeV nominal energy from a Varian Clinac 2100C accelerator. The Monte Carlo simulations used for this purpose were performed for a variety of beam geometries including narrow to broad beams, normal to oblique angulation and various SSDs

for homogeneous water phantoms as well as heterogeneous phantoms, for various detector materials. The homogeneous water phantom calculations in this energy range were consistent with protocol recommended values for water-to-air ratios under broad, normal incidence conditions (AAPM 1983). The ratios for narrow realistic clinical beams differed by up to 1% compared with the broad realistic clinical beams, the differences being most significant for water-to-air, film materials and silicon and much smaller for water-to-detector materials such as graphite, ferrous sulphate, PMMA, polystyrene and lithium fluoride. In heterogeneous phantoms comprising water and layered lung- or bone-like plastic materials, stopping power ratios for water-to-detector were compared with the same in identical sized water phantoms using the stopping power ratio correction factors. These factors were found to vary in depth most for water-to-air, film materials and silicon, and to a lesser extent for the other detector materials described above. The extent of variation depended on the actual construction and geometry of the heterogeneous phantoms.

4.2.3. The work of the T-SRCC group. Faddegon *et al* (1998) described their work on implementing Monte Carlo for electron beam treatment planning at the Toronto-Sunnybrook Regional Cancer Center (T-SRCC). Beam data for their current clinical implementation consisted entirely of full phase space data sets simulated using the EGS4/BEAM code (Rogers *et al* 1995a). All 14 beams on a Siemens MXE (5–14 MeV) and a Philips SL20 (4–20 MeV) were commissioned for two applicators, covering nominal $10 \times 10 \text{ cm}^2$ and $15 \times 15 \text{ cm}^2$ fields. After spending substantial effort in commissioning, they still had unresolved discrepancies of 3% (or 2 mm in isodose lines) in the measured and calculated dose distributions (Faddegon *et al* 1998). They considered it likely to be sufficient to weight the beam data with some simple, slowly varying functions of energy and position to improve the calculation accuracy from a clinical perspective. Preliminary work on deriving beam data from measured dose distributions was done using a simple beam model of a point source with spectral distribution (Faddegon 1995). An unfolding technique was utilized to extract appropriate weights for a response matrix of monoenergetic depth doses to yield the measured depth doses. The unfolded spectral distribution had a 50% excess of low-energy electrons to compensate for the assumption of a point source with no angular distribution about the ray lines. Further work was proposed to resolve the level of detail and accuracy required in a beam model to adequately represent a beam, and to determine which concise set of measurements and methodology was most clinically viable for determining the beam model parameters (Faddegon *et al* 1998).

4.2.4. The work of Karlsson et al. Karlsson *et al* (1999) investigated the electron beam characteristics for a Varian Clinac 2300C/D accelerator. The purpose was to find out how a conventional treatment head could be modified to use multileaf collimated electron beams. Using the computer controlled multileaf collimator (MLC) for both photon and electron fields, automatic setup would be possible and complex field shapes and beam matching could be achieved. The physical parameters investigated in this work were beam penumbra and virtual/effective source position which were considered to be essential in beam matching and for dosimetry calculations. A 9 MeV nominal electron energy beam was simulated using the EGS4/BEAM code for various geometry combinations. Karlsson *et al* (1999) reported that the beam characteristics would fulfil their preset criteria for clinical use for electron beams of nominal energies down to 9 MeV by replacing the air in the treatment head with helium, changing the primary scattering foil position, using a thinner monitor chamber and lowering the MLC. Another proposal was made based on their Monte Carlo simulations that the electron beam characteristics would still be acceptable by inserting a helium balloon between the MLC and the patient. Thus, no change to the MLC would be necessary.

5. Discussion

During the last two decades, significant efforts have been made in Monte Carlo modelling of the clinical electron beams from medical accelerators. Many major issues have been addressed through detailed Monte Carlo simulations. Such efforts have been facilitated by the development of the BEAM code. Electron beams from various clinical accelerators have been studied more systematically for different purposes by different research groups. The accelerator manufacturers have studied the beam characteristics to improve accelerator design, although they have not published any detailed reports in the literature. The accelerator users have studied the beam phase space information to derive necessary dosimetric data for accurate dosimetry measurement and to perform accurate dose calculations for radiotherapy treatment planning. However, there are still a variety of practical problems associated with the accuracy of the accelerator simulation using the Monte Carlo techniques.

5.1. Simulation accuracy

The most basic information required for a Monte Carlo simulation of a treatment head is the specifications of the accelerator parts, such as their locations, dimensions and materials. Without knowing the component specifications precisely, the simulation results may be of limited usefulness. So far, it seems difficult to get adequate information about a specific accelerator from the manufacturers (Udale-Smith 1992, Rogers *et al* 1995a). Because of the commercial value of the detailed specifications of the accelerator parts, manufacturers are usually reluctant to provide the information with the necessary details for Monte Carlo modelling. Furthermore, newly purchased accelerators are often adjusted on-site for individual users, for example by selection of scattering foils or tuning of the waveguide, to match the beam characteristics of the machine to be replaced, or the existing machines. The situation may be further complicated due to accelerator repair, improvement or update. Accelerators of the same model may not consist of exactly the same components. For example, the same type of accelerator may have different scattering foils, flattening filters, monitor chambers or applicators.

Another practical problem is that it is difficult for users to know the precise phase space information of electrons at the vacuum exit window, such as spot size and location, electron energy distribution and angular distribution. When performing Monte Carlo electron beam simulations it has been common practice to assume a pencil beam of monoenergetic electrons at the accelerator vacuum window. The initial energy of the pencil beam is determined by matching the calculated and measured values of some dosimetric quantities, say, R_{50} or R_p (Udale 1988, Udale-Smith 1990, 1992, Keall and Hoban 1994, Rogers *et al* 1995a, Kapur *et al* 1998, Ma *et al* 1999). It has been found that the final depth dose curve is not sensitive to the width of the incident energy spectrum, unless the spectrum was very broad (Rogers *et al* 1995a). This approach has been demonstrated to be practical and adequate for radiotherapy dose calculations. However, the introduction of these empirical procedures does call into question the accuracy of the simulation results, such as the characteristics of the actual beam phase space data, even though the final dose distribution agrees well with the measured data. For example, the calculated energy spectrum is not necessarily an accurate representation of the realistic spectrum. In addition, as pointed out by Rogers *et al* (1995a), there may be other, more subtle effects, for which this approach may fail. There is a paucity of experimental data on the fluence of clinical electron beams (Deasy *et al* 1996). Thus, there is still rationale for establishing a benchmark for treatment head simulation based on fluence and dose measurements using a research accelerator with well known source and treatment head details (Faddegon *et al* 1998).

It is clear that the required accuracy of accelerator simulation depends on the required accuracy of the end point quantities to be investigated. For Monte Carlo treatment planning, the accuracy of the electron phase space data is usually ensured in such a way that the Monte Carlo calculated dose distributions would be consistent with the measured data to within 2% of the maximum dose (Kapur *et al* 1998, Ma *et al* 1999). This criterion seems to be practical and adequate as the 1σ uncertainty on the dose distributions measured clinically is usually about 2% following the recommended dosimetry procedures (cf IAEA 1987, AAPM 1983, 1991). The 1σ uncertainty in the dose at a point in a phantom in a routine clinical measurement is more likely to be about 3% (Khan 1994). Experience has shown that agreement better than 1% could be achieved between Monte Carlo simulations and measurements by fine-tuning the parameters used in the accelerator simulations (Kapur *et al* 1998, Ma *et al* 1999). High-precision measurements could be predicted to within 0.3% by Monte Carlo simulations (Ma *et al* 1993b, Ma and Seuntjens 1997). Such agreement seems to be overkill for clinical accelerator simulations if the dosimetric uncertainty remains at 2–3% in the dose data used for machine commissioning. Faddegon *et al* (1998) estimated the various uncertainties in electron dose delivery and concluded that an overall accuracy of 5% in dose or 5 mm in the location of the isodose lines, or in shorthand 5%/5 mm, would be achievable if relative doses were calculated to 3%/3 mm (point-to-point variation of dose within a given dose distribution) and the dose in water relative to reference conditions was calculated to 2%/2 mm.

5.2. Simulation time

The major drawback of the Monte Carlo method is the computing time required to obtain an acceptable statistical uncertainty in the simulated quantities. Ma *et al* (1997a) reported that to achieve a 1% statistical uncertainty in the dose distribution in a water phantom consisting of 1 cm^3 cubic voxels, about 1×10^4 phase space electrons were needed for every 1 cm^2 area within the field. The number of particles per unit area would increase for smaller voxels to achieve the same statistical uncertainty. Rogers *et al* (1995a) showed that the ratio of the number of phase space electrons per cm^2 scored at the scoring plane for a $10 \times 10\text{ cm}^2$ field to the number of incident electrons at the vacuum exit window increased with incident electron energy. For a Varian Clinac 2100C accelerator, this ratio was about 0.0002 for a 6 MeV electron beam and 0.0008 for a 20 MeV electron beam. This means that one has to simulate up to 5×10^7 histories in the accelerator simulation in order to achieve the specified 1% statistical uncertainty in the dose calculation. More than 10^8 electron histories will be needed for a 6 MeV, $25 \times 25\text{ cm}^2$ electron field. This may require over 300 h of CPU time on a SGI R4400 200 MHz workstation (Rogers *et al* 1995a) or a few days of CPU time on a Pentium Pro 200 MHz PC (Kapur *et al* 1998). The total CPU time required to simulate five nominal electron energies and five applicators will be close to a month. Because of the iterative process of fine-tuning electron incident energy and other accelerator parameters, the overall CPU time for commissioning all the beams properly may be several months. Clearly, most cancer centres do not possess such computing resources or the necessary Monte Carlo expertise.

5.3. Beam characterization and source modelling

An important reason for simulating the treatment head is to obtain the electron beam phase space information needed for Monte Carlo treatment planning. The phase space data generated with the BEAM code contain almost all the phase space information needed (Rogers *et al* 1995a). However, there are some problems associated with the direct application of such phase space

data in Monte Carlo dose calculations (Ma and Rogers 1995b, c, Ma *et al* 1997a, Ma 1998, Jiang *et al* 1999). Since the beam characteristics are usually different, even for the same type of accelerator, it is necessary to simulate each individual accelerator to obtain the phase space data for Monte Carlo treatment planning. The generation and quality assurance of phase space information by simulating the treatment head is not an easy task, even with the BEAM code. It requires both Monte Carlo simulation experience and much more time than that required for commissioning a conventional electron treatment planning system. This places a practical limit on the clinical implementation of Monte Carlo treatment planning in an ordinary cancer clinic.

Another problem is the storage of the Monte Carlo simulated phase space data. It was found that the beam characteristics for different electron applicators may differ significantly due to the variation of the electrons collimated by the movable jaws and scattered from the applicator scrapers (Zhang *et al* 1998, Kapur *et al* 1998). This means that separate phase space files have to be obtained for each electron energy/applicator combination. In order to achieve a statistical uncertainty of 1–2% in a phantom consisting of $0.1\text{--}1\text{ cm}^3$ voxels, $10^6\text{--}10^7$ phase space particles are usually required in a Monte Carlo simulation, depending on the electron beam field size (Rogers *et al* 1995a, Zhang *et al* 1998, Kapur *et al* 1998, Ma *et al* 1999). For a clinical linear accelerator with five nominal energies and five applicator sizes, this means more than 10^8 phase space particles or a few gigabytes of computer disk space. More disk space is required if photon phase space data are also stored. This represents a significant burden for the limited computer resources at most clinical centres. Obviously a more concise description for the clinical electron beam with sufficient accuracy is necessary for performing routine Monte Carlo treatment planning.

A methodology has been proposed to replace the phase space file with a multiple source model with parameters derived from the simulated phase space data (Ma *et al* 1993a, 1994, 1997a, Ma and Rogers 1995b, Ma 1998, Jiang *et al* 1999). Based on the observations that particles from different components of an accelerator have different energy, angular and spatial distributions while the particles from the same component have very similar characteristics, it was considered that the particles from different parts of an accelerator come from different subsources. Each subsurface represented a critical component in the treatment head and its geometrical dimensions were determined by the component in question. Each subsurface had its own spectral and planar fluence distributions derived from the simulated phase-space data. By sampling the particle position on the subsurface and on the phantom surface, the correlation between the particle position and incident angle was naturally retained. A special program, BEAMDP, was written to help derive parameters for the source model from the simulated phase space data using BEAM (Ma and Rogers 1995a, c). This multiple source model has been evaluated against the full phase-space data for various accelerators and beam setups (Ma *et al* 1997a, Ma 1998). Figure 7 gives an example which demonstrates the correlation between electron incidence direction and position on the phantom surface as reconstructed using this multiple source model. Figure 8 illustrates that using the multiple source model can reduce the accelerator simulation time by a factor of 10 to achieve the same statistical uncertainty (i.e. requiring a factor of 10 fewer original phase-space particles).

A practical commissioning procedure for electron beam Monte Carlo treatment planning was proposed by Ma *et al* (1997c). The idea was to derive the basic source model parameters from the simulated phase space data and then to modify the source model parameters based on the measured beam data for clinical implementation. Ma (1998) demonstrated the feasibility of this approach using a multiple source model developed previously (Ma *et al* 1997a). By varying the bin boundaries of the energy spectra for each subsurface, the depth dose distributions calculated using the phase space reconstructed from the multiple source model for one nominal beam energy matched the depth dose distributions for another nominal energy. By varying the

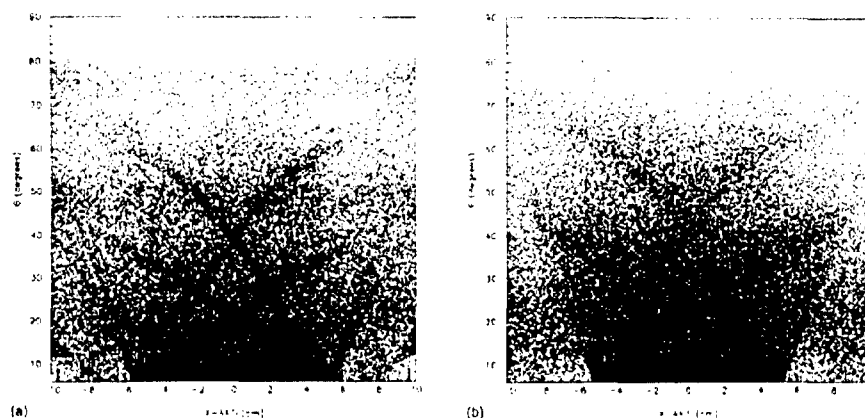


Figure 7. Scatter plot of θ (the angle between the incident direction and the beam central axis) versus x (distance from the central axis along the x -axis) showing correlation between direction of electron incidence and position for an 18 MeV electron beam, Varian 2100C, 10 cm \times 10 cm treatment field defined at 100 cm nominal SSD: (a) from the original phase-space data and (b) simulated by the multiple-source model. Each point (x, θ) in the graph corresponds to the incident angle and position of an electron. All the electrons within the 20 cm \times 20 cm scoring field are presented except for those with θ less than 5° (most of them are 'direct' electrons within the treatment field). The arcs are formed by the scattered electrons from the applicator scrapers (Ma *et al* 1997a).

bin boundaries of the planar fluence distribution for each subsource, the lateral dose profiles calculated using the phase space reconstructed from the multiple source model for one field size matched the dose profiles for another field size (Ma 1998).

Jiang *et al* (1999) further improved the methodology for electron beam modelling and commissioning (Ma *et al* 1997a, c, Ma 1998). They improved the source model representation and reconstruction algorithms and investigated the minimum number of subsources of dosimetric significance to obtain the required beam commissioning accuracy. This method was applied to electron beams from a Varian Clinac 2100C machine with a type III applicator. It was found that a four-source model was adequate for all the energy/applicator combinations. The source model consisted of an electron point source, a photon point source and two extended electron sources. The scoring plane was placed directly above the upper surface of the last scraper of the applicator, rather than the phantom surface. The last scraper or a cutout placed on the scraper was not handled by the source model but simulated separately in a further BEAM simulation or in the patient dose calculation. The model was benchmarked by comparing the dose distributions calculated with the source model and the full phase space data. Figure 9 shows an example for a 20 MeV beam with a 6 \times 6 cm² applicator and 120 cm SSD. The chosen Varian Clinac 2100C acted as the reference accelerator. The model established for the reference accelerator was used to commission electron beams from other machines of similar design such as a Varian Clinac 2300C/D by tuning a few parameters in the model. The calculated dose distributions agreed to within 1–2% with the measured data (Jiang *et al* 1999).

6. Conclusions

We have reviewed the work on the simulation of clinical electron beams from medical accelerators using the Monte Carlo method. It is well accepted that the only accurate

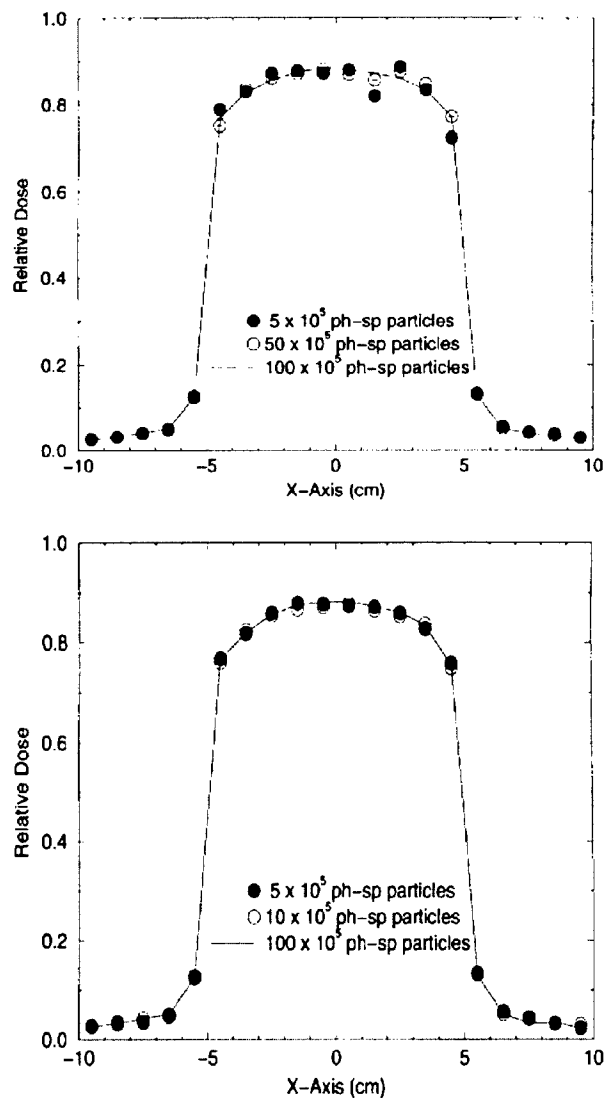


Figure 8. The surface dose profiles along the x -axis calculated using the original phase space data of varying size (a) and using the multiple-source model based on the corresponding phase-space data (b) for an 18 MeV electron beam from a Varian Clinic 2100C accelerator. The field is 10 cm \times 10 cm defined at 100 cm SSD. The voxel size in the phantom is 1 cm³ for the dose calculation. The number of phase space particles in each of the data sets is given in the figures. 10⁷ particles are reconstructed for the dose calculations in (b) while the phase space data are recycled (Ma *et al* 1997a).

and practical way to obtain detailed information on a clinical electron beam is the Monte Carlo simulation of the treatment head. Accurate Monte Carlo treatment planning cannot be performed without accurate beam phase space data. In addition, detailed information

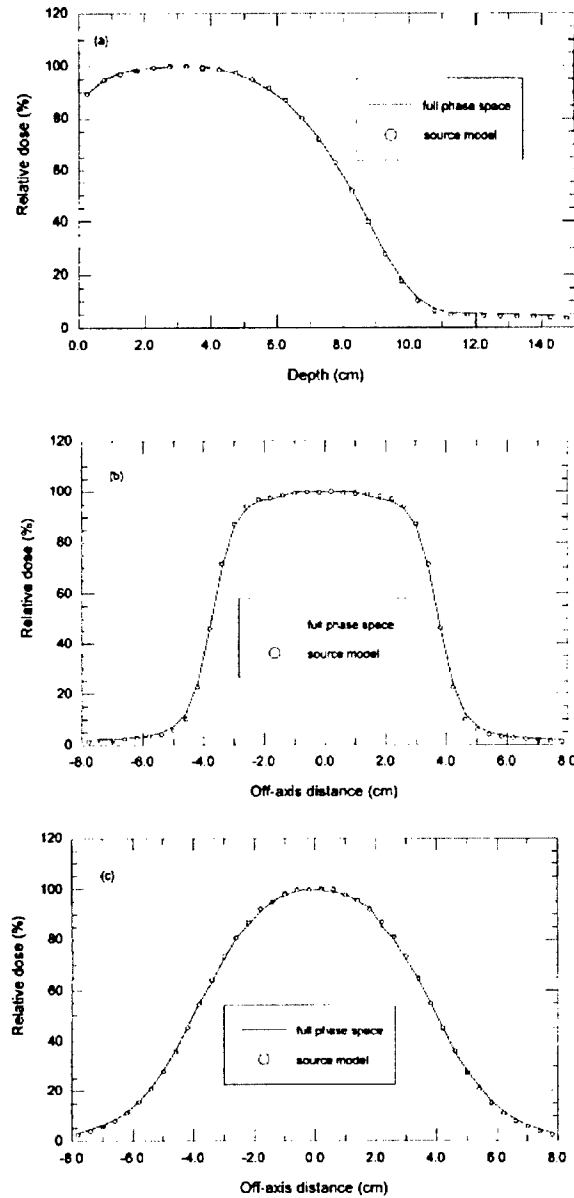


Figure 9. Dose distributions in water for a 20 MeV electron beam from a Varian 2100C machine with 6 cm \times 6 cm applicator at 120 cm SSD, calculated with full phase space data and a four-source model: (a) depth dose distributions, (b) dose profiles at 2 cm depth, (c) dose profiles at 7 cm depth. Each curve is normalized to its own maximum (Jiang *et al* 1999).

about radiotherapy beams has a wide variety of applications in clinical physics and radiation dosimetry. Monte Carlo simulation of medical accelerators can increase our understanding

of clinical beam characteristics, improve accelerator design and also improve the accuracy of clinical dosimetry by providing realistic beam data.

Optimistically, accurate accelerator simulation will result in accurate dose calculation and eventually in accurate dose delivery. Accurate dose calculation also plays a vital role in dose uniformity or conformity in intensity-modulated radiation therapy. It is exceedingly difficult to match the prescribed dose throughout the treatment volume in fields with heterogeneities due to the large dose discontinuities present in such fields. Treatment plans optimized on the basis of overly simplified dose calculation algorithms can become non-physical due to the uncertainties in the beam profiles. With accurate dose calculations, on the other hand, beam modifiers, mixed beams (electrons and photons) and optimization techniques may be used with confidence to improve the uniformity and conformity of the delivered dose distribution to the ideal prescription.

The following summarizes the current status of the work on electron accelerator simulation:

- (a) Although Monte Carlo simulation of electron medical accelerators has been performed by a number of investigators who focused on the effect of one or two components of dosimetric significance, more detailed beam characteristics and accurate particle phase space did not become available until the complete accelerator geometry could be simulated accurately.
- (b) Since the work of Udale and the development of the EGS4/BEAM system, our knowledge of clinical electron beams has been greatly improved. A large number of scientific findings and important results have been reported based on the EGS4/BEAM studies. However, these studies have only been for a few accelerators and a few beams. Systematic simulations of all the beams on various clinical accelerators need to be carried out.
- (c) The availability of electron beam phase space has led to the clinical implementation of the Monte Carlo technique for radiotherapy treatment planning dose calculations. The Monte Carlo simulated beam data have been used as input to the Monte Carlo code for accurate phantom and patient dose calculations. Accurate beam information has also resulted in more accurate dosimetric data.
- (d) The computing time required to simulate the beam data from a clinical accelerator is significant. This may not be a problem for a once-and-for-all study on some dosimetric data such as the conversion factors or correction factors for radiation dosimeters but will be a burden for a small cancer clinic after major changes in beam parameters due to machine upgrade, replacement of components or any other reasons. Faster computers and parallel processing methods can be used to speed up the simulation in large research centres. Variance reduction techniques are called for to further reduce the CPU time for accelerator simulation and patient dose calculation.
- (e) Accurate simulation of an electron beam from a clinical accelerator requires not only a specifically developed Monte Carlo code but also a great deal of Monte Carlo expertise. As the specifications of the accelerator components are often not known adequately and the machines are also tuned individually at the installation sites (leading to the variation in the incident electron energy), it can be a real challenge to match the Monte Carlo calculated dose distributions with the measured beam data, and dosimeter perturbation effects often need to be well understood to make this possible. Small inaccuracies in the simulation geometry can result in significant changes in the calculated dose distributions. If necessary, accurate energy, angle and fluence distributions should be used for the electrons incident on the vacuum exit window to achieve accurate end-point quantities (such as electron spectrum).
- (f) The phase space data can contain very detailed information about a clinical electron beam.

However, the simulation of the phase space of a clinical beam can be time-consuming and it also requires a large amount of disk space. Well-designed beam models can accurately represent the beam characteristics and reconstruct the beam phase space. By using beam models rather than the raw beam phase space data, one can save accelerator simulation time and reduce the disk storage requirement.

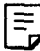
- (g) It is probably impossible to simulate the beam phase space for all the clinical electron beams at every cancer clinic because of the lack of computer resources and Monte Carlo expertise. However, it has been demonstrated that well-developed beam models can be used to reconstruct any clinical electron beam. A reference machine needs to be simulated accurately to derive the beam model parameters and these parameters can be further adjusted based on the measured beam data for any machines of the same type. Further studies on source modelling and beam commissioning are needed for widespread clinical application of the Monte Carlo dose calculation technique.


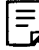

Acknowledgments

We are grateful to Alan Nahum, Pedro Andreo, Dave Rogers, Alex Bielajew, Rock Mackie, Bruce Faddegon, Iwan Kawrakow and Frank Verhaegen for their useful suggestions and detailed comments on the manuscript. We would like to thank Alan Nahum, Dave Rogers, Alex Bielajew, Pedro Andreo, Rock Mackie, Bruce Faddegon, Jan Seuntjens, Iwan Kawrakow and many other colleagues who have directly or indirectly taught us the Monte Carlo simulation technique over the years. We would also like to thank our colleagues at Stanford, Art Boyer, Gary Luxton, Ed Mok, David Findley, Sam Brain, Ajay Kapur, Todd Pawlicki, Jun Deng and Jinsheng Li for encouragement and valuable comments on the manuscript. We acknowledge the financial support of the RSN Research and Education Fund Seed Cycle 1, DOD BC971292 and NIH CA78331 during the writing of this review.

References

- AAPM 1983 A protocol for the determination of absorbed dose from high-energy photons and electrons *Med. Phys.* **10** 741
- 1991 Clinical electron beam dosimetry: report of AAPM Radiation Therapy Committee Task Group No. 25 *Med. Phys.* **18** 73–109
- al-Beteri A A and Raeside D E 1992 Optimal electron-beam treatment planning for retinoblastoma using a new three-dimensional Monte Carlo-based treatment planning system *Med. Phys.* **19** 125–35
- Andreo P 1980 Monte Carlo simulation and electron transport in water. Absorbed dose and fluence distributions *Report FANZ/80/3* (University of Zaragoza, Spain: Department of Nuclear Physics)
- 1991 Monte Carlo techniques in medical radiation physics *Phys. Med. Biol.* **36** 861–920
- Andreo P and Brahme A 1984 Restricted energy loss straggling and multiple scattering of electrons in mixed Monte Carlo procedures *Radiat. Res.* **100** 16–29
- Andreo P, Brahme A, Nahum A and Mattsson O 1989 Influence of energy and angular spread on stopping-power ratios for electron beams *Phys. Med. Biol.* **34** 751–68
- Andreo P and Fransson A 1989 Stopping-power ratios and their uncertainties for clinical electron beam dosimetry *Phys. Med. Biol.* **34** 1847–61
- Ayyangar K M and Jiang S B 1998 Do we need Monte Carlo treatment planning for Linac based stereotactic radiosurgery?—A case study *Med. Dosim.* **23** 161–7
- Balog J P, Mackie T R, Wenman D L, Glass M, Fang G and Pearson D 1999 Multileaf collimator interleaf transmission *Med. Phys.* **26** 176–86
- Berger M J and Seltzer S M 1978 The influence of scattering foils on absorbed dose distributions from electron beams *Report NBSIR 78-1552* (Gaithersburg: NBS)

- Bielajew A F 1994 Monte Carlo Modeling in external electron-beam radiotherapy—why leave it to chance? *Proc. 11th Int. Conf. on the Use of Computers in Radiation Therapy* ed A R Hounsell, J M Wilkinson and P C Williams (Manchester: North Western Medical Physics Department, Christie Hospital NHS Trust) pp 2–5
- Bielajew A F, Hirayama H, Nelson W R and Rogers D W O 1994 History, overview and recent improvements of EGS4 *Report PIRS-0436* (Ottawa: NRCC)
- Bielajew A F and Rogers D W O 1987 PRESTA: the parameter reduced electron-step transport algorithm for electron Monte Carlo transport *Nucl. Instrum. Methods B* **18** 165–81
- 1988 Variance-reduction techniques *Monte Carlo Transport of Electrons and Photons* ed T M Jenkins *et al* (New York: Plenum) pp 407–19
- 1992 A standard timing benchmark for EGS4 Monte Carlo calculations *Med. Phys.* **19** 303–4
- Bielajew A F and Weibe P E 1991 EGS-Windows—a graphics interface to EGS *Report PIRS-0274* (Ottawa: NRCC)
- Borrelli-Carbonell A, Patau J P, Terrissol M and Tronc D 1980 Comparison between experimental measurements and calculated transport simulations for electron dose distributions inside homogeneous phantoms *Strahlentherapie* **156** 186–91
- Briesmeister J F 1993 MCNP—a general Monte Carlo N-particle transport code, version 4A *Report LA-12625* (Los Alamos, NM: Los Alamos National Laboratory)
- Burlin T E, Sidwell J M and Wheatley B M 1973 Applications of Monte Carlo methods in medical radiology *Br. J. Radiol.* **46** 398–9
- Burns D, Duane S and McEwen M R 1995 A new method to determine ratios of electron stopping powers to an improved accuracy *Phys. Med. Biol.* **40** 733–9
- Chaney E L, Cullip T J and Gabriel T A 1994 A Monte Carlo study of accelerator head scatter *Med. Phys.* **21** 1383–90
- Deasy J O, Almond P R and McEllistrem M T 1996 Measured electron energy and angular distributions from clinical accelerators *Med. Phys.* **23** 675–84
- DeMarco J J, Solberg T D and Smathers J B 1998 A CT-based Monte Carlo simulation tool for dosimetry planning and analysis *Med. Phys.* **25** 1–11
- Desobry G E and Boyer A L 1994 An analytic calculation of the energy fluence spectrum of a linear accelerator *Med. Phys.* **21** 1943–52
- Ding G X and Rogers D W O 1995 Energy spectra, angular spread, and dose distributions of electron beams from various accelerators used in radiotherapy *Report PIRS-0439* (Ottawa: NRCC)
- Ding G X, Rogers D W O and Mackie T R 1994 Calculation of backscatter into beam monitor chamber for electron beams (abstract) *Med. Phys.* **21** 923–4
- 1995 Calculation of stopping power ratios using realistic clinical electron beams *Med. Phys.* **22** 489–501
- 1996 Mean energy, energy–range relationship and depth-scaling factors for clinical electron beams *Med. Phys.* **23** 361–76
- 1997 Electron fluence correction factors used in conversion of dose measured in plastic to dose in water *Med. Phys.* **24** 161–76
- Ebert M A and Hoban P W 1995a A model for electron-beam applicator scatter *Med. Phys.* **22** 1419–29
- 1995b A Monte Carlo investigation of electron-beam applicator scatter *Med. Phys.* **22** 1431–5
- Ebert M A, Hoban P W and Keall P J 1996 Modeling clinical accelerator beams: a review *Australas. Phys. Eng. Sci. Med.* **19** 131–50
- Eyges L 1948 Multiple scattering with energy loss *Phys. Rev.* **74** 1534–5
- Faddegon B A 1995 Spectrometry for advanced treatment planning in electron therapy (abstract) *Med. Phys.* **22** 666
- Faddegon B, Balogh J, Mackenzie R and Scora D 1998 Clinical considerations of Monte Carlo for electron radiotherapy treatment planning *Radiat. Phys. Chem.* **53** 217–27
- Faddegon B A, O'Brien P and Mason D L D 1999 The flatness of Siemens linear accelerator x-ray field *Med. Phys.* **26** 220–8
-  Fermi E 1941 Cosmic-ray theory *Rev. Mod. Phys.* **13** 265–8
- Ford R L and Nelson W R 1978 The EGS code system: computer programs for the Monte Carlo simulation of electromagnetic cascade showers (version 3) *Report SLAC-210* (Stanford, CA: SLAC)
- Halbeib J A and Mehlhorn T A 1984 ITS: the Integrated Tiger Series of coupled electron photon Monte Carlo transport codes *Report SAND84-0573* (Albuquerque, NM: Sandia National Laboratories)
- Han K, Ballon D, Chui C S and Mohan R 1987 Monte Carlo simulation of a cobalt-60 beam *Med. Phys.* **14** 414–19
- Hartmann-Siantar C L *et al* 1997 Lawrence Livermore National Laboratory's PEREGRINE project *Proc. 12th Int. Conf. on the Use of Computers in Radiation Therapy* ed D D Leavitt and G Starkschall (Madison: Medical Physics Publishing) pp 19–22
- Hendricks J S and Briesmeister J F 1992 Recent MCNP developments *Report LA-UR-91-3456* (Los Alamos, NM: Los Alamos National Laboratory)
- Hogstrom K R, Mills M D and Almond P R 1981 Electron beam dose calculations *Phys. Med. Biol.* **26** 445–59

- Holmes M A, Mackie T R, Sohn W, Reckwerdt P J, Kinsella T J, Bielajew A F and Rogers D W O 1993 The application of correlated sampling to the computation of electron beam dose distributions in heterogeneous phantoms using the Monte Carlo method *Phys. Med. Biol.* **38** 675–88
- IAEA 1987 An International Code of Practice *IAEA Technical Report Series 277* (Vienna: IAEA)
- Jenkins T M, Nelson W R, Rindi A, Nahum A E and Rogers D W O 1988 *Monte Carlo Transport of Electrons and Photons* (New York: Plenum)
- Jiang S B and Ayyangar K M 1998 On compensator design for photon beam intensity modulated radiation therapy *Med. Phys.* **25** 668–75
-  Jiang S B, Kapur A and Ma C-M 1999 Electron beam modeling and commissioning for Monte Carlo treatment planning *Med. Phys.* (accepted)
- Jiang S B, Luo Z M and Ayyangar K M 1998 Incorporation of the electron energy-loss straggling into the Fermi–Eyges equation *Radiat. Phys. Chem.* **53** 477–82
- Kapur A and Ma C-M 1999 Stopping power ratios for clinical electron beams from a scatter-foil linear accelerator *Phys. Med. Biol.* **44** 2321–41
- Kapur A, Ma C M, Mok E C and Findley D O 1997 Characterization of small field electron beams for radiotherapy using Monte Carlo simulations *Proc. 12th Int. Conf. on the Use of Computers in Radiation Therapy* ed D D Leavitt and G Starkschall (Madison: Medical Physics Publishing) pp 157–8
- Kapur A, Ma C M, Mok E C, Findley D O and Boyer A L 1998 Monte Carlo calculations of electron beam output factors for a medical linear accelerator *Phys. Med. Biol.* **43** 3479–94
-  Karlsson M G, Karlsson M K and Ma C-M 1999 Treatment head design for multileaf collimated high-energy electrons *Med. Phys.* (accepted)
- Kassaei A, Altschuler M D, Ayyalsomayajula S and Bloch P 1994 Influence of cone design on the electron beam characteristics on clinical accelerators *Med. Phys.* **21** 1671–6
- Kawrakow I, Fippel M and Friedrich K 1996 3D electron dose calculation using a voxel based Monte Carlo algorithm (VMC) *Med. Phys.* **23** 445–57
- Keall P J and Hoban P W 1994 The angular and energy distribution of the primary electron beam *Australas. Phys. Eng. Sci. Med.* **17** 116–23
- 1996 Calculating the angular standard deviation of electron beams using Fermi–Eyges theory *Phys. Med. Biol.* **41** 1511–15
- Khan F M 1994 *The Physics of Radiation Therapy* (Baltimore, MD: Williams and Wilkins)
- Lee P C 1997 Monte Carlo simulations of the differential beam hardening effect of a flattening filter on a therapeutic x-ray beam *Med. Phys.* **24** 1485–9
- Lewis R D, Ryde S J S, Hancock D A and Evans C J 1999 An MCNP-based model of a linear accelerator x-ray beam *Phys. Med. Biol.* **44** 1219–30
- Liu H H, Mackie T R and McCullough E C 1997 A dual source photon beam model used in convolution/superposition dose calculations for clinical megavoltage x-ray beams *Med. Phys.* **24** 1960–74
- Liu S, Andreo P, Satherberg A, Gudowska I and Brahme A 1995 Monte-Carlo simulation of therapy accelerators: application to a MM50 Racetrack microtron (abstract) *Radiother. Oncol.* **37** (suppl 1) 119
- Lovelock D M J, Chui C S, Kutcher J and Mohan R 1994 Analysis of the photon beam treatment planning data for a scanning beam machine *Med. Phys.* **21** 1969–77
- Lovelock D M J, Chui C S and Mohan R 1995 A Monte Carlo model of photon beams used in radiation therapy *Med. Phys.* **22** 1387–94
- Ma C-M 1992 Monte Carlo simulation of dosimeter response using transputers *PhD Thesis* University of London (Report ICR-PHY-1/92 (Sutton, UK: ICR))
- 1998 Characterization of computer simulated radiotherapy beams for Monte Carlo treatment planning *Radiat. Phys. Chem.* **53** 329–44
- Ma C-M, Faddegon B A, Rogers D W O and Mackie T R 1997a Accurate characterization of Monte Carlo calculated electron beams for radiotherapy *Med. Phys.* **24** 401–16
- Ma C-M, Kapur A, Mok E and Findley D 1997c Monte Carlo treatment planning: procedures for commissioning computer simulated clinical beams (abstract) *J. Int. Fed. Med. Biol. Eng.* **35** 995
- Ma C-M, Mok E C, Kapur A and Findley D O 1997b Improvement of small-field electron beam dosimetry using Monte Carlo simulation *Proc. 12th Int. Conf. on the Use of Computers in Radiation Therapy* ed D D Leavitt and G Starkschall (Madison: Medical Physics Publishing) pp 159–62
-  Ma C-M, Mok E, Kapur A, Pawlicki T, Findley D O, Brain S, Forster K and Boyer A L 1999 Clinical implementation of a Monte Carlo treatment planning system *Med. Phys.* (accepted)
- Ma C-M and Nahum A E 1993 Calculation of absorbed dose ratios using correlated Monte Carlo sampling *Med. Phys.* **20** 1189–99
- Ma C-M, Reckwerdt P, Holmes M, Rogers D W O Geiser and Walters B 1995 DOSXYZ users manual *Report*

PIRS-0509(b) (Ottawa: NRCC)

Ma C-M and Rogers D W O 1995a BEAMDP users manual *Report* PIRS-0509(C) (Ottawa: NRCC)

— 1995b Beam characterization: a multiple source model *Report* PIRS-0509(D) (Ottawa: NRCC)

— 1995c BEAMDP—as a general-purpose utility *Report* PIRS-0509(E) (Ottawa: NRCC)

Ma C-M, Rogers D W O, Ding G X and Mackie T R 1994 Electron beam characterization: reconstruction models and dose distributions in a homogeneous phantom (abstract) *Med. Phys.* **21** 895

Ma C-M, Rogers D W O, Faddegon B A, Ding G X, Wei J S, Bielajew A F and Mackie T R 1993a Simplified models of electron beams from a 2100C accelerator (abstract) *Med. Phys.* **20** 1295

Ma C-M, Rogers D W O, Shortt K, Ross K, Nahum A E and Bielajew A F 1993b Wall correction and absorbed dose conversion factors for Fricke dosimetry: Monte Carlo calculations and measurements *Med. Phys.* **20** 283–93

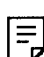
Ma C-M and Seuntjens J P 1997 Correction factors for waterproofing sleeves in kilovoltage x-ray beams *Med. Phys.* **24** 1507–13

Mackie T R 1990 Applications of the Monte Carlo method in radiotherapy *Dosimetry of Ionizing Radiation* vol 3, ed K Kase, B Bjarnagard and F H Attix (San Diego, CA: Academic) pp 541–620

Mackie T R, Holmes T W, Reckwerdt P J and Yang J 1995 Tomotherapy: optimized planning and delivery of radiation therapy *Int. J. Imaging Syst. Technol.* **6** 43–55

Mackie T R, Holmes T W, Swerdloff S, Reckwerdt P J, Deasy J, Yang J, Paliwal B and Kinsella T 1993 Tomotherapy: a new concept for the delivery of conformal therapy *Med. Phys.* **20** 1709–19

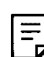
Mackie T R, Kubstad S S, Rogers D W O and Bielajew A F 1990 The OMEGA project: electron dose planning using Monte Carlo simulation (abstract) *Med. Phys.* **17** 730

 Mackie T R *et al* 1994 The OMEGA project: comparison among EGS4 electron beam simulations, 3D Fermi–Eyges calculations, and dose measurements *Proc. Xth ICCR (Manchester, UK)* pp 152–3

Mackie T R, Scrimger J W and Battista J J 1985 A convolution method of calculating dose for 15-MV x-rays *Med. Phys.* **12** 188–96

Manfredotti C, Nastasi U, Marchisio R, Ongaro C, Gervino G, Ragona R, Anglesio S and Sannazzari G 1990 Monte Carlo simulation of dose distribution in electron beam radiotherapy treatment planning *Nucl. Instrum. Methods A* **291** 646–54

Manfredotti C, Nastasi U, Ragona R and Anglesio S 1987 Comparison of three dimensional Monte Carlo simulation and the pencil beam algorithm for an electron beam from a linear accelerator *Nucl. Instrum. Methods A* **255** 355

 Mazurier J, Salvat F, Chauvenet B and Barthe J 1999 Simulation of photon beams from a Saturne 43 accelerator using the code PENELOPE *Phys. Med.* (accepted)

McCall R C, McIntyre R D and Turnbull W G 1978 Improvement of linear accelerator depth-dose curves *Med. Phys.* **5** 18–24

Mohan R 1988 Monte Carlo simulation of radiation treatment machine heads *Monte Carlo Transport of Electrons and Photons* ed T M Jenkins *et al* (New York: Plenum) pp 453–68

— 1997a Why Monte Carlo? *Proc. 12th Int. Conf. on the Use of Computers in Radiation Therapy* ed D D Leavitt and G Starkschall (Madison: Medical Physics Publishing) pp 16–18

— 1997b Monte Carlo dose calculations for radiation treatment planning (abstract) *Med. Phys.* **24** 987

Mohan R, Chui C S and Lidofsky L 1985 Energy and angular distributions of photons from medical linear accelerators *Med. Phys.* **12** 592–7

Mok E, Ma C-M, Kapur A, Findley D and Boyer A L 1997 Predicting air gap factors for electron fields at extended treatment distances (abstract) *J. Int. Fed. Med. Biol. Eng.* **35** 1026

Murray D 1990 Using EGS4 Monte Carlo in medical radiation physics *Australas. Phys. Eng. Sci. Med.* **13** 132–47

Nahum A E 1985 Monte Carlo electron transport simulation II: Application to dose planning *The Computation of Dose Distributions in Electron Beam Radiotherapy* ed A E Nahum (Umeå, Sweden: Umeå University) p 319

— 1988 Overview of photon and electron Monte Carlo *Monte Carlo Transport of Electrons and Photons* ed T M Jenkins *et al* (New York: Plenum) pp 3–20

Nelson W R, Hirayama H and Rogers D W O 1985 The EGS4 code system *Report* SLAC-265 (Stanford, CA: SLAC)

Nelson W R and Jenkins T M 1980 *Computer Techniques in Radiation Transport and Dosimetry* (New York: Plenum)

Neuenschwander H, Mackie T R and Reckwerdt P J 1995 MMC—a high-performance Monte Carlo code for electron beam treatment planning *Phys. Med. Biol.* **40** 543–74

Nilsson B and Brahme A 1981 Contamination of high-energy photon beams by scattered photons *Strahlentherapie* **157** 181–6

Patau J P, Vernes C E, Terrisot M and Malbert M 1978 Calcul des caracteristiques qualitatives (TEL, FQ, equivalent dose) d'un faisceau de photons de freinage a usage medical, par simulation de sa creation et de son transport *Proc. 6th Symp. Microdosimetry (1978), Brussels, Belgium (EUR 6064)* ed J Booz and H G Ebert (London: Harwood Academic) pp 579–88

Pawlicki T 1998 Application of a new mixed-simulation Monte Carlo code system to electron beam radiotherapy

- treatment planning with computed tomography data *PhD Thesis* Medical College of Ohio
- Petti P L, Goodman M S, Gabriel T A and Mohan R 1983a Investigation of buildup dose from electron contamination of clinical photon beams *Med. Phys.* **10** 18–24
- Petti P L, Goodman M S, Sisterson J M, Biggs P J, Gabriel T A and Mohan R 1983b Sources of electron contamination for the Clinac-35 25-MV photon beam *Med. Phys.* **10** 856–61
- Raeside D E 1976 Monte Carlo principles and applications *Phys. Med. Biol.* **21** 181–97
- Rogers D W O 1991 The role of Monte Carlo simulation of electron transport in radiation dosimetry *Int. J. Appl. Radiat. Isot.* **42** 965–74
- Rogers D W O and Bielajew A F 1984 The use of EGS for Monte Carlo calculations in medical physics *Report PXR-2692* (Ottawa: NRCC)
- 1986 Differences in electron depth-dose curves calculated with EGS and ETRAN and improved energy-range relationships *Med. Phys.* **13** 687–94
- 1990 Monte Carlo techniques of electron and photon transport for radiation dosimetry *The Dosimetry of Ionizing Radiation* vol 3, ed K Kase, B Bjärngard and F Attix (San Diego, CA: Academic) pp 427–539
- Rogers D W O, Bielajew A F, Mackie T R and Kubsad S S 1990 The OMEGA project: treatment planning for electron-beam radiotherapy using Monte Carlo techniques (abstract) *Phys. Med. Biol.* **35** 285
- Rogers D W O, Ewart G M, Bielajew A F and van Dyk G 1988 Calculation of electron contamination in a Co-60 therapy beam *Proc. IAEA Int. Symp. on Dosimetry in Radiotherapy* vol 1 (Vienna: IAEA) pp 303–12
- Rogers D W O, Faddegon B A, Ding G X, Ma C-M, We J and Mackie T R 1995a BEAM: a Monte Carlo code to simulate radiotherapy treatment units *Med. Phys.* **22** 503–24
- Rogers D W O, Ma C-M, Ding G X and Walters B 1995b BEAM users manual *Report PIRS-0509(A)* (Ottawa: NRCC)
- Rustgi S N, Rustgi A K, Jiang S B and Ayyangar K M 1998 Dose perturbation caused by high density inhomogeneities in small beams in stereotactic radiosurgery *Phys. Med. Biol.* **43** 3509–18
- Salvat F, Fernandez-Vera J M, Baro J and Sempau J 1996 *PENELOPE, an Algorithm and Computer Code for Monte Carlo Simulation of Electron-Photon Showers* (Spain: Informes Tecnicos Ciemat)
- Sheikh-Bagheri D 1998 Monte Carlo study of photon beams from medical linear accelerators: optimization, benchmark and spectra *PhD Thesis* Carleton University, Canada
- Shortt K R, Ross C K, Bielajew A F and Rogers D W O 1986 Electron beam dose distributions near standard inhomogeneities *Phys. Med. Biol.* **31** 235–49
- Sixel K E and Faddegon B A 1995 Calculation of x-ray spectra for radiosurgical beams *Med. Phys.* **22** 1657–61
- Solberg T D, DeMarco J J, Holly F E, Smathers J B and DeSalles A F 1998 Monte Carlo treatment planning for stereotactic radiosurgery *Radiother. Oncol.* **49** 73–84
- Treurniet J R and Rogers D W O 1998 BEAM and DOSXYZ GUI user's manual *Report PIRS-0623* (Ottawa: NRCC)
- Turner J E, Wright H A and Hamm R N 1985 Review article: a Monte Carlo primer for health physicists *Health Phys.* **48** 717–33
- Udale M 1988 A Monte Carlo investigation of surface doses for broad electron beams *Phys. Med. Biol.* **33** 939–54
- Udale-Smith M 1990 A Monte Carlo investigation of high energy electron beams used in radiotherapy *PhD Thesis* Leeds University
- 1992 Monte Carlo calculations of electron beam parameters for three Philips linear accelerators *Phys. Med. Biol.* **37** 85–105
- van der Zee W 1996 Photon beam radiotherapy planning using Monte Carlo systems *MSc Thesis* Utrecht University
- Verhaegen F, Nahum A E, Van de Putte S and Namito Y 1999 Monte Carlo modelling of radiotherapy KV x-ray units *Phys. Med. Biol.* **44** 1767–89
- Wallace S and Allen B J 1998 CT based 3D Monte Carlo radiation therapy treatment planning *Aust. Phys. Eng. Sci. Med.* **21** 41–50
- Wang L, Chui C S and Lovelock M 1998 A patient-specific Monte Carlo dose-calculation method for photon beams *Med. Phys.* **25** 867–78
- Zhang G G, Rogers D W O, Cygler J E and Mackie T R 1998 Effects of changes in stopping-power ratios with field size on electron beam relative output factors *Med. Phys.* **25** 1711–16
- 1999 Monte Carlo investigation of electron output factors versus size of square cutout *Med. Phys.* **26** 743–50

Modeling The Extrafocal Radiation and Monitor Chamber Backscatter for Photon Beam Dose Calculation

Steve B. Jiang*, Arthur L. Boyer and C.-M. Charlie Ma

Department of Radiation Oncology,
Stanford University School of Medicine,
300 Pasteur Drive, Stanford, CA 94305-5304

September 13, 1999

*Corresponding author. Tel: (650)498-4074, Fax: (419)498-4015, E-mail: stevej@reyes.stanford.edu

1

Keywords: Photon beam Extrafocal radiation
Monitor chamber backscatter Dose calculation
In-air output factor

1 INTRODUCTION

Photon beam dose calculations usually consist of the calculation of absolute dose for a specific monitor unit setting and the calculation of relative dose distribution. The relative in-air output factor (collimator scatter factor), S_c , is one of the basic quantities required to calculate monitor unit settings. Traditionally, S_c has been determined indirectly from empirical data and tabulated as a function of the square field sizes at the isocenter. The S_c values for rectangular fields are then estimated using the concept of the equivalent square. The collimator exchange effect is often ignored and may introduce errors in the S_c calculation that are as great as 3% [1, 2, 3, 4]. To reduce this error, extensive measurements need to be carried out for rectangular and irregularly shaped fields.

In order to deliver intensity-modulated radiation therapy (IMRT), intensity patterns are usually generated by sweeping a window formed by the multileaf collimator (MLC) leaves across the field, either dynamically or as a step-and-shoot sequence [5]. An IMRT field can be considered to be a stack of many static fields with irregular shapes, each defined by an MLC. Using a conventional method such as the equivalent square, it is difficult to predict correctly the beam output of each of the windows that form IMRT fields. Since a significant fraction of the dose is accumulated in penumbra regions placed inside an IMRT field, it is necessary to account for the penumbra dose accurately to obtain accurate relative dose distributions.

The radiation backscattered from the collimator jaws to the monitor chamber produces an extraneous signal in the monitor chamber, resulting in a decrease in the delivered dose for a given total monitor unit setting. This effect increases as the field size decreases since the irradiated area on the target side of the jaws is larger for smaller fields. The magnitude of the monitor backscatter (MBS) depends on the design of the monitor chambers, such as the thickness and material of the

exit window, and the distance from the chamber to the jaws. For some accelerators, such as the Varian Clinac 2100C with a kapton monitor chamber, the MBS effect contributes significantly to the variation of the beam output as a function of jaw setting. Therefore, it is necessary to model the MBS for accurate output calculations.

In addition to the MBS, it has been found that the change in S_c with field size is dependent on the scattered radiation that can reach the measurement point as the positions of the collimators are varied [6]. The scattered radiation is also a major contribution to the penumbra dose in the field, resulting in different penumbra dose for different field sizes and for different (X or Y) field edge-defining jaws. The sources of scattered radiation are components inside the accelerator treatment head. It has been demonstrated that the flattening filter and the primary collimator are the major sources for scattered photons [6, 7]. Other components, such as the photon jaws, contribute a negligible amount to the scattered radiation [8]. The scattered radiation can be modeled as a planar source located at the level of the bottom of the flattening filter, which is usually called the extrafocal source, in contrast to the the focal spot (or point source at the target) for primary photons which come from the target directly to the measurement point.

In the past decade, many efforts have been made to model the extrafocal radiation (EFR). The EFR can be calculated analytically [9] or by a Monte Carlo simulation of the linac treatment head [7]. It can also be measured using a tertiary collimator with increasingly larger apertures [10, 11]. Another approach to model the EFR, which may be more useful in clinical practice, is to represent the radial distribution of the extrafocal source using an analytical function and then determine the parameters in the function by fitting the measured S_c values [12, 13, 14, 15, 16, 17, 18].

The MBS was usually measured using specially designed experimental approaches. Patterson and Shragge [19] measured the MBS for a 18 MV photon beam from a Therac 20 accelerator utilizing the photoactivation of copper. Luxton and Astrahan

[20] assessed the MBS by covering the downstream portion of the monitor chamber with an acrylic plate for a CGR Saturne 25 machine. Kubo [21] designed a simple and elegant telescopic method to measure the MBS for an 18 MV beam from a Therac 20 and 6 and 18 MV beams from a Varian Clinac 1800. This method was used later by many other investigators to study MBS effect, such as Duzenli *et al* [22], Waldron [14], Yu *et al* [23], and Lam *et al* [16]. The MBS can also be measured accurately by counting the target current pulses [11, 23, 24] or measuring the charge deposited in the target [25]. It is also possible to calculate the MBS analytically [26] or through the Monte Carlo simulation of the treatment head [24].

In the present paper, we develop a simple analytic method for modeling both the EFR and MBS for accurate photon beam (especially IMRT) dose calculations. In order to be practical clinically, the method does not rely on any special experimental or sophisticated numerical techniques. The EFR and MBS are represented analytically and determined simultaneously using only conventional measured data, *i.e.*, measured S_c values at the isocenter for jaw-defined fields. The model has been verified extensively using the measured S_c values for various jaw and MLC settings and at various source-detector distances (SDD) and off-axis distances.

2 MATERIALS and METHODS

2.1 General theory

2.1.1 In-air output factor

In the present work, we use the measured linac in-air output factor S_c to determine the EFR and MBS. The S_c factor is usually defined as the ratio of the linac in-air output at the isocenter per monitor unit for a certain field size (fs) to that for a reference field size (fs_{ref}). The field size dependence of the in-air output factor,

$S_c(fs)$, is caused by the change of the contributions due to EFR and MBS with the field size. Following Lam *et al* [16], we define the term *head scatter factor*, S_h , in a strict sense to represent the part of S_c contributed from the EFR. The effect of the MBS on S_c is considered as the MBS factor, S_b . Then, we have

$$S_c(fs) = S_h(fs) \cdot S_b(fs) \quad (1)$$

where

$$S_h(fs) = [1 + F_{efs}(fs)]/[1 + F_{efs}(fs_{ref})] \quad (2)$$

$$S_b(fs) = [1 - F_{mbs}(fs)]/[1 - F_{mbs}(fs_{ref})] \quad (3)$$

F_{efs} is the contribution to the beam output from the EFR normalized to the contribution from the primary point source. F_{mbs} is the decrease in the beam output caused by the MBS, normalized to beam output without the presence of MBS. In the rest of this section, we will discuss our model for EFR and MBS, and how to use the model to calculate F_{efs} and F_{mbs} .

2.1.2 Monitor chamber backscatter

The model for the MBS is much simpler than that for EFR, so we will discuss it first. As shown by many other investigators, it is a good approximation to assume that the backscattered radiation to the monitor chamber has a linear relationship with the irradiated area on the jaw's upper surface. Therefore, under the first-order approximation [16], F_{mbs} for a rectangular field ($X_1 : X_2 \times Y_1 : Y_2$, where X_1 and X_2 are the positions of X jaws and Y_1 and Y_2 are positions of Y jaws) can be modeled as

$$F_{mbs}(fs) = \alpha[1 - (Y_1 + Y_2)/fs_{max}] + \beta[1 - (X_1 + X_2)/fs_{max}] \cdot (Y_1 + Y_2)/fs_{max} \quad (4)$$

where $f_{s_{max}}$ is the maximum jaw opening (40 cm for a Varian accelerator) and is assumed to have zero backscatter to the monitor chamber. α and β give the relative importance of the upper and lower jaws, respectively.

2.1.3 Extrafocal source

The primary photons can be modeled as a point source located at the position of the target. The extrafocal radiation is assumed to originate from a planar source with an intensity distribution peaked at the central axis and monotonically decreasing with off-axis distance. The extrafocal source distribution can then be approximated by a series of Gaussian functions

$$f(x, y) = \sum_{i=1}^N \frac{A_i}{2\pi\sigma_i^2} e^{-(x^2+y^2)/2\sigma_i^2} \quad (5)$$

where A_i and σ_i are the amplitude and standard deviation for the i -th Gaussian, respectively. N is determined as the minimum number of Gaussian functions necessary to approximate the extrafocal source intensity distribution. This number can be different for different machines and different beam energies. A_i gives the relative weight and σ_i characterizes the width of the i -th Gaussian. The sum of $A_i, i = 1, \dots, N$, is the total intensity of the extrafocal source relative to the primary point source.

The field size dependence of F_{efs} is caused by the fact that the extent of the extrafocal source visible from the measurement point is different for different collimator settings. It is reasonable to assume that the extrafocal source plane emits photons isotropically over the angle subtended by the primary collimator, since the Klein-Nishina cross section varies slowly over the interval of interest. The distance from a different position on the source plane to the measurement point is different, but the inverse-square-law correction for this effect is very small and can be ignored. Under these approximations, F_{efs} can be calculated by integrating the source intensity distribution over the area of the extrafocal plane visible from the measurement

point (it is referred to as *visible area* henceforth).

A visible area with irregular shape can be approximated with a sum of rectangles. The relative contribution to beam output from a rectangular visible area ($x \in [x_{e1}, x_{e2}]$ and $y \in [y_{e1}, y_{e2}]$) can be given as

$$\begin{aligned} F_{efs}(x_{e1}, x_{e2}, y_{e1}, y_{e2}) &= \int_{x_{e1}}^{x_{e2}} dx \int_{y_{e1}}^{y_{e2}} dy f(x, y) \\ &= \sum_{i=1}^N \frac{A_i}{4} \left[\operatorname{erf} \left(\frac{x_{e1}}{\sqrt{2}\sigma_i} \right) - \operatorname{erf} \left(\frac{x_{e2}}{\sqrt{2}\sigma_i} \right) \right] \cdot \left[\operatorname{erf} \left(\frac{y_{e1}}{\sqrt{2}\sigma_i} \right) - \operatorname{erf} \left(\frac{y_{e2}}{\sqrt{2}\sigma_i} \right) \right] \quad (6) \end{aligned}$$

where erf is the error function which can be pre-calculated and stored in a look-up table.

2.1.4 Visible area

A. General case

To use Eq. (6), we need first to determine the visible area. A visible area may be defined by the jaws, MLC, or block. Usually we need to calculate the projections of the edges of the jaws, MLC leaves, or blocks, if they are present, on the extrafocal plane and determine which define the boundary of the visible area.

In a general notation, we assume that the extrafocal plane is perpendicular to the central axis and is located at a distance SED from the target. Similarly the collimation plane is located at a distance SCD ($SCD > SED$) from the target and is perpendicular to the central axis. The point of measurement is at (x_d, y_d) and SDD away from the target along the central axis. From the view of the measurement point, a point (x_c, y_c) on the collimation plane has a projection on the extrafocal plane

$$x_e = x_d + \frac{SDD - SED}{SDD - SCD}(x_c - x_d) \quad (7)$$

$$y_e = y_d + \frac{SDD - SED}{SDD - SCD}(y_c - y_d) \quad (8)$$

B. Photon jaws

If the visible area is defined by the movable jaws, and if the detector is inside the field, the visible area is limited by the upper edges of the jaws. Assume the distance from the target to the upper edges is SCD_x for the lower (X) jaws and SCD_y for the upper (Y) jaws. A rectangular field ($X_1 : X_2 \times Y_1 : Y_2$), defined by the jaws at the SAD , corresponds to a rectangular visible area on the extrafocal plane in the view of the measurement point, that is

$$x \in [x_{e1}, x_{e2}] \quad (9)$$

$$y \in [y_{e1}, y_{e2}] \quad (10)$$

$$x_{e1} = x_d - \frac{SDD - SED}{SDD - SCD_x} \left(\frac{SCD_x}{SAD} X_1 + x_d \right) \quad (11)$$

$$x_{e2} = x_d + \frac{SDD - SED}{SDD - SCD_x} \left(\frac{SCD_x}{SAD} X_2 - x_d \right) \quad (12)$$

$$y_{e1} = y_d - \frac{SDD - SED}{SDD - SCD_y} \left(\frac{SCD_y}{SAD} Y_1 + y_d \right) \quad (13)$$

$$y_{e2} = y_d + \frac{SDD - SED}{SDD - SCD_y} \left(\frac{SCD_y}{SAD} Y_2 - y_d \right) \quad (14)$$

Then F_{efs} for this field size can be calculated using Eq. (6).

If the detector is placed at the central axis, Eq. (6) can be simplified for jaw-defined rectangular fields as

$$\begin{aligned} F_{efs}(X_1 : X_2 \times Y_1 : Y_2) \\ = \sum_{i=1}^N \frac{A_i}{4} \left[\operatorname{erf} \left(\frac{k_x X_1}{\sqrt{2}\sigma_i} \right) + \operatorname{erf} \left(\frac{k_x X_2}{\sqrt{2}\sigma_i} \right) \right] \cdot \left[\operatorname{erf} \left(\frac{k_y Y_1}{\sqrt{2}\sigma_i} \right) + \operatorname{erf} \left(\frac{k_y Y_2}{\sqrt{2}\sigma_i} \right) \right] \end{aligned} \quad (15)$$

where

$$k_x = \frac{SDD - SED}{SDD - SCD_x} \cdot \frac{SCD_x}{SAD} \quad (16)$$

$$k_y = \frac{SDD - SED}{SDD - SCD_y} \cdot \frac{SCD_y}{SAD} \quad (17)$$

For a symmetric rectangular field ($a \times b$), Eq. (15) can be further simplified as

$$F_{efs}(a \times b) = \sum_{i=1}^N A_i \cdot \operatorname{erf} \left(\frac{k_x a/2}{\sqrt{2}\sigma_i} \right) \cdot \operatorname{erf} \left(\frac{k_y b/2}{\sqrt{2}\sigma_i} \right) \quad (18)$$

The above discussion of photon jaws is also applicable to blocks and MLCs with flat ends. The only difference is the distance from the target to the collimator.

C. Multileaf collimator with rounded leaf ends

If all or part of the boundary of the visible area is defined by a MLC with rounded leaf ends, we need to calculate the projection of the leaf ends on the extrafocal plane. This is a two-step process. First, the leaf tip position, X_c , is derived from the light-field size, X , defined by this leaf at the SAD . As shown in Fig. 1, after simple geometric manipulations we have

$$X_c = \frac{X}{SAD}(SCD + R \sin \theta) - R(1 - \cos \theta) \quad (19)$$

where SCD is the distance from the target to the center of the leaf depth, R is the radius of the rounded leaf end, and $\theta = \tan^{-1}(X/SAD)$. X and X_c are defined to be positive when the leaf is at the full open position side and to be negative when the leaf travels across the central axis. Equation 19 applies to both A and B leaves.

For the second step, the projection of the leaf end on the extrafocal plane, x_e , is calculated by drawing a line tangent to the leaf end from the measurement point, as shown in Fig. 1. For A leaves, we have

$$x_e = x_d + \frac{SDD - SED}{SDD - SCD + R \sin \theta'} [x_c - x_d + R(1 - \cos \theta')] \quad (20)$$

where $\theta' \simeq \tan^{-1}[(x_c - x_d)/(SDD - SCD)]$. For B leaves, we have

$$x_e = x_d - \frac{SDD - SED}{SDD - SCD + R \sin \theta'} [x_c + x_d + R(1 - \cos \theta')] \quad (21)$$

where $\theta' \simeq \tan^{-1}[(x_c + x_d)/(SDD - SCD)]$. The deduction of Eqs. (19), (20), and (21) is similar to the work of Boyer and Li [27], so the details are not given here.

2.1.5 Relative in-air output

The model is commissioned using the S_c values measured at isocenter. We also measure the beam in-air output at positions other than the isocenter and normalize

to the reading at isocenter for the reference field (referred to as *relative in-air output*). These measured data are compared with the corresponding calculations to check if the model works in situations different from that of commissioning. The MBS factor, S_b , can still be calculated using Eqs. (3) and (4) since the MBS does not depend on the position of the measurement point. However, Eq. (2) needs to be modified to predict the head scatter contribution. By taking into account the horn effect and inverse-square-law correction, we have

$$S_h(fs, x_d, y_d, SDD) = [F_{isl}^{(p)}(x_d, y_d, SDD) \cdot F_{horn}(x_d, y_d) + F_{isl}^{(e)}(x_d, y_d, SDD) \cdot F_{efs}(fs, x_d, y_d, SDD)] / [1 + F_{efs}(fs_{ref}, 0, 0, SAD)] \quad (22)$$

where $F_{horn}(x_d, y_d)$ is the beam energy fluence (normalized to the central axis) at an off-axis position, (x_d, y_d) . $F_{isl}^{(p)}$ and $F_{isl}^{(e)}$ are the inverse-square-law correction factors for the point source and extrafocal source, respectively. They are given by

$$F_{isl}^{(p)}(x_d, y_d, SDD) = SAD^2 / (SDD^2 + x_d^2 + y_d^2) \quad (23)$$

$$F_{isl}^{(e)}(x_d, y_d, SDD) = (SAD - SED)^2 / [(SDD - SED)^2 + x_d^2 + y_d^2] \quad (24)$$

For the extrafocal source, we ignore the variation of the distance from different positions on the extrafocal plane to the detector. Using Eqs. (1), (3), and (22), we can predict the relative in-air output at positions other than the isocenter.

2.2 Model commissioning

When applying the model to a clinical beam from a linear accelerator, there are $2(N+1)$ parameters in the model to be determined (N is defined in Eq. (5)). These parameters can be determined using three sets of conventional measured data, namely: (1) the in-air output factor S_c at the isocenter for square fields with field sizes from $4 \times 4 \text{ cm}^2$ to $40 \times 40 \text{ cm}^2$, (2) S_c for rectangular fields with X jaws at a fixed opening of 10 cm and Y jaws moving from 4 cm to 40 cm, and (3) S_c for rectangular fields

with Y jaws at a fixed opening of 10 cm and X jaws moving from 4 cm to 40 cm. The S_c values for rectangular fields are needed to determine the MBS for which the influence of the upper and lower pairs of jaws is different.

The calculated in-air output factors, $S_c^{(c)}$, were fitted with the measured data, $S_c^{(m)}$, using the least χ^2 method. The χ^2 merit function is defined as

$$\chi^2 = \sum_i \frac{1}{\delta_i^2} [S_c^{(c)}(fs_i) - S_c^{(m)}(fs_i)]^2 \quad (25)$$

where δ_i is the measurement uncertainty for the i -th data point, which is assumed to be unity here. χ^2 function was minimized to get the best-fit parameters. The modified Marquardt method was used to handle this nonlinear fitting problem [28]. The $S_c^{(c)}$ was calculated using Eqs. (1), (2), (3), (4), and (18). One should notice that the χ^2 function may have many local minima in the parameter space. Therefore, different initial guesses for the set of fitting parameters may end up with different solutions. A solution reached after a large number of iterations may be physically unrealistic, or may be realistic but not “optimal”. In order to find an “optimal” solution, we combine the Marquardt method with a random search technique and add additional constraints to remove unrealistic solutions. The constraints can be, for example, that $A_i, \alpha, \beta \geq 0$, $F_{efs} \leq \epsilon_{efs}$ and $F_{mbs} \leq \epsilon_{mbs}$ for any field size. ϵ_{efs} and ϵ_{mbs} are the maximum possible values for F_{efs} and F_{mbs} , respectively. They are set empirically, e.g., $\epsilon_{efs} = 20\%$ and $\epsilon_{mbs} = 5\%$. There is no constraint on σ_i , because it makes no difference whether positive and negative values of σ_i are used for a Gaussian distribution. What matters is the absolute value of σ_i .

The fitting algorithm used here can be summarized as follows:

1. Randomly sample the initial value for each parameter from an empirically pre-set range.
2. Run the Marquardt method to get a set of the best-fit parameters.

3. Check the constraints. If one of them is violated, abandon this set of fitted parameters and go back to Step 1.
4. Store this set of parameters in a stack.
5. Check the termination criterion. If it is satisfied, finish the fitting process; otherwise go back to Step 1.

A stack is used to store the best-fit parameters which satisfy all the constraints. The stack is dynamically updated during the fitting process; only the 10 best sets of parameters are stored. The best set of parameters gives the minimum value of the χ^2 function. The termination criterion is defined as one of three conditions: (1) all the 10 best sets of parameters are the same within a tolerance, (2) the pre-set maximum number of sets of initial values have been sampled, and (3) the pre-set maximum computer CPU time has reached.

2.3 Model verification

The model was commissioned using S_c values measured at isocenter for square and rectangular fields defined by the jaws. To see if the model worked for situations different from the commissioning setups, we tested the model using the relative in-air output measured at various setups, including measurement points not at isocenter, asymmetric fields, and fields defined by an MLC.

2.4 Measurements

Relative beam in-air outputs were measured using a 0.6 cm³ PTW chamber placed at the measurement point in air. Brass build-up caps of 1.76 mm thick for 6 MV beam and 3.17 mm thick for 15 MV beam were used. The chamber was oriented along the rotation axis of the collimator. The measurements were taken using the 6

6 MV and 15 MV x-ray modes of a medical linear accelerator (Clinac 2300C/D, Varian Oncology Systems, Palo Alto, CA). The reference field size was 10×10 cm² and the maximum field size was 40×40 cm².

3 RESULTS

The parameters needed in the model for the calculation, such as the distance from the target to the collimator and flattening filter base, were taken from the manufacturer's specifications.

Three sets of measured S_c values were used to commission the model, using square fields from 4×4 cm² to 40×40 cm², and rectangular fields with one pair of jaws fixed at 10 cm and the other pair moving from 4 cm to 40 cm. Figure 2 shows the comparison between fitted and measured S_c values. The maximum fitting error is about 0.1% for both 6 MV and 15 MV. The S_c values for jaw openings down to 2 cm were also measured but not used for fitting. These results are compared with the calculated values and shown in Fig. 2. We can see that even for very small field sizes our model can still predict S_c values accurately ($\leq 0.1\%$).

For both beams it was found that three Gaussians were sufficient, because no significant improvement could be achieved with additional Gaussians. The fitted extrafocal source intensity distributions for 6 MV and 15 MV beams are given in Fig. 3. For each distribution we show the three Gaussian components. The best-fit parameters are given in Table 1. Using the best-fit parameters, we could easily calculate other quantities of interest. The total intensity of the extrafocal source, which is relative to the primary point source and is the sum of A_i ($i = 1, 2, 3$), equals 11.7% for the 6 MV beam and 7.7% for the 15 MV beam. The MBS contribution to S_c when the field size increased from 5×5 cm² to 40×40 cm², which can be calculated using Eq. (4), was about 1.2% for the 6 MV beam and 1.6% for the 15 MV beam.

The model was verified using an extensive set of relative in-air outputs measured under various conditions. All the calculated and measured in-air outputs were normalized to the reference condition, *i.e.*, at isocenter and for a 10×10 cm² field size. Figure 4 shows the comparison between the calculated and the measured S_c values for 6 MV and 15 MV beams and for four sets of rectangular fields that were defined by setting one pair of jaws at 4 or 40 cm and moving the other pair of jaws from 2 cm to 40 cm. In most situations, the agreement is within 0.1%. The maximum discrepancy is less than 0.2%, even for extremely elongated fields such as 2×40 cm².

Figure 5 shows the calculated and measured S_c data at the isocenter for 6 MV and 15 MV beams and for three sets of asymmetric rectangular fields, *i.e.*, X jaws set to 4, 10, or 40 cm and Y₂ jaw set to 20 cm while Y₁ jaw moving from 1 cm to 20 cm. The calculation agreed with the measurement within 0.2% for 6 MV and 0.1% for 15 MV.

Figure 6 shows the 6 MV beam in-air outputs measured and calculated at 80 cm and 120 cm SDD. The calculation is in good agreement with the measurement (maximum difference is 0.5% for 80 cm SDD and 0.3% for 120 cm SDD).

The model was also tested for fields defined by a MLC. The 6 MV beam in-air outputs, relative to that at isocenter and for jaw-defined 10×10 cm² fields, were measured and calculated for MLC-defined square fields from 2×2 cm² to 28×28 cm² with jaws at a variety of positions including: (1) both X and Y jaws are at the recommended positions for each field (X jaw opening is 8 mm wider and Y jaw is 2 mm wider at SAD than the MLC opening), (2) X jaw opening is 30 cm and Y jaws are at the recommended positions, (3) X jaws are at the recommended positions and Y jaw opening is 30 cm, and (4) both X and Y jaw openings are 30 cm. Figure 7 shows a comparison between measurement and calculation. The calculation agrees with the measurement very well (within about 0.1%) for small field sizes ($< 15 \times 15$ cm²) for all jaw settings except for case (4). At larger field sizes, for all jaw settings the

calculation underestimated the relative in-air output and the discrepancy increased with the field size. The maximum difference is about 0.3% for jaw setting (1), 0.4% for jaw setting (2), 0.6% for jaw setting (3), and 0.9% for jaw setting (4).

The model was also used to calculate the 6 MV beam in-air outputs for MLC defined off-axis square fields from $2 \times 2 \text{ cm}^2$ to $10 \times 10 \text{ cm}^2$. The calculation point was at the center of the fields as well as 5 cm from both X and Y axes. The beam outputs were calculated and measured for two jaw settings that were: (1) both X and Y jaws at the recommended positions for each field with the limit that the maximum distance over central axis for the X jaws is 2 cm, and (2) Y jaws are opened to 30 cm, X_1 jaw is at 10 cm and X_2 jaw is at 15 cm. The calculated and measured beam outputs were normalized to the reading at isocenter and for a $10 \times 10 \text{ cm}^2$ jaw-defined field. The calculation is compared with the measurement as shown in Fig. 8. For jaws at the recommended positions, the maximum difference between calculation and measurement was about 0.7%. For jaw setting (2), the average difference was about 0.7% but the maximum difference was 1.7% which happened at a field size $2 \times 2 \text{ cm}^2$. We can see that the calculation systematically predicts lower beam outputs. The reason might be that we use the measured d_{max} dose profile in water to approximate the off-axis primary energy fluence F_{horn} in Eq. (22).

4 DISCUSSION

A model for extrafocal radiation and MBS was derived and commissioned and tested for 6 MV and 15 MV photon beams produced by a medical linear accelerator. For these two beams, we found that three Gaussians are optimal to represent the relative intensity distributions for extrafocal sources. For Varian high energy accelerators, the primary collimator opening at the level of the flattening filter is about 3.1 cm, which limits the radial extent for most scattered photons. We can see in Fig. 3 that

the first two Gaussians actually model these photons. A small amount of photons, which are scattered from the treatment head components other than the flattening filter and primary collimator, such as the photon jaws, have a large radial extent when they are backprojected on the extrafocal plane. The relative intensity distribution for these photons is modeled by the third Gaussian and forms a low-intensity long tail of the total distribution. The extrafocal source distributions calculated with our model for both 6 MV and 15 MV beams from a Varian Clinac 2300C/D accelerator are qualitatively in agreement with the work of Lam *et al* (see Fig. 5 in Ref. [16]) and the measurement of Jaffray *et al* (see Fig. 6 in Ref. [10]) for the Varian Clinac 2100C machines.

The contribution of the extrafocal source to S_c at the isocenter, relative to that of the primary point source, is 11.7% for the 6 MV beam and 7.7% for the 15 MV beam. Our result for 6 MV beam agrees very well with the Monte Carlo result of Liu *et al* [7] (11.5% for 6 MV beam from a Varian Clinac 2100C machine). Jaffray *et al* [10] and Sharpe *et al* [11] measured the contribution of the extrafocal radiation to the total photon energy fluence at the isocenter for 40×40 cm² field size and 6 MV beams from Varian Clinac 2100C machines. The result of Jaffray *et al* was 8% and the result of Sharpe *et al* was 12%. Our result for 6 MV beam from a Varian Clinac 2300C/D accelerator, if normalized to the total photon energy fluence, is 10.5%.

The MBS contribution to S_c when the square field size changes from 5×5 cm² to 40×40 cm², which can be calculated using Eq. (4), was about 1.2% for the 6 MV beam and 1.6% for the 15 MV beam. The results are in good agreement with the measurement of Yu *et al* [23] using a target-current-pulse-counting technique for a Varian Clinac 2300C/D machine. Their results were $1.2 \pm 0.3\%$ for 6 MV and $1.8 \pm 0.3\%$ for 15 MV beam when the jaw-defined square field width varied from 5 cm to 40 cm.

The accuracy achieved with our model demonstrates that by using three sets of

measured S_c values for square and rectangular fields for commissioning, our model can separate the extrafocal radiation and MBS even though their contributions to S_c show same trend as field size varies. Specially designed experiments or sophisticated numerical calculations (such as Monte Carlo simulation) are avoided by using our model. Therefore, our model provides a simple and accurate way to model the extrafocal radiation and MBS for routine clinical use.

For square or rectangular fields defined by photon jaws, S_c can be accurately calculated using our model. When the calculation point is at the isocenter, for either symmetric or asymmetric fields, the calculation accuracy is within 0.2%. When the calculation point is at an extended SDD, the accuracy is within 0.5%.

For fields defined by an MLC, the accuracy of the calculated in-air outputs using our model is related to the jaw positions. Higher accuracy can be achieved if jaws are at the recommended positions, where most of the time the visible area is limited by jaws instead of by the MLC even though the MLC defines the field shape at the isocenter. If at least one pair of jaws are at the recommended positions, the model can predict the in-air output with an accuracy of about 0.1% for small field sizes (less than 15×15 cm²). For larger field sizes, the model always underestimates the relative in-air output. For jaws at the recommended positions, the underestimation is less than 0.3%. However, if both jaws are fully open, the underestimation can be 0.9%.

The slightly decreased accuracy for some MLC-defined fields was expected. The model was commissioned for jaw-defined fields, and only accounts for major effects. Some minor effects, such as MLC leaf end scatter, MLC inter-leaf transmission and scatter, and jaw transmission and scatter, may play a role in beam output calculations for large fields defined by an MLC. The influence of electron contamination was studied. We measured the 6 MV data again using the 15 MV buildup cap and found no difference. It implies that the 6 MV buildup cap was able to screen all

contaminant electrons. The influence of leaf carriage position was also investigated. By retracting one pair of the most outside leaves (1A and 1B), we were able to keep both carriages at the same places while the size of the MLC-defined field was varied. No effect was found for leaf carriages. The reason for the underestimation of beam output for large MLC-defined fields is not clear. Our future work will investigate the scatter and leakage from the MLC in the model.

When the calculation point is at about 7 cm off-axis distance, the model underestimates the relative in-air output (less than 0.7%) for jaws at the recommended positions. If jaws are widely open, the average underestimation is about the same but the maximum is about 1.7% for the smallest field (2×2 cm²). At the off-axis position we always underestimate the in-air output. The reason might be that the horn factor (F_{horn}) used is smaller than its real value.

For static fields defined by the MLC with jaws at the recommended positions, the in-air output can be predicted using our model to within about 0.2 - 0.3% accuracy. For IMRT fields, since the jaws are usually fixed at the recommended positions for the largest MLC opening while the MLC leaves sweep across the field, the accuracy of the calculated beam output might be slightly worse but still within 1%. Therefore, the model can be used to predict the beam output not only for static irregular fields shaped with blocks or MLCs, but also for IMRT fields delivered using dynamic jaws or MLCs.

The model can be incorporated into a dose calculation algorithm, such as a pencil beam algorithm or the Monte Carlo method, to calculate the dose in beam penumbra regions more accurately. This would be very useful for IMRT dose calculation since a large amount of penumbra dose is accumulated in the field.

5 CONCLUSION

A simple and accurate model for both extrafocal source and monitor chamber backscatter has been developed and investigated. We have demonstrated that the relative intensity distribution of the extrafocal radiation can be modeled accurately using a series of Gaussian functions. Both extrafocal source and monitor chamber backscatter can be determined simultaneously using conventional measured data, *i.e.*, S_c values at the isocenter for square and rectangular fields defined by photon jaws. The model can be used to predict accurately the relative in-air outputs analytically. By including the model in a dose algorithm, the penumbra dose will be calculated more accurately than using a point source. The model will be very useful for monitor unit and dose distribution calculations in IMRT.

ACKNOWLEDGEMENTS

The authors would like to thank Drs. Michael Sharpe and Kwok Lam for providing some of their results and for helpful discussions. The authors are also grateful to Drs. Frank Verhaegen, Todd Pawlicki, and Yunping Zhu for useful comments on the manuscript. The work was supported in part by the US Army breast cancer research program (BC971292) and the NCI grant CA43840.

References

- [1] K. R. Kase and G. K. Svensson. Head scatter data for several linear accelerators (4-18 MV). *Med. Phys.*, 13:530–532, 1986.
- [2] P. Vadash and B. Bjarngard. An equivalent-square formula for head-scatter factors. *Med. Phys.*, 20:733–734, 1993.
- [3] M. Tatcher and B. Bjarngard. Head-scatter factors in rectangular photon fields. *Med. Phys.*, 20:205–206, 1993.
- [4] M. K. Yu, B. Murray, and R. Sloboda. Parametrization of head-scatter factors for rectangular photon fields using an equivalent square formalism. *Med. Phys.*, 22(8):1329–1332, 1995.
- [5] A. L. Boyer and C. X. Yu. Intensity-modulated radiation therapy with dynamic multileaf collimators. *Semin. Radiat. Oncol.*, 9(1):48–59, 1990.
- [6] E. L. Chaney, T. J. Cullip, and T. A. Gabriel. A Monte Carlo study of accelerator head scatter. *Med. Phys.*, 21(9):1384–1390, 1994.
- [7] H. H. Liu, T. R. Mackie, and E. C. McCullough. A dual source photon beam model used in convolution/superposition dose calculation for clinical megavoltage x-ray beams. *Med. Phys.*, 24(12):1960–1974, 1997.
- [8] A. Ahnesjö. Collimator scatter in photon therapy beams. *Med. Phys.*, 22(3):267–278, 1995.
- [9] A. Ahnesjö. Analytical modeling of photon scatter from flattening filters in photon therapy beams. *Med. Phys.*, 21(8):1227–1235, 1994.

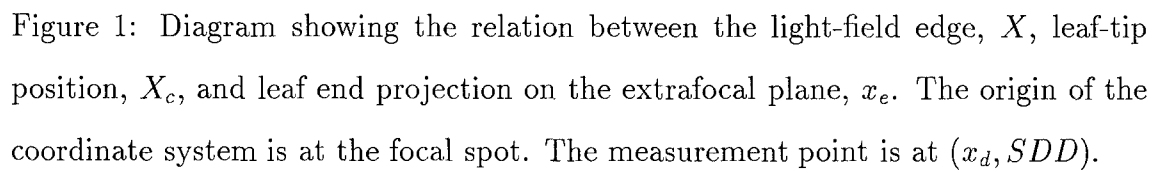
- [10] D. A. Jaffray, J. J. Battista, A. Fenster, and P. Munro. X-ray sources of medical linear accelerators: Focal and extra-focal radiation. *Med. Phys.*, 20(5):1417–1427, 1993.
- [11] M. B. Sharpe, D. A. Jaffray, J. J. Battista, and P. Munro. Extrafocal radiation: A unified approach to the prediction of beam penumbra and output factors for megavoltage x-ray beams. *Med. Phys.*, 22(12):2065–2074, 1995.
- [12] P. B. Dunscombe and J. M. Nieminen. On the field-size dependence of relative output from a linear accelerator. *Med. Phys.*, 19(6):1441–1444, 1992.
- [13] E. Ihnen and J. M. Jensen. A new source model for linear accelerators. In A. Breit, editor, *Advances in Radiation Therapy: Tumor Response Monitoring and Treatment Planning*, pages 509–513. Springer-Verlag, 1992.
- [14] T. J. Waldron. Calculation of dynamically-wedged isodose distributions using segmented treatment tables and open-field measurements. Master’s thesis, The University of Texas, 1995.
- [15] M. K. Yu and R. Sloboda. Analytical representation of head scatter factors for shaped photon beams using a two-component x-ray source model. *Med. Phys.*, 23(6):973–984, 1996.
- [16] K. L. Lam, M. S. Muthuswamy, and R. K. Ten Haken. Flattening-filter-based empirical methods to parametrize the head scatter factor. *Med. Phys.*, 23(3):343–352, 1996.
- [17] P. A. Jursinic. Clinical implementation of a two-component x-ray source model for calculation of head-scatter factors. *Med. Phys.*, 12(12):2001–2007, 1997.
- [18] D. Convery and S. Webb. Calculation of the distribution of head-scattered radiation in dynamically-collimated MLC fields. In D. D. Leavitt and G. Starkschall,

- editors, *Proceedings of The 12th International Conference on The Use of Computers in Radiation Therapy*, pages 350–353, Salt Lake City, Utah, USA, 1997. Medical Physics Publishing.
- [19] M. S. Patterson and P. C. Shragge. Characteristics of an 18 mv photon beam from a Therac 20 Medical Linear Accelerator. *Med. Phys.*, 8(3):312–318, 1981.
 - [20] G. Luxton and M. A. Astrahan. Output factor constituents of a high-energy photon beam. *Med. Phys.*, 15(1):88–91, 1988.
 - [21] H. Kubo. Telescopic measurements of backscattered radiation from secondary collimator jaws to a beam monitor chamber using a pair of slits. *Med. Phys.*, 16(2):295–298, 1989.
 - [22] C. Duzenli, B. McClean, and C. Field. Backscatter into the beam monitor chamber: Implications for dosimetry of asymmetric collimators. *Med. Phys.*, 20(2):363–367, 1993.
 - [23] M. K. Yu, R. Sloboda, and F. Mansour. Measurement of photon beam backscatter from collimators to the beam monitor chamber using target-current-pulse-counting and telescope techniques. *Phys. Med. Biol.*, 41:1107–1117, 1996.
 - [24] H. H. Liu, T. R. Mackie, and E. C. McCullough. Calculating output factors for photon beam radiotherapy using a convolution/superposition method based on a dual source photon beam model. *Med. Phys.*, 24(12):1975–1985, 1997.
 - [25] K. L. Lam, M. S. Muthuswamy, and R. K. Ten Haken. Measurement of backscatter to the monitor chamber of medical accelerators using target charge. *Med. Phys.*, 25(3):334–338, 1998.

- [26] A. Ahnesjö, T. Knöös, and A. Montelius. Application of the convolution method for calculation of output factors for therapy photon beams. *Med. Phys.*, 19(2):295–301, 1992.
- [27] A. L. Boyer and S. Li. Geometric analysis of light-field position of a multileaf collimator with curved ends. *Med. Phys.*, 24(5):757–762, 1997.
- [28] W. H. Press, S. A. Teukolsky, W. T. Vetterling, and B. P. Flannery. *Numerical recipes*. Cambridge University Press, Cambridge, second edition, 1992.

Table 1: The best-fit parameters in the extrafocal source and monitor chamber backscatter models for 6 and 15 MV photon beams from a Varian Clinac 2300C/D accelerator.

Beam	A_1	A_2	A_3	σ_1	σ_2	σ_3	α	β
6 MV	0.332e-1	0.517e-1	0.320e-1	0.650e+0	0.133e+1	0.452e+1	0.140e-1	0.181e-4
15 MV	0.192e-1	0.314e-1	0.264e-1	0.671e+0	0.100e+1	0.421e+1	0.185e-1	0.522e-5



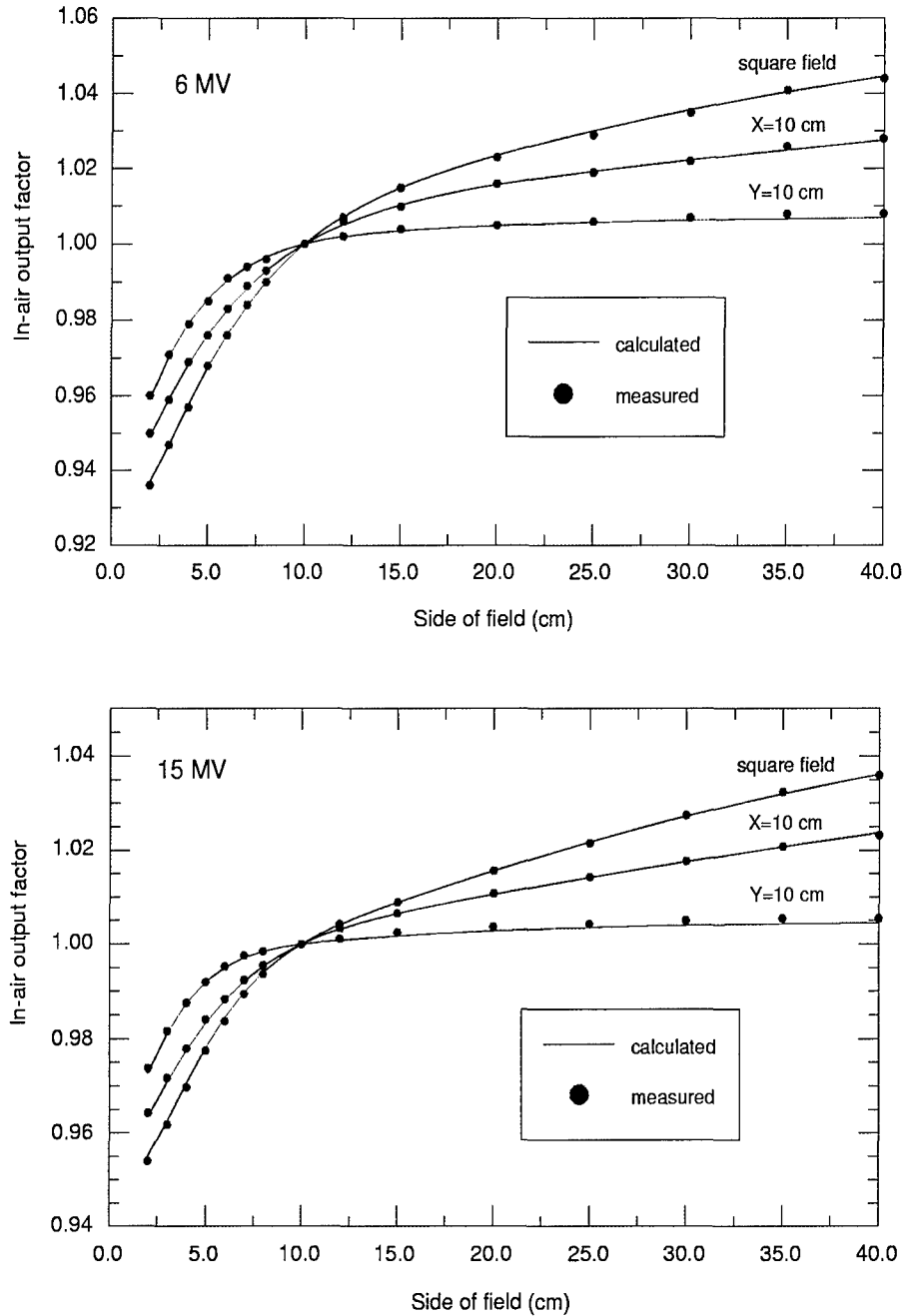


Figure 2: The comparison between the fitted and measured in-air output factors for 6 MV and 15 MV beams and for three sets of fields: (1) square fields with field sizes from $4 \times 4 \text{ cm}^2$ to $40 \times 40 \text{ cm}^2$, (2) rectangular fields with the X jaws at a fixed opening of 10 cm and the Y jaws moving from 4 cm to 40 cm, and (3) rectangular fields with the Y jaws at a fixed opening of 10 cm and the X jaws moving from 4 cm to 40 cm. The results for jaw openings down to 2 cm are also plotted for comparison.

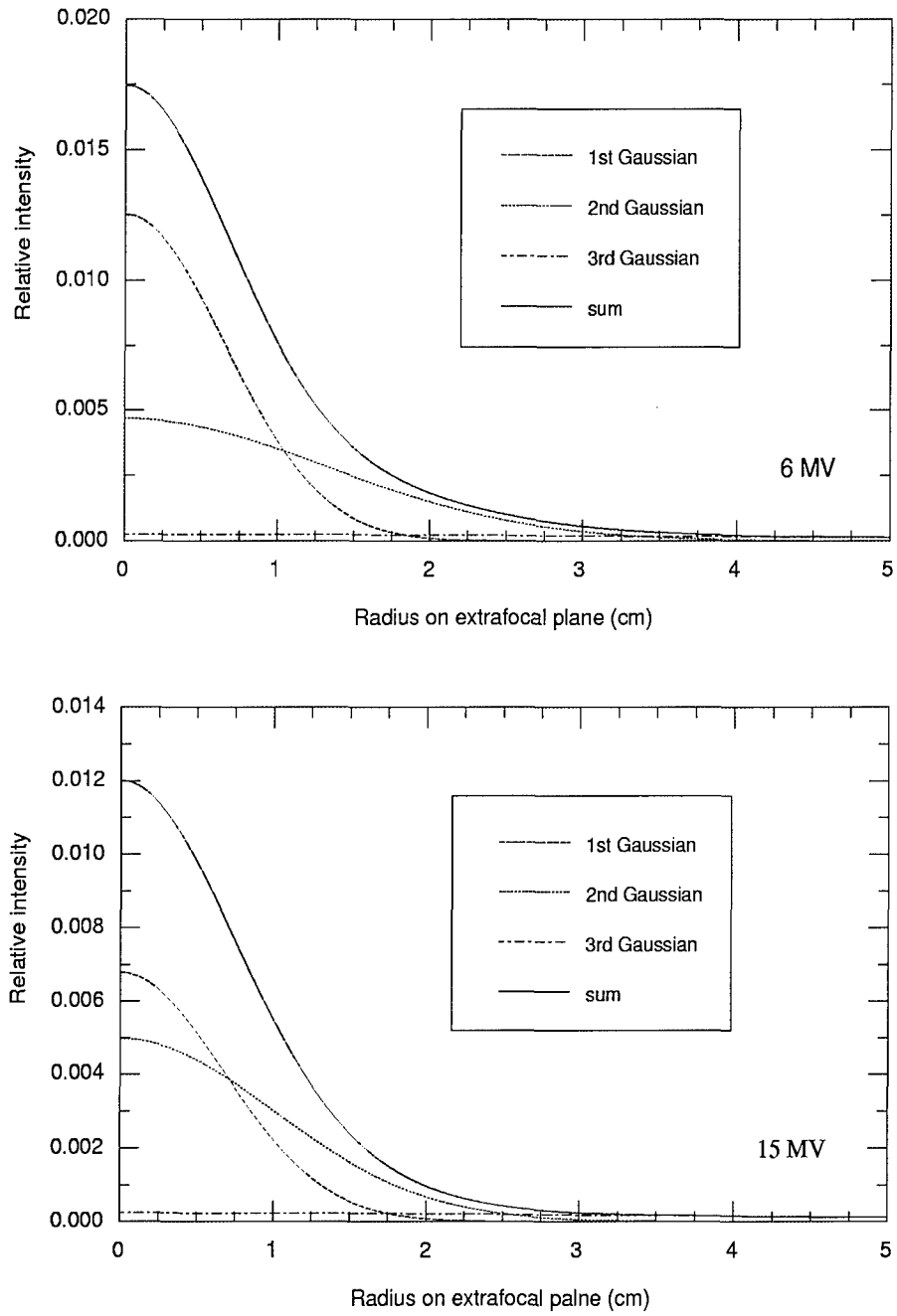


Figure 3: The relative intensity distributions of the extrafocal source and the three Gaussian components for 6 and 15 MV photon beams. The distributions are normalized to the intensities of primary photons.

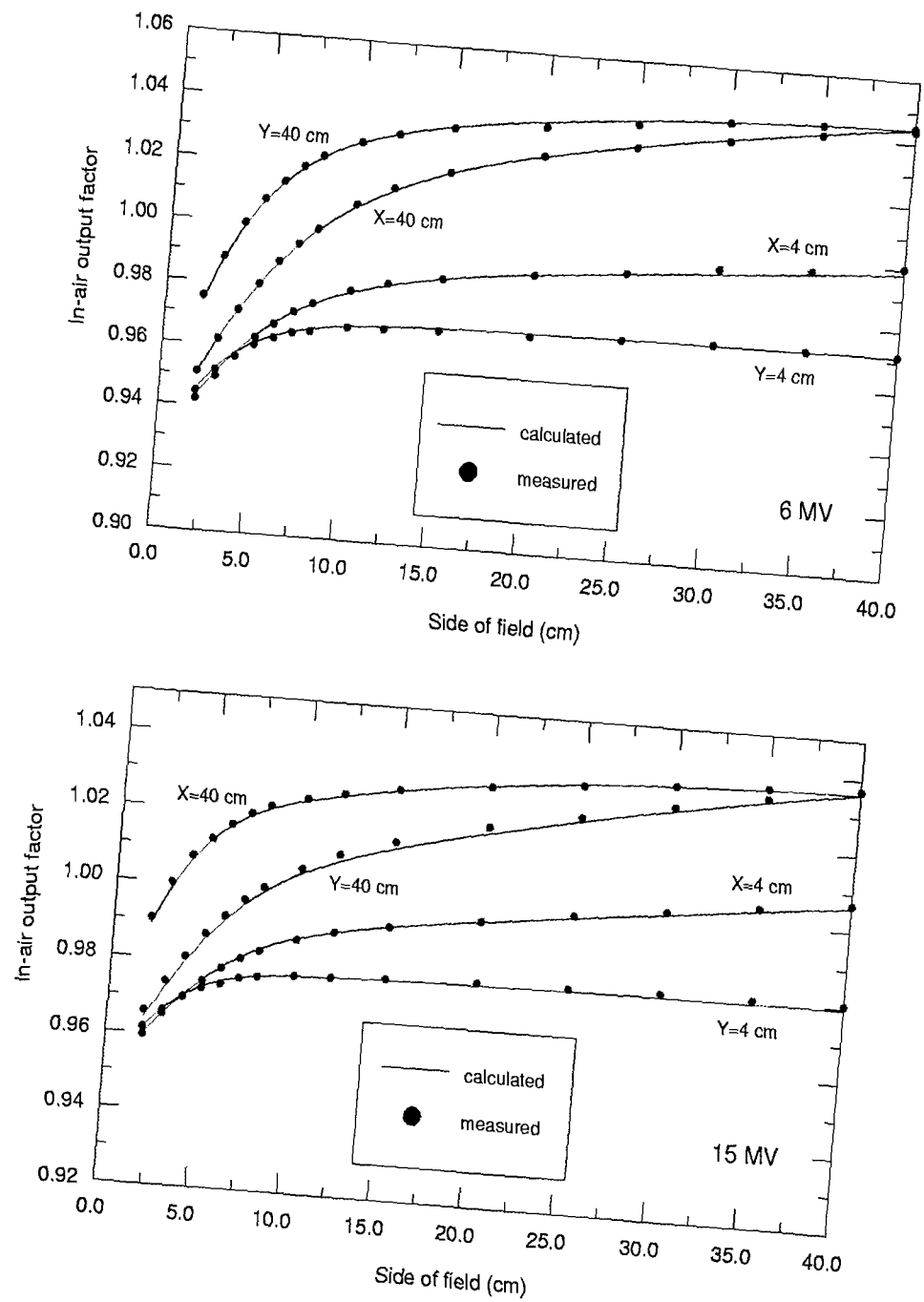


Figure 4: The comparison between the calculated and measured in-air output factors for 6 MV and 15 MV beams and for four sets of rectangular fields with one pair of jaws setting at 4 or 40 cm and the other pair of jaws moving from 2 cm to 40 cm.

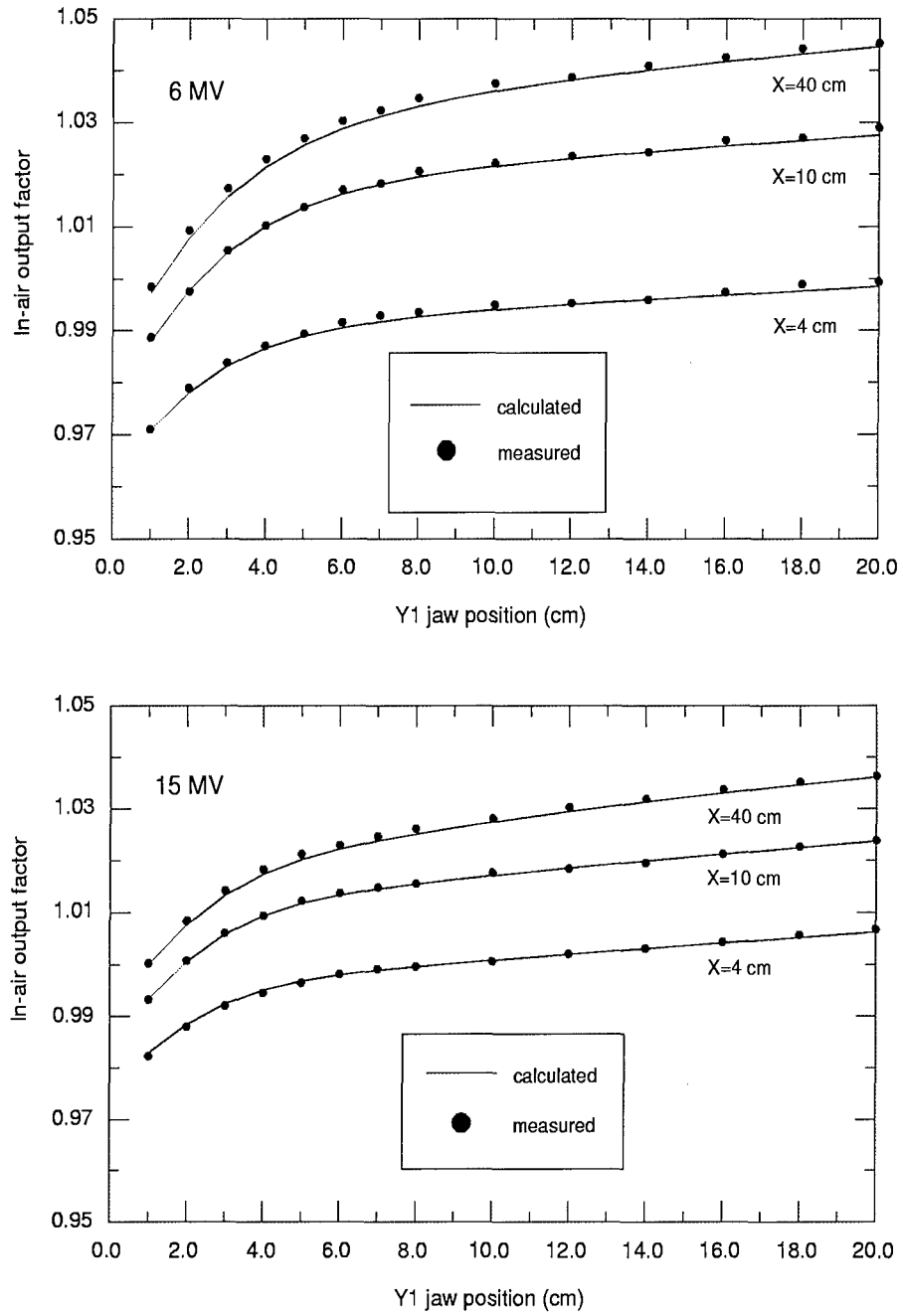


Figure 5: The comparison between the calculated and measured in-air output factors for 6 MV and 15 MV beams and for asymmetric rectangular fields. X jaws are fixed at 4, 10, 40 cm openings. Y₂ jaw is fixed at 20 cm. Y₁ jaw moves from 1 cm to 20 cm.

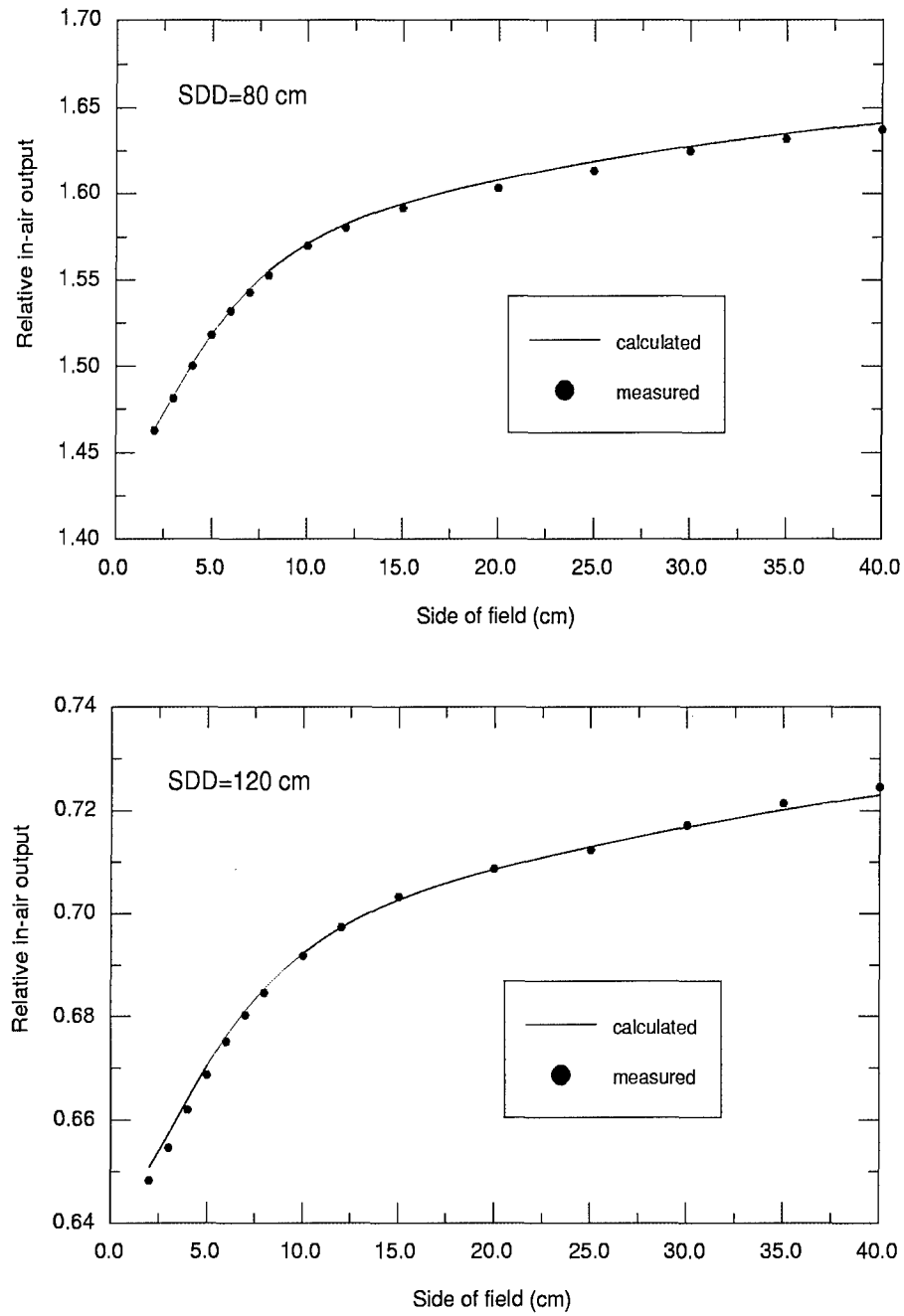


Figure 6: The comparison between the calculated and measured relative in-air outputs for 6 MV square fields and at 80 and 120 cm SDD. All the data are normalized to the beam in-air output at the isocenter for $10 \times 10 \text{ cm}^2$ field.

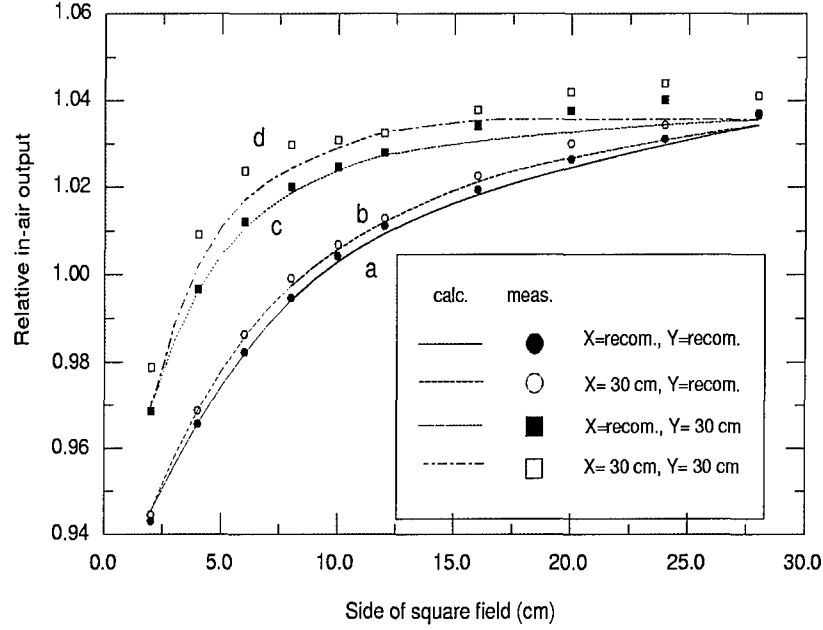


Figure 7: The comparison between the calculated and measured 6 MV relative in-air output for MLC-defined square fields for four different jaw setups. Lines are the calculated and symbols are measured data. All data are normalized to the beam in-air output at the isocenter for 10×10 cm² jaw-defined field. (a) Both X and Y jaws are at the recommended positions for each field, i.e., X jaw opening is 8 mm wider at SAD than MLC opening and Y jaw is 2 mm wider; (b) X jaw opening is 30 cm and Y jaws are at the recommended positions; (c) X jaws are at the recommended positions and Y jaw opening is 30 cm; (d) Both X and Y jaw openings are 30 cm.

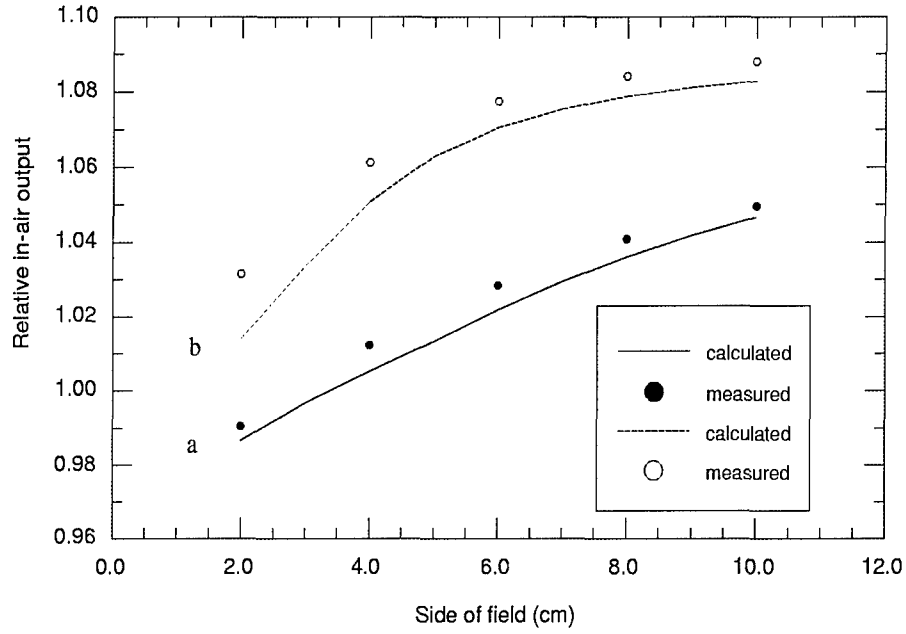


Figure 8: The comparison between the calculated and measured relative beam in-air outputs for MLC defined off-axis square fields. The detector is placed at the field center and 5 cm away from both X and Y axes. Lines are the calculated and symbols are measured data. (a) Both X and Y jaws are at the recommended positions for each field, i.e., X jaw opening is 8 mm wider at SAD than MLC opening and Y jaw is 2 mm wider. The maximum distance over central axis for X jaws is 2 cm; (b) Y jaws are opened to 30 cm. X_1 jaw is at 10 cm and X_2 jaw is at 15 cm.

Electron Beam Modeling and Commissioning for Monte Carlo Treatment Planning

Steve B. Jiang*, Ajay Kapur and C.-M. Ma

Department of Radiation Oncology,
Stanford University School of Medicine,
300 Pasteur Drive, Stanford, CA 94305-5304

October 12, 1999

*Corresponding author. Tel: (650)498-4074, Fax: (419)498-4015, E-mail: stevej@reyes.stanford.edu

Abstract

A hybrid approach for commissioning electron beam Monte Carlo treatment planning systems has been studied. The approach is based on the assumption that accelerators of the same type have very similar electron beam characteristics and the major difference comes from the on-site tuning of the electron incident energy at the exit window. For one type of accelerator, a reference machine can be selected and simulated with the Monte Carlo method. A multiple source model can be built on the full Monte Carlo simulation of the reference beam. When commissioning electron beams from other accelerators of the same type, the energy spectra in the source model are tuned to match the measured dose distributions. A Varian Clinac 2100C accelerator was chosen as the reference machine and a four-source beam model was established based on the Monte Carlo simulations. This simplified beam model can be used to generate Monte Carlo dose distributions accurately (within 2%/2 mm compared to those calculated with full phase space data) for electron beams from the reference machine with various nominal energies, applicator sizes, and SSDs. Three electron beams were commissioned by adjusting the energy spectra in the source model. The dose distributions calculated with the adjusted source model were compared with the dose distributions calculated using the phase space data for these beams. The agreement is within 1% in most of cases and 2% in all situations. This preliminary study has shown the capability of the commissioning approach for handling large variation in the electron incident energy. The possibility of making the approach more versatile is also discussed.

Keywords: Electron beam Treatment planning
 Monte Carlo simulation Beam Commissioning
 Source Modeling

1 Introduction

Electron beam radiation therapy is used extensively to treat head and neck cancers to avoid the irradiation of the spinal cord, and to treat chest walls to limit the irradiated volume of lung. The currently available commercial systems for electron treatment planning mostly utilize the Hogstrom algorithm as the dose calculation engine[1], which is based on Fermi-Eyges theory[2, 3]. Due to the inappropriate treatment of electron transport in inhomogeneous phantoms, large discrepancies (10% or more) in the dose distributions have been observed between the current analytical algorithms and measurements or Monte Carlo simulations in some clinical situations where the treatment volumes encompass air cavities and bone[4, 5, 6, 7]. Accurate dose calculation is an important factor for the wide-spread clinical use of electron therapy and the development of new electron therapy techniques, such as electron beam or mixed electron/photon beam intensity modulated therapy, which are expected to improve the conformality of the delivered dose distribution to the target volume for some disease sites[8, 9, 10].

The Monte Carlo method is generally considered to be the most accurate approach for electron dose calculation under all circumstances [11, 12, 13, 14, 15, 16]. In particular, Monte Carlo simulation can handle electron multiple scattering in the presence of inhomogeneities (such as bone and air cavity) much more accurately than any existing analytical dose models. The necessity of accurate electron dose calculation has motivated many efforts to develop Monte Carlo electron beam treatment planning systems[6, 7, 17, 18, 19, 20, 21, 22]. Due to the rapid development of computer technology and the employment of innovative variance reduction techniques, it is expected that treatment planning systems utilizing a Monte Carlo dose engine will begin to serve in routine clinical practice in the next few years [6, 7, 20, 21, 22, 23, 24, 25, 26, 27, 28, 29].

The commissioning procedure for a Monte Carlo treatment planning system can be different from that for a conventional planning system, since it requires more detailed and accurate clinical beam data[22]. For example, the phase space information (position, direction and energy) is needed to represent particles coming out of the accelerator treatment head. This information is extremely difficult, if not impossible, to acquire experimentally, mainly due to the very high intensity of the therapeutic electron beam[30]. Some researchers tried to extract the phase space information from the a limited set of measured dose data (such as depth dose curves and dose profiles) by using a simple beam model[31]. Although the approach may have great potential, at least currently it uses many approximations and the accuracy of the reconstructed phase space cannot be guaranteed. The only method to obtain the accurate electron beam phase space information is to simulate the accelerator treatment head using the Monte Carlo method[32, 33, 34]. An EGS4 Monte Carlo user code, OMEGA BEAM, was developed specifically for this purpose [34]. Using the BEAM code, the accelerator treatment head and electron applicator can be simulated to yield a data file containing the phase space information for tens of millions of particles exiting the treatment head. The phase space data can then be used as input to calculate dose distributions in a patient's CT phantom[34].

However, direct simulation of the accelerator treatment head using the Monte Carlo method is not a viable commissioning approach for Monte Carlo treatment planning. The beam characteristics are usually different due to variation in accelerator designs and on-site beam tuning. The simulated electron beam phase space for one accelerator may not be used directly for another. It is necessary to simulate each accelerator individually to obtain the phase space information. This fact presents three problems for the clinical acceptance of Monte Carlo treatment planning systems. First, the simulation of the accelerator treatment head for every energy/applicator combination takes much more time than the commissioning of a

conventional electron planning system. As estimated by Faddegon et al[22], even for users with Monte Carlo simulation experience, it takes about 2 months of CPU time to generate a complete set of beam data for a single accelerator. Second, the storage of the phase space information requires a lot of computer disk space. For each energy/applicator combination, a phase space file is usually pre-calculated and stored in the treatment planning computer. For accurate treatment planning, a phase space file occupies hundreds of megabytes of disk space. This is certainly a substantial burden for the computer resources at most clinical centers. Third, the generation and quality assurance of the phase space data files by simulating the treatment head requires Monte Carlo simulation experience. Therefore, it is a prohibitive task for general users to perform Monte Carlo simulations for their own accelerators.

In this paper, a hybrid approach for commissioning electron beam Monte Carlo treatment planning systems is proposed. This method combines the advantages of the full Monte Carlo simulation and the method of Janssen *et al* [31]. It is based on the assumption that accelerators of the same type have very similar electron beam characteristics and the major difference is the electron incident energy at the exit window due to beam tuning during linac acceptance. By simulating a reference accelerator for a particular type of accelerator using the Monte Carlo BEAM code[34], a beam model is constructed using the resultant phase space information. The beam model is a simplified implementation of a previously developed multiple source model which can compress the Monte Carlo phase space data by a factor of 1000 or more[35, 36, 37]. When commissioning another accelerator of the same type, the energy spectra in the beam model are tuned to match standard measured data such as depth doses and dose profiles. Using this approach, we do not have to simulate every accelerator individually. Only one reference accelerator needs to be simulated for a type of accelerator, and this can be done carefully by someone with Monte Carlo expertise. In this paper, a Varian Clinac 2100C accelerator is chosen as the reference

machine. The machine is simulated using the BEAM code[34] and a four-source beam model is established based on the simulated beam phase space information. The accuracy of the Monte Carlo dose distributions calculated with the model is verified. Then, the model based on the reference beam is used to commission three other electron beams. Two beams are also from the reference machine but with incident energies significantly different from that of the reference beam. The third beam is from another Clinac 2100C machine at a different institution [38]. The validity of the proposed commissioning approach is demonstrated by commissioning these three beams.

2 Methods and Material

2.1 Beam Modeling

2.1.1 General considerations

Beam modeling is the first step in our hybrid commissioning procedure for a Monte Carlo treatment planning system. A beam model for a type of accelerator is established using the Monte Carlo simulated phase space information for the reference beam. The beam data is modeled using the multiple source model developed by Ma et al[35, 36, 37], which is modified in the current work for use in the commissioning procedure. The major modifications of the model are discussed here.

The multiple source model is based on the observation that particles from different components of an accelerator have significantly different energy, angular and spatial distributions while the particles from the same component have very similar characteristics[35, 36, 37]. Therefore, the particles from different components of an accelerator can be treated as they are from different sub-sources. Each sub-source represents a critical component in the treatment head and its geometrical dimensions are determined by the component dimensions. Each sub-source has its own energy spectrum and planar fluence distribution derived from the simulated phase space data. When the model is used for dose calculation, the incident energy and position of a particle are sampled from the corresponding stored energy spectrum and planar fluence distribution. The incident direction of the particle is reconstructed by sampling the position of the particle on the sub-source and on the phantom surface. The correlation between the particle position and incident angle is naturally retained.

A primary reason to develop the multiple source model was to find a concise way to replace the huge phase space data files generated from Monte Carlo simulations[35, 36]. The emphasis of the current work is to develop a clinically prac-

tical commissioning procedure for Monte Carlo treatment planning. The multiple source model is simplified to make the commissioning procedure as simple as possible while trying to maintaining dose calculation accuracy under all circumstances of clinical relevance. The number of sub-sources in the model is minimized and only those sub-sources of dosimetric significance are retained. The dependence of the model on the detailed information of accelerators is reduced. Sub-sources are represented by dimensionless geometric objects, such as points and lines, instead of the actual geometrical shapes and sizes of the treatment head components as used previously[35, 36].

Ma et al established their multiple source model from the Monte Carlo simulated phase space data on the patient surface (at 100 cm SSD) and the last scraper of the electron applicator was included in the model as a sub-source[35, 36]. In this work, the treatment head is simulated using the BEAM code down to just above the last scraper of the electron applicator[34], where the patient specific cutout is inserted. The last scraper, as well as the field-defining cutout, are simulated together with the patient CT phantom when performing Monte Carlo treatment planning dose calculations. The advantage of this method is that the beam model is patient independent. However, this approach, compared to that of Ma et al[35, 36], requires more careful beam modeling since an air gap between the last scraper and patient surface is not included in the original BEAM simulation.

In the present paper, the beam modeling approach is applied to a Varian Clinac 2100C machine at Stanford Medical Center, which is chosen as the reference machine to build beam models. At first, a very detailed model for each beam is used as the starting point. All the critical components of the treatment head are modeled as sub-sources. With this model, the phase space information of the electron beam can be precisely reconstructed and the dose distribution in a water phantom can be accurately calculated. Then, the number of sub-sources is gradually reduced while main-

taining the accuracy in dose distribution calculation. We find that a point electron source with the energy spectrum obtained from the Monte Carlo simulation is able to give a reasonably accurate depth-dose curve, which is consistent with the previous observation[36]. By adding another point photon source, the bremsstrahlung tail in the depth dose distribution can be reproduced accurately. However, it is found that the penumbra at the phantom surface generated with this two point source model is sharper compared to that generated with the full phase space data. In order to get the dose profiles correct, we find that, in addition to the two point sources, two square ring electron sources (which emit electrons isotropically) are needed to represent electrons scattered from the applicator scrapers. (The term *square ring* is used here to represent the edge of a square.) Therefore, the beam model should include four sub-sources: a point electron source for direct electrons (which do not interact with the beam defining system) and electrons scattered from the primary collimator, movable jaws and shieldings, a point photon source for all contaminant photons, and two square ring electron sources for electrons scattered from the first two scrapers of the electron applicator (the third also last scraper is not included in the model).

As described previously, beam modeling consists of two steps, namely, beam representation and beam reconstruction[35, 36]. In beam representation, parameters in the model are extracted from the simulated phase space file. In the current simplified model, these parameters include the positions and relative intensities of the sub-sources, the energy spectra for particles inside and outside the field for each sub-source, and the planar fluence distributions on the scoring plane (directly above the last scraper) for each sub-source. Beam reconstruction is performed when using the model for dose calculations. The phase space information for each particle, including the energy, position and direction, is reconstructed from the scored source parameters.

2.1.2 Beam representation

The positions of the virtual electron and photon point sources can be determined using a method described in ref. [36], which is analogous to the pin-hole method[39]. A thin annular aperture is selected on the scoring plane and phase space particles are allowed to pass through the aperture and form an image at a distance below the scoring plane. Ray-lines drawn through the center of the aperture and the peak of the aperture image form a virtual focal spot, which is adopted as the position of the point source. This pin-hole method is very effective for the photon point source. However, we find that for electrons, this method is only applicable to high energy beams. For lower energy beams, e.g., 6 MeV, the virtual SSD determined with this method is greatly overestimated and dependent on the radius of the thin annular aperture on the scoring plane. This is due to the fact that the in-air multiple scattering of low energy electrons is significant. To overcome this problem we performed another Monte Carlo simulation of the accelerator treatment head by replacing the intervening air with vacuum. Then, based on the new phase space data, this pin-hole method can be used to generate the correct position for the virtual electron point source, which is independent of the sampling radius. The effect of in-air multiple scattering is taken into account during beam reconstruction by adding a perturbation to the electron incident direction, as discussed later.

Two square ring sources of electrons are located at the corresponding positions of the two applicator scrapers. The sides of the square rings correspond to the actual openings of the scrapers.

The energy spectrum for each sub-source is derived from the simulated phase space data. It was found that the mean energy of the electrons is relatively uniform inside the field as well as outside the field. The change of mean energy with the distance from the central axis is more like a step function[36]. Therefore, in the

current model, each sub-source has two different energy spectra, one for electrons inside and the other for electrons outside the treatment field. Parameters stored in the model are the minimum and maximum energies, number of energy bins as well as the relative fluence for each energy bin. The minimum and maximum energies correspond to the cutoff energies (ECUT or PCUT) and the incident energy used in the accelerator simulation. The number of bins is determined by the desired resolution. For example, if we want the uncertainty in the calculated depth of 50% dose, R_{50} , to be less than 1%, the uncertainty in the peak position of the energy spectrum should be within 1% and therefore the bin width should be smaller than 1% of the peak energy. For the 12 MeV beam, we used 128 bins and then the bin width is less than 0.1 MeV. This bin width is also found to be small enough to represent the peak width of the energy spectrum, which has a significant effect on the slope of the depth dose fall-off.

The planar fluence distribution for each sub-source is also derived from the simulated phase space data and recorded on the scoring plane using a grid scheme. Within each pixel of the grid, the planar fluence is assumed to be uniform. The dimension of a pixel is dependent on field size, usually from 1 to 3 mm. Parameters used to represent the planar fluence distribution include the treatment field dimension, the number of pixels and the relative intensity of each pixel, for each sub-source. It has been found that in general, the mean energy varied from position to position in the treatment field by less than 10% for a given sub-source[36]. Thus, it is reasonable to store and then sample the particle energy and position independently.

The angular distributions are not scored explicitly. They are reconstructed during the dose calculation, as described in the next section.

Finally, the simulated phase space information is represented with a set of parameters for each sub-source. The resultant source parameter file is much smaller (about 100 kilobytes) than the original phase space file (> 100 megabytes).

2.1.3 Beam reconstruction

When performing dose calculation in a patient's CT phantom, the source parameter file is used to reconstruct the phase space information (energy, position and direction) of every incident particle. The beam reconstruction process consists of the following steps:

1. Determine from which particular sub-source a particle originates by sampling from the relative source intensity of each sub-source.
2. Determine the position on the sub-source (excluding point sources) where the particle is emitted.
3. Sample the particle position on the scoring plane from the fluence pattern for the sub-source.
4. Sample the particle energy from the energy spectrum for the given sub-source based on the particle position (inside or outside the treatment field).
5. Determine the particle incident angle by connecting the position on the sub-source from where the particle is emitted and the position of the particle on the scoring plane.
6. Add in-air perturbation on the particle direction if it is an electron.

The sampling from the relative source intensity distribution is done by a table-look-up method[35]. All the sub-sources are in turn numbered from 1 to N (here $N = 4$ for accelerators with designs similar to the Varian Clinac 2100C machine) and the relative intensity of the i -th sub-source is $p_i (i = 1, \dots, N)$. The accumulative source intensity for the i -th sub-source, $P_i (= \sum_{j=1}^i p_j)$, is multiplied by a large integer M . The value of M is determined according to the desired sampling precision of the relative source intensity. For example, $M = 1000$ corresponds to the precision

of 0.1% in sampling from the relative source intensity distribution. Then, a one dimensional array of M elements is prepared by assigning value i to array elements from $INT(MP_{i-1})$ to $INT(MP_i)$, where the operator INT returns the integer part of a real number. During the beam reconstruction, a random integer number K between 1 and M is generated and the value of the K -th array element is the sub-source number where the particle is emitted. Such a table-look-up method is of very high sampling speed and efficiency. Its speed is also independent of the number of sub-sources. The sampling precision is usually adequate as long as an large enough array is used.

According to the energy spectra on the scoring plane, the bin number in which the particle energy falls is also sampled using the table-look-up method. An additional uniform sampling is done within the given energy bin to make the particle energy continuous.

The same table-look-up method is also used to sample the pixel number corresponding to a particle position on the scoring plane. Another sampling is performed uniformly to determine the particle's coordinates within the chosen pixel.

For the point sources, the incident angle of the particle is determined by constructing a ray line from the point source to the position of the particle on the scoring plane. For the square ring electron sources, we need to determine where the electron comes from on the ring. This is done in two steps. First, we determine from which edge of the square ring the electron is emitted. Second, we determine from where on the chosen edge the electron comes.

As illustrated in figure 1, a square ring of size $a \times a$ is located above the scoring plane at a distance d . We assume that the square ring edge emits electrons uniformly and isotropically. Under this approximation, the probability for an electron on the scoring plane to come from a point on the ring is proportional to the inverse square of the distance between the points on the ring and plane. This approximation greatly

simplifies the sampling process. It is found that the angular distribution of the scattered electrons reconstructed based on the fluence distribution on the scoring plane and the emitting position on the square ring source is reasonably accurate, although electrons scattered from the applicator scraper mainly correspond to electrons incident on the vertical face of the scraper and are dominantly forward directed[40]. Furthermore, the dose profile at the patient surface is greatly influenced by electrons scattered from the last scraper or cutouts, which are not included in the source model but will be accurately simulated with the patient CT phantom.

For an electron at position (x_0, y_0) on the scoring plane (see figure 1), the probability for it to have come from the i -th edge is given as

$$p'_i(x_0, y_0) \sim \frac{1}{C_i} \left[\arctan \left(\frac{x_0 + a/2}{C_i} \right) - \arctan \left(\frac{x_0 - a/2}{C_i} \right) \right] \quad \text{for } i = 1, 2 \quad (1)$$

$$p'_i(x_0, y_0) \sim \frac{1}{C_i} \left[\arctan \left(\frac{y_0 + a/2}{C_i} \right) - \arctan \left(\frac{y_0 - a/2}{C_i} \right) \right] \quad \text{for } i = 3, 4 \quad (2)$$

where

$$C_1 = \sqrt{(y_0 + a/2)^2 + d^2} \quad (3)$$

$$C_2 = \sqrt{(y_0 - a/2)^2 + d^2} \quad (4)$$

$$C_3 = \sqrt{(x_0 + a/2)^2 + d^2} \quad (5)$$

$$C_4 = \sqrt{(x_0 - a/2)^2 + d^2} \quad (6)$$

Using the probabilities given above, the edge from which the electron has come can be sampled. Then, the position (x, y) on the chosen edge is further sampled. For edges 1 and 2,

$$x = x_0 - C_i \cdot \tan \left[(1 - \xi) \cdot \arctan \left(\frac{x_0 + a/2}{C_i} \right) + \xi \cdot \arctan \left(\frac{x_0 - a/2}{C_i} \right) \right] \quad i = 1, 2 \quad (7)$$

$$y = \begin{cases} -a/2 & \text{for } i = 1 \\ a/2 & \text{for } i = 2 \end{cases} \quad (8)$$

and for edges 3 and 4,

$$x = \begin{cases} -a/2 & \text{for } i = 3 \\ a/2 & \text{for } i = 4 \end{cases} \quad (9)$$

$$y = y_0 - C_i \cdot \tan \left[(1 - \xi) \cdot \arctan \left(\frac{y_0 + a/2}{C_i} \right) + \xi \cdot \arctan \left(\frac{y_0 - a/2}{C_i} \right) \right] \quad (10)$$

$i = 3, 4$

where ξ is a random number uniformly distributed from 0 to 1.

After the electron position on the square ring is determined, the connection of this position to the position on the scoring plane gives the electron's incident direction, which needs to be additionally perturbed to address the in-air multiple scattering.

In a previous implementation of this model, the effect of electron multiple scattering in air as well as other materials on its path to the scoring plane was taken into account by sampling the electron perturbation angle from a Monte Carlo simulated angular distribution[36]. This angular distribution was stored while performing the Monte Carlo simulation for the accelerator and only included electrons falling into a small region (e.g., of 1 cm radius) around beam central axis. In the current work, the effect of in-air multiple scattering is considered more accurately using the Fermi-Eyges theory[2, 3]. The effect of other materials is considered by adding a parameter to the standard deviation of the angular distribution. The Fermi-Eyges theory is a well-known small-angle theory and can predict the multiple scattering effect of megavoltage electrons in air or other heavier materials as long as the electron effective pathlengths are small[41, 42].

Assume that an electron initially travels along the z axis. According to the Fermi-Eyges theory, the distributions for the projections of the polar angle, θ , on the $x - z$ plane, θ_x and on the $y - z$ plane, θ_y , are both Gaussian after electrons

travel a distance, and are given as[3, 42]

$$f(\theta_x) = \frac{1}{\sqrt{2\pi}\sigma_{\theta_x}} \exp\left(-\frac{\theta_x^2}{2\sigma_{\theta_x}^2}\right) \quad (11)$$

$$f(\theta_y) = \frac{1}{\sqrt{2\pi}\sigma_{\theta_y}} \exp\left(-\frac{\theta_y^2}{2\sigma_{\theta_y}^2}\right) \quad (12)$$

where σ_{θ_x} and σ_{θ_y} are the standard deviations for each Gaussian distribution, respectively. In a homogeneous material, and without the presence of an electromagnetic field, both standard deviations should be the same, so we let $\sigma = \sigma_{\theta_x} = \sigma_{\theta_y}$. Under the small angle approximation

$$\theta^2 = \theta_x^2 + \theta_y^2 \quad (13)$$

therefore the polar angle θ obeys a radial Gaussian distribution while the azimuthal angle ϕ is uniformly distributed in $[0, 2\pi]$. Hence the sampling method for these two angles is given as following

$$\theta = \sigma\sqrt{-2\ln\xi_1} \quad (14)$$

$$\phi = 2\pi\xi_2 \quad (15)$$

where ξ_1 and ξ_2 are random numbers uniformly distributed in $[0, 1]$.

According to the Fermi-Eyges theory, σ can be calculated as[3, 42]

$$\sigma^2 = A_0 - A_1^2/A_2 \quad (16)$$

where

$$A_i = \frac{1}{2} \int_0^l K(l-t)^i dt, \quad i = 0, 1, 2 \quad (17)$$

Here, K is the electron linear scattering power and l is the distance at which electrons travel. The electron linear scattering power can be fitted well using a simple formula proposed by Werner et al[43].

$$K(E) = \alpha E^{-\beta} \quad (18)$$

Using this formula we fitted the linear scattering power data in air supplied by ICRU Report 35[44] and found that $\alpha = 3.329 \times 10^{-3} \text{radian}^2/\text{cm}$ and $\beta = 1.638$. E is the electron energy in MeV and sampled from the energy spectrum at the scoring plane. The energy loss of electrons in air is usually very small and can be ignored when they travel from the virtual source to the scoring plane. The mean energy loss of 6 MeV electrons after traveling 100 cm in air is about 4% of its initial energy (estimated using the stopping power) and it is about 2% for 20 MeV electrons. Therefore σ can be given as

$$\sigma^2 = \frac{1}{8}K(E)l \quad (19)$$

which is a function of electron energy and the distance between the virtual source and the position on scoring plane. During beam reconstruction, according to the sampled electron energy, positions on the scoring plane and on the virtual source, σ can be calculated. Then using eqs.(14) and (15) θ and ϕ are sampled and a perturbation is added to the electron's incident direction.

The perturbation caused by in-air multiple scattering can be directly calculated using eq.(19) for electrons from the squaring ring sources. For direct electrons, there are other accelerator components in their paths from the virtual point source to the scoring plane in addition to the intervening air, such as the exit window, scattering foil, monitor chamber, mirror and protection window. The effect of these materials on electron angular distribution has been mainly included in the determination of the virtual electron point source position. We also need to take into account the angular perturbation caused by these materials. If we know precisely the material and thickness of these parts, we can calculate their effect on σ , as done by Keall and Hoban[41]. However, it is usually difficult for users to know this information about their accelerator when commissioning a Monte Carlo treatment planning system. Therefore, we introduce a factor k to account for the effect of these materials. For

direct electrons, σ is then given as

$$\sigma^2 = \frac{1}{8} K(E) l k \quad (20)$$

The factor k is determined by fitting the angular distribution calculated using Fermi-Eyes theory to that simulated with the Monte Carlo method for direct electrons. The introduction of k factor provides a potentially tunable parameter in the source model.

2.1.4 Model verification

The four-source model is verified dosimetrically by comparing the dose distributions in a water phantom calculated using the model with those calculated using the full phase space data. Dose distributions are calculated for various combinations of three electron energies (6, 12, and 20 MeV), three applicator sizes (6×6 , 10×10 , and 20×20 cm²), and two SSDs (100 cm and 120 cm).

The measurement of electron beam applicator factors (defined as the ratio of the open field dose in water at d_{max} for a given applicator to that of the reference applicator, typically the 10×10 or 15×15 cm², for the same beam energy) is done during accelerator commissioning for all energy/cone combinations. Therefore, the applicator factors will be supplied by the user when performing the model commissioning. Cutout factors (defined as the ratio of the dose in water at d_{max} for a blocked field to that of the open field for the same applicator and beam energy) are patient specific and not always easy to measure accurately for all clinical situations. Therefore, the model should be able to calculate cutout factors. To demonstrate this, we compare the model calculated cutout factors with those measured and calculated by Kapur et al using a full Monte Carlo simulation[45].

2.2 Beam Commissioning

The four-source model which is built using a Varian Clinac 2100C accelerator as the reference machine can be used to reconstruct electron beams from other Clinac 2100C accelerators by tuning the energy spectra in the model.

For accelerators with exactly the same design, the major different is the electron incident energy due to the on-site tuning to suit the user. This energy approximately corresponds to the maximum energy of all the stored energy spectra in the source model. It is found that the energy spectra for all sub-sources are very similar for different accelerators of the same type. When the incident energy is changed, the energy spectra can be approximated as stretched or compressed along the energy axis accordingly. The depth dose curve is very sensitive to the electron incident energy and therefore used to adjust the maximum energy, E_{max} , in the model. The relationship between the incident energy, E_{in} , and R_{50} has been studied by simulating the reference accelerator using a 10×10 cm² cone and 100 cm SSD with various incident energies. Then, the variation of E_{in} as a function of the variation of R_{50} is established for this type of accelerator. This relationship is used as a guide to tune the maximum energy in the model to commission a clinical beam.

The proposed commissioning approach can be summarized as follows:

1. Chose an accelerator as the reference machine for all other accelerators of the same design, and carefully perform full Monte Carlo simulations for the electron beams of various nominal energies from the reference machine with 10×10 cm² applicator.
2. Build the source models for the simulated beams based on the Monte Carlo phase space data, perform Monte Carlo dose calculation in water for 100 cm SSD, and record the maximum energy, $E_{max}^{(ref)}$, in the model and the $R_{50}^{(ref)}$ value for each beam.

3. For the beam to be commissioned, find the $R_{50}^{(mea)}$ value of the measured depth curve in water for 10×10 cm² applicator and 100 cm SSD.
4. Select the reference beam which has the same or closest nominal energy as the commissioning beam. Let $i = 0$, $E_{max}^{(i)} = E_{max}^{(ref)}$, and $R_{50}^{(i)} = R_{50}^{(ref)}$.
5. Calculate $\Delta R_{50}^{(i)} = R_{50}^{(i)} - R_{50}^{(mea)}$. If $\Delta R_{50}^{(i)} \leq \epsilon$, where ϵ is the pre-set convergence tolerance, stop iteration and use $E_{max}^{(i)}$ as the maximum energy in the source model for the commissioning beam; otherwise, go to the next step.
6. According to the relationship between ΔE_{in} and ΔR_{50} , calculate $\Delta E^{(i)}$ using $\Delta R_{50}^{(i)}$ and then calculate $E_{max}^{(i+1)} = E_{max}^{(i)} - \Delta E^{(i)}$.
7. Calculate the dose distribution using the source model with $E_{max}^{(i+1)}$ and find the corresponding $R_{50}^{(i+1)}$.
8. Let $i \leftarrow i + 1$; go back to step 5.

The first two steps only need to be do once for all accelerators of the same design. The convergence tolerance, ϵ , is set by the user, usually according to the estimated measurement error in R_{50} . For example, $\epsilon = 1$ mm is good enough in most clinical situations. The iteration process converges very fast, usually only two or three iterations are needed even for ϵ much smaller than 1 mm.

The commissioning approach has been applied to three electron beams, A, B, and C. The reference beam is the same for all three beams, which is from the reference Clinac 2100C accelerator with $E_{in} = 12.0$ MeV. Beam A and beam B are also from the reference machine but with E_{in} as 9.0 MeV and 15.0 MeV, respectively. These two beams are used to mimic two clinical beams of the same nominal energy as the reference beam but with significantly different incident energies. Of course, in reality, the electron incident energy will not be tuned so much (± 3 MeV). These two beams are used as extreme cases to test the commissioning approach. Beam C is a 9

MeV electron beam from another Clinac 2100C accelerator. The dose distributions for beam C are taken from the published data [38].

3 Results and Discussion

Figure 2 shows the effects of intervening air and sampling radius on the electron and photon virtual SSD determined with the pin-hole method for 6 MeV and 20 MeV beams. It can be seen that for photons and high energy electrons (20 MeV) effects of intervening air and sampling radius on the positions of virtual point sources are negligible. However, for low energy electrons (6 MeV), these effects are significant. Therefore, to obtain the accurate virtual electron point source position for low energy beams, the phase space simulated without intervening air should be used.

Figure 3 shows the comparison between the angular distributions for direct electrons in 6, 12 and 20 MeV beams calculated with the Fermi-Eyges theory and the Monte Carlo method. We can see that, in general, the fitted angular distributions based on the Fermi-Eyges theory match well with those calculated with the Monte Carlo simulation. We also notice that, at large angles the Fermi-Eyges theory slightly underestimates electron fluence due to the fact that it is a small-angle theory. We found that the small discrepancy does not have any significant effect on the final dose distributions. Therefore, the Fermi-Eyges theory with the fitted k factor can be used to account for the angular perturbations of electrons on their way from the source to the scoring plane.

The four-source model was tested by comparing the dose distributions calculated by the model with those calculated by full phase space data for various combinations of three electron energies (6, 12, and 20 MeV), three applicator sizes (6×6 , 10×10 , and 20×20 cm²), and two SSDs (100 cm and 120 cm). For all the cases tested, the agreement of 1~2%/1~2 mm has been achieved. Figure 4 shows the comparison for a 12 MeV beam with a 10×10 cm² cone at 100 cm SSD. Figure 5 gives the depth dose curves and dose profiles for 20 MeV beam with 6×6 cm² cone at 120 cm SSD, calculated with both the source model and full phase space data. All the

curves in figures 4 and 5 are normalized to the doses at d_{max} . The Monte Carlo uncertainty is always less than 0.5% and therefore not shown on the curves. In both figures the agreement between the full Monte Carlo simulations and the source model calculations is better than 1%/1 mm. Keep in mind that 20 cm air gap is rarely used in actual clinical situations. Therefore, we have demonstrated that the simplified four-source model can be used for accurate dose calculations even for extreme cases (such as very large extended SSDs).

The capability of the model for calculating the relative beam output was also tested. Table 1 shows cutout factors for various square inserts in a 10×10 cm² applicator for 6, 12 and 20 MeV electron beams. It is found that the cutout factors calculated with the four-source model are within about $\pm 2\%$ compared to the measured values except for one case where we see 2.5% difference. This is at about the same accuracy level as the full Monte Carlo simulation and considered to be acceptable for clinical use.

The relationship between E_{in} and R_{50} for the reference accelerator with a 10×10 cm² cone and 100 cm SSD is shown in figure 6. A linear relationship was found and fitted as

$$E_{in} = 2.597 R_{50} + 0.633 \quad (21)$$

It gives the relationship between the variation in the incident energy and the variation in R_{50} as

$$\Delta E_{in} = 2.597 \Delta R_{50} \quad (22)$$

Eq. (22) is used for tuning the maximum energy in the source model to match the measured depth dose curves when commissioning a clinical beam.

Figure 7 shows the dose distributions for the reference beam, beam A, and beam B with the applicator size of 10×10 cm² and SSD of 100 cm. All the curves are

normalized to the dose at d_{max} . The statistical uncertainty (1σ) in all the Monte Carlo dose calculations was kept to be smaller than 0.5%, therefore, the error bars are smaller than the symbol size and not shown on the curves. The maximum energy in the source model was adjusted to 8.87 MeV to match the dose distributions of the beam A ($E_{in} = 9.0$ MeV) and to 15.17 MeV to match the dose distributions of the beam B ($E_{in} = 15.0$ MeV). The difference between the depth dose curves calculated by the adjusted models and the full Monte Carlo simulation is always less than 0.5% for both beam A and beam B. For dose profiles, the difference is usually less than 1% except that in the shoulder region for beam B the difference is about 2%.

Figure 8 shows the dose distributions for the reference beam and beam C with the applicator size of 10×10 cm² and SSD of 100 cm. Again, the curves are normalized to the dose at d_{max} and the Monte Carlo uncertainty is lower than 0.5%. In this case, the maximum energy in the source model was adjusted to 11.25 MeV. The dose distributions calculated by the source model with the adjusted maximum energy agree very well (1%/1 mm) with the published data [38].

Table 2 gives E_{in} and R_{50} for the reference and Monte Carlo simulated beams, and E_{max} and R_{50} for the adjusted source models. For the reference beam, E_{max} was directly obtained from the full Monte Carlo simulation. For beam C, E_{in} is unknown. In this study, we set $\epsilon = 0.01$ cm. Therefore, the R_{50} 's calculated using the adjusted source model match with the full Monte Carlo simulation to within 0.01 cm. Of course, we will not use such a small ϵ in real clinical applications since it is much smaller than the measurement uncertainty in R_{50} . Here, we just want to demonstrate the capability of the method to reproduce R_{50} accurately.

We have applied the commissioning approach to electron beams from a Clinac 2300C/D accelerator in our institution. The reference machine is still the same Clinac 2100C accelerator. These two machines are sufficiently similar to each other in treatment head geometry. Their dosimetric characteristics are very close to each

other due to the beam tuning during linac acceptance. Therefore, it is not surprising to see that the dose distributions calculated with the adjusted source model agree well (within 1~2% or 1~2 mm) with the measured data.

These preliminary results have shown that the proposed hybrid commissioning approach can be used for accelerators of the same design to account for the dosimetric variations mainly caused by the on-site tuning of the electron incident energy. The capability of the approach to handle large variation in the electron incident energy has been demonstrated. It is believed that for most clinical accelerators of the same type, their treatment head designs are exactly the same or at least very similar, therefore the dosimetric difference can usually be traced back to the difference in the electron incident energy. Therefore, the current approach should be applicable in most clinical situations. In the future work, the method will be evaluated under more critical conditions, such as small field sizes, extended SSD, and heterogeneous phantoms.

The general idea proposed here should also work for other types of accelerators, although we have selected the Varian Clinac 2100C accelerators in the current study. For each type of accelerator, a reference machine should be carefully simulated using the Monte Carlo method. A source model, which may consist of a different number of sub-sources, can be established based on the simulated data. Then, the maximum energy in the model can be adjusted to commission electron beams from other accelerators of the same type.

In some situations, the proposed commissioning approach may not be directly applicable. For example, the measured dose distributions used for commissioning more or less contain measurement errors, depending on the measurement techniques and the experience of the person who performs the measurements. Since only the maximum energy is the adjustable parameter in the current source model, our approach may not be able to exactly match the measured data. Occasionally, an accelerator

used in the clinic may differ from its original design in addition to the electron incident energy. Some parts in the accelerator treatment head may be replaced with non-standard ones. In this case, we can always perform a full Monte Carlo simulation for this unique accelerator and build its own source model. Alternatively, we can make the present approach more versatile to handle those situations. More parameters in the source model other than the maximum energy, such as the relative intensity of each sub-source, the k factor for in-air perturbation for the direct electrons, and the field size, can be adjusted to match the measured dose distributions. For example, the adjustment of the relative intensity of the photon source will ensure a good match to the bremsstrahlung tail in the depth dose curve. If some of the materials in the paths of direct electrons, such as the scattering foil, monitor chamber or mirror, are different from those used in the reference accelerator, the adjustment of the k factor can yield a better estimation of the electron angular perturbation. The adjustment of the field size in the source model should recover the measurement error in the width of the dose profiles (e.g., errors of the order of about 1 mm are not rare in a clinical situation). In summary, the introduction of more adjustable parameters in the source model will make the current commissioning approach more powerful. This possibility will be investigated in our future study.

4 Conclusions

A hybrid commissioning approach based on a multiple source model has been proposed for Monte Carlo treatment planning. It has been demonstrated that a simplified four-source model can be used to generate accurate Monte Carlo dose distributions for electron beams from Varian Clinac 2100C accelerators. The model includes a point electron source for direct electrons and electrons scattered from primary collimator and jaws, a point photon source for all contaminant bremsstrahlung photons, and two square ring electron sources representing electrons scattered from two scrapers (other than the last scraper) of the Varian electron applicator (type III). It was found that, the position of the virtual point source can be determined accurately using the pin-hole method for photons in all cases and electrons in high energy beams. For low energy beams, we should use the Monte Carlo phase space data which is obtained by simulating the treatment head with the intervening air replaced by vacuum. We also found that the in-air perturbation on the electron incident direction can be properly accounted for using the Fermi-Eyges model. The source model which was built based on the simulated phase space data for the reference accelerator can be used for other accelerators of the same type, by simply adjusting the energy spectra in the model. The capability of this commissioning approach for handling large variation in the electron incident energy has been demonstrated.

Acknowledgement

The authors are grateful to the referees, Drs. Art Boyer, Alan Nahum, Alex Biela-jew, David Findley, Gary Luxton, Ed Mok, Todd Pawlicki and Frank Verhaegen for useful comments on the manuscript. The authors would also like to thank Dr. Sam Brain, Todd Koumian and Behrooz Tofighrad for computer support, Dr. Dave Rogers and his OMEGA/BEAM team at the National Research Council of Canada for the Monte Carlo simulation system, and Eva Papiez for supplying some measured data. The work was supported in part by the US Army breast cancer research program (BC971292), the NCI grant CA78331 and a consortium agreement with the NumeriX Cooperation.

References

- [1] K. R. Hogstrom, M. D. Mills, and P. R. Almond. Electron beam dose calculations. *Phys. Med. Biol.*, 26:445–459, 1981.
- [2] E. Fermi. in B. Rossi and K. Greisen, Cosmic-ray theory. *Rev. Mod. Phys.*, 13:265–268, 1941.
- [3] L. Eyges. Multiple scattering with energy loss. *Physics Review*, 74:1534–1535, 1948.
- [4] J. Cygler, J. J. Battista, J. W. Scrimger, E. Mah, and J. Antolak. Electron dose distributions in experimental phantoms: a comparison with 2D pencil beam calculations. *Phys. Med. Biol.*, 32:1073–1086, 1987.
- [5] E. Mah, J. Antolak, J. W. Scrimger, and J. J. Battista. Experimental evaluation of a 2D and a 3D electron pencil beam algorithm. *Phys. Med. Biol.*, 34:1179–1194, 1989.
- [6] I. Kawrakow, M. Fippel, and K. Friedrich. 3D electron dose calculation using a voxel based Monte Carlo algorithm (VMC). *Med. Phys.*, 23(4):445–457, 1996.
- [7] C. M. Ma, E. C. Mok, A. Kapur, T. Pawlicki, D. O. Findley, S. Brain, K. Forster, and A. L. Boyer. Clinical implementation of a Monte Carlo treatment planning system. *Med. Phys.*, 26(10):2133–2143, 1999.
- [8] M. A. Ebert and P. W. Hoban. Possibilities for tailoring dose distributions through the manipulation of electron beam characteristics. *Phys. Med. Biol.*, 42(11):2065–2081, 1997.

- [9] M. G. Karlsson, M. Karlsson, and B. Zackrisson. Intensity modulation with electrons: calculations, measurements and clinical applications. *Phys. Med. Biol.*, 43(5):1159–1169, 1998.
- [10] M. Åsell, S. Hyödynmaa abd S. Söderström, and A. Brahme. Optimal electron and combined electron and photon therapy in the phase space of complication-free cure. *Phys. Med. Biol.*, 44:235–252, 1999.
- [11] A. E. Nahum. Monte Carlo electron transport simulation II: Application to dose planning. In A. E. Nahum, editor, *The Computation of Dose Distributions in Electron Beam Radiotherapy*, pages 319–340. Umeå University, Umeå, Sweden, 1985.
- [12] T. M. Jenkins, W. R. Nelson, A. Rindi, A. E. Nahum, and D. W. O. Rogers. *Monte Carlo transport of electrons and photons*. Plenum Press, New York, 1988.
- [13] T. R. Mackie. Applications of the Monte Carlo method in radiotherapy. In K. Kase, B. Bjärngard, and F. H. Attix, editors, *Vol. III of Dosimetry of Ionizing Radiation*, pages 541–620. Academic Press, New York, 1990.
- [14] D. W. O. Rogers and A. F. Bielajew. Monte Carlo techniques of elctron and photon transport for radiation dosimetry. In K. R. Case, B. E. Bjarngard, and F. H. Attix, editors, *Vol. III of The Dosimetry of Ionizing Radiation*, pages 427–539. Academic, New York, 1990.
- [15] D. W. O. Rogers. The role of Monte Carlo simulation of electron transport in radiation dosimetry. *International Journal of Applied Radiation and Isotopes*, 42:965–974, 1991.
- [16] P. Andreo. Monte Carlo techniques in medical radiation physics. *Phys. Med. Biol.*, 36(7):861–920, 1991.

- [17] C. Manfredotti, U. Nastasi, R. Ragona, and S. Anglesio. Comparison of three dimensional Monte Carlo simulation and the pencil beam algorithm for an electron beam from a linear accelerator. *Nucl. Instr. Meth.*, A255:355–359, 1987.
- [18] C. Manfredotti, U. Nastasi, R. Marchisio, C. Ongaro, G. Gervino, R. Ragona, S. Anglesio, and G. Sannazzari. Monte Carlo simulation of dose distribution in electron beam radiotherapy treatment planning. *Nucl. Instr. Meth.*, A291:646–654, 1990.
- [19] A. A. al-Beteri and D. E. Raeside. Optimal electron-beam treatment planning for retinoblastoma using a new three-dimensional Monte Carlo-based treatment planning system. *Med. Phys.*, 19(1):125–135, 1992.
- [20] H. Neuenschwander, T. R. Mackie, and P. J. Reckwerdt. MMC - a high-performance Monte Carlo code for electron beam treatment planning. *Phys. Med. Biol.*, 40(4):543–574, 1995.
- [21] P. J. Keall and P. W. Hoban. Super-Monte Carlo: a 3-D electron beam dose calculation algorithm. *Med. Phys.*, 23(12):2023–2034, 1996.
- [22] B. Faddegon, J. Balogh, R. Mackenzie, and D. Scora. Clinical considerations of Monte Carlo for electron radiotherapy treatment planning. *Radiation Physics and Chemistry*, 53:217–227, 1998.
- [23] C. M. Ma and A. E. Nahum. Calculation of absorbed dose ratios using correlated Monte Carlo sampling. *Med. Phys.*, 20:1189–1199, 1993.
- [24] M. A. Holmes, T. R. Mackie, W. Sohn, P. J. Reckwerdt, T. J. Kinsella, A. F. Bielajew, and D. W. O. Rogers. The application of correlated sampling to the computation of electron beam dose distributions in heterogeneous phantoms using the Monte Carlo method. *Phys. Med. Biol.*, 38(6):675–688, 1993.

- [25] A. F. Bielajew. Monte Carlo modeling in external electron-beam radiotherapy - Why leave it to chance? In A. R. Hounsell, J. M. Wilkinson, and P. C. Williams, editors, *Proceedings of The 11th International Conference on The Use of Computers in Radiation Therapy*, pages 2–5, Manchester, UK, 1994. North Western Medical Physics Department, Christie Hospital NHS Trust.
- [26] R. Mohan. Why Monte Carlo? In D. D. Leavitt and G. Starkschall, editors, *Proceedings of The 12th International Conference on The Use of Computers in Radiation Therapy*, pages 16–18, Salt Lake City, Utah, USA, 1997. Medical Physics Publishing.
- [27] C. L. Hartmann-Siantar, P. M. Bergstrom, W. P. Chansler, L. Chase, L. J. Cox, T. P. Daly, D. Garrett, S. M. Hornstein, R. K. House, E. I. Moses, R. W. Patterson, J. A. Rathkopf, and A. S. von Wittenau. Lawrence Livermore National Laboratory’s PEREGRINE project. In D. D. Leavitt and G. Starkschall, editors, *Proceedings of The 12th International Conference on The Use of Computers in Radiation Therapy*, pages 19–22, Salt Lake City, Utah, USA, 1997. Medical Physics Publishing.
- [28] J. J. DeMarco, T. D. Solberg, and J. B. Smathers. A CT-based Monte Carlo simulation tool for dosimetry planning and analysis. *Med. Phys.*, 25(1):1–11, 1998.
- [29] L. Wang, C. S. Chui, and M. Lovelock. A patient-specific Monte Carlo dose-calculation method for photon beams. *Med. Phys.*, 25(6):867–878, 1998.
- [30] J. O. Deasy, P. R. Almond, and M. T. McEllistrem. Measured electron energy and angular distributions from clinical accelerators. *Med. Phys.*, 23(5):675–684, 1996.

- [31] J. J. Janssen, E. W. Korevaar, L. J. van Battum, P. R. M. Storchi, and H. Huizenga. Clinical electron beam dose calculations with the Phase Space Evolution model. In D. D. Leavitt and G. Starkschall, editors, *Proceedings of The 12th International Conference on The Use of Computers in Radiation Therapy*, pages 195–196, Salt Lake City, Utah, USA, 1997. Medical Physics Publishing.
- [32] M. Udale. A Monte Carlo investigation of surface doses for broad electron beams. *Phys. Med. Biol.*, 33:939–954, 1988.
- [33] M. Udale-Smith. Monte Carlo calculations of electron beam parameters for three Philips linear accelerators. *Phys. Med. Biol.*, 37:85–105, 1992.
- [34] D. W. O. Rogers, B. A. Faddengon, G. X. Ding, C. M. Ma, J. We, and T. R. Mackie. BEAM: A Monte Carlo code to simulate radiotherapy treatment units. *Med. Phys.*, 22(5):503–524, 1995.
- [35] C. M. Ma and D. W. O. Rogers. Beam characterization: a multiple-source model. Technical Report PIRS 509d, National Research Council of Canada, Ottawa, Canada, 1995.
- [36] C. M. Ma, B. A. Faddegon, D. W. O. Rogers, and T. R. Mackie. Accurate characterization of Monte Carlo calculated electron beams for radiotherapy. *Med. Phys.*, 24(3):401–416, 1997.
- [37] C. M. Ma. Characterization of computer simulated radiotherapy beams for Monte-Carlo treatment planning. *Radiation Physics and Chemistry*, 53:329–344, 1998.
- [38] G. X. Ding and D. W. O. Rogers. Energy spectra, angular spread and dose distributions of electron beams from various accelerators used in radiotherapy.

Technical Report PIRS 0439, National Research Council of Canada, Ottawa, Canada, 1995.

- [39] AAPM TG-25. Clinical electron beam dosimetry: Report of AAPM Radiation Therapy Committee Task Group No. 25. *Med. Phys.*, 18:73–109, 1991.
- [40] M. A. Ebert and P. W. Hoban. A Monte Carlo investigation of electron-beam applicator scatter. *Med. Phys.*, 22(9):1431–1435, 1995.
- [41] P. J. Keall and P. W. Hoban. Calculating the angular standard deviation of electron beams using Fermi-Eyges theory. *Phys. Med. Biol.*, 41:1511–1515, 1996.
- [42] S. B. Jiang, Z. M. Luo, and K. M. Ayyangar. Incorporation of the electron energy-loss straggling into the Fermi-Eyges equation. *Radiation Physics and Chemistry*, 53:477–482, 1998.
- [43] B. L. Werner, F. M. Khan, and F. C. Deibel. A model for calculating electron beam scattering in treatment planning. *Med. Phys.*, 9(2):180–187, 1982.
- [44] ICRU 35. *Radiation Dosimetry: Electron Beams with Energies Between 1 and 50 MeV*. International Commission on Radioation Units and Measurements, Bethesda, MA, 1984.
- [45] A. Kapur, C. M. Ma, E. C. Mok, D. O. Findly, and A. L. Boyer. Monte Carlo calculations of electron beam output factors for a medical linear accelerator. *Phys. Med. Biol.*, 43:3479–3494, 1998.

Table 1: The electron cutout factors for various square inserts in $10 \times 10 \text{ cm}^2$ applicator for 6, 12 and 20 MeV beams calculated with the source model and the full phase space data and compared with the measurement of Kapur et al[45]. The values in parenthesis indicate the difference of the data calculated with the source model or the full phase space from the measured data.

Energy (MeV)	Insert (cm^2)	Cutout factor		
		Source model	Full phase space	Measurement
6	2×2	0.803 (2.5%)	0.765 (-1.3%)	0.778
	3×3	0.930 (0.3%)	0.923 (-0.4%)	0.927
	4×4	0.970 (-1.8%)	0.982 (-0.6%)	0.988
	8×8	1.002 (-0.1%)	1.005 (0.2%)	1.003
12	2×2	0.881 (-0.8%)	0.861 (-2.8%)	0.889
	3×3	0.908 (-2.0%)	0.930 (0.2%)	0.928
	4×4	0.942 (-2.1%)	0.956 (-0.7%)	0.963
	8×8	0.999 (0.8%)	1.002 (1.1%)	0.991
20	2×2	0.963 (-1.1%)	0.957 (-1.9%)	0.976
	3×3	0.989 (-0.4%)	0.968 (-2.5%)	0.993
	4×4	0.993 (-1.8%)	0.993 (-1.8%)	1.011
	8×8	0.999 (-0.5%)	0.993 (-1.1%)	1.004

Table 2: Some parameters for the full Monte Carlo simulations and the adjusted source models. E_{in} is the electron incident energy at the exit window in the simulation. E_{max} is the maximum energy in the source model. R_{50} is the depth of 50% dose of the depth dose curve in water for 10×10 cm² applicator and 100 cm SSD. A source model was built based on the full Monte Carlo simulation of the reference beam. For beams to be commissioned (A, B, and C), E_{max} in the model was adjusted to match the corresponding R_{50} from the Monte Carlo simulation.

Beam tested	MC simulation		Source model	
	E_{in} (MeV)	R_{50} (cm)	E_{max} (MeV)	R_{50} (cm)
Reference	12.0	4.397	12.00	4.397
Beam A	9.0	3.197	8.87	3.192
Beam B	15.0	5.622	15.17	5.624
Beam C	unknown	4.116	11.25	4.119

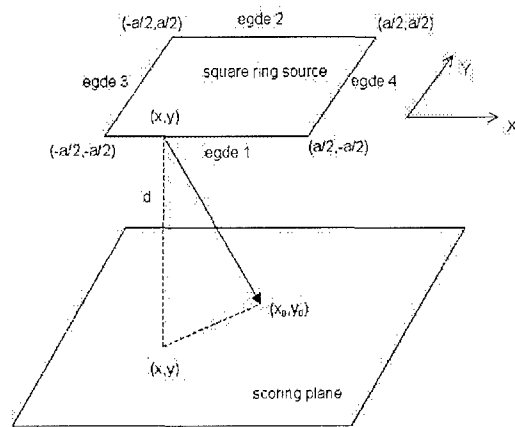


Figure 1: A diagram for illustrating the sampling algorithm from a square ring source. The origin of the coordinate system is at the center of the square ring.

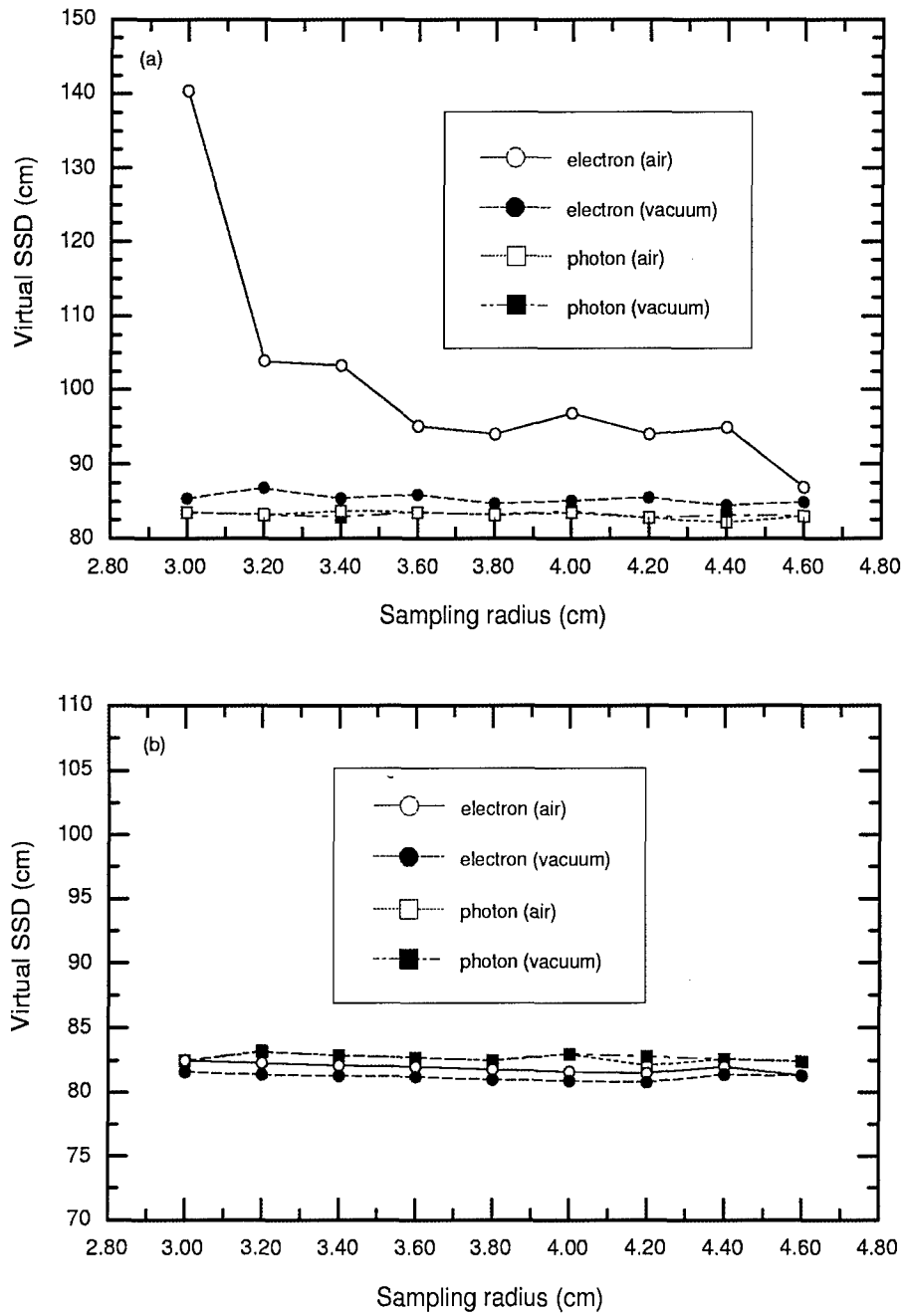


Figure 2: Effects of intervening air and sampling radius on virtual SSD (defined here as the distance from the point source to the scoring plane) for the electron point source determined with the pin-hole method. (a) 6 MeV; (b) 20 MeV.

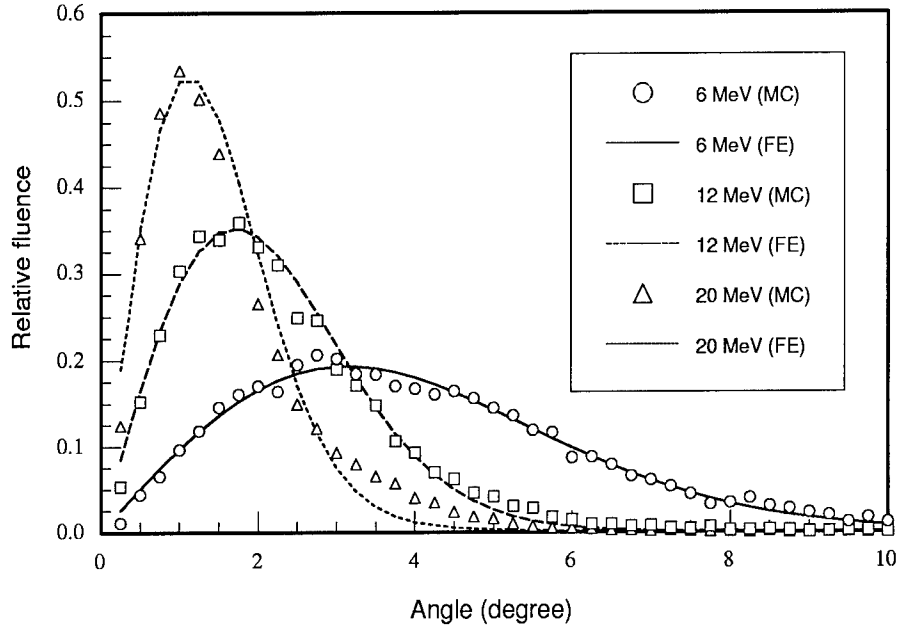


Figure 3: Angular distributions for direct electrons calculated using the Fermi-Eyges theory and the Monte Carlo method. Beam energies are (a) 6 MeV, (b) 12 MeV and (c) 20 MeV. The fitted k factor is 1.540 for 6 MeV, 1.501 for 12 MeV and 1.571 for 20 MeV. Each distribution is normalized to have unit area under the curve.

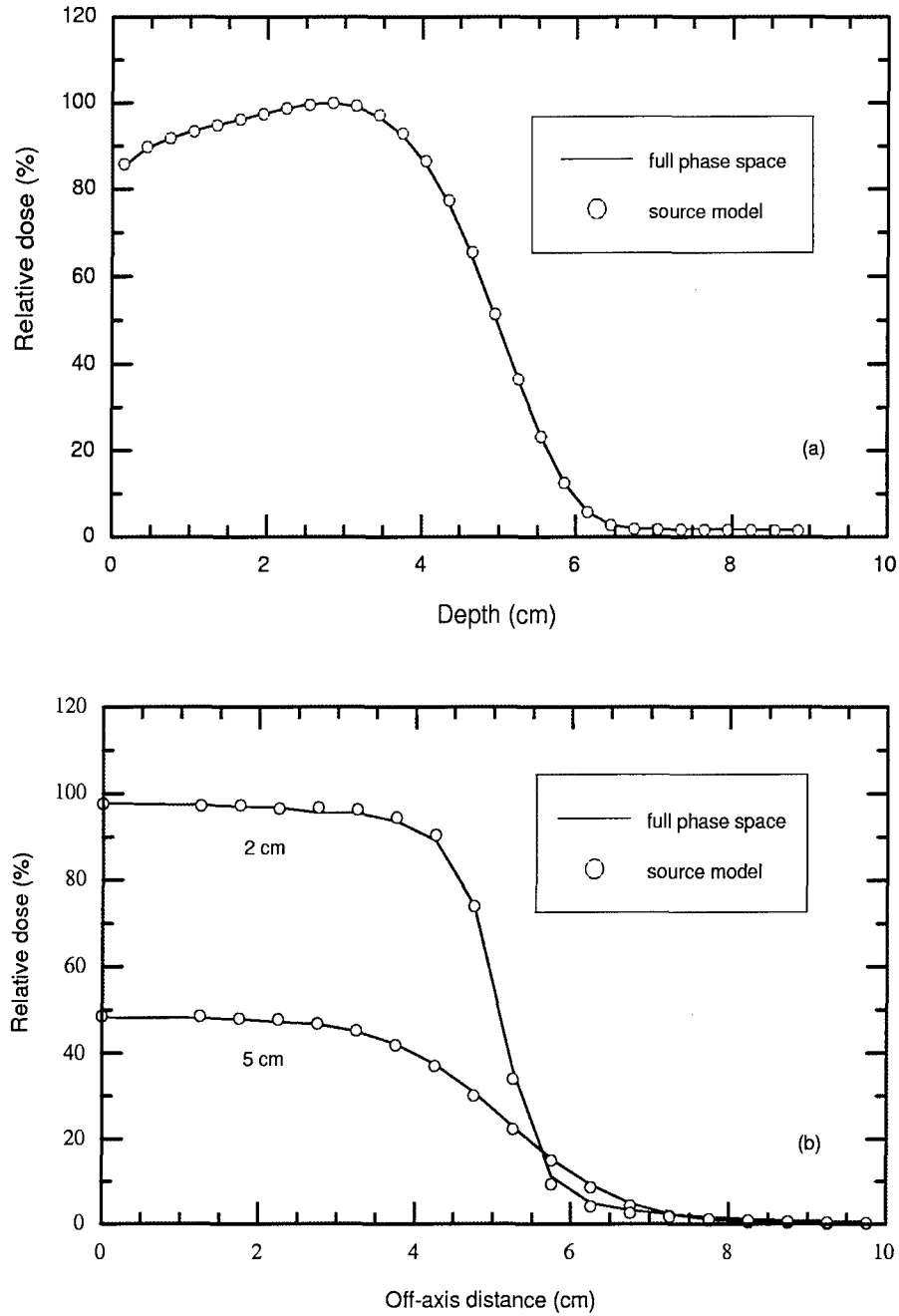


Figure 4: Dose distributions in water for 12 MeV electron beam with $10 \times 10 \text{ cm}^2$ applicator at 100 cm SSD, calculated with full phase space data and source model: (a) depth dose distributions; (b) dose profiles at depths of 2 cm and 5 cm. Curves are normalized to the dose at d_{max} .

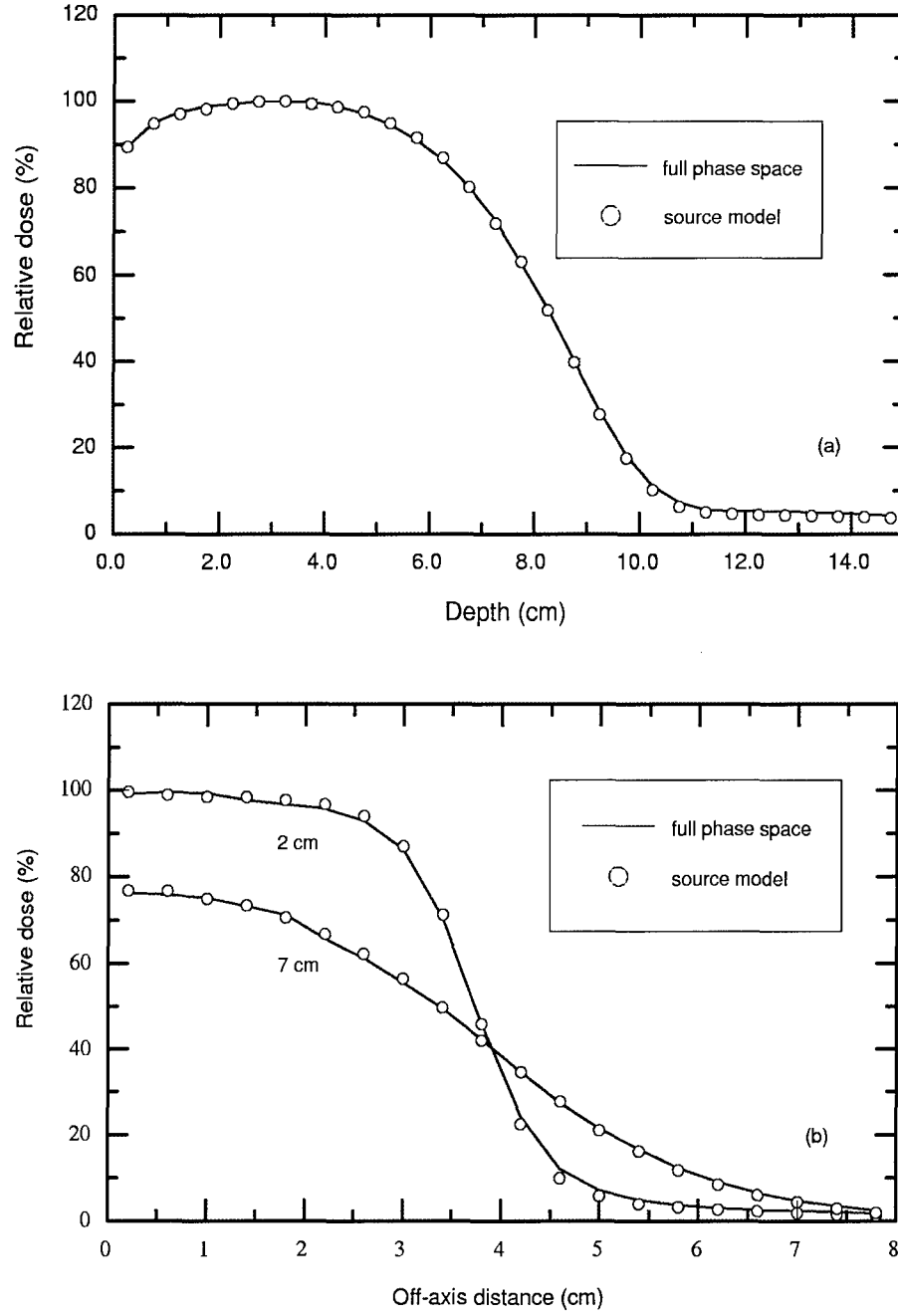


Figure 5: Dose distributions in water for 20 MeV electron beam with $6 \times 6 \text{ cm}^2$ applicator at 120 cm SSD, calculated with full phase space data and source model: (a) depth dose distributions; (b) dose profiles at depths of 2 cm and 7 cm. Curves are normalized to the dose at d_{max} .

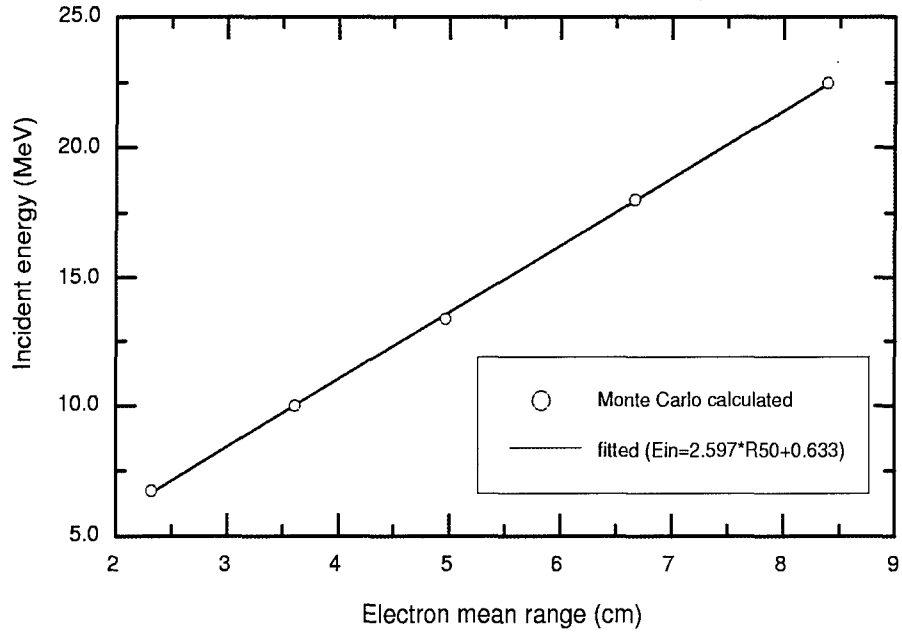
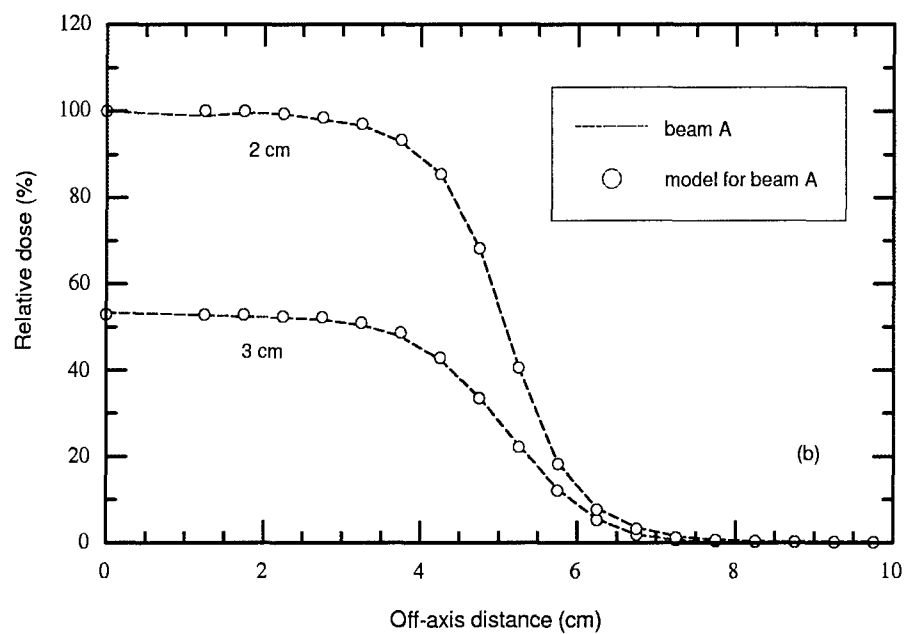
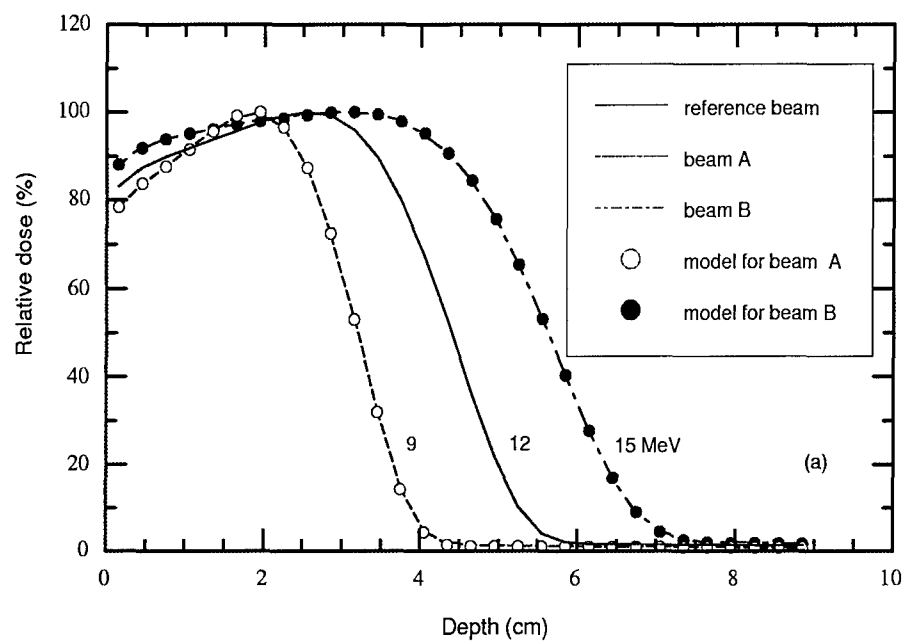


Figure 6: The relationship between electron incident energy at accelerator exit window (E_{in}) and the depth of 50% dose (R_{50}) for electron beams from the reference accelerator with $10 \times 10 \text{ cm}^2$ applicator and 100 cm SSD. Symbols are calculated with Monte Carlo simulation of the accelerator treatment head. Solid line is the fitted result with formula $E_{in} = 2.597R_{50} + 0.633$.



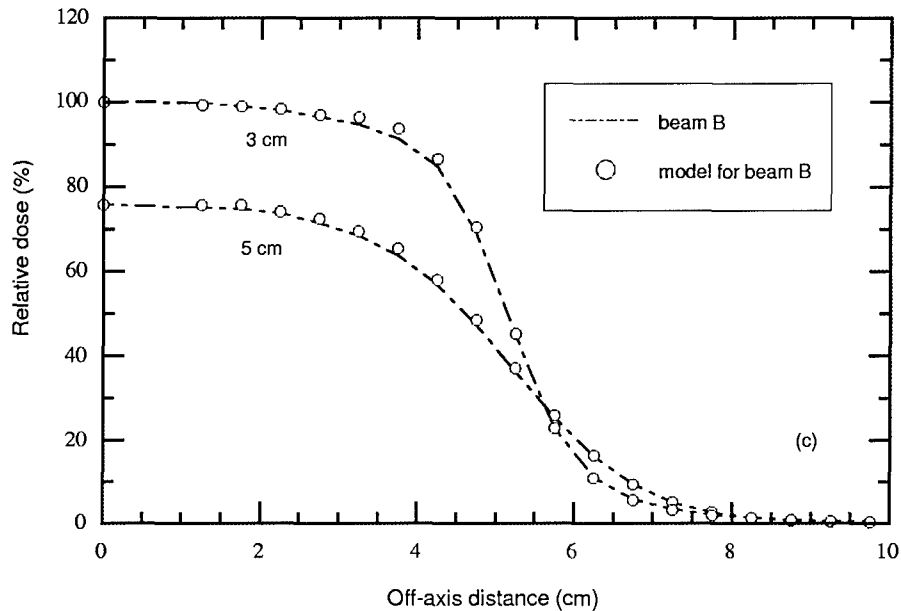


Figure 7: Dose distributions in water for electron beams from the reference accelerator with 10×10 cm² applicator and at 100 cm SSD. The reference beam has the electron incident energy of 12.0 MeV. A source model was built based on the Monte Carlo simulation of the reference beam. The maximum energy of the energy spectra in the model was adjusted to 8.87 MeV to match the beam A (with $E_{in} = 9.0$ MeV) and 15.17 MeV to match the beam B (with $E_{in} = 15.0$ MeV). Lines are dose distributions from the full Monte Carlo simulations. Symbols are data calculated by the source model with adjusted maximum energies. All data are normalized to the doses at d_{max} . (a) Depth dose distributions; (b) dose profiles at depths of 2 cm and 3 cm for beam A; (c) dose profiles at depths of 3 cm and 5 cm for beam B.

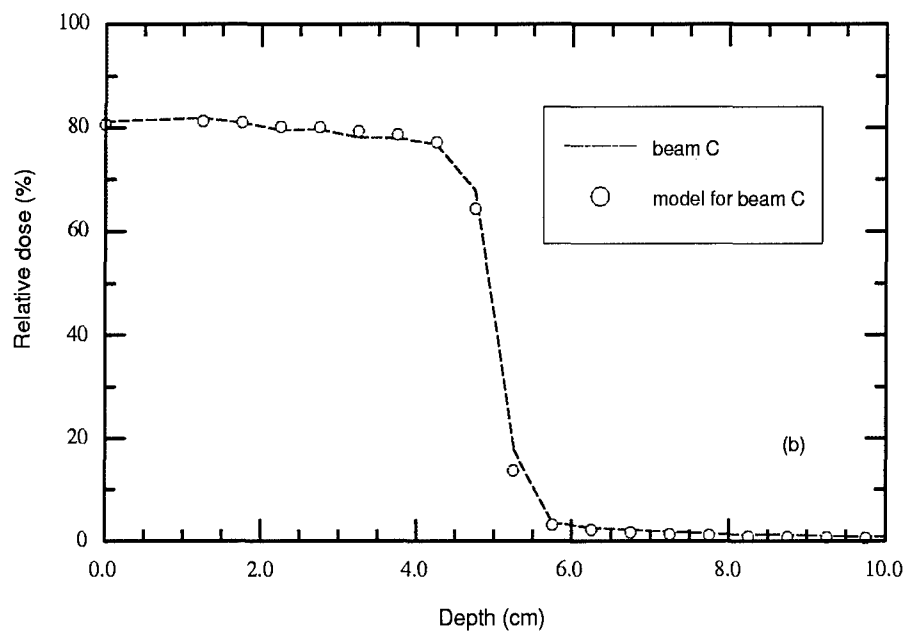
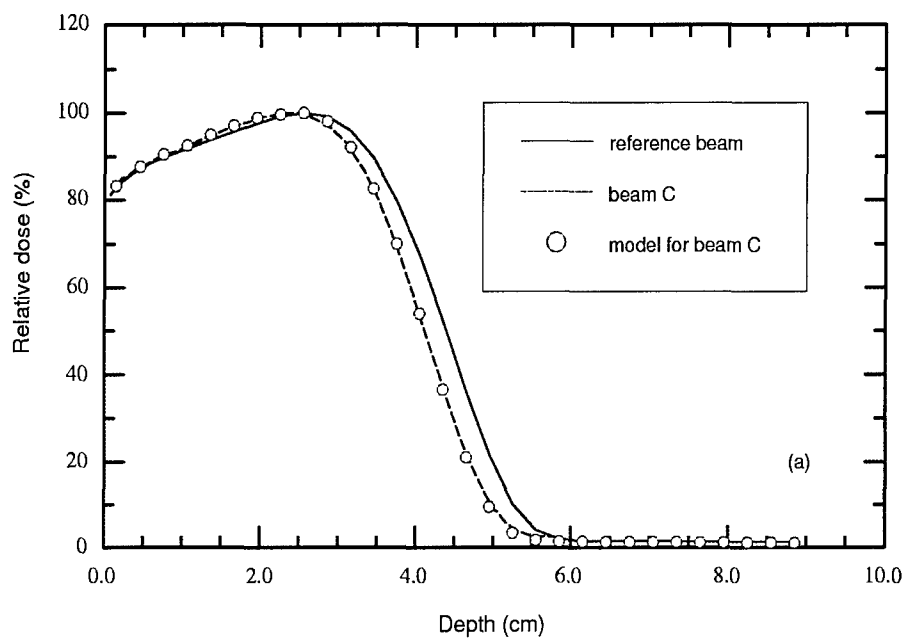


Figure 8: Dose distributions in water for electron beams with 10×10 cm² applicator and at 100 cm SSD. The reference beam (solid line) is from a Clinac 2100C accelerator with $E_{in} = 12.0$ MeV. The dose distributions for beam C (dashed lines) is taken from the published data for a 9 MeV beam from another Clinac 2100C accelerator with type III applicator [38]. A source model built based on the Monte Carlo simulation of the reference beam is used to match beam C by adjusting the maximum energy to 11.25 MeV (open circles). All data are normalized to the dose at d_{max} . (a) Depth dose distributions; (b) dose profiles at depth of 0.1 cm.